

**A NUMERICAL STUDY OF HEAT TRANSFER AND FLUID
FLOW IN A CORRUGATED CHANNEL**

SHOHEL MAHMUD



DEPARTMENT OF MECHANICAL ENGINEERING
BANGLADESH UNIVERSITY OF ENGINEERING AND TECHNOLOGY
DHAKA, BANGLADESH



A NUMERICAL STUDY OF HEAT TRANSFER AND FLUID FLOW IN A CORRUGATED CHANNEL

By
SHOHEL MAHMUD
B.Sc. Engg. (Mech.)

A thesis
Submitted to the Department of Mechanical Engineering in partial fulfilment of the requirements
for
the degree of Master of Science in Mechanical Engineering.



BANGLADESH UNIVERSITY OF ENGINEERING AND TECHNOLOGY,
Dhaka, Bangladesh.

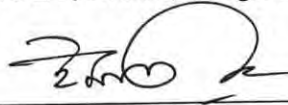
October, 1999

RECOMMENDATION OF THE BOARD OF EXAMINERS

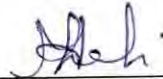
The board of examiners hereby recommends to the Department of Mechanical Engineering, BUET, Dhaka, the acceptance of this thesis, “ **A NUMERICAL STUDY OF HEAT TRANSFER AND FLUID FLOW IN A CORRUGATED CHANNEL**”, submitted by Shohel Mahmud, in partial fulfillment of the requirements for the degree of Master of Science in Mechanical Engineering.



Chairman : **Dr. A. K. M. Sadrul Islam**
Professor
Department of Mechanical Engineering
BUET, Dhaka, Bangladesh



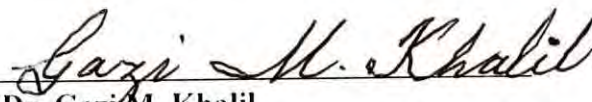
Member : **Dr. Md. Imtiaz Hossain**
Professor and Head
Department of Mechanical Engineering
BUET, Dhaka, Bangladesh



Member : **Dr. Mohammad Ali**
Assistant Professor
Department of Mechanical Engineering
BUET, Dhaka, Bangladesh



Member : **Dr. C. M. Feroz**
Assistant Professor
Department of Mechanical Engineering
BUET, Dhaka, Bangladesh



Member (External) : **Dr. Gazi M. Khalil**
Professor
Department of Naval Architecture and
Marine Engineering
BUET, Dhaka, Bangladesh

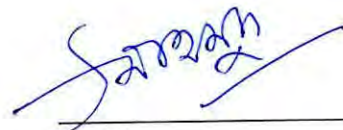
CERTIFICATE OF RESEARCH

This is to certify that the work presented in this dissertation is the outcome of the investigation carried out by the author under the supervision of Dr. A.K. Sadrul Islam, Professor, Department of Mechanical Engineering, Bangladesh University of Engineering and Technology (BUET), Dhaka, Bangladesh and that it has not been submitted anywhere for the award of any degree or diploma.



Supervisor

Dr. A.K.M. Sadrul Islam



Author

Shohel Mahmud

ACKNOWLEDGEMENT

The author wishes to express his deep gratitude and indebtedness to Dr. A.K.M. Sadrul Islam, Professor, Department of Mechanical Engineering, Bangladesh University of Engineering and Technology (BUET), Dhaka for his supervision, guidance, invaluable suggestions and constructive criticism throughout this investigation and specially grateful to him for showing the way of go inside the beauty of CFD.

ABSTRACT

Hydrodynamic and thermal characteristics are investigated numerically in the present research work. The integral forms of governing equations are discretized using control volume based Finite Volume method with collocated variable arrangement. Simple algorithm is used and TDMA solver is applied for solution of system of equations. Both axisymmetric and plane geometry are taken for study. Effect of surface waviness, determined by wavelength-amplitude ratio λ/a ($=L^*$), on flow and thermal field is extensively studied in the present investigation. The simulation work has been carried out for $L^*=11.0, 13.0, 15.0, 17.0, 19.0, 21.0, 23.0, 25.0, 30.0$ for a Reynolds number range 50 to 2000 for axisymmetric geometry. Steady-laminar flow condition is assumed throughout the simulation. Results are presented in the form of streamfunction, isothermal lines, velocity & vorticity profiles, change of mean friction factor, variation in skin friction, local and average Nusselt number with Reynolds number, wave number and L^* . For a particular geometry, lengths of circulation zone increase with Reynolds number and approach a limiting value for higher Reynolds number. Wall shear stress in the bulge part of the channel shows smaller values that affect largely heat transfer and Nusselt number shows minimum values in this region. This circulation zone dramatically increases with the increase of surface waviness showing high mean friction factor per wavelength. Mean friction factor shows linear variation with Reynolds number. A correlation is proposed for calculating friction factor in the form $f=C/(Re)^m$, where C and m represents two polynomials of degree 4 and 2 respectively with independent variable for L^* . This shows good results with $\pm 6\%$ accuracy. Lower waviness of the surface show the higher heat transfer than higher waviness. Variation in Nusselt number with Reynolds number become independent like circular pipe with lower waviness of the surface. Heat transfer rate falls almost exponentially along the axial direction with the increase of wave number.

CONTENTS

| | Page | |
|-------------------------|---|----|
| TITLE | i | |
| CERTIFICATE OF APPROVAL | ii | |
| CERTIFICATE OF RESEARCH | iii | |
| ACKNOWLEDGEMENTS | iv | |
| ABSTRACT | v | |
| CONTENTS | vi | |
| LIST OF FIGURES | viii | |
| LIST OF TABLES | xiii | |
| NOMENCLATURE | xiv | |
| | | |
| CHAPTER 1 | INTRODUCTION | |
| 1.1 | General | 1 |
| 1.2 | Background | 1 |
| 1.3 | Application | 2 |
| 1.4 | Motivation of present work | 3 |
| 1.5 | Objectives | 3 |
| 1.6 | Order of presentation | 4 |
| | | |
| CHAPTER 2 | LITERATURE REVIEW | |
| 2.1 | General | 5 |
| 2.2 | Previous work | 5 |
| | | |
| CHAPTER 3 | MATHEMATICAL MODEL & SOLUTION PROCEDURE | |
| 3.1 | General | 8 |
| 3.2 | Governing equation | 9 |
| 3.2.1 | Boundary condition | 9 |
| 3.3 | Generalized form of governing equation | 10 |
| 3.4 | Numerical solution of governing equation | 11 |
| 3.4.1 | Numerical grid and data structure | 12 |
| 3.4.2 | Approximation of surface and volume integrals | 14 |
| 3.5 | Algebraic equation system | 17 |
| 3.6 | Calculation of pressure | 17 |
| 3.7 | Solution algorithm | 19 |
| 3.8 | Axisymmetric problem | 21 |
| | | |
| CHAPTER 4 | RESULTS AND DISCUSSIONS | |
| 4.1 | General | 24 |
| 4.2 | Computational domain | 24 |
| 4.3 | Steps of simulation | 25 |
| 4.4 | Grid sensitivity test | 26 |
| 4.5 | Validation of numerical model | 27 |
| 4.6 | Hydrodynamic characteristic | 28 |
| 4.6.1 | Flow pattern | 29 |
| 4.6.2 | Separation and reattachment point | 32 |
| 4.6.3 | Axial velocity | 34 |

| | | |
|------------|---------------------------------------|----|
| 4.6.4 | Wall shear stress | 34 |
| 4.6.5 | Skin friction coefficient | 36 |
| 4.6.6 | Mean friction coefficient | 37 |
| 4.7 | Thermal characteristic | 38 |
| 4.7.1 | Thermal field | 38 |
| 4.7.2 | Heat transfer | 39 |
| 4.8 | Plane geometry | 41 |
| | | |
| CHAPTER 5 | CONCLUSIONS AND RECOMMENDATIONS | |
| 5.1 | General | 43 |
| 5.2 | Conclusions | 43 |
| 5.3 | Recommendation for future works | 43 |
| | | |
| REFERENCES | | 45 |
| | | |
| APPENDIX A | Programme segment for grid generation | 47 |
| | | |
| FIGURES | | |

LIST OF FIGURES

| | | Page no. |
|--------------|---|----------|
| Fig.3.1 | A typical CV and notation used | 12 |
| Fig.4.1 | Computational domain with physical boundary of wavy channel | 48 |
| Fig.4.2 (a) | Geometric parameter with axis system for axisymmetric geometry | 49 |
| Fig.4.2 (b) | Geometric parameter with axis system for plane geometry | 50 |
| Fig.4.3 (a) | Grid sensitivity test with axial velocity profile at $Re=800$ & $L^*=15.0$ for $X=0.0$ & 0.14 (axisymmetric case) | 51 |
| Fig.4.3 (b) | Grid sensitivity test with axial velocity profile at $Re=800$ & $L^*=15.0$ for $X=0.28$ & 0.42 (axisymmetric case) | 52 |
| Fig.4.3 (c) | Grid sensitivity test with axial velocity profile at $Re=800$ & $L^*=15.0$ for $X=0.71$ & 0.85 (axisymmetric case) | 53 |
| Fig.4.4 (a) | Grid sensitivity test with axial velocity profile at $Re=800$ & $L^*=15.0$ for $X=0.0$ & 0.14 (Plane geometry) | 54 |
| Fig.4.4 (b) | Grid sensitivity test with axial velocity profile at $Re=800$ & $L^*=15.0$ for $X=0.28$ & 0.42 (Plane geometry) | 55 |
| Fig.4.4 (c) | Grid sensitivity test with axial velocity profile at $Re=800$ & $L^*=15.0$ for $X=0.71$ & 0.85 (Plane geometry) | 56 |
| Fig.4.5 | Friction factor as a function of Reynolds number for $L^*=19.0$ | 57 |
| Fig.4.6 | Variation in separation and reattachment points in first cycle with Reynolds number at $L^*=8.0$ (Plane geometry) | 58 |
| Fig.4.7 | Comparison of present prediction of Nusselt number with numerical and experimental results of Russ & Beer [8,9] | 59 |
| Fig.4.8 | Comparison of measured wall vorticity profile with experimental data of Nishimura et. al. [11] | 60 |
| Fig.4.9 (a) | Combination of wall vorticity distribution and constant stream function contour | 61 |
| Fig.4.9 (b) | Combination of axial pressure gradient and constant stream function contour | 61 |
| Fig.4.10 (a) | Streamlines for $L^*=30.0$, $Re=100$, $n=1 - 4$ | 62 |
| Fig.4.10 (b) | Streamlines for $L^*=30.0$, $Re=150$, $n=1 - 4$ | 63 |
| Fig.4.10 (c) | Streamlines for $L^*=30.0$, $Re=200$, $n=1 - 4$ | 64 |

| | | |
|--------------|--|----|
| Fig.4.10 (d) | Streamlines for $L^*=30.0$, $Re=300$, $n=1-4$ | 65 |
| Fig.4.10 (e) | Streamlines for $L^*=30.0$, $Re=400$, $n=1-4$ | 66 |
| Fig.4.10 (f) | Streamlines for $L^*=30.0$, $Re=600$, $n=1-4$ | 67 |
| Fig.4.10 (g) | Streamlines for $L^*=30.0$, $Re=800$, $n=1-4$ | 68 |
| Fig.4.10 (h) | Streamlines for $L^*=30.0$, $Re=1000$, $n=1-4$ | 69 |
| Fig.4.10 (i) | Streamlines for $L^*=30.0$, $Re=1200$, $n=1-4$ | 70 |
| Fig.4.10 (j) | Streamlines for $L^*=30.0$, $Re=1400$, $n=1-4$ | 71 |
| Fig.4.10 (k) | Streamlines for $L^*=30.0$, $Re=1600$, $n=1-4$ | 72 |
| Fig.4.10 (l) | Streamlines for $L^*=30.0$, $Re=1800$, $n=1-4$ | 73 |
| Fig.4.10 (m) | Streamlines for $L^*=30.0$, $Re=2000$, $n=1-4$ | 74 |
| Fig.4.11 (a) | Streamlines for $L^*=21.0$, $Re=100$, $n=1-4$ | 75 |
| Fig.4.11 (b) | Streamlines for $L^*=21.0$, $Re=150$, $n=1-4$ | 76 |
| Fig.4.11 (c) | Streamlines for $L^*=21.0$, $Re=200$, $n=1-4$ | 77 |
| Fig.4.11 (d) | Streamlines for $L^*=21.0$, $Re=300$, $n=1-4$ | 78 |
| Fig.4.11 (e) | Streamlines for $L^*=21.0$, $Re=400$, $n=1-4$ | 79 |
| Fig.4.11 (f) | Streamlines for $L^*=21.0$, $Re=600$, $n=1-4$ | 80 |
| Fig.4.11 (g) | Streamlines for $L^*=21.0$, $Re=800$, $n=1-4$ | 81 |
| Fig.4.11 (h) | Streamlines for $L^*=21.0$, $Re=1000$, $n=1-4$ | 82 |
| Fig.4.11 (i) | Streamlines for $L^*=21.0$, $Re=1200$, $n=1-4$ | 83 |
| Fig.4.11 (j) | Streamlines for $L^*=21.0$, $Re=1400$, $n=1-4$ | 84 |
| Fig.4.11 (k) | Streamlines for $L^*=21.0$, $Re=2000$, $n=1-4$ | 85 |
| Fig.4.12 (a) | Streamlines for $L^*=11.0$, $Re=100$, $n=1-4$ | 86 |
| Fig.4.12 (b) | Streamlines for $L^*=11.0$, $Re=150$, $n=1-4$ | 87 |
| Fig.4.12 (c) | Streamlines for $L^*=11.0$, $Re=200$, $n=1-4$ | 88 |
| Fig.4.12 (d) | Streamlines for $L^*=11.0$, $Re=300$, $n=1-4$ | 89 |
| Fig.4.12 (e) | Streamlines for $L^*=11.0$, $Re=400$, $n=1-4$ | 90 |
| Fig.4.12 (f) | Streamlines for $L^*=11.0$, $Re=600$, $n=1-4$ | 91 |
| Fig.4.12 (g) | Streamlines for $L^*=11.0$, $Re=800$, $n=1-4$ | 92 |
| Fig.4.12 (h) | Streamlines for $L^*=11.0$, $Re=1000$, $n=1-4$ | 93 |
| Fig.4.12 (i) | Streamlines for $L^*=11.0$, $Re=1200$, $n=1-4$ | 94 |
| Fig.4.12 (j) | Streamlines for $L^*=11.0$, $Re=1400$, $n=1-4$ | 95 |

| | Page no. |
|---|----------|
| Fig.4.12 (k) Streamlines for $L^*=11.0$, $Re=1600$, $n=1 - 4$ | 96 |
| Fig.4.12 (l) Streamlines for $L^*=11.0$, $Re=1800$, $n=1 - 4$ | 97 |
| Fig.4.12 (m) Streamlines for $L^*=11.0$, $Re=2000$, $n=1 - 4$ | 98 |
| Fig.4.13 Variation of location of separation and reattachment points on wavy wall with Reynolds number for $L^*=11.0$ | 99 |
| Fig.4.14 Variation of location of separation and reattachment points on wavy wall with Reynolds number for $L^*=19.0$ | 100 |
| Fig.4.15 Variation of location of separation and reattachment points on wavy wall with Reynolds number for $L^*=30.0$ | 101 |
| Fig.4.16 Variation of location of separation and reattachment points on wavy wall with L^* at $Re=600$ | 102 |
| Fig.4.17 Variation of location of separation and reattachment points on wavy wall with L^* at $Re=1200$ | 103 |
| Fig.4.18 Variation of location of separation and reattachment points on wavy wall with L^* at $Re=1800$ | 104 |
| Fig.4.19 (a) Axial velocity profiles for $L^*=30.0$, $Re=100$, $n=1 - 4$ | 105 |
| Fig.4.19 (b) Axial velocity profiles for $L^*=30.0$, $Re=300$, $n=1 - 4$ | 106 |
| Fig.4.19 (c) Axial velocity profiles for $L^*=30.0$, $Re=800$, $n=1 - 4$ | 107 |
| Fig.4.19 (d) Axial velocity profiles for $L^*=30.0$, $Re=1400$, $n=1 - 4$ | 108 |
| Fig.4.19 (e) Axial velocity profiles for $L^*=30.0$, $Re=2000$, $n=1 - 4$ | 109 |
| Fig.4.20 (a) Axial velocity profiles for $L^*=21.0$, $Re=100$, $n=1 - 4$ | 110 |
| Fig.4.20 (b) Axial velocity profiles for $L^*=21.0$, $Re=300$, $n=1 - 4$ | 111 |
| Fig.4.20 (c) Axial velocity profiles for $L^*=21.0$, $Re=800$, $n=1 - 4$ | 112 |
| Fig.4.20 (d) Axial velocity profiles for $L^*=21.0$, $Re=1400$, $n=1 - 4$ | 113 |
| Fig.4.20 (e) Axial velocity profiles for $L^*=21.0$, $Re=2000$, $n=1 - 4$ | 114 |
| Fig.4.21 (a) Axial velocity profiles for $L^*=11.0$, $Re=100$, $n=1 - 4$ | 115 |
| Fig.4.21 (b) Axial velocity profiles for $L^*=11.0$, $Re=300$, $n=1 - 4$ | 116 |
| Fig.4.21 (c) Axial velocity profiles for $L^*=11.0$, $Re=800$, $n=1 - 4$ | 117 |
| Fig.4.21 (d) Axial velocity profiles for $L^*=11.0$, $Re=1400$, $n=1 - 4$ | 118 |
| Fig.4.21 (e) Axial velocity profiles for $L^*=11.0$, $Re=2000$, $n=1 - 4$ | 119 |
| Fig.4.22 Wall vorticity distribution along first & fourth cycle for $L^*=11.0$ | 120 |

| | | Page no. |
|--------------|---|----------|
| Fig.4.23 | Wall vorticity distribution along first & fourth cycle for $L^*=13.0$ | 121 |
| Fig.4.24 | Wall vorticity distribution along first & fourth cycle for $L^*=17.0$ | 122 |
| Fig.4.25 | Wall vorticity distribution along first & fourth cycle for $L^*=19.0$ | 123 |
| Fig.4.26 | Wall vorticity distribution along first & fourth cycle for $L^*=21.0$ | 124 |
| Fig.4.27 | Wall vorticity distribution along first & fourth cycle for $L^*=23.0$ | 125 |
| Fig.4.28 | Wall vorticity distribution along first & fourth cycle for $L^*=25.0$ | 126 |
| Fig.4.29 | Wall vorticity distribution along first & fourth cycle for $L^*=30.0$ | 127 |
| Fig.4.30 | Wall vorticity distribution along first & fourth cycle for $Re=200$ | 128 |
| Fig.4.31 | Wall vorticity distribution along first & fourth cycle for $Re=300$ | 129 |
| Fig.4.32 | Wall vorticity distribution along first & fourth cycle for $Re=400$ | 130 |
| Fig.4.33 | Wall vorticity distribution along first & fourth cycle for $Re=600$ | 131 |
| Fig.4.34 | Wall vorticity distribution along first & fourth cycle for $Re=1000$ | 132 |
| Fig.4.35 | Wall vorticity distribution along first & fourth cycle for $Re=1400$ | 133 |
| Fig.4.36 | Wall vorticity distribution along first & fourth cycle for $Re=2000$ | 134 |
| Fig.4.37 | Skin friction distribution along the wavy wall at $Re=200$ | 135 |
| Fig.4.38 | Skin friction distribution along the wavy wall at $Re=300$ | 136 |
| Fig.4.39 | Skin friction distribution along the wavy wall at $Re=400$ | 137 |
| Fig.4.40 | Skin friction distribution along the wavy wall at $Re=600$ | 138 |
| Fig.4.41 | Skin friction distribution along the wavy wall at $Re=800$ | 139 |
| Fig.4.42 | Skin friction distribution along the wavy wall at $Re=1000$ | 140 |
| Fig.4.43 | Skin friction distribution along the wavy wall at $Re=1200$ | 141 |
| Fig.4.44 | Skin friction distribution along the wavy wall at $Re=1400$ | 142 |
| Fig.4.45 | Skin friction distribution along the wavy wall at $Re=1600$ | 143 |
| Fig.4.46 | Skin friction distribution along the wavy wall at $Re=1800$ | 144 |
| Fig.4.47 | Skin friction distribution along the wavy wall at $Re=2000$ | 145 |
| Fig.4.48 (a) | Mean friction coefficient per wavelength for various L^* | 146 |
| Fig.4.48 (b) | Mean friction coefficient per wavelength for various L^* | 146 |
| Fig.4.49 | Variation of correlation constant (C) and correlation exponent (m) with L^* | 147 |
| Fig.4.50 | Isobars at $Re=300$ & 2000 for $L^*=15.0$ | 148 |
| Fig.4.51 (a) | Contours of normalized temperature for $n=1-4$, $L^*=19.0$, $Re=50$ | 149 |

| | Page no. |
|--------------|---|
| Fig.4.51 (b) | Contours of normalized temperature for $n=1 - 4$, $L^*=19.0$, $Re=100$ 150 |
| Fig.4.51 (c) | Contours of normalized temperature for $n=1 - 4$, $L^*=19.0$, $Re=150$ 151 |
| Fig.4.51 (d) | Contours of normalized temperature for $n=1 - 4$, $L^*=19.0$, $Re=200$ 152 |
| Fig.4.51 (e) | Contours of normalized temperature for $n=1 - 4$, $L^*=19.0$, $Re=300$ 153 |
| Fig.4.51 (f) | Contours of normalized temperature for $n=1 - 4$, $L^*=19.0$, $Re=1000$ 154 |
| Fig.4.52 | Contours of normalized temperature for third cycle at $Re=200$ and $L^*=11.0, 19.0, 30.0$ 155 |
| Fig.4.53 | Contours of normalized temperature for third cycle at $Re=1000$ and $L^*=11.0, 19.0, 30.0$ 156 |
| Fig.4.54 | Combination of streamlines and isothermal lines for first cycle at $Re=200$ and $L^*=11.0$ & 19.0 157 |
| Fig.4.55 | Distribution of local Nusselt number as a function of channel length for $L^*=30.0$ 158 |
| Fig.4.56 | Distribution of local Nusselt number as a function of channel length for $L^*=11.0$ 159 |
| Fig.4.57 | Local Nusselt number distribution for first and third cycle at $Re=300$ & $L^*=11.0, 19.0, 30.0$ 160 |
| Fig.4.58 | Local Nusselt number distribution for first and third cycle at $Re=1000$ & $L^*=11.0, 19.0, 30.0$ 161 |
| Fig.4.59 (a) | Local Nusselt number distribution for 10 waves for $L^*=19.0$ & $Re=300$ 162 |
| Fig.4.59 (b) | Decay of upper and lower peak values of Nusselt number along the channel for each cycle for $L^*=300$ 162 |
| Fig.4.60 | Distribution of average values of Nusselt number per wavelength with Reynolds numbers at different geometric parameters L^* 163 |
| Fig.4.61 | Mean friction coefficient per wavelength as a function of Reynolds number for plane geometry at $L^*=8.0, 11.0, 15.0, 25.0, 30.0$ 164 |
| Fig.4.62 | Variation of correlation constant (C) and exponent (m) with Reynolds number 165 |

LIST OF TABLES

| | | Page no. |
|------------|--|----------|
| Table: 3.1 | Special cases with source term of general equation | 11 |
| Table: 4.1 | Range of Under Relaxation Factor (URF) for different variables | 25 |
| Table: 4.2 | Three grid levels with their sizes and names | 26 |
| Table: 4.3 | Critical ranges of Reynolds number | 30 |
| Table: 4.4 | Lower range of Reynolds number at different L^* | 31 |
| Table: 4.5 | Correlation constant (C) and exponent (m) as a function of L^* | 37 |

NOMENCLATURE

| | | |
|------------|---|---|
| a | = | Amplitude |
| A | = | Constant of polynomial |
| C | = | Correlation constant |
| C_f | = | Skin friction coefficient |
| D | = | Diameter of the wavy channel (axisymmetric geometry) |
| f | = | Mean friction coefficient per wave length (friction factor) |
| h | = | Convective heat transfer coefficient |
| H | = | Inter wall spacing of plane geometry |
| K_f | = | Thermal conductivity of fluid |
| L | = | Length of the pipe |
| L^* | = | Dimensionless geometric parameter, (λ/a) |
| m | = | Exponent of the correlation |
| n | = | Wave number |
| Nu_{av} | = | Average Nusselt number |
| Nu_x | = | Local Nusselt number |
| Pr | = | Prandtl number |
| q | = | Heat flux |
| r | = | Radial distance |
| R | = | Normalized radial distance, (r/λ) |
| Re | = | Reynolds number |
| T | = | Field temperature |
| T_w | = | Constant wall temperature |
| T_α | = | Temperature of fluid |
| u | = | Axial component of velocity |
| v | = | Radial or normal component of velocity |
| U_0 | = | Free stream velocity |
| U_m | = | Mean velocity |
| x | = | Axial distance |
| y | = | Vertical distance |
| X | = | Normalized axial distance, (x/λ) |
| Y | = | Normalized vertical distance, (y/λ) |
| z | = | Independent variable of polynomial |

Greek Symbol

| | | |
|-----------|---|----------------------------|
| ρ | = | Density of fluid |
| μ | = | Viscosity |
| ψ | = | Normalized stream function |
| τ | = | Shear stress |
| ξ | = | Vorticity |
| θ | = | Dimensionless temperature |
| λ | = | Wavelength |
| Γ | = | Diffusion coefficient |

Superscript

/ = New value
* = Corrected value

Subscript

w = At wall
i,j = Cartesian notation of longitudinal and transverse direction
av = Average value
max = Maximum value
min = Minimum value

Special symbol

| | = Absolute value
 Δ = Difference between two parameters



1.1 GENERAL

Quite often we encounter fluid flow and heat transfer over flat plate or cylindrical objects at different orientations. These classical problems have some analytical and huge numerical solutions along with many experimental verifications. Results from these research works are widely used in many engineering applications for predicting their performance, designing of many equipment, machine parts like small microchips to large nuclear reactor. But things used in practical purpose are much more complicated in design and prediction of their performance using results from simple geometry cause huge error. For this complexity, in recent years, attention has been given to study hydrodynamic and thermal characteristics of complex geometry. Among them corrugated and wavy passages and surfaces are given special attention due to their wide application in computer hardware, heat exchanger, solar heat collector, some air-conditioning equipment, open channel flow etc. Mathematical models used to predict flow and thermal behavior are mainly of coupled partial differential equations of non-linear in nature and their solution is quite impossible analytically except some special cases. Experimental works are too much costly and in some cases impossible. Computational fluid dynamics (CFD) plays dominant role here and it gives too much luxury to go inside many complex problems. Due to increasing rate of computer performance now a days even a personal computer can solve a complex problem within a minute which was a matter of day for some supercomputers at early in the '70s.

1.2 BACKGROUND

A tube with periodically converging-diverging cross-section is one of the several devices employed for enhancing the heat and mass transfer efficiency. The fluid flow, in the flow passages with a periodically varying cross-section, attains a fully developed regime that differs fundamentally from that for a conventional constant-area flow channel. In the periodically varying cross-sections, the fully developed velocity field repeats itself at

corresponding axial stations in successive cycles. The change of flow pattern with changes in duct dimensions is a special feature of the complex corrugated-duct geometry that is not encountered in conventional ducts such as circular and annular tubes and rectangular ducts. Flow through wavy or corrugated channel serves as a simple example of separated flow, in which the complex interactions of separated vortices, free shear layers, driving wall-bounded shear flows and the resulting heat and mass transfer can be examined in some details. These types of channel are widely used for heat transfer augmentation in recent years. Geometrical complexity of such channel or ducts affects largely the flow pattern and heat transfer characteristics. Their fabrication depends on many parameters like amplitude, wavelength, phase angle, inter-wall spacing, corrugation angle, sharpness or roundness of successive peaks and valleys of the wall etc. and each of the parameter significantly affects the hydrodynamic and thermal behavior of fluid flow through this channel. This geometric not idealities and its effect on flow phenomenon motivates many researchers to perform experimental or analytical work on this topic.

1.3 APPLICATION

Wavy and corrugated passages or surfaces are widely used in small to large electrical or electronic devices such as processor of computer, transformer. Recently many of the industrial heat exchangers are made of corrugated surfaces for compactness along with tube banks. In fossil fuel power plant, rotary air preheater of regenerative type are widely used for heat recovery and increase efficiency of the plant and most of them are made of cross corrugated geometry. It is also used in solar heat collector that increases heat transfer area and give compactness to the device. In some cases it is used for heat transfer augmentation is case of ribbed surface that cause large pressure drop. These type surfaces have some application in catalytic reactor [11], chemical reactor and gas turbine [4]. Conjugate heat transfer finds many applications in daily life. Examples representative of this class of problems are air-conditioning machines, air heaters, power station. Variety of wavy surfaces are widely used in such cases. Various types of roof design include corrugated surface of different orientations.

1.4 MOTIVATION OF PRESENT RESEARCH WORK

Some applications of wavy or corrugated surfaces are briefly discussed in previous section. In recent years major attention has been given to the compactness of equipment, machine parts, devices etc. One of the excellent examples of compact channel is corrugated geometry that has large surface area compared to the conventional circular or rectangular straight duct. But in many cases it causes large pressure drop and thus frictional loss occurs that causes large pumping power. At the same time this type of geometry proves itself as high performance heat transfer device compared to the conventional one. For the complexity of such geometry, there are many parameters that can be studied for checking their influence and seek the optimum design of corrugated duct or wavy channel. Fewer numbers of literatures is available on such topic (these are discussed in Chapter 2). Nishimura et. al. [10] and Goldstein et. al. [3] have done lots of work on wavy and corrugated channel, but their work is limited to mainly on a single set of geometry and mass transfer. Still so many things left behind for studying. In this research work some of the extended work of previous research works have been given attention along with some new aspect of corrugated geometry that will be helpful for many of the fabrication and design work.

1.5 OBJECTIVES

The present research work is done for the prediction of fluid flow and heat transfer characteristics of two-dimensional corrugated surfaces at laminar and turbulent flow condition using computational fluid dynamic technique. The study has the following objectives:

- a) To test the capability of the computer code CAFFA (Computer aided fluid flow analysis) for solving problem associated with complex geometry
- b) To compare available numerical and some experimental data with present simulated data
- c) To study the effect of , amplitude and wavelength of the corrugated surface on fluid flow , frictional loss and heat transfer

- d) To study the effect of Reynolds number, corrugation geometry and asymmetric heating of corrugated surface on fluid flow, frictional loss and heat transfer
- e) To find the distance between the separation and reattachment point with the variation of corrugated geometry and flow parameters at different wave
- f) To find the mathematical relation between different parameters, correlation from available simulated data.

1.6 ORDER OF PRESENTATION

For convenience of presentation, the total contents of this research paper are divided into several chapters. In this chapter a brief introduction has been presented with aim and objective and application. There is nothing new to say about it. Chapter-2 consists of brief discussion of available literatures related to the present investigation along with their limitations and scope of further work. In Chapter-3 mathematical model has been presented along with discretization technique. Specialty of Finite Volume method is briefly discussed. Detail discretization of general coordinate-free generic conservation equation has been presented along with solution algorithm, boundary condition and handling procedure of instability, oscillatory solution etc. Chapter-4 consists of result and brief discussion of simulated data from present investigation.

Finally, the conclusions drawn from the present investigation are given in Chapter-5. This chapter also includes suggestions for further research in this field.

2.1 GENERAL

Flow through corrugated channel or a wavy passage has not been investigated to a great extent because of geometric complexity and variety of influential parameters. Some of the problems, associated with it, are discussed in previous chapter. Researchers put emphasis on a particular geometry and restricted to one set of geometrical parameter and mass transfer; not to heat transfer and fluid flow at a great extent. However, for convenience, this type of geometry can be divided into two broad categories according to Nishimura [10]. One is axisymmetric, that is flow passage is converging-diverging and symmetrical about an axis passing through the center of the channel. The second type of geometry having constant cross sectional area and centroidal axis undergoes a periodical change. Different investigators investigate both types of problems. For convenience of present investigation, literature related to these two geometrical configurations have been presented briefly in this chapter.

2.2 PREVIOUS WORK

Flow and heat transfer through wavy channel associated with boundary layer formation, flow separation, frictional loss and there is no reason to discuss about such things here, because these are well known phenomenon and already published.

Saidi et. al. [1] studied laminar flow past a sinusoidal cavity. They presented how increase of flow velocity give birth vortex inside cavity and affect thermal performance. **Wang & Vanka** [2] represented that steady flow did not provide any enhancement of heat transfer in a periodic wavy passage before Re (based on average inter wall spacing) around 180 and after which self sustained oscillations lead to the destabilisation of laminar thermal boundary layers, replenish the near wall-fluid with fluid in the core region, and thus provide a natural mechanism of enhancement of heat transfer. They also reported heat transfer is 2.5 times higher in a corrugated wall channel than that of parallel wall channel. **Goldstein & Sparrow** [3] studied laminar, transitional and low Reynolds number turbulent

flow in a corrugated wall channel. They reported that heat transfer coefficients slightly higher than those for a parallel plate channel up to Re (based on average channel height) 1000. In the case of turbulent flow, they found significant increase in heat transfer coefficient (2.5 to 3 times) at $Re=1500$ to $Re=25000$. **Yao et. al. [5]** reported and mixed convection along a vertical wavy surface and found significant increase in heat transfer coefficient. **Yang et. al. [6]** carried out computation using low Reynolds number turbulent model for three different inner wall spacing for $100 < Re < 2500$, $15^\circ < \theta < 30^\circ$ in a corrugated wall channel and reported transitional Reynolds number is lower than the value for the parallel plate duct and it decreases with increasing corrugation angle. **Nishimura et. al. [7]** investigated flow characteristics such as flow pattern , pressure drop and wall shear stress in channel with symmetric sinusoidal wavy wall. It was reported an increase in Reynolds number ($Re > 350$) caused turbulent flow to develop, owing to the onset of unsteady vortex motion. Friction factor is inversely proportional to Re at laminar range and independent of Re at turbulent region. **Russ & Beer [8]** found maximum Nusselt number near the reattachment point of the flow near the converging part of the wavy passage and mean convective transport over one wave for fully developed flow is nearly the same as that for straight pipe. **Sparrow et. al. [20]** performed experimental study to determine the heat transfer, pressure drop, and flow field responses to the rounding of the peaks of a corrugated wall duct at a Reynolds number range 2000 to 33000 based on inter wall spacing. They reported that due to rounding of, friction factor decreases corresponding to a given Reynolds number even more than did the Nusselt number. On the other hand , at equal pumping power, the Nusselt number was relatively insensitive to whether the peaks were sharp or rounded. **Asako & Faghri [21]** developed a finite volume method using co-ordinate transformation for predicting flow and heat transfer performance in a corrugated duct. The basis of the method is an algebraic co-ordinate transformation, which maps the complex fluid domain onto a rectangle. They reported that flow pattern are highly complex including large recalculation zones. The pressure drops and friction factor results are higher than the corresponding values for a straight duct. From a performance analysis model, they found that there are small differences in the heat transfer ratios under the different constraints- fixed pumping power, fixed pressure drop, fixed mass flow rate. **Sparrow et. al. [23]** experimentally measured heat transfer and pressure drop and visualise flow in a corrugated duct. **Sparrow & Comb [20]** analyse the effect of interwall spacing and inlet condition on fluid flow in a corrugated wall heat exchanger. Performance evaluations were

carried out for three different constraints- fixed pumping power, fixed pressure drop, and fixed mass flow. For all of these cases, the heat transfer coefficient for the larger interwall spacing was slightly lower than that for the smaller interwall spacing, but the pressure drop also lower. **Faghri & Asako [22]** used a finite difference scheme to predict periodic fully developed heat transfer and fluid flow characteristics in a converging-diverging flow channel. The wall of the channel linearly diverges from minimum cross-section to its peak then again linearly converges to its minimum cross-section. Representative results were carried out for laminar flow, Prandtl number of 0.7, in the Reynolds number range from 90 to 1635, for various taper angles and for three ratios of maximum / minimum height of the flow channel. They found a moderate enhancement in the Nusselt number at high values of Reynolds number with a pressure drop penalty when compared with the corresponding values for straight duct. **Amano [13]** performed numerical study to predict hydrodynamic and heat transfer characteristics in a periodically corrugated wall channel for both laminar and turbulent ('k- ϵ turbulent model) flows. As a corrugated channel, a channel which has a cyclically corrugated wall at a 90^0 angle is considered. The Reynolds number considered in his study ranging from 10 to 25000 and step ratio (height / width) ranging from 2 to 4. It is reported that the effect of the step ratio on the local Nusselt number is minor but skin friction and heat transfer pattern change drastically from laminar to turbulent flows.

The present work will be undertaken to study the flow field, friction factor, temperature variation and heat transfer during laminar and turbulent flow over the two dimensional corrugated surface

CHAPTER 3

MATHEMATICAL MODEL & SOLUTION PROCEDURE

3.1 GENERAL

In this chapter method of numerical simulation, mathematical model with boundary condition, discretization technique and solution of algorithm along with solution procedure linear equation system are briefly discussed. For convenience of presentation, total chapter is divided into several subsections.

Problem studied in this investigation having computational domain of wavy-surface consists of complex boundary. The treatment of complex boundary is very difficult one and in many cases writing computer code for grid generation of such geometry is sometime impossible. Boundary-fitted non-orthogonal grids are most often used to calculate flows in complex geometries (most commercial codes use such grids). They can be structured, block-structured, or unstructured. The advantage of such grids is that they can be adapted to any geometry, and that optimum properties are easier to achieve than with orthogonal curvilinear grids. Since the grid lines follow the boundaries, the boundary conditions are more easily implemented than with stepwise approximation of curved boundaries. The grid can also be adapted to the flow, i.e. one set of grid lines can be chosen to follow the streamlines (which enhances the accuracy) and the spacing can be made smaller in regions of strong variable variation, especially if block-structured or unstructured grids are used.

Non-orthogonal grids have also several disadvantages. The transformed equations contain more terms thereby increasing both the difficulty of programming and the cost of solving the equations, the grid non-orthogonality may cause unphysical solutions and the arrangement of variables on the grid affects the accuracy and efficiency of the algorithm.

Control volume based finite-volume method is best suited for complex-geometry problem. This method uses integral form of the conservation equations as its starting point. The solution domain is subdivided into a finite number of contiguous control volumes (CVs), and the conservation equations are applied to each CV. At the centroid of

each CV lies a computational node at which the variable values are to be calculated. Computer coding for grid generation or flow solving is not too much difficult in this method. Recently, many commercial codes use this method efficiently. Some important features of Finite Volume method are discussed later sections.

3.2 GOVERNING EQUATIONS

Control volume based Finite Volume method uses integral form of conservation equations as mentioned earlier for mass, momentum, and scalar quantity (temperature, kinetic energy etc.). Considering an incompressible, steady flow with a Newtonian constant viscosity fluid, the integral form governing equations are as follows:

$$\int_S \rho \mathbf{v} \cdot \mathbf{n} dS = 0 \quad (3.1)$$

$$\int_S \rho u_i \mathbf{v} \cdot \mathbf{n} dS = \int_S \mu \text{grad } u_i \cdot \mathbf{n} dS - \int_S p \mathbf{i}_i \cdot \mathbf{n} dS + \int_V \rho b_i dV \quad (3.2)$$

$$\int_S \rho u_j \mathbf{v} \cdot \mathbf{n} dS = \int_S \mu \text{grad } u_j \cdot \mathbf{n} dS - \int_S p \mathbf{i}_j \cdot \mathbf{n} dS + \int_V \rho b_j dV \quad (3.3)$$

$$\int_S \rho T \mathbf{v} \cdot \mathbf{n} dS = \int_S k \text{grad } T \cdot \mathbf{n} dS \quad (3.4)$$

In these equations, ρ is the fluid density, V is the control volume (CV) bounded by a closed surface S , \mathbf{v} is the fluid velocity vector whose Cartesian components are u_i , μ is the dynamic viscosity, T is the temperature, p is the pressure, \mathbf{n} is the unit vector normal to S and directed outwards and b_i is the body force in the direction of the Cartesian coordinate x_i . The another part of the present study deals with an axisymmetric problem. The governing equations, specialty, assumption and modification of same computer code to handle the axisymmetric problem is discussed in section 3.8.

3.2.1 BOUNDARY CONDITION

Implementation of boundary condition for complex geometry is not so easy as regular geometry. A separate section will present handling and implementation of boundary

condition for complex geometry in general sense. Here, specially, what is used particularly in present investigation, is discussed briefly.

a) INLET BOUNDARY:

At inlet fully developed velocity profile is assumed. The corresponding equation for such profile for circular pipe (axixymmetric geometry) shown in Eq.3.5a and for plane geometry, velocity profile between two parallel plates (Eq.3.5b) is used.

$$\frac{u(r)}{u_m} = 2 \left[1 - \left(\frac{2r}{D_{av} - 2a} \right)^2 \right] \quad (3.5a)$$

$$\frac{u(y)}{u_m} = \frac{2}{3} \left[1 - \left(\frac{2y}{H_{av} - 2a} \right)^2 \right] \quad (3.5b)$$

Where u_m is the mean velocity of flow equal to half of the centerline velocity, $u(r)$ is the velocity at different radial position measured from centerline.

b) OUTLET CONDITION:

The imposed exit boundary condition is a parallel outflow with the pressure gradient in the direction perpendicular to the axis is set equal to zero and the vertical velocity component set equal to zero as well.

c) SYMMETRY PLANE:

At the symmetry plane, the normal gradient is zero for all scalar quantities and velocity components parallel to the plane; the velocity component normal to the plane is set to zero.

d) SOLID WALL:

Wall is considered impermeable, convective fluxes of all quantities through wall are kept zero. No slip boundary condition is applied all wall except inlet, outlet i.e. $u_i = u_{i,wall}$

3.3 GENERALIZED FORM OF GOVERNING EQUATIONS:

The governing integral equations, discussed above, can be expressed in general form. The integral form of this generic conservation is:

$$\frac{\partial}{\partial t} \int_V \rho \phi dV + \int_S \rho \phi \mathbf{v} \cdot \mathbf{n} dS = \int_S \Gamma \text{grad } \phi \cdot \mathbf{n} dS + \int_V q_\phi dV \quad (3.6)$$

This equation is independent of type of grid, i.e. coordinate free form. The first term of the equation stands for unsteady term, second for convective, third for diffusive and the last one is source term. For $\phi=1$, this becomes mass conservation equation of (3.1); for $\phi=u_i$, u_j , this becomes momentum equation of (3.2), (3.3), for $\phi=T$, this becomes energy equation. For steady flow, the first term is always equal to zero, because there is no change of variables with respect to time. Source term may be zero or may be given particular value depending on the problem being solved. In general, the thing discussed above can be summarized in a tabular form:

TABLE-3.1

Special cases with source term of general equation

| Value of ϕ | Velocity vector, \mathbf{v} | Γ | Name of the equation | Source term |
|-----------------|-------------------------------|----------|----------------------|-------------|
| 1 | \mathbf{v} | μ | Continuity | 0 |
| u_i | \mathbf{v} | μ | U-momentum | S_i |
| u_j | \mathbf{v} | μ | V-momentum | S_j |
| T | \mathbf{v} | k | Energy | 0 |

Where,

$$S_i = - \int_S p \mathbf{i}_i \cdot \mathbf{n} dS + \int_V \rho b_i dV$$

$$S_j = - \int_S p \mathbf{i}_j \cdot \mathbf{n} dS + \int_V \rho b_j dV$$

The set of equations presented above has been solved for two velocity components u_i , u_j for pressure p and for temperature T.

3.4 NUMERICAL SOLUTION OF GOVERNING EQUATIONS:

As discussed earlier, the governing equations are the special forms of the generic conservation equation (3.6)

There is no need to discuss the solution technique of the governing equations separately. As they are the special cases of equation (3.6), any methodology of solution of equation (3.6) can give total idea of solution procedure of special cases. Equation (3.6) consists of surface and volume integral. Convective and diffusive terms need surface integral and source term needs volume integral.

The principles of discretization are described in later section. This is independent of the type of grid used; however, as the geometry considered in this investigation is a complex one, there are several special features have to be discussed that are absent in the regular orthogonal grid.

3.4.1 NUMERICAL GRID AND DATA STRUCTURE:

The solution domain is first subdivided into a finite number of contiguous control volumes (CVs), and the conservation equations are applied to each CV. At the centroid of each CV lies a computational node at which the variable values are to be calculated. The computational node at which all unknowns are stored in one-dimensional (1D) arrays and sorted level-wise, starting with level 1 of grid (coarsest grid level).

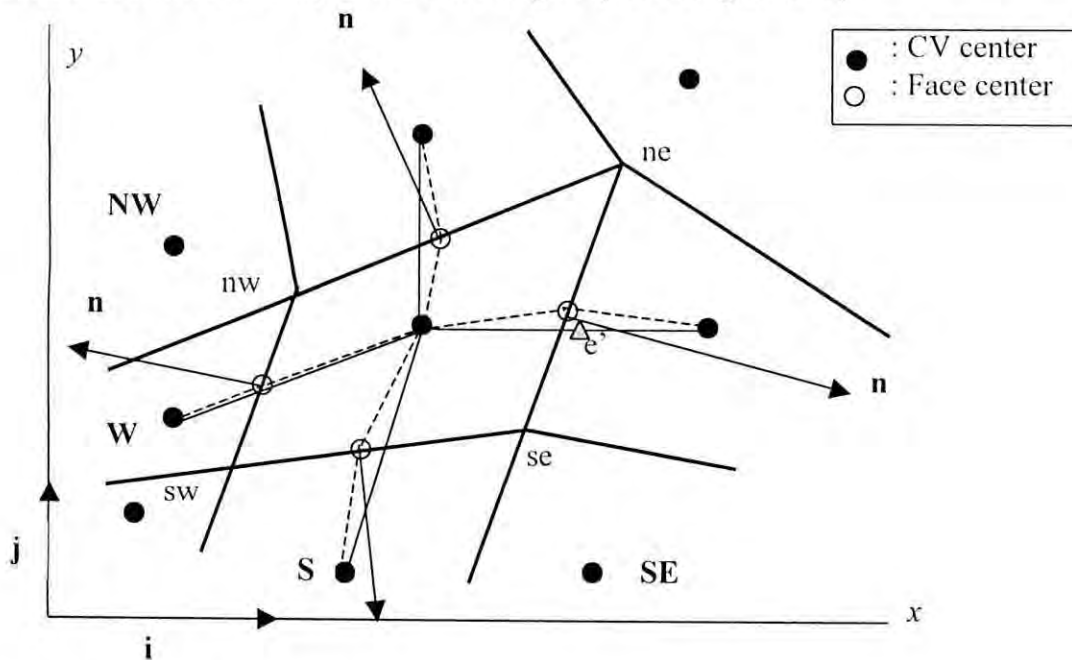


Fig. 3.1: A typical CV and the notation used

The FV method can accommodate any type of grid, so it is suitable for complex geometries. The grid defines only the control volume boundaries and need not be related to a coordinate system. The method is conservative by construction, so long as surface

integrals are the same for the CVs sharing the boundary. A typical CV used in complex geometry shown Fig. 3.1.

Both surface and volume integrals in the conservation equations (3.1) - (3.4), (3.6) are approximated here using midpoint rule, i.e. the value of the integrand at the center of cell face or CV is multiplied by the face area or CV volume. To make computations efficient, the geometrical parameters of each CV needed for integral approximations are computed once upon grid generation and stored. These quantities are:

- CV-volume, which is for plane geometries calculated as:

$$V = \frac{1}{2} [(\mathbf{r}_{ne} - \mathbf{r}_{sw}) \times (\mathbf{r}_{nw} - \mathbf{r}_{se})] \quad (3.7)$$

Where \mathbf{r}_{ne} is the position vector of the cell corner 'ne', cf. Fig.3.1. For axisymmetric geometries, the CV-volume is defined by the rotation of the front surface by one radian around the axis of symmetry and can be calculated as:

$$V = \frac{1}{6} \sum_{l=1}^4 (x_l + x_{l+1})(y_l^2 + y_{l+1}^2 + 1 + y_l y_{l+1}) \quad (3.8)$$

Where x denotes the axial and y the radial direction, and l denotes CV vertices numbered counter-clockwise.

- Components of the surface vector $S \mathbf{n} = S^x \mathbf{i} + S^y \mathbf{j}$

$$\left. \begin{aligned} S^x_c &= (y_{ne} - y_{se})r_c, & S^y_c &= (x_{se} - x_{ne})r_c, \\ S^x_n &= (y_{nw} - y_{ne})r_n, & S^y_n &= (x_{ne} - x_{nw})r_n, \end{aligned} \right] \quad (3.9)$$

where r_c and r_n are the distances of cell-face center from the axis of symmetry (for plane 2D problems, r is set to unity). It should bear in mind that $(S \mathbf{n})_s$ for a CV centered around node P equals $-(S \mathbf{n})_n$ of the CV centered around node S; thus, only surface vector components for the east and north faces are computed and stored.

- Interpolation factors λ_c and λ_n , which are defined as:

$$\lambda_c = \frac{|\mathbf{r}_c - \mathbf{r}_p|}{|\mathbf{r}_c - \mathbf{r}_p| + |\mathbf{r}_e - \mathbf{r}_p|}, \quad \lambda_n = \frac{|\mathbf{r}_n - \mathbf{r}_p|}{|\mathbf{r}_n - \mathbf{r}_p| + |\mathbf{r}_n - \mathbf{r}_n|} \quad (3.10)$$

The above quantities related to the east and north faces of a CV are calculated once and stored at a location associated with that CV. However, this is done for inner faces only: if the east or north side of a CV coincides with either a domain boundary, the memory locations reserved for these quantities remain empty. For the boundary a separate data structure is introduced.

3.4.2 APPROXIMATION OF SURFACE AND VOLUME INTEGRALS

As already mentioned, both surface and volume integrals are approximated using midpoint rule (14). Since all unknowns and fluid properties are calculated and stored at CV center, there are no additional approximations involved in the evaluation of volume integrals: one simply multiplies the CV-center value of the integrand with CV-volume. For the calculation of surface integrals, further approximations are necessary since the values of the integrand $\mathbf{f} = \rho \phi \mathbf{v}$ in convective and $\mathbf{f} = \Gamma \text{grad } \phi$ in diffusive fluxes (Eq. 3.4) are not known at the cell-face center. Therefore, interpolation and numerical differentiation have to be used to express the cell-face values of variables and their derivatives through the nodal values. Details on various options can be found in Ferziger and Peric [14]; here only the methods used in the present calculations will be briefly described.

Cell-face values of variables are approximated using linear interpolation:

$$\phi_e \approx \phi_{e'} = \phi_P \lambda_e + \phi_P (1 - \lambda_e) \quad (3.11)$$

where λ_e was introduced in Eq. (3.10). This is a second-order approximation at the location 'e' on the straight line connecting nodes P and E. If the cell-face center 'e' does not coincide with the location 'e'', as in Fig.3.1, the integral approximation

$$\int_{S_e} \mathbf{f} \cdot \mathbf{n} dS \approx f_e^x S_e^x + f_e^y S_e^y \quad (3.12)$$

will not be second-order accurate. As long as 'e' is close to 'e'', as is the case in Fig. 1, the first-order error term is small; however, if 'e' comes close to cell corners, the first-order

term will dominate. Thus, the grid quality can be analyzed by comparing $|\mathbf{r}_e - \mathbf{r}_e|$ and $|\mathbf{r}_{nc} - \mathbf{r}_{se}|$. The second-order accuracy can be restored by adding a correction term as follows:

$$\phi_e \approx \phi_{e'} + (\text{grad } \phi)_{e'} \cdot (\mathbf{r}_e - \mathbf{r}_{e'}) \quad (3.13)$$

where the gradient at 'e' can be obtained by interpolating the cell-center gradients using Eq. (3.11)

Linear interpolation leads in a FV-method to the same result as the use of central differences for the first derivatives in finite-difference (FD) methods, which is why it is usually referred to as *central-differencing scheme* (CDS).

It is advantageous to use the so called deferred correction approach when implementing this scheme in implicit solution algorithms [15]. In that case only the first-order upwind approximation (UDS: $\phi_e \approx \phi_p$ if the flow is from P to E, otherwise $\phi_e \approx \phi_E$) is used to calculate the elements of the coefficient matrix, while the explicitly calculated difference between the CDS and UDS approximation is added to the right-hand side of the equation system:

$$\phi_e = \phi_e^{\text{UDS}} + \gamma(\phi_e^{\text{CDS}} - \phi_e^{\text{CDS}})^{\text{old}} \quad (3.14)$$

The term in brackets is multiplied by a factor $0 \leq \gamma \leq 1$, this is called blending factor. Blending is necessary in order to suppress the oscillations near discontinuities.

In order to calculate the diffusive fluxes, the gradient vector at the cell face is required. To this end one can use coordinate transformation, as is most often done in conjunction with structured grids. However, a much simpler approach, developed by Muzaferija et. al. [14], is possible. The gradient is first explicitly calculated at CV centers using midpoint-rule approximation based on the Gauss-theorem:

$$\left(\frac{\partial \phi}{\partial x_i} \right)_p \approx \frac{\sum_k \varphi_k k S_k}{V}, \quad (k = e, w, n, s, \dots). \quad (3.15)$$

Here, ϕ_k is calculated in the same way as in convective fluxes (although one could use a different approximation; however, to preserve the accuracy of the gradient approximation, the interpolation should be of at least second order).

The above approximation of the gradient is valid for CVs of arbitrary shape. Also, in the case of axi-symmetric geometries, one has to take into account the contribution of the front and back face when calculating the derivative with respect to r , since they do not cancel out as in the case of plane geometries. The additional term to be added on the right-hand side of Eq. (3.15) is $-\phi_p S$, where S is the area of the front face.

The cell-center derivatives can now be interpolated to the cell-face centers using the same interpolation technique as for convective terms. However oscillatory solutions may develop in this case (for detailed [14]). Muzaferija et. al. [15] suggested the following approximation which prevents oscillations and retains the second-order accuracy:

$$(\text{grad } \phi)_c \cdot \mathbf{n}_c = \left(\frac{\partial \phi}{\partial n} \right)_c \approx \frac{\phi_E - \phi_P}{|\mathbf{r}_E - \mathbf{r}_P|} - \underbrace{(\text{grad } \phi)_c}_{\text{old}} \left(\frac{\mathbf{r}_E - \mathbf{r}_P}{|\mathbf{r}_E - \mathbf{r}_P|} \cdot \mathbf{n}_c \right) \quad (3.16)$$

The underlined term is calculated using prevailing values of the variables and treated as another deferred correction, see above. If the line connecting nodes P and E is orthogonal to the cell face, the underlined term is zero (since the vectors $\mathbf{r}_E - \mathbf{r}_P$ and \mathbf{n}_c are then co-linear) and the usual central-difference approximation of the derivative is recovered. The explicitly calculated gradient at the cell face (denoted by over-bar in the above expression and obtained by linear interpolation) is used only to account for the cross derivative. Thus, the implicit part of the approximation involves only the nearest neighbors, resulting in a compact coefficient matrix. Note that in the momentum equations, not only the normal derivative of the dominant velocity component, but also tangential derivatives of the other components are needed at the cell-face center. These can be obtained by interpolating cell-center values, as they cause no problems.

The convective fluxes are non-linear terms, so linearization is necessary. Here the simple Picard iteration is employed: the mass flux through the cell face is taken from the previous iteration:

$$\int_{S_c} \rho \phi \mathbf{v} \cdot \mathbf{n} dS \approx \phi_e \int_{S_c} \rho \mathbf{v} \cdot \mathbf{n} dS = \phi_e \dot{m}_e \quad (3.17)$$

Source terms are also be non-linear; the same approach is used to linearize them.

3.5 ALGEBRAIC EQUATION SYSTEM

Upon separation of the terms involving unknown variables and the explicitly calculated ones, an algebraic equation of the form

$$A_p \phi_p + \sum_l A_l \phi_l = Q_p, \quad l = E, W, N, S, \dots \quad (3.18)$$

is obtained for each CV. The coefficients A_E , A_W , A_N , and A_S contain contributions from surface integrals over faces common to the cell around node P and the corresponding neighbor; A_p contains in addition from source terms (volume integrals). Q_p contains all terms, which are treated as known (source terms, parts of surface integrals treated explicitly as deferred corrections). These coefficients are stored as cell-data, i.e., they are associated with the cell-index..

For the solution domain as a whole, the algebraic equation system can be written as:

$$\mathbf{A} \boldsymbol{\varphi} = \mathbf{Q} \quad (3.19)$$

Where \mathbf{A} is a square $N \times N$ coefficient matrix, $\boldsymbol{\varphi}$ is the vector of unknowns, \mathbf{Q} is the vector of right-hand sides, and N is the number of CVs. The global matrix \mathbf{A} is irregular; however, since an iterative method is used to solve the linearized equation systems, the irregularity can be easily dealt with.

3.6 CALCULATION OF PRESSURE

The pressure-velocity coupling is achieved using the well-known SIMPLE algorithm [16]. The solution process starts with a guessed pressure field. Each time the linearized

momentum equations are solved, the mass conservation is imposed on the new velocities (to within a certain tolerance) by applying a velocity correction, which is proportional to the gradient of the pressure correction. The dependence of velocity on pressure gradient is obvious from the momentum equation. Special care is needed in a co-located variable arrangement to avoid pressure-velocity decoupling. Detailed discussion of this issue and the method of solve the problem is available in [14]; here only the main steps will be given.

The velocity field obtained by solving the linearized momentum equations is denoted by u_i^* . Superscript '*' indicates uncorrected variable of new solution. The normal velocity component at the cell face 'e' is calculated by interpolating neighbor nodal values and subtracting a correction term which should detect oscillations and help smooth them out [15]:

$$\left(\mathbf{v}^* \cdot \mathbf{n}\right)_e = \overline{\left(\mathbf{v}^* \cdot \mathbf{n}\right)_e} - \left(\overline{\frac{V}{A_p}}\right)_e \left[\frac{p_E - p_P}{(\mathbf{r}_E - \mathbf{r}_P) \cdot \mathbf{n}} - \frac{\overline{(\text{grad } p)} \cdot (\mathbf{r}_E - \mathbf{r}_P)}{(\mathbf{r}_E - \mathbf{r}_P) \cdot \mathbf{n}} \right] \quad (3.20)$$

The over-bar denotes interpolation from neighbor nodal values (here linear; see Lilek and Peric [14] for details about using higher-order Interpolation and integration techniques); double over-bar denotes arithmetic averaging. The correction term in square brackets vanishes when the pressure variation is linear or quadratic; it is proportional to the square of mesh spacing and a third derivative of pressure [14]. Thus, this term is a second-order correction that goes consistently towards zero as the rid is refined; it is large only when the pressure variation is not smooth.

The normal velocity component is proportional to the normal derivative of pressure, which can be approximated at the cell-face center by the following central-difference approximation:

$$\left(\frac{\partial p}{\partial n}\right)_e \approx \frac{p_{E'} - p_{P'}}{(\mathbf{r}_E - \mathbf{r}_P) \cdot \mathbf{n}} \quad (3.21)$$

Here, an approximation is made in that the pressure values at locations E' and P' are replaced by pressure values at E and P. This neglecting of the non-orthogonality does not affect the convergence of the procedure if the non-orthogonality is not severe (i.e. when the angle between vectors $(\mathbf{r}_E - \mathbf{r}_P)$ and \mathbf{n} is smaller than 45°). The use of the correct

normal derivative would complicate the resulting algebraic equation; the error can be eliminated by applying another correction, as described in [14].

The mass fluxes calculated using the above normal velocity do not - in general - satisfy the mass conservation law. They need to be corrected by invoking a pressure-correction, in the spirit of the SIMPLE method [16]. From the above equation one can derive a relation between the corrections of the normal velocity and the pressure-derivative:

$$(\mathbf{v}' \cdot \mathbf{n})_e \approx \left(\frac{V}{A_p} \right)_e \frac{p'_E - p'_P}{|\mathbf{r}_E - \mathbf{r}_P|} \quad (3.22)$$

The mass flux is calculated using the above approximations as follows:

$$\dot{m} = \rho \left[(\mathbf{v}^* \cdot \mathbf{n})_e + (\mathbf{v}' \cdot \mathbf{n})_e - \dot{V}_e \right] S_e \quad (3.23)$$

The detail procedure is available in ref. [15]

3.7 SOLUTION ALGORITHM

The solution algorithm follows the well-known SIMPLE-pattern and can be summarized as follows:

First, all variables are assigned initial values. An iterative procedure is then started in order to find solution of the coupled non-linear equations using the following steps:

- The momentum equations are discretized and linearized, leading to algebraic equation systems for each velocity component, in which the pressure, the other velocity components, temperature, and all fluid properties are treated as known (values from previous iteration are used). These linear equation systems are solved iteratively in turn to obtain an improved estimate of the velocity, u_i^* . The iterations in the linear equation solver are called inner iterations. There is no need to solve these equation systems very accurately, since the equations were linearized and decoupled; experience shows that it is enough to reduce the residual level by an order of magnitude. Usually only few (one to five depending on the type of geometry) inner iterations are necessary.

- The improved velocity field is used to calculate new mass fluxes through CV faces and to invoke the mass-conservation equation; the result is the pressure-correction equation, which is solved using the same linear equation solver and to the same tolerance. Since the pressure-correction equation converges much slower than other equations (it represents a Poisson-equation with Neumann boundary conditions), more inner iterations are necessary than for the momentum equations. The maximum number is usually limited (here 15-20), but iterations are stopped earlier if the residual level drops by an order of magnitude. Upon solving for p' , the mass fluxes, CV-center velocities, and pressure are corrected using expressions given above. Only an α -fraction of p' is added to pressure, where $\alpha \approx (0.1 - 0.8)$; smaller values are used for large time steps in the case unsteady flow and highly non-orthogonal grids.
- Additional transport equations are solved in the same manner to obtain better estimates of the new solution (Here temperature).
- This completes one outer iteration; the above steps are repeated until residual level before the first inner iteration in each equation becomes sufficiently small. Usually, a reduction by three to four orders of magnitude corresponds to a convergence error of the order of 0.1%.

For further stabilization of the numerical algorithm, underrelaxation factors of 0.55-0.9 are used for velocity components depending on the geometry, 0.2 for pressure and 1.0 for temperature.

Both inner and outer iterations can be speeded up by multi-grid methods. For the inner iterations, this is meaningful only for the pressure-correction equation and very fine grids. For the outer iterations, the multi-grid method increases the efficiency tremendously in steady flow calculations. In present study, three-grid level is chosen. Grid level 1 is coarse, 2 is medium and grid level 3 is the finest one and all results are presented for the finest level.

3.8 AXISYMMETRIC PROBLEM

As discussed earlier chapters, two separate types of geometry are considering in present study. The first one is plane geometry; two sinusoidally varied wavy surface having same cross-sectional area from inlet to outlet and the second one is axisymmetric geometry; a pipe with sinusoidally converging-diverging cross-sectional area from inlet to outlet.

Axisymmetric flows are three-dimensional with respect to Cartesian coordinates i.e. the velocity components are functions of all three coordinates, but they are only two-dimensional in a cylindrical coordinate system (all derivatives with respect to the circumferential direction are zero, and all three velocity components are functions of only the axial and radial coordinates, z and r). In cases without swirl, the circumferential velocity component is zero everywhere. As it is much easier to work with two independent variables than three, for axisymmetric flows, it makes sense to work in a cylindrical coordinate system rather than a Cartesian one.

In differential form, the 2D conservation equations for mass and momentum, written in a cylindrical coordinate system, read (Bird et al., 1962):

$$\frac{\partial(\rho v_z)}{\partial z} + \frac{1}{r} \frac{\partial(\rho r v_r)}{\partial r} = 0 \quad (3.24)$$

$$\frac{\partial(\rho u_z v_z)}{\partial z} + \frac{1}{r} \frac{\partial(\rho r u_r u_z)}{\partial r} = -\frac{\partial p}{\partial z} + \frac{\partial \tau_{zz}}{\partial z} + \frac{1}{r} \frac{\partial(r \tau_{rz})}{\partial r} + \rho b_z \quad (3.25)$$

$$\frac{\partial(\rho u_z v_r)}{\partial z} + \frac{1}{r} \frac{\partial(\rho r u_r u_r)}{\partial r} = -\frac{\partial p}{\partial z} + \frac{\partial \tau_{rz}}{\partial z} + \frac{1}{r} \frac{\partial(r \tau_{rr})}{\partial r} + \frac{\tau_{\theta\theta}}{r} + \frac{\rho u_\theta^2}{r} + \rho b_r \quad (3.26)$$

$$\frac{\partial(\rho u_z u_\theta)}{\partial z} + \frac{1}{r} \frac{\partial(\rho r u_r u_\theta)}{\partial r} = -\frac{\rho u_r u_\theta}{r} + \frac{\partial \tau_{rz}}{\partial z} + \frac{1}{r^2} \frac{\partial(r^2 \tau_{r\theta})}{\partial r} + \rho b_\theta \quad (3.27)$$

Where the non-zero stress tensor components are:

$$\tau_{zz} = 2\mu \frac{\partial u_z}{\partial z} + \frac{2}{3} \mu \operatorname{div} v \quad (3.28)$$

$$\tau_{rr} = 2\mu \frac{\partial u_r}{\partial r} + \frac{2}{3} \mu \operatorname{div} v \quad (3.29)$$

$$\tau_{\theta\theta} = 2\mu \frac{u_r}{r} + \frac{2}{3} \mu \operatorname{div} v \quad (3.30)$$

$$\tau_{rz} = \tau_{zr} = \mu \left(\frac{\partial u_z}{\partial r} + \frac{\partial u_r}{\partial z} \right) \quad (3.31)$$

$$\tau_{\theta r} = \tau_{r\theta} = \mu r \frac{\partial}{\partial r} \left(\frac{u_\theta}{r} \right) \quad (3.32)$$

$$\tau_{\theta z} = \tau_{z\theta} = \mu \frac{\partial u_\theta}{\partial z} \quad (3.33)$$

The above equations contain two terms which have no analog in Cartesian coordinates: $\rho v_\theta^2 / r$ in the equation for v_r , which represents the apparent centrifugal force, and $\rho v_r v_\theta / r$ in the equation for v_θ , which represents the apparent Coriolis force. These terms arise from the coordinate transformation should not be confused with the centrifugal and Coriolis forces that appear in a rotating coordinate frame. If the swirl velocity v_θ is zero, the apparent forces are zero and the third equation becomes redundant.

When a FD method is used, the derivatives with respect to both axial and radial coordinates are approximated in the same way as in Cartesian coordinates; method described in earlier sections can be used.

Finite volume methods requires some care. The conservation equation in integral form given earlier (3.1 – 3.5) remain the same, with the addition of apparent forces as source terms. These are integrated over the volume as described in Sect.3.4.2. The CV size in the θ -direction is units i.e. one radian.

If the coordinates z and r of the cylindrical coordinate system are replaced by x and y , the analog with the equations in Cartesian coordinates becomes obvious. Indeed, if r is set to unity and v_θ and $\tau_{\theta\theta}$ are set to zero, these equations become identical to those in Cartesian coordinates, with $v_z = u_x$ and $v_r = u_y$. Thus the same computer code can be used for both

plane and axisymmetric 2D flows; for axisymmetric problems, one sets $r = y$ and includes $\tau_{\theta\theta}$ and, if the swirl component is non-zero, the v_θ equation [15]

4.1 GENERAL

In previous chapter, computational technique along with detail discretization of governing equations is presented. In this chapter, analysis of results from present numerical simulation of laminar flow through wavy channel and its hydrodynamic and thermal characteristic will be discussed. For convenience of presentation, this chapter is subdivided into several subsections. However, the well known and classical phenomenon behind the flow physics related to present investigation have not been discussed details. Just a brief outline is presented when necessary but new phenomenon that is the outcome of present numerical simulation has been presented details.

4.2 COMPUTATIONAL DOMAIN

The geometry of present investigation is shown in Fig.4.1. This is a wavy channel consisting of four cycles. Both axisymmetric and plane geometry with wavy boundary is considered in this investigation. Same computer code is adapted and capable of solving both problems. In this section, computational domain along with geometrical parameter is discussed for both geometry together, but computational results are discussed later separately for two geometry. In Fig.4.1. dark-heavy lines show the physical boundary. The physical boundary is symmetrical about centroidal axis and is defined by the sinus function:

$$r = a \left[1 - \sin \frac{\pi}{2} \left(1 + \frac{4x}{\lambda} \right) \right] ; \text{ Axisymmetric geometry} \quad (4.1)$$

$$y = a \left[1 - \sin \frac{\pi}{2} \left(1 + \frac{4x}{\lambda} \right) \right] ; \text{ Plane geometry} \quad (4.2)$$

As the geometry is symmetrical about its centroidal axis, only one half is taken as computational domain. Light lines inside the physical boundary consist of computational

domain showing inlet, outlet, symmetry and impermeable wall. Grid generation code of 'CAFFA' [12] could produce straight line, circular arc and arbitrary line segments. For present investigation, a new subroutine is introduced that can produce wavy lines of any wavelength, amplitude and phase angle. A portion of the subroutine that introduced the wavy line is presented in the appendix [A].

Fig.4.2a. and Fig.4.2b. show the geometrical parameters associated with present investigation for axisymmetric and plane geometry respectively with coordinate system.

4.3 STEPS OF SIMULATION

After setting a particular geometry (for constant λ/a ratio), the simulation is started. A systematic progression in Reynolds number was obtained by decreasing the fluid kinematic viscosity ν . This also decreased the pressure drop through the channel appropriately to simulate a nearly linear decrease of friction factor with Reynolds number. Because the kinematic viscosity was the independent variable, the Reynolds numbers actually did not turn out to be integer values. The discretized equations are solved using sufficiently large number of iterations. For convergence of field value, residual levels are monitored at previously specified monitoring location. Iterations were continued until difference between two last solutions was less than 10^{-5} to 10^{-6} . For the further stabilization of numerical algorithm underrelaxation factors were used as shown:

TABLE: 4.1

Range of Under Relaxation Factor (URF) for different variables

| Variable | Range of URF | Range of Re |
|-------------|--------------|---------------|
| U-velocity | 0.85 – 0.90 | $300 \geq Re$ |
| | 0.82 – 0.85 | 300 – 600 |
| V-velocity | 0.75 – 0.80 | 600 – 1200 |
| | 0.65 – 0.76 | 1200 - 2000 |
| Pressure | 0.2 | 100 – 2000 |
| Temperature | 0.9 – 1.0 | 100 – 2000 |

4.4 GRID SENSITIVITY TEST

Numerical solution of any problem strongly depends on grid size. Effect of grid size influence the hydrodynamic and thermal parameter of solution and sometime cause huge error with unfeasible solution. For present investigation, three-grid size is chosen:

TABLE: 4.2
Three grid levels with their sizes and names

| Fineness of grid | Grid size | Name of the level |
|------------------|-----------|-------------------|
| Coarse | 140*16 | first level grid |
| Medium | 280*32 | second level grid |
| Fine | 560*64 | third level grid |

The first numerical value indicates the number of control volume in axial direction and second for radial direction. The code 'CAFFA' is a multi-grid flow solver, solves problem from coarse grid to fine grid level. For present simulation, axial velocity profile is chosen for sensitivity testing. For several λ/a ratio and Reynolds number, axial velocity profiles for three grid level are calculated and compared. The computed results of $\lambda/a=15.0$ and Reynolds number 800 is presented in Fig.4.3a, Fig.4.3b and Fig.4.3c for first cycle at six axial positions ($X=0.0,0.14,0.28,0.42,0.71,0.85$) calculated from the inlet. Up to $X=0.42$ there is no considerable difference in three profiles of coarse, medium coarse and fine grid level. Second and third level profiles almost overlaps each other. A considerable difference is observed at first level profiles with second and third levels profiles at $X=0.71,0.85$. Though second level and third levels profiles do not overlap but shows good agreement to each other. Second and third levels profiles clearly show the negative velocity profile at upper side. Because it is in the separation region, but the thickness of negative velocity profile is very small and it is difficult to show this region by first level profile due to smaller number of grid at radial direction (16 only). Fig.4.4a to Fig.4.4c show the velocity profiles for plane geometry. And above discussion is also suitable for plane geometry. Proceeding simulation in grid size finer

than 560*64 is not possible due to lack of computer hardware facility. The whole simulation work is done on three grid levels but result of third grid level (560*64) is stored for further calculations.

4.4 VALIDATION OF NUMERICAL MODEL

To validate the present numerical model, simulated data is tested against available experimental and numerical data of other investigator, deal with wavy channel. For axisymmetric geometry, mean friction coefficient (f) per wave length (λ) is calculated for present simulated data using the equation [9] shown below:

$$f = \frac{D_{av}}{L} \frac{\Delta P}{\frac{1}{2} \rho U_m^2} \quad (4.3)$$

Where ΔP is the pressure difference between inlet and outlet. There is a slight variation in pressure value along the radial direction at inlet and outlet. For simplicity of calculation, arithmetic mean of cell value of pressure at inlet and outlet is taken for the calculation of ΔP . Here length of the channel L is calculated by wave length (λ) times the no. of cycle. In present investigation the value of L is '4 λ '. Mean friction coefficient is calculated for $L^* = 19.0$ for a range of Reynolds number 100 to 1000 based on average diameter of the channel. Variation of friction coefficient 'f' with Reynolds number is shown in Fig.4.5. This is compared with the experimental data of Russ & Beer [9], because they carried out their experiment in a geometry exactly like the geometry used in present investigation with $L^* = 19.0$. The only difference is they took 10 cycles and in present investigations 4 cycles are considered. Friction coefficient for straight pipe is also presented for comparison. This is calculated using relation:

$$f = \frac{64}{Re} \quad (4.4)$$

Present prediction shows good agreement with experimental data. Only some deviation is observed between Reynolds number range 250 to 400. Pressure was measured by pressure cell and they reported 1% error in their experiment. In this range of Re, flow separation starts at the bulge part of the channel and separation bubble grows in size with large positive

pressure gradient along the flow direction. Details of this phenomenon will be discussed in later sections, as we will see there after $Re=400$ there is slight change in size in vortex with further increase in Re . Vortex formation and growing up in size may introduce some instability in flow field.

For the case of plane geometry, present prediction is compared against similar work done by Nishimura et. al. [10] and Wang & Vanka [2]. In Fig. 4.7, solid line indicates the position of predicted separation and reattachment point at the wavy wall for Reynolds number range 10 to 1000. The region inside this profile indicates the separation region. For this range of Re , position of separation point show good agreement with the experimental data of Nishimura et. al. [10] and Wang & Vanka [2]. At low Re , positions of reattachment point do not agree with present prediction. For plane geometry, the iterative solution does not converge up to prescribed accuracy. At third level grid, some oscillation in numerical simulation is observed. That's why some uncertainty in calculation arises. But at higher Re , present prediction shows fair agreement with experimental data. Fig. 4.8. shows the predicted vorticity profile and experimental data of Nishimura et. al. [11] at $L^*=8.0$, $Re=350$ for first cycle. The first and second sharp edges of solid line that touch the zero vorticity line indicate separation and reattachment point respectively. Present prediction shows good agreement with experimental data except the pick near reattachment point. This pick indicates the maximum axial velocity gradient in separation region. Numerical calculation of Nishimura et. al. [11] shows this value is equal to 50 and in present prediction this is equal to 30. But the experimental value is approximately 40. The reason is this is the critical Reynolds number ($Re=350$) and actual flow pattern becomes unsteady at this Re . In present investigation, we do not consider the unsteady calculation. This may create discrepancy between experimental and numerical prediction.

4.5 HYDRODYNAMIC CHARACTERISTIC

Throughout the whole simulation work, mainly two parameters, Reynolds number and geometric ratio L^* (λ/a) are varied. For axisymmetric geometry, ten values of L^* are chosen. They are 11.0, 13.0, 15.0, 17.0, 19.0, 21.0, 23.0, 25.0, 30.0, 40.0. One thing should be borne

in mind that higher the ratio L^* smaller the waviness of the surface. Because throughout the investigation, the parameter λ is constant and only amplitude (a) is varied. For straight pipe there is no amplitude (a=0). So L^* for straight pipe is infinity. For each geometric ratio, flow field is solved for 13 Reynolds number. They are $Re = 100, 150, 200, 300, 400, 600, 800, 1000, 1200, 1400, 1600, 1800, 2000$. Inlet velocity profile is assumed the fully developed velocity profile of straight pipe. Plane geometry is studied in different section for convenience.

The dependent variables are friction factor (f) per wavelength, wall vorticity (ξ_w), skin friction coefficient (C_f). Parametric presentation of streamlines is also studied along with streamwise axial velocity profiles. Positions of separation and reattachment points have also been given special attention.

The following subsections present the brief discussion of influence of independent variables on dependent variables for the convenience of presentation.

4.5.1 FLOW PATTERN

As mentioned earlier, the whole simulation is done for 10 geometric parameter L^* and 13 Reynolds number (100 – 2000). Parametric presentation of flow field is given by constant streamline contours. Here $L^*=11.0, 21.0, 30.0$ are chosen for discussion. Calculated streamlines are shown for Reynolds number range 100 – 2000 in Fig.4.10. to Fig. 4.12. These three values of L^* actually represent high waviness ($L^*=11.0$), medium waviness ($L^*=21.0$) and low waviness ($L^*=30.0$) of the surface.

Streamfunction values are calculated at CV corners [12] using mass fluxes through cell faces [14], since the mass flow rate between two streamlines is constant. The field value of stream function is normalized using the relation:

$$\text{Normalized streamfunction, } \psi = \frac{\text{CV corner value of streamfunction}}{\sum_{j=1}^{64} \dot{m}_{l,j}} \quad (4.5)$$

Here the denominator represents the inlet mass flux per unit width. For all calculations, line grid size is taken as mentioned earlier. So the 'j' index varies from 1 to 64 in equation (4.5).

Effect of Re: Fig.4.11 presents the streamlines of $L^*=21.0$. At low Reynolds number, streamlines are approximately symmetrical about the maximum cross section of the channel. This indicates that inertial effects are not important. The streamlines become asymmetrical with increasing Reynolds number. First indication of circulatory vortex is observed at Reynolds number 200 upstream of the maximum cross section of the channel. With further increase of Reynolds number, this vortex grows in size and its center shifts towards downstream. This growing-up tendency of vortex continues up to Reynolds number 800 shown in Fig.4.11 (c) – Fig.4.11 (h). After $Re=800$, vortex size increases very slowly with further increase of Reynolds number. In this range, shown in Fig.4.11 (i) – 4.11 (k), vortex shows large core towards downstream. From above discussion, three distinguishable range of Reynolds number is observed:

TABLE: 4.3

Critical ranges of Reynolds number

| Observation | Range of Re | Range name |
|--|------------------------|---------------------|
| <i>No vortex formation</i> | $200 > Re$ | <i>Lower range</i> |
| <i>Vortex formed & rapid-growing in size</i> | $200 \geq Re \geq 800$ | <i>Middle range</i> |
| <i>Large core of vortex & slow-growing in size</i> | $800 > Re \geq 2000$ | <i>Upper range</i> |

One reason may be concluded from such behavior of flow field that with increasing Reynolds number, vortex changes from steady to unsteady motion, i.e. the vortex size varies with time. Nishimura et. al. [10] reported that the unsteadiness is not periodical but is an intermittent phenomenon.

Effect of $L^*(\lambda/a)$: In previous sub-section, effect of Reynolds number is discussed for a constant geometric parameter ($L^*=21.0$). Observation is tabulated in TABLE-4.3. It should be bear in mind that this observation is only restricted for that particular geometry. Geometrical parameter strongly influences the flow pattern in wavy channel. The three ranges (TABLE: 4.3) are dramatically varied by the change of L^* . Because change of wavelength to amplitude

ratio (L^*) increases or reduces the divergence of the waviness of the channel surface. For a constant Reynolds number, more the divergence (smaller L^*), earlier will be the change of sign (negative to positive) of axial pressure gradient $\left(\frac{dP}{dx}\right)$. This is the well known ‘*diffuser-effect*’ of flow physics [18]. This phenomenon is graphically present in Fig. 4.9 (b). When axial pressure-gradient profile touches the zero gradient line flow separation occurs. Circulation bubble continues until this profile touches again zero gradient line downstream side. The second intersection point between axial pressure gradient line and zero gradient line indicates the reattachment of the separated streamline ($\psi=1$) and end of separation bubble. All previous investigations were restricted to a particular L^* . Geometrical complexity, problem in convergence in iterative procedure and dramatic variation of different parameter is the main reason for this restriction reported by Wang & Vanka [2]. Large separation bubble is observed at $Re=200$ for $L^*=11.0$ in Fig.4.12 (c). For $L^*=21.0$ the size of separation bubble shown in Fig. 4.11 (c) is small and just start to grow-up but there is no flow separation hence no separation bubble at $L^*=30.0$ at the same Reynolds number (200) shown in Fig. 4.10. (c). The ‘*lower-range*’ of Reynolds number indicated in TABLE: 4.3 is now presented for different L^* below:

TABLE: 4.4

Lower range of Reynolds number at different L^*

| L^* | Lower range of Re |
|-------|-------------------|
| 11.0 | 100>Re |
| 13.0 | 100>Re |
| 15.0 | 130>Re |
| 17.0 | 150>Re |
| 19.0 | 180>Re |
| 21.0 | 200>Re |
| 23.0 | 250>Re |
| 25.0 | 300>Re |
| 30.0 | 400>Re |

These are not exact values of lower range of Re for different L^* . For a particular geometrical ratio (L^*), hundreds of Reynolds number should be chosen at lower range with close gap (e.g. Re = ---, 99,100,101, ----) and also interpolation is needed to determine exact Reynolds number where formation of vortex just started. This becomes an exhaustive job when L^* varies. But present investigation gives an approximate idea for the starting point of searching 'lower range' of Reynolds number at different L^* . The above discussion is true for other two ranges.

Effect of wave number n: For a particular L^* and Re, the variation of flow pattern with wave number n is so small that is not distinguishable. At low Reynolds number ($Re < 200$) almost there is no variation. But for medium ($800 \geq Re > 200$) and high ($2000 \geq Re > 800$) the vortex size of first cycle ($n=1$) is slightly larger than the other three cycles ($n=2-4$). This is because of entrance effect. Other three cycles show no variation in vortex size, only core is shifted slightly downstream with the increase of n at high Reynolds number. This is also reported by Russ & Beer [8].

4.3.2 SEPARATION AND REATTACHMENT POINT

As discussed earlier, with the increase of Reynolds number flow separation occurs upstream of the maximum cross section. Moving downstream into the diverging part of the pipe, the axial pressure gradient change its sign (Fig.4.9b.) from negative to positive, which causes a flow separation and the development of flow reversal in the bulge part of the pipe. In the converging part the axial pressure gradient changes its sign again, causing the reattachment of the flow.

However, there are different ways of locating separation and reattachment point. Eaton & Johnston [19] interpolate the near wall axial velocities for locating the distance (from inlet) of zero axial velocity, Wang & Vanka [2] used the sign (negative to positive and positive to negative) of axial pressure gradient $\left(\frac{dP}{dx}\right)$, Nishimura et. al. [10] used the wall vorticity

profile to locate the separation and reattachment point. In present investigation, streamline $\psi=1$ is chosen for locating separation and reattachment point. As it is seen in Fig.4.10a, streamline $\psi=1$ follows the upper wall of the wavy channel and no formation of vortex. At Fig.4.10e $\psi=1$ line separates at some distance from the starting point of the wave, continues and at last again touches the wall. The second point is the reattachment point. These two regions are magnified 10 to 50 times using TECPLOT-7 software and axial locations are pointed out using 'Data-Probing' option up to 4 decimal places accuracy. Fig.4.13 – Fig.4.18 show the location of separation and reattachment point at different Reynolds number and geometric parameter L^* for first cycle ($n=1$) only.

Effect of Re: Fig.4.13 shows the variation of positions of separation and reattachment point with Reynolds number for $L^*=11.0$. For convenience, separated streamline ($\psi=1$) for $Re=800$ is also shown below and separation and reattachment points are indicated by down arrow. With the increase of Reynolds number, separation point is shifted upstream around $Re \approx 700$, then show a little variation with further increase of Reynolds number. Reattachment point is also shifted downstream with high variation around $Re \approx 700$ and show little variation with further increase of Reynolds number. The region inside the separation and reattachment line indicates the circulation zone and it expands with Reynolds number and nearly approaches a limiting value in laminar flow condition. The distance between a square and round symbol in the figure at any Reynolds number indicates the length of vortex at axial direction. Fig.4.14 and Fig.4.15 show the same variation for $L^*=19$ & 30 respectively. It is easily concluded that, increase of L^* (i.e. reduction of waviness of surface) reduces the circulatory zone.

Effect of L^* : Fig.4.16 - Fig.4.18 show the variation of separation and reattachment points with L^* at constant Reynolds number. Fig.4.16 shows this variation for $Re=600$. As it is seen from the figure, separation and reattachment point approaches each other with the increase of L^* . The rate of approaching reduces with increase of Reynolds number as shown in Fig.4.17 & Fig.4.18.

4.5.3 AXIAL VELOCITY

Fig.4.19 – Fig.4.21 show the axial velocity profiles with reference line at different Reynolds number for $L^*=30.0, 21.0, 11.0$. For the convenience of study profiles are presented at their original locations (indicated by reference lines). The original values of velocity are reduced by 50% for easy observation.

Effect of wave number n: Fig.4.19a shows the axial velocity profiles for $L^*=30.0$ at different $Re=100$ for $n=1$ to 4. Each individual cycle consists of velocity profiles at equal distance of $\lambda/7$. As mentioned earlier, inlet condition is fully developed laminar flow condition for circular pipe. The profile in the narrowest cross section shows a larger velocity gradient compared to the parabolic profile of the flow through a straight pipe. At first cycle with the increase of axial distance velocity profile become flatter and up to the maximum cross section then again velocity gradient increase due to gradual reduction of cross sectional area. This pattern remains similar in second, third and fourth cycles. But only difference in later cycles is reduction of magnitude of velocity.

Effect of Re: For high Reynolds number, velocity profile shows earlier inflection point than low Reynolds numbers for a constant L^* and the profiles become flatter at the diverging part of the channel compared to low Reynolds number.

Effect of L^* : Effect of L^* is too much distinguishable on velocity profile at a constant Reynolds number. Lower the L^* higher will be the waviness of the surface earlier will be the appearance of negative velocity profile.

4.5.4 WALL SHEAR STRESS

The calculated wall vorticity profiles are shown in Fig.4.22 – Fig.4.36. Wall vorticity is calculated and normalized according to Wang & Vanka [2]

$$\xi_w = \frac{1}{2} Re C_r \left(\frac{D_{max}}{D_{av}} \right) \quad (4.6)$$

$$C_f = \frac{\tau_w}{\frac{1}{2} \rho U_m^2} \quad (4.7)$$

$$\tau_w = \mu \left(\frac{\partial u}{\partial r} \right)_w \quad (4.8)$$

Where C_f and τ_w are the skin friction coefficient and wall shear stress respectively.

Effect of Re: Fig.4.22 – Fig.4.29 show the absolute wall vorticity profiles for constant geometric parameter L^* at different Reynolds number. The first and second point that touch the zero vorticity line are corresponding separation and reattachment point. At these two point

the axial velocity gradient $\frac{\partial u}{\partial r}$ is zero. It is easily viewed from equation (4.6) to (4.8). The

zone between these two points actually indicates the separation bubble, sometime called circulatory zone. Fig.4.22 presents the vorticity profiles of $L^*=11.0$ for first and fourth cycle at $Re=200,600,1000,1400,2000$. Before studying the effect of Reynolds number on vorticity profile, attention should be given to a single profile to understand the physics behind such profile formation. Fig.4.9a shows an individual vorticity profile. As already discussed, at the converging region of channel velocity gradient is high, as a result vorticity is also high in this region. Downstream to the flow, velocity gradient starting to reduce due to the divergence of the channel and magnitude of vorticity falls and becomes zero at separation point as there is no velocity gradient present there. Flow reversal is observed from here (Fig.4.19, Fig.4.20, and Fig.4.20) with small region of negative velocity profiles compared to positive velocity profiles. Just after separation point, a negative velocity profile shows a first maximum

velocity gradient $\frac{\partial u}{\partial r}$, then again decreases due to approach the maximum diversity of the channel. Magnitude of vorticity at the maximum cross section of the channel shows the smaller value. When flow approach further downstream side negative velocity gradient again increases and somewhere before the reattachment point it shows the maximum negative gradient. This phenomenon can easily be observed in velocity profiles in Fig.4.21(c), Fig.4.21 (d), and Fig.4.21 (e).

Now come to the discussion (influence of Reynolds number) again. At low Reynolds number (e.g. $Re=200$) where viscous force dominates, there is no sharp peak as discussed earlier. Increase of Reynolds number grows up this pick and shifts it slightly towards the downstream side. The gap between the two intersection points of vorticity profiles with zero vorticity line increases with the increase of Reynolds number for constant L^* . This is obvious, because increase of Reynolds number increases the gap between separation and reattachment point discussed earlier. This is true for other L^* . Only difference is the reduction of peak values in circulation zone with the increase of L^* .

Effect of L^* : Fig.4.30 – Fig.4.36 show the wall vorticity profiles for constant Reynolds number at different L^* for first and fourth cycle. For comparison, vorticity of straight pipe is indicated along with the wavy channel. Fig.4.30 shows the vorticity profiles for $Re=200$ and for $L^*=11.0, 17.0, 23.0, 30.0$. The vorticity for $L^*=23.0$ & 30.0 show positive value everywhere indicating no separation zone and profiles are symmetrical concave shape about the maximum cross section. $L^*=11.0$ & 17.0 shows smaller circulatory zone with no sharp peak near separation and reattachment point. So, at lower value of Reynolds number, curvature effect (L^*) not too much dominating. Fig.4.36 shows the vorticity profiles for same L^* at $Re=2000$. Here effect of surface waviness or curvature effect dominates vorticity profiles. $L^*=11.0$ shows the highest peak near reattachment point and this peak decreases for lower waviness (higher L^*) of the surface.

4.5.5. SKIN FRICTION COEFFICIENT

Fig.4.37 – Fig.4.47 show the distribution skin friction coefficient along axial direction from inlet to outlet at constant Reynolds numbers for $L^*=13.0, 17.0, 23.0, 30.0$. Skin friction coefficient (C_f) is calculated using equation (4.7) and (4.8). C_f is actually distribution of local friction coefficient along the wall. For straight pipe, C_f is constant for particular Reynolds number and decreases with the increase of Reynolds number as indicated in Fig.4.37 to Fig.4.47. For wavy channel, C_f is almost periodic, and shows sharp peak at the minimum cross section. At constant Reynolds number (e.g. Fig.4.37) this sharp peak increases with the

increase of surface waviness (lower L^*). This sharp peak amplified in magnitude downstream to the axial direction due to pressure drop. At lower Reynolds number this amplification occurs at smaller rate but at high Reynolds number (e.g. Fig.4.45) this rate is larger. This peak values for any L^* reduces for higher Reynolds number.

4.5.6 MEAN FRICTION COEFFICIENT

The calculation procedure of mean friction coefficient (f) is already described in equation (4.3) according to Russ & Beer [9]. Fig.4.48a and Fig.4.48b present the variation of mean friction coefficient per wavelength (λ) with Reynolds number. For comparison, variation of friction coefficient of straight pipe is also given for same Reynolds numbers range. In logarithmic (log-log) plot, friction factor linearly decreases with the increase of Reynolds number keeping a constant slope for a particular L^* . For a constant Reynolds number, friction factor increases with the decrease of L^* (increasing the waviness). Furthermore the slope of the curves are slightly reduced with the decrease of the geometric parameter L^* .

The linear variation of friction factor with Reynolds number in logarithmic plot enables to make a correlation between Reynolds number and friction factor for different L^* . The proposed correlation is in the form given below:

$$f = \frac{C}{Re^m} \quad (4.9)$$

Where 'C' is a correlation constant and 'm' is the correlation exponent. TABLE: 4.5 shows the values of C and m for different L^* calculated from Fig.4.48a and Fig.4.48b.

The tabulated values of 'C' and 'm' are plotted against L^* in Fig.4.49. Figure shows the best-fit curves. For curve fitting, a polynomial equation (4.10) is chosen.

$$P_n = A_n z^n + A_{n-1} z^{n-1} + A_{n-2} z^{n-2} + \dots + A_2 z^2 + A_1 z + A_0 \quad (4.10)$$

Where 'n' is the order of polynomial, 'z' is independent variable and A is polynomial constant. For correlation constant 'C' a fourth order polynomial and for correlation exponent 'm' a second order polynomial is proposed with $\pm 6\%$ accuracy:

$$C = 0.016 \left(\frac{\lambda}{a}\right)^4 - 1.0136 \left(\frac{\lambda}{a}\right)^3 + 22.21 \left(\frac{\lambda}{a}\right)^2 - 182.61 \left(\frac{\lambda}{a}\right) + 685.27 \quad (4.11)$$

$$m = -0.0011 \left(\frac{\lambda}{a}\right)^2 + 0.0529 \left(\frac{\lambda}{a}\right) + 0.5216 \quad (4.12)$$

TABLE: 4.5

Correlation constant (C) and exponent (m) as a function of L^*

| $L^* = \frac{\lambda}{a}$ | Correlation constant, C | Correlation exponent, m |
|---------------------------|-------------------------|-------------------------|
| 11.0 | 253.0 | 0.958 |
| 13.0 | 278.0 | 1.022 |
| 15.0 | 355.0 | 1.08 |
| 17.0 | 346.0 | 1.098 |
| 19.0 | 357.0 | 1.115 |
| 21.0 | 372.0 | 1.13 |
| 23.0 | 375.0 | 1.135 |
| 25.0 | 406.0 | 1.154 |
| 40.0 | 457.0 | 1.185 |

4.6 THERMAL CHARACTERISTIC

The foregoing chapter gives detail discussion about hydrodynamic characteristic of wavy axisymmetric channel for different L^* and Reynolds number. However, for studying thermal behavior of wavy channel, three geometrical parameter $L^* = 11.0, 19.0, 30.0$ are chosen. Actually these three L^* represent the high, medium and low waviness of the surface. Results are presented in the form of isothermal contour plots, average and local value of Nusselt number.

4.6.1 THERMAL FIELD

Thermal field is presented by isothermal contours from Fig.4.51 to Fig.4.54. Temperature is normalized using free stream temperature (T_α) and wall temperature (T_w) using the relation:

$$\text{Normalized Temperature, } \theta = \frac{T - T_\alpha}{T_w - T_\alpha} \quad (4.13)$$

Temperature of the wall is kept constant through out the simulation and it is assumed there is no internal heat generation and wall temperature is higher than the free stream temperature. Prandtl number (Pr) is kept constant and equal to 0.7. Fig.4.51(a)-Fig.4.51(f) present the isothermal contours for $L^* = 19.0$ for a $Re=50$ to 1000 and $n=1$ to 4. For low Reynolds number ($Re=50$), near the inlet thermal boundary layer starting to form showing temperature gradient in first cycle only (Fig.4.51c). With the increase of Reynolds number, isothermal lines propagate towards the downstream because of higher convective current. Temperature gradient is higher in converging section than diverging section.

The effect of waviness of the surface on thermal field is studied if Fig.4.52 & Fig.4.53 for two constant Reynolds number 200 & 1000. It is easily observed form Fig.4.52 that temperature gradient is higher at converging section for lower L^* , and gradient is lower at diverging cross section for lower L^* . Because, lower the geometric parameter L^* , decrease inter wall spacing in the converging part of the channel and increases the interwall spacing in the diverging cross section.

Fig.4.54 shows the combination of streamlines and isothermal lines for $L^*=11.0$ & 19.0 $Re=200$ & $n=1$ for studying how velocity field affect the thermal field. At $Re=200$, separation bubble is already formed and grows in size for $L^*=11.0$. Convective transport is occurred in this circulatory region compared to the channel with $L^*=19.0$. That's why space between $\theta=0.9$ isothermal line and wall is larger for $L^*=11.0$ than $L^*=19.0$.

4.6.2 HEAT TRANSFER

Heat transfer rate is measure by local and average value of Nusselt number. Local Nusselt number (Nu_x) is calculated using the equations:

$$Nu_x = \frac{h_x D_{av}}{K_f} \quad (4.14)$$

$$h_x = \frac{q_r}{\Delta T} \quad (4.15)$$

$$q_r = K_r \frac{dT}{dr} = \frac{\mu}{Pr} \frac{dT}{dr} \quad (4.16)$$

The average value of Nusselt number is calculated by integrating the local value over the total length of the channel using the relation:

$$Nu_{av} = \frac{1}{L} \int_0^L Nu_x dx \quad (4.17)$$

Fig.4.55 – Fig.4.56 show the distribution of local Nusselt number along the channel as a function of channel length for $L^* = 30.0, 11.0$ respectively for $Re=100, 500, 1000, 2000$. Average value of Nusselt number is also indicated in figure. Fig.4.57 – Fig.4.58 show the resulting distribution of local Nusselt number for $Re=300$ & 1000 respectively at $L^* = 11.0, 19.0, 30.0$. for first and third cycles. The increasing wall velocity gradient in the narrowest cross section causes a very thin thermal boundary layer, resulting in growing Nusselt numbers. Near to the reattachment point where high velocity components normal to the wall occur [9], boundary layer is additionally reduced, leading to a second maximum heat transfer coefficient downstream of the reattachment point.

Fig.4.57 shows that Nusselt number increases with the increase of L^* . Only at the first cycle the first sharp peak of Nusselt number is higher at lower value of L^* . This is because, increasing L^* reduces the surface waviness and narrowing the circulatory zone and also interwall spacing at maximum cross section is reduced helping enhancement of heat transfer.

One most interesting characteristic of wavy channel is shown in Fig.4.59a – Fig.4.59b. The local Nusselt number distribution show rise and fall in each cycle and this tendency decreasing with the increase of wave number or axial distance. Russ & Beer [9,10] suggested this tendency as '*exponential-decay*'. They numerically and experimentally proved this phenomenon. The upper peak and lower peak of local Nusselt number are plotted as a function of axial distance in Fig.4.59b. The two curves show the exponential-decay tendency.

Fig.4.60 shows the distribution of average Nusselt number as function of Reynolds number for $L^* = 11.0, 19.0, 30.0$. For comparison, average Nusselt number distribution for straight pipe is plotted in the same figure. For a particular Reynolds Number, average Nusselt number increases with the increase of geometric parameter L^* . Average Nusselt number distribution

curve shows a positive slope at lower L^* and this slope decreases with the increase of L^* (reduction of waviness). $L^*=30.0$ almost shows no variation with change in Reynolds number just like straight channel.

Numerical calculation of Russ & Beer [9] shows invariant average Nusselt number with the change of Reynolds number shown in Fig.4.61. This is for $L^*=19.0$. They actually calculated Sherwood number from mass transfer coefficient and using analogy function [9,10], converted it to Nusselt number. They found average value of Nusselt number slightly lower than the straight pipe ($Nu_{av}=3.66$, isothermal wall condition) shown in Fig.4.61. But their experimental value [10] does not agree with numerical prediction. Present prediction shows fair agreement with their experimental data approximately at Reynolds number lower than 700, but experimental results show 2 to 2.5 times higher average Nusselt number at higher Reynolds number range. One reason may be concluded from above result that both Russ & Beer [9] and present investigation calculated Nu_{av} using fully developed laminar flow condition. Somewhere around $Re=700$ transition begins. That's why experimental values do not agree with numerical prediction after this region.

4.8 PLANE GEOMETRY

Some of the characteristic of plan geometry has already been mentioned during code validation and grid sensitivity test. In present investigation, simulation is carried out for $L^*=8.0, 11.0, 15.0, 19.0, 25.0, 30.0$ and Reynolds number ranging from 50 to 600. It has already been published by Nishimura et. al. [10] and Wang & Vanka [2] that critical Reynolds number is 350. After which self sustained oscillatory vortex generate. Flow pattern, axial velocity profile, vorticity variation have the similar pattern as discussed for axisymmetric geometry. So, these things are not extensively discussed here again. Only pressure drop characteristics are presented for comparison of same characteristic in axisymmetric case.

The mean friction coefficient (f) per wavelength is calculated using the equation suggested by Nishimura et. al. [10]:

$$f = \frac{1}{4} \left(\frac{H_{av}}{\lambda} \right) \left(\frac{2\Delta P}{\rho u_m^2} \right) \quad (4.18)$$

Mean friction per wavelength as a function of Reynolds number is presented in Fig.4.61 for different geometric parameter L^* . For a particular Reynolds number, friction factor increases with the increase of surface waviness (decrease of L^*). The variation is smaller at higher L^* . Again for a fixed geometry, friction factors inversely proportional to the Reynolds number. It should bear in mind that all calculations have been carried out considering steady-laminar (fully developed) flow condition. This assumption shows the linear variation of friction factor with Reynolds number. Nishimura et. al. [10] got invariant nature of friction factors with Reynolds number after $Re=350$. The reason for this nature is starting of transition towards turbulence, which is not studied in present research work. However, a correlation is proposed in the form of equation (4.9) to determine friction factor (f) as a function of Reynolds number and geometric parameter L^* using figure 4.61. The proposed correlation constant C and correlation exponent m is summarized by a third order and a fourth order polynomial calculated using Fig.4.61. These polynomials are in the form:

$$C = 0.0652 \left(\frac{\lambda}{a} \right)^3 - 3.387 \left(\frac{\lambda}{a} \right)^2 + 4.347 \left(\frac{\lambda}{a} \right) + 615.36 \quad (4.19)$$

$$m = 5.10^{-7} \left(\frac{\lambda}{a} \right)^4 + 2.10^{-5} \left(\frac{\lambda}{a} \right)^3 - 0.0029 \left(\frac{\lambda}{a} \right)^2 + 0.0671 \left(\frac{\lambda}{a} \right) + 1.1038 \quad (4.20)$$

5.1. GENERAL

Hydrodynamic and thermal behavior of wavy channel have been studied in present investigation numerically. This chapter summarizes the accuracy and reliability of the present prediction, embodied in the computer code CAFFA [12] by comparing with the experimental data and suggests the scope of further extension of the present study.

5.2 CONCLUSIONS

The important conclusions from present study are summarized below:

- 1) Surface waviness causes early separation of fluid from wavy surface and point of separation shifts upstream with the increase of both Reynolds number and amplitude of wave. Similar pattern is true for point of reattachment, which shifts downstream for same condition.
- 2) Pressure drop and frictional loss are nearly linear and inversely proportional to Reynolds number. For larger amplitude of the wavy surface pressure drop as well as friction factor is higher at constant Reynolds number.
- 3) There is a significant range of Reynolds number where vortex is formed and starting to grow up in size. This range is observed in lower Reynolds numbers for high waviness of the surface.
- 4) Wall vorticity is negative and smaller in magnitude in separation region compared to non separated zone. Negative vorticity show the highest peak near the reattachment point for larger gradient in reverse flow.
- 5) Heat transfer rate falls exponentially along the axial direction from inlet to outlet of the channel. Separation bubble suppress the heat transfer rate and narrowest cross section show higher local value of Nusselt number than the bulge part of the channel.
- 6) Heat transfer increases with Reynolds number and this rate of increasing decreases for lower amplitude of the wavy surface and almost become invariant like circular pipe at very low waviness of the surface.

5.3 RECOMMENDATION FOR FUTURE WORKS

Present research work can be extended further

- a) to study the effect of phase shift between two opposite wall
- b) to study the effect of divergence of wall
- c) to determine the critical Reynolds number at different L^*
- d) to locate the range of transition
- e) to study the effect of turbulence
- f) to study the effect of asymmetric heating

Especially this works are recommended because these are capable of solving by CAFFA. One need first adaptation with finite volume method and also with CAFFA for modification it to make it suitable for solving recommended problems.

REFERENCES:

1. C. Saidi, F. Legay & B. Pruent Fotch, Laminar flow past a sinusoidal cavity, Vol.30, No.4, Int.J.Heat & Mass Transfer, 1987
2. G. Wang & S.P. Vanka, Convective heat transfer in periodic wavy passages, Vol.38, No.17, Int.J.Heat & Mass Transfer, 1995
3. L. Goldstein & E.M. Sparrow, Heat and mass transfer characteristic for flow in a corrugated wall channel , J. Heat Transfer ,1977
4. L.S. Yao, Natural convection along a vertical wavy surface, J. Heat Transfer,465-468,1983
5. S.G. Moulic, L.S. Yao, Mixed convection along a wavy surface, J. Heat Transfer,974-979,1989
6. L.C.Yang, Y.Asako, Y. Yamaguchi, M. Faghri, Numerical prediction of transitional characteristics of flow and heat transfer in a duct. Transaction of heat transfer, Vol.119, Feb. 1997.
7. T. Nishimura, Y, Ohori & Y. Kawamura, Flow characteristics in a channel with symmetric wavy wall for steady flow, J. Chemical Engg. Japan, 466-471,1984.
8. G. Russ & H. Beer, Heat transfer and flow field in a pipe with sinusoidal wavy surface-1 –Numerical investigation, Vol.40 No.5, Int.J.Heat & Mass Transfer, 1997
9. G.Russ & H. Beer, Heat transfer and flow field in a pipe with sinusoidal wavy surface-2 –Experimental investigation, Vol.40 No.5, Int.J.Heat & Mass Transfer, 1997
10. T.Nishimura, Y.Kajjimoto, Y.Kawamura, Mass transfer enhancement in channel with a wavy wall, Journal of Chemical Engineering of Japan, Vol.19 No.2, 1986
11. T.Nishimura, Y.Kajjimoto, Y.Kawamura, Y. Ohori, Mass transfer characteristics in channel with symmetric wavy wall for steady flow, Journal of Chemical Engineering of Japan, Vol.18, No.16, 1985
12. M.Peric & M. Schhimid, 'CAFFA', Verson 1.3, August,97, University of Humburg, Germany
13. R. S. Amano, A numerical study of laminar and turbulent heat transfer in a periodically corrugated wall channel, ASME, Vol. 107, August, 1985
14. Z. Lilek, S. Muzaferjia, M.Peric, V. Seidl, An implicit finite volume method using non matching blocks of structured grid, Num. Meth. of Fluid, 1997

15. J. Ferziger, M. Peric, Computational methods for fluid dynamics, Springer Verlag, Berlin Heidelberg, 1996
16. S. V. Patankar, Numerical heat and mass transfer, McGraw-Hill Book Company, 1984
17. T. Mizushima, Advanced heat transfer, Vol. 7, p. 87, Academic Press, 1971
18. R.C. Binder, Advanced fluid mechanics, Vol. 2, p. 80-81, Prentice – Hall, Englewood Cliffs, N.J., 1958
19. J.K. Eaton, J.P. Johnston, Turbulent flow reattachment: An experimental study of the flow and structure behind a backward-facing step. Report MD-39 Department of Mechanical Engg. Stanford University, June 1980
20. E.M. Sparrow, L.M. Hossfeld, Effect of protruding edges on heat transfer and pressure drop in duct. Vol.27 No.10, Int.J.Heat & Mass Transfer, 1984
21. Y. Asako, M. Faghri, Finite volume solution for laminar flow and heat transfer in a corrugated duct. Vol.109, Transaction of ASME, 1987
22. M. Faghri, Y. Asako, Numerical determination of heat transfer and pressure drop characteristic for a converging-diverging flow channel. Vol.109, Transaction of ASME, 1987
23. E. M. Sparrow & J. W. Comb, Effect of interwall spacing and fluid flow inlet conditions on a corrugated-wall heat exchanger. Vol.26, No.7, Transaction of ASME, 1983

The programme segment of the SUBROUTINE that create the grid data for wavy channel is presented here:

```

C.....READ COORDINATES OF GRID POINTS ALONG THE LINE
  print*, 'NO. OF PERIOD ,AMPLITUDE, PHASE ANGLE: '
  read(6,*)mm,amp,pangle
  write(5,*)mm,amp,pangle, ' NO.OF PERIOD,AMPLITUDE,PHASE-ANGLE'
*   phase=(pangle/360.)
    per=mm*1.0
    xxx=sqrt((xle-xls)**2.+(yle-yis)**2.)
    theta=atan(abs((yis-yle)/(xls-xle)))
    xlamda=xxx/per
    x=xxx/nseg
    xcount=0.0
    xxcoun=0.0
    yycoun=0.0
    pie=(22./7.)
    do i=1,nseg+1
      xpt(i)=xls+xxcoun
      ypt(i)=yis+yycoun
      xcount=xcount+x

      if(pangle .eq. 0.)
+ ycount=(amp-amp*cos((xcount/xlamda)*pie*2.0))
      if(pangle .eq. 180.)
+ ycount=0.0 -(amp-amp*cos((xcount/xlamda)*pie*2.0))

      xxcoun=xcount*cos(theta)-ycount*sin(theta)
      yycoun=xcount*sin(theta)+ycount*cos(theta)

    end do

```

C

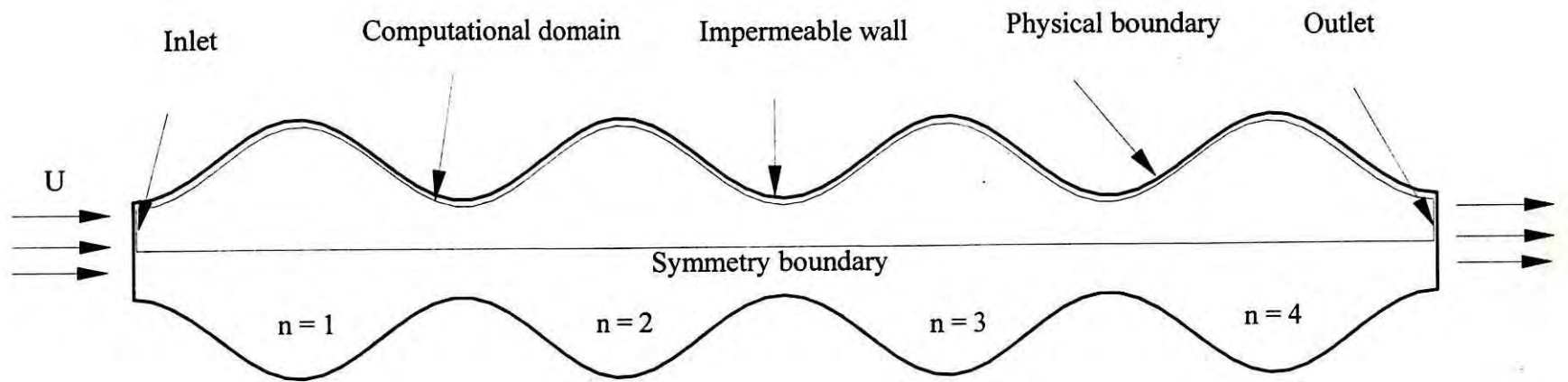


Fig. 4.1 Computational domain with physical boundary of wavy channel

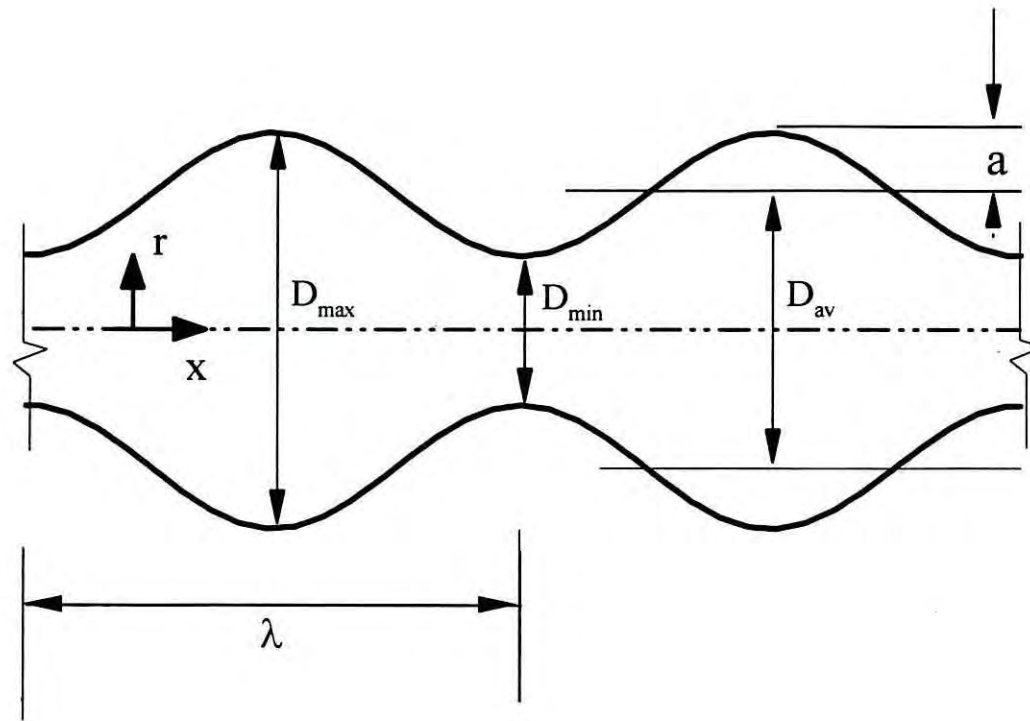


Fig. 4.2a Geometrical parameter with axis system for axisymmetric geometry

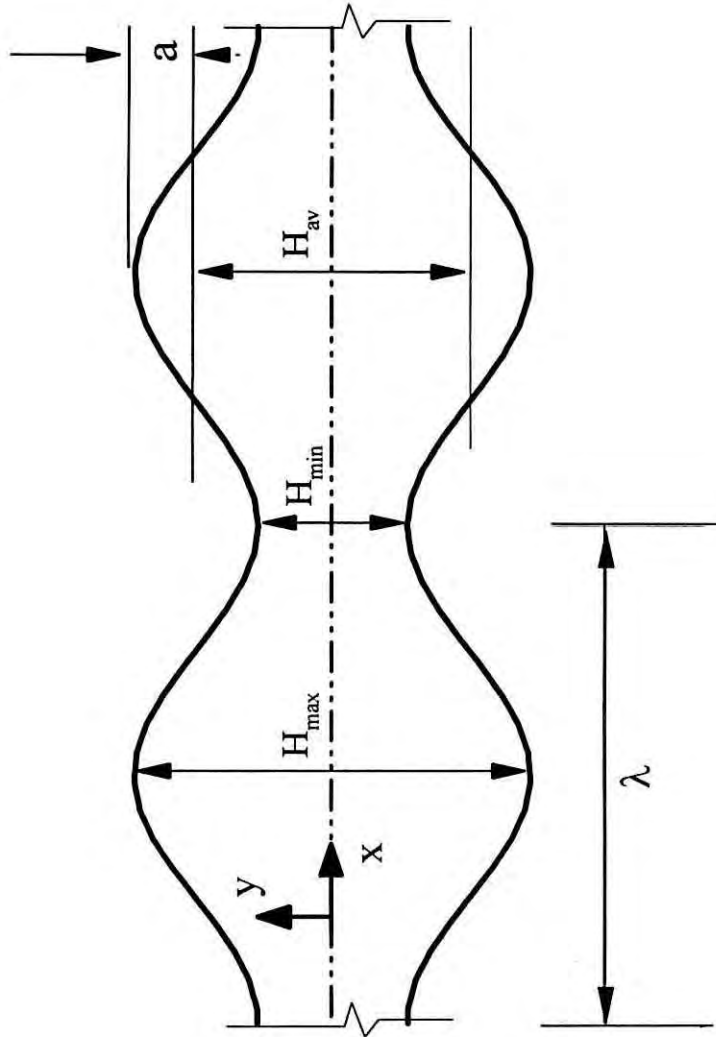


Fig.4.2b Geometrical parameter with axis system for plane geometry

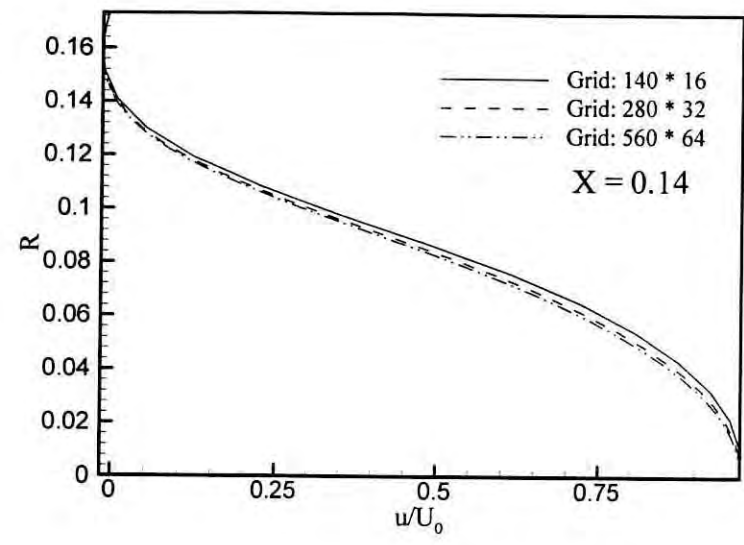
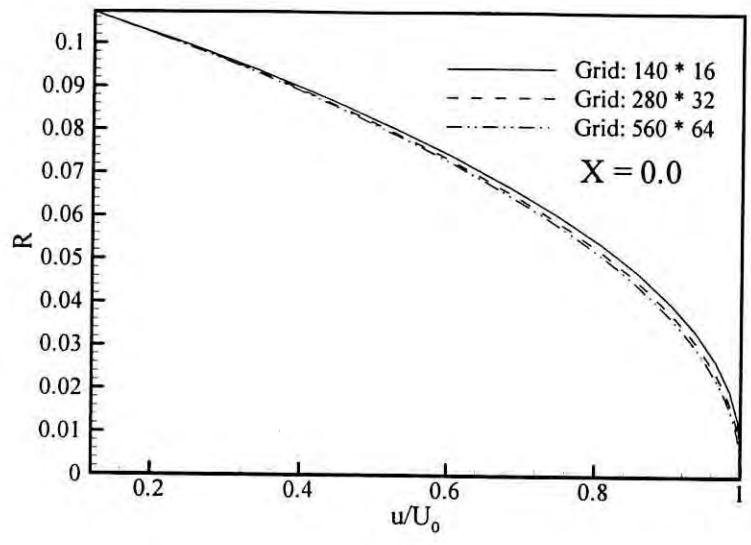


Fig. 4.3a Grid sensitivity test with axial velocity profile at $Re=800$ & $L^*=15.0$ for $X=0.0$ & $X=0.14$ (axisymmetric case)

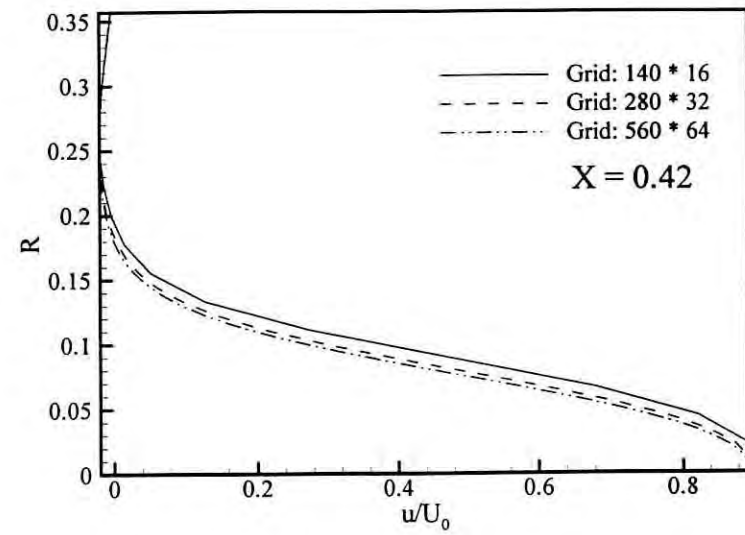
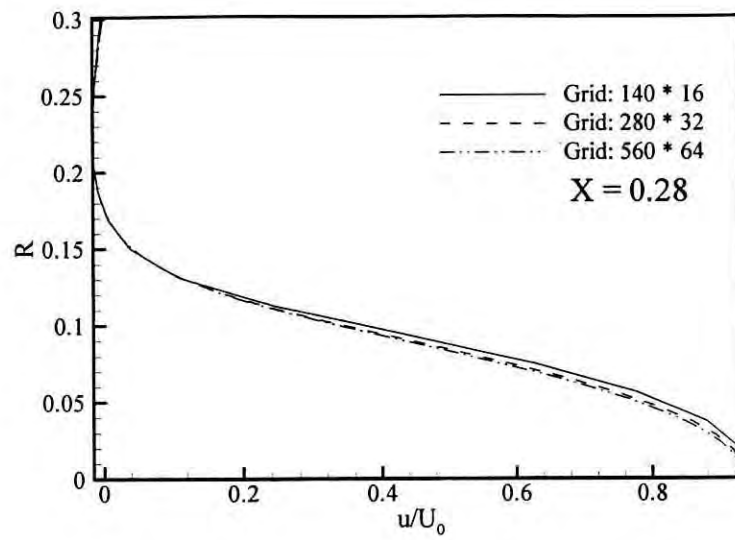


Fig.4.3b_c Grid sensitivity test with axial velocity profile at $Re=800$ & $L^*=15.0$ for $X=0.28$ & $X=0.42$ (axisymmetric case)

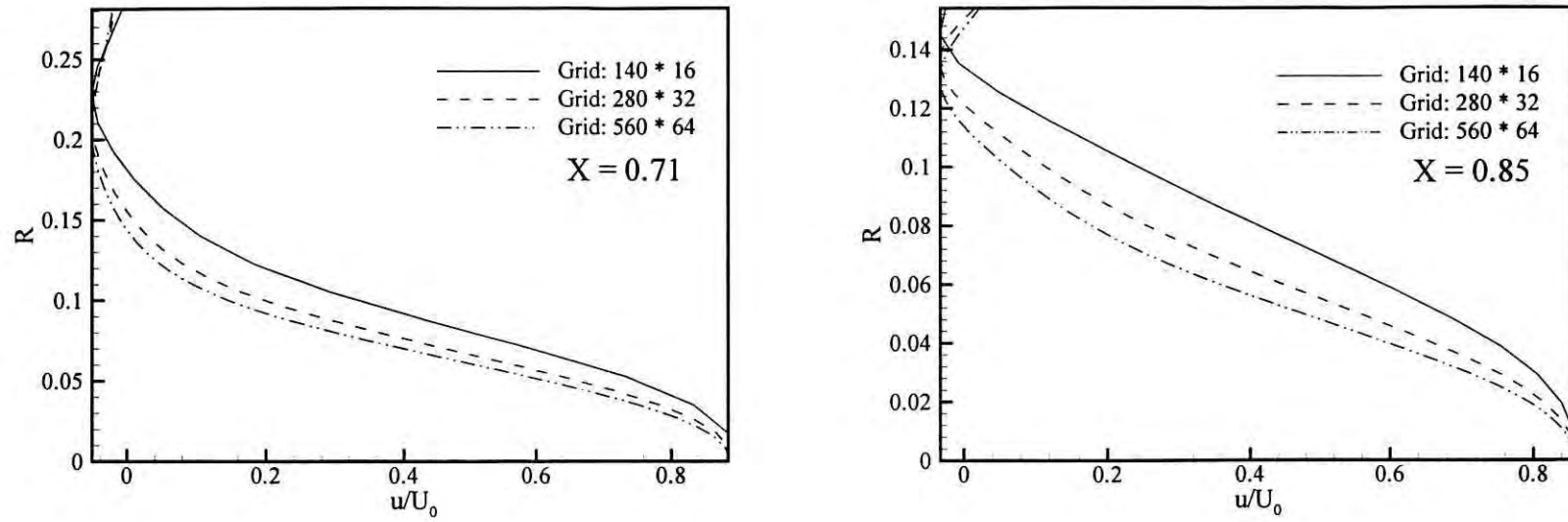


Fig. 4.3c. Grid sensitivity test with axial velocity profile at $Re=800$ & $L^*=15.0$ for $X=0.71$ & $X=0.85$ (axisymmetric case)

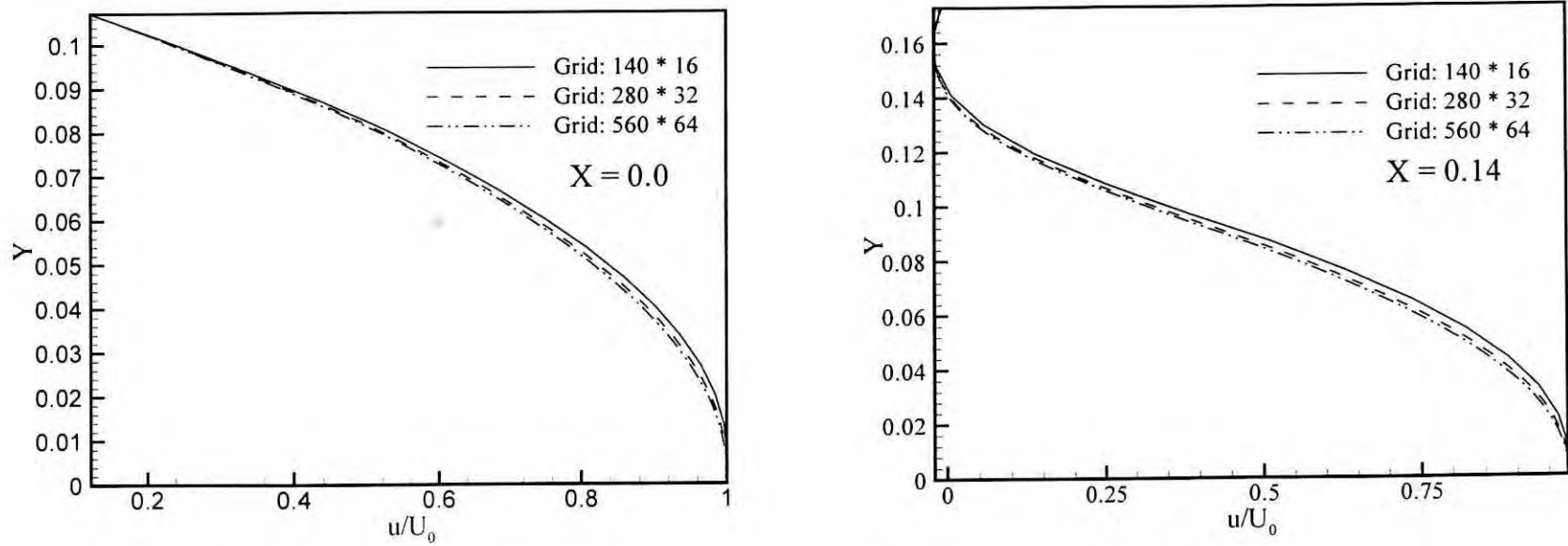


Fig.4.4a Grid sensitivity test with axial velocity profile at $Re=800$ & $L^*=15.0$ for $X=0.0$ & 0.14

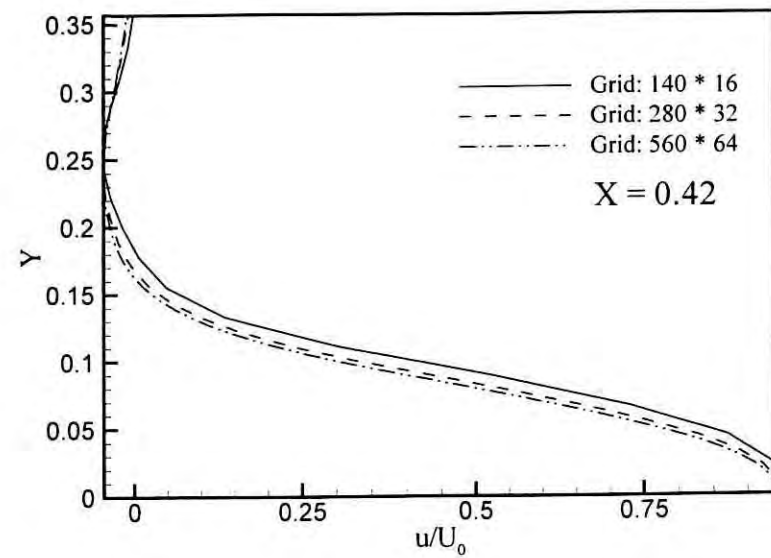
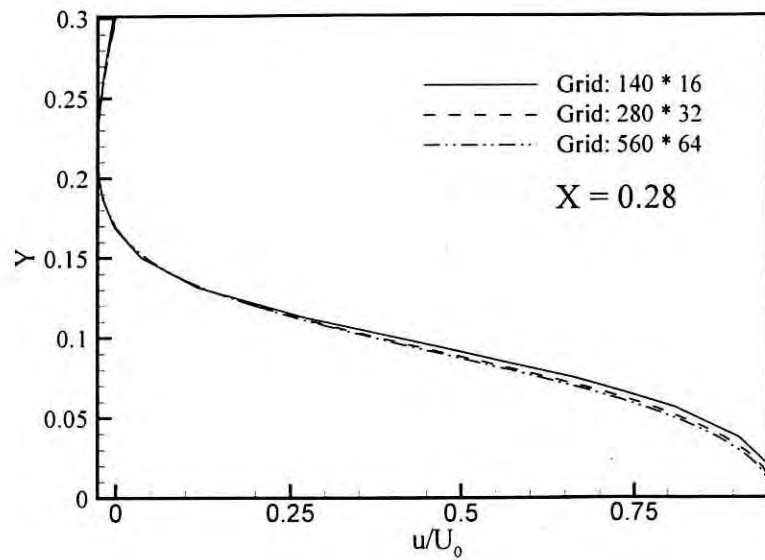


Fig.4.4b Grid sensitivity test with axial velocity profile at $Re=800$ & $L^*=15.0$ for $X=0.28$ & 0.42

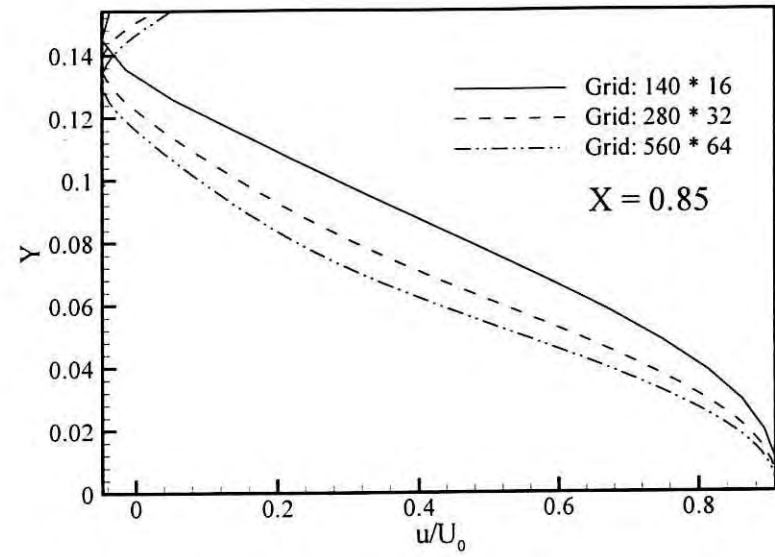
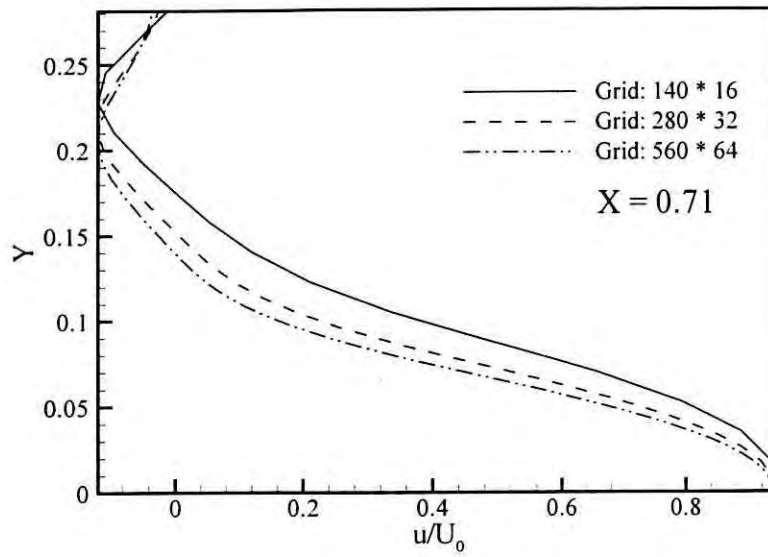


Fig. 4.4c. Grid sensitivity test with axial velocity profile at $Re=800$ & $L^*=15.0$ for $X=0.71$ & 0.85

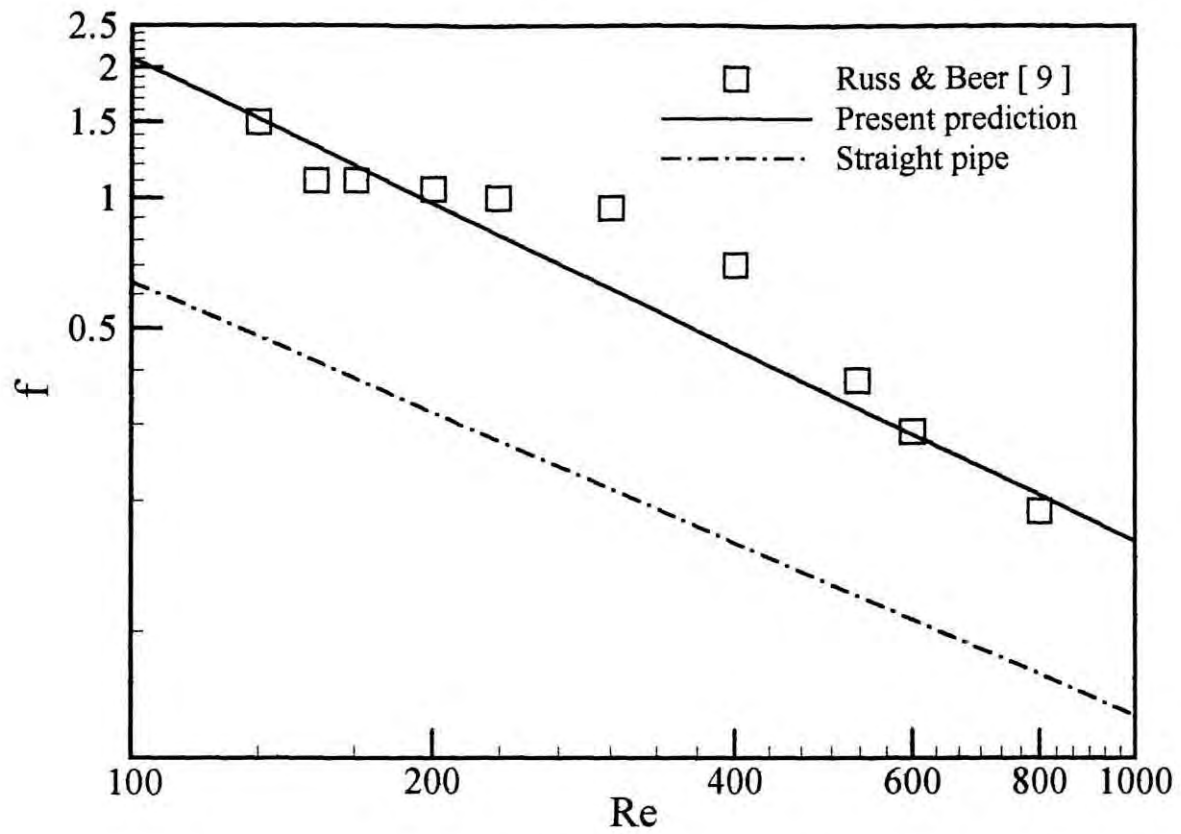


Fig.4.5. Friction factor as a function of Reynolds number for $L^* = 19.0$

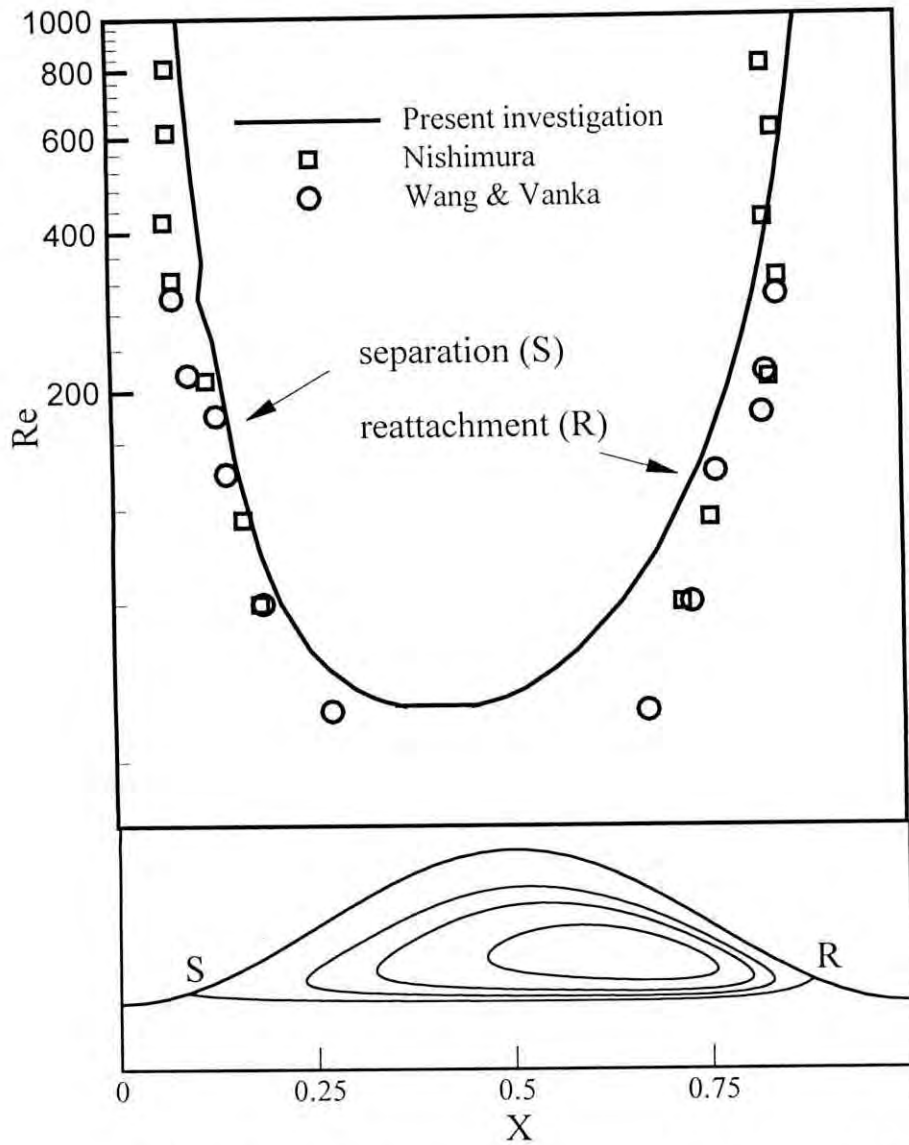


Fig. 4.6 Variation in separation and reattachment points in first cycle with Reynolds number at $L^* = 8.0$ (Plan geometry)

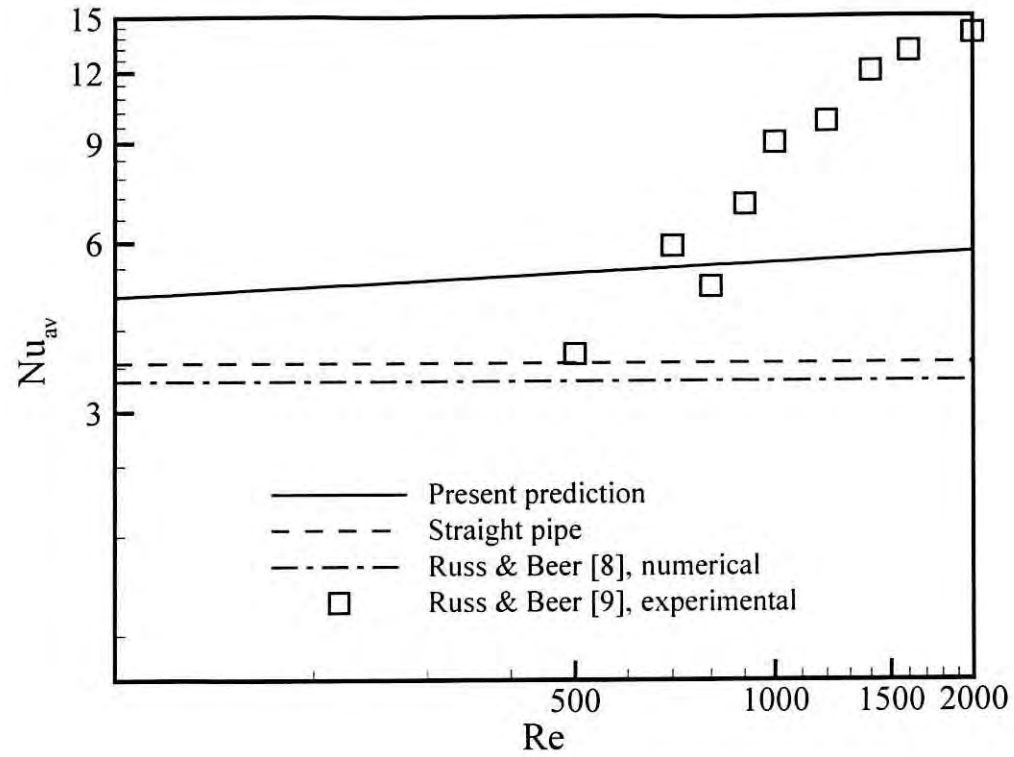


Fig. 4.7 Comparison of present prediction of average Nusselt number with numerical & experimental results of Russ & Beer [8], [9]

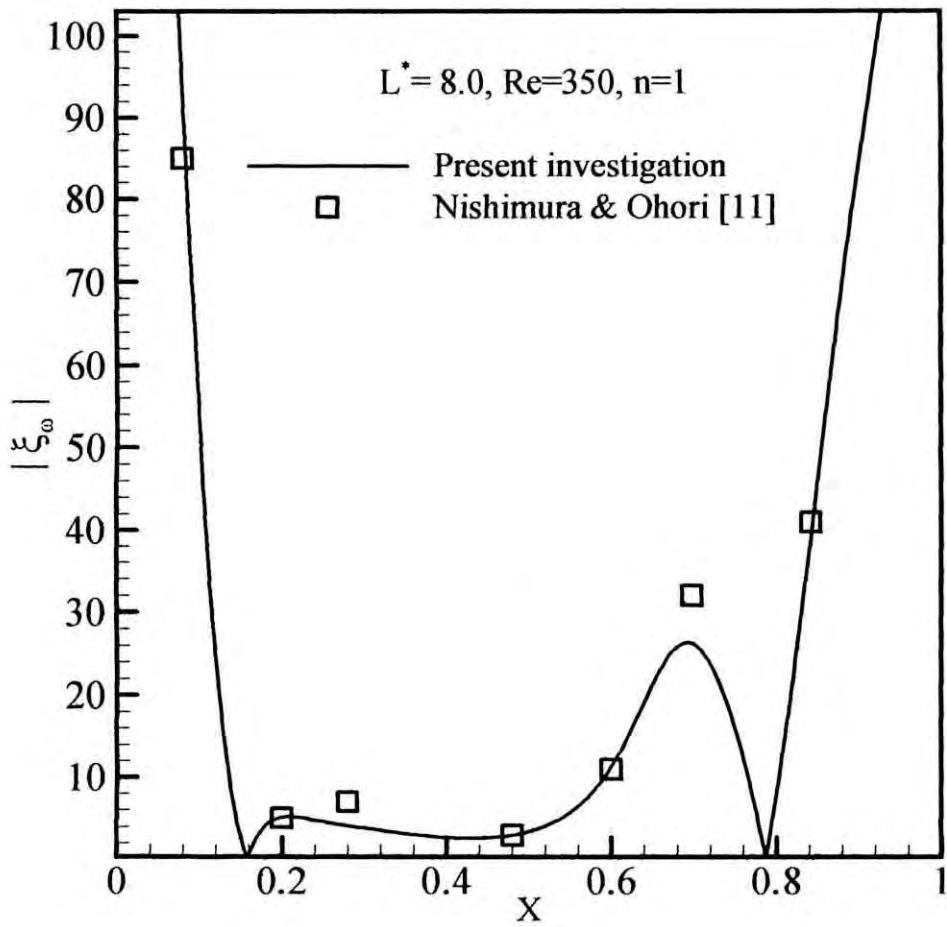


Fig. 4.8. Comparison of measured wall vorticity profile with experimental data of Nishimura & Ohori [11]

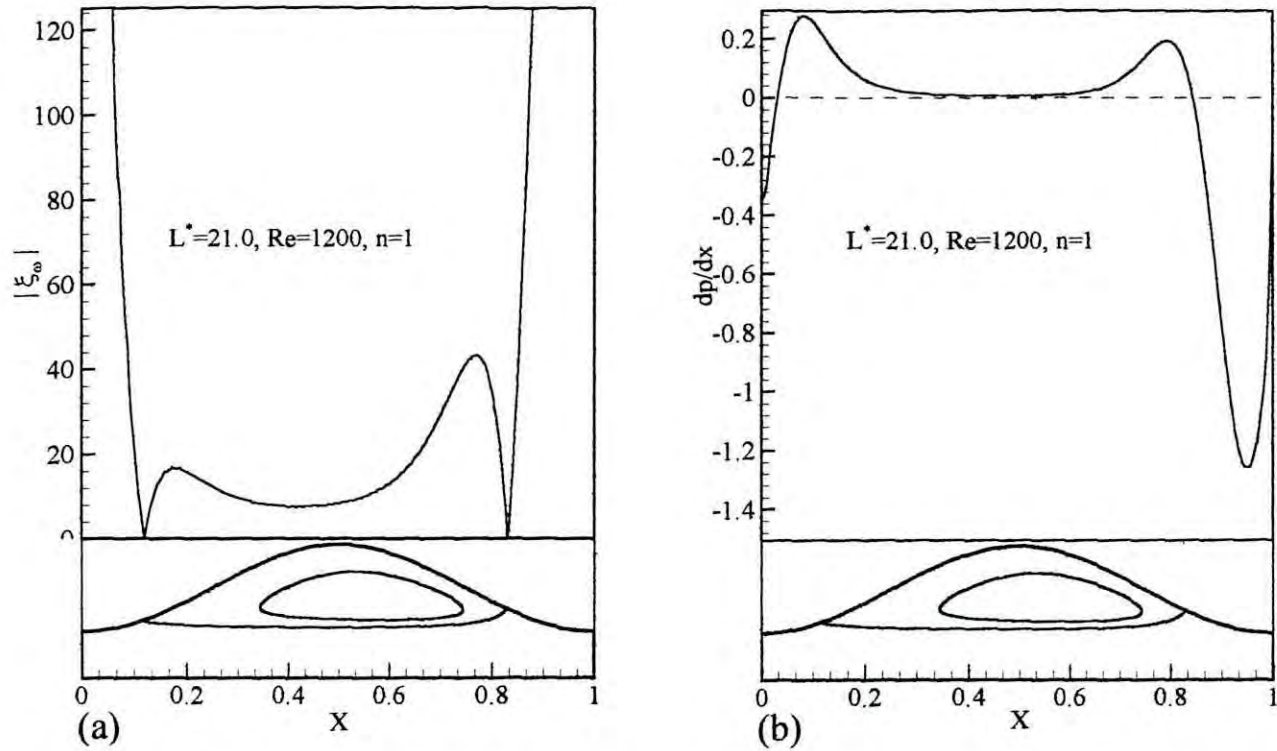


Fig. 4.9(a) Combination of wall vorticity distribution and constant stream function contour
 (b) Combination of axial pressure gradient and constant stream function contour
 (dashed line indicates the zero pressure gradient)

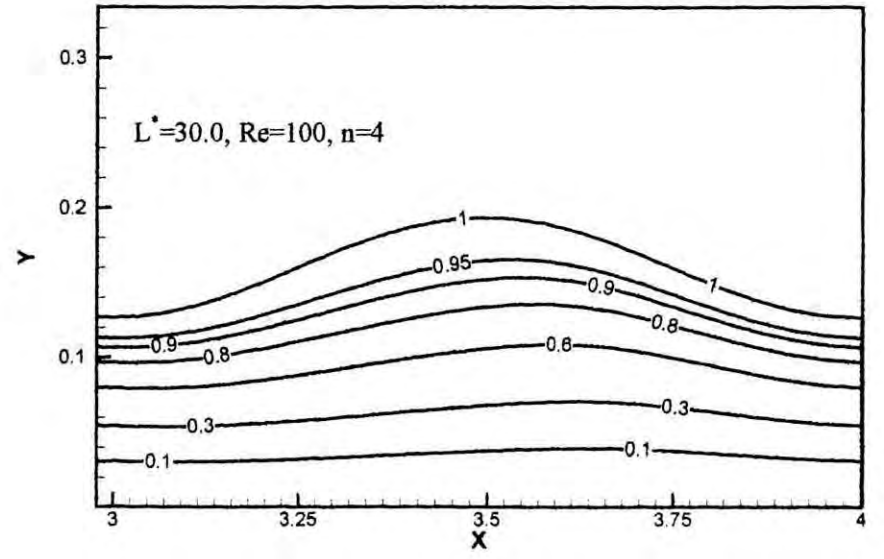
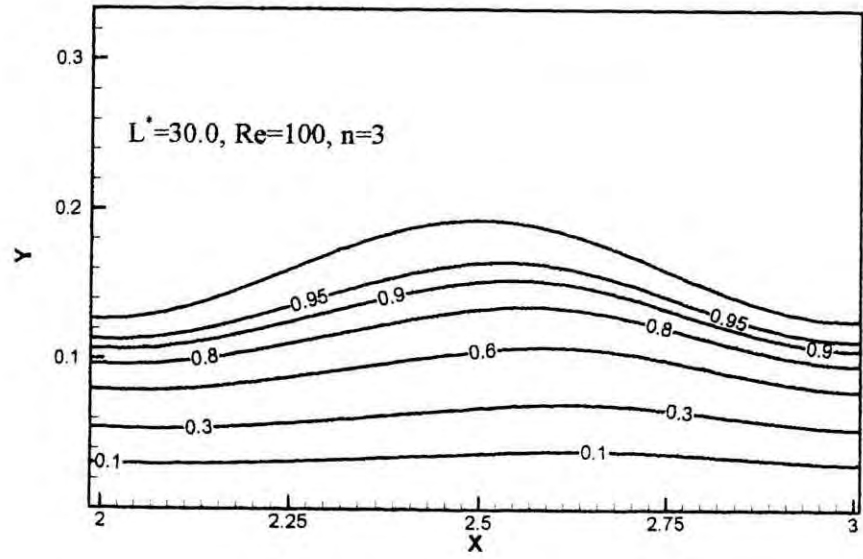
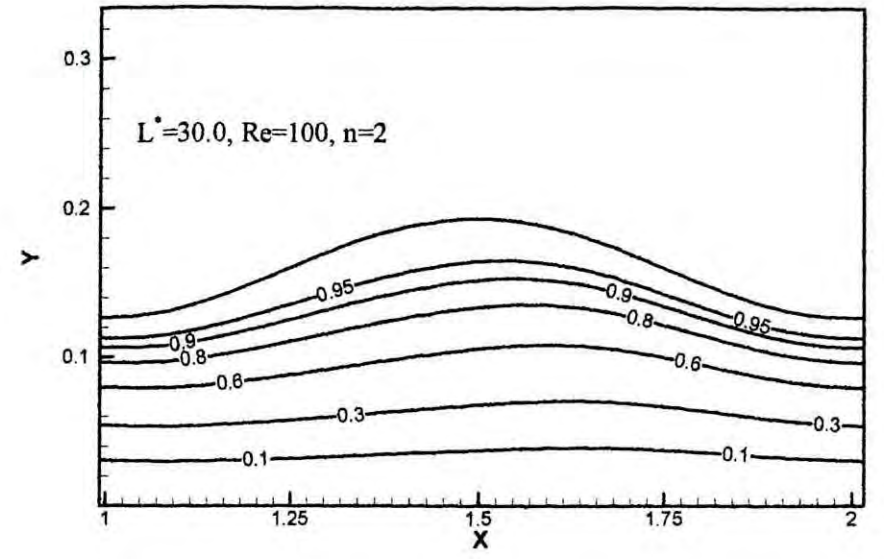
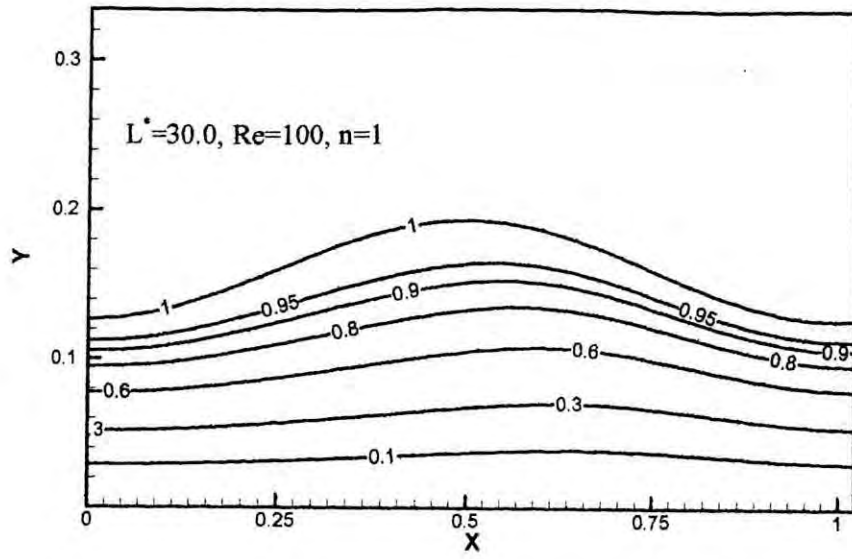
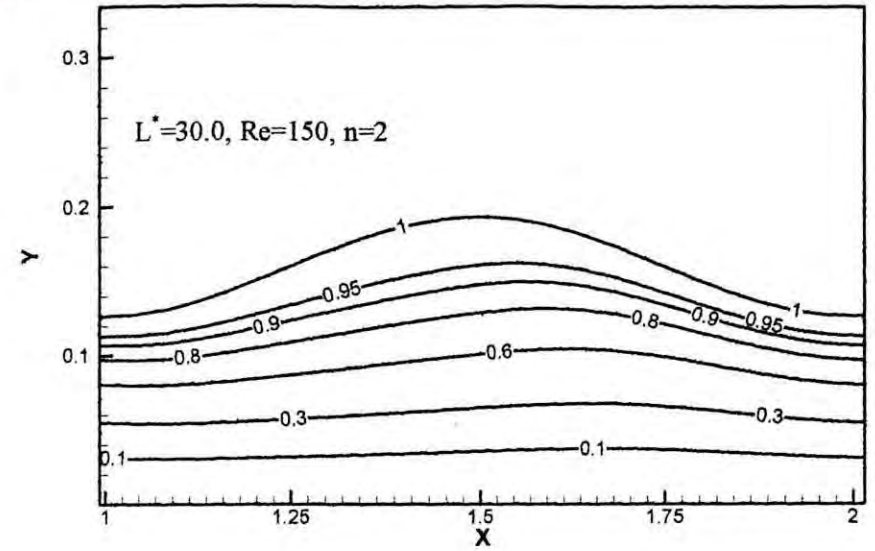
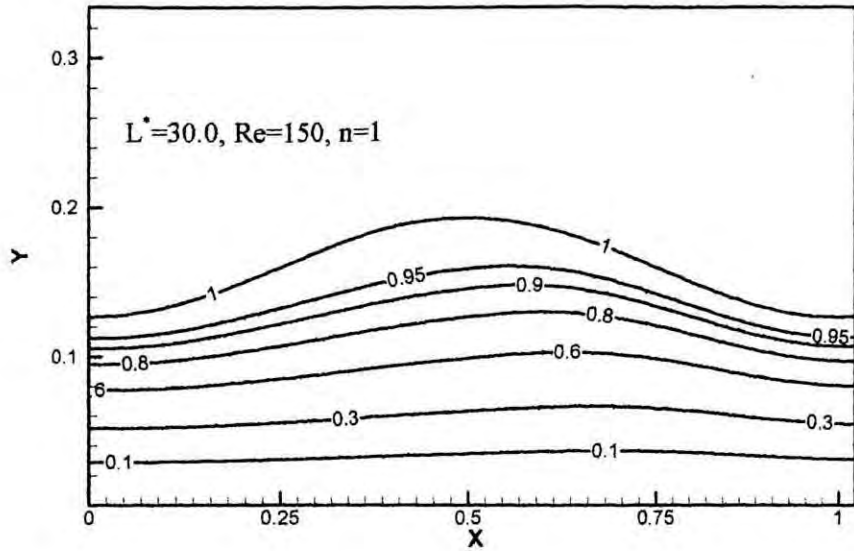


Fig.4.10 (a) Streamlines for $L^* = 30.0, Re = 100, n = 1-4$

93718



63

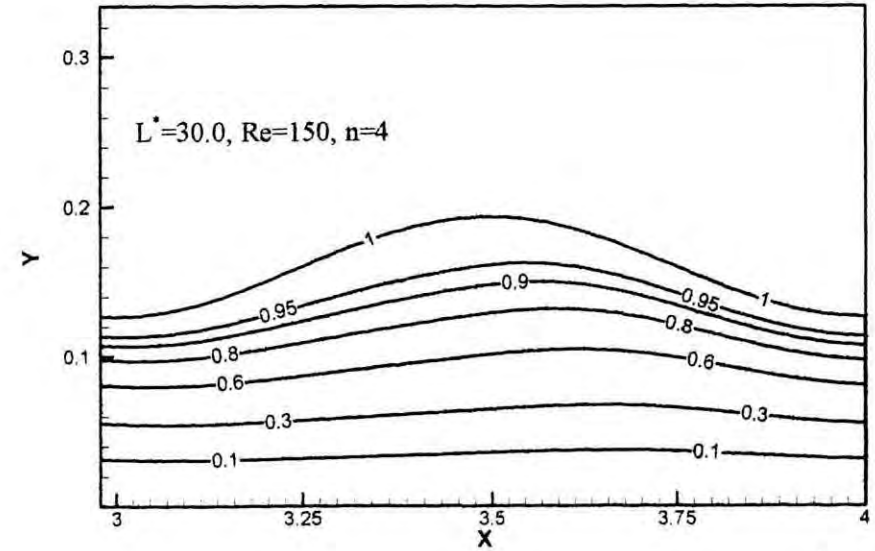
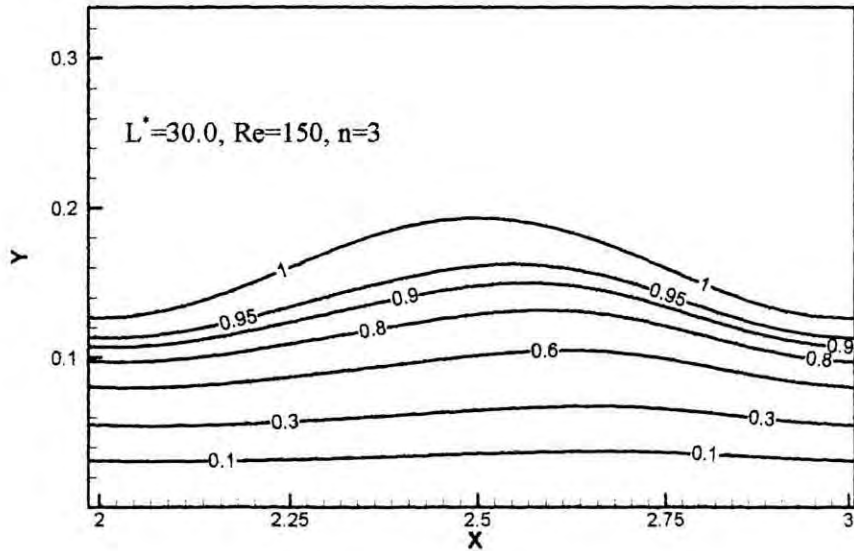
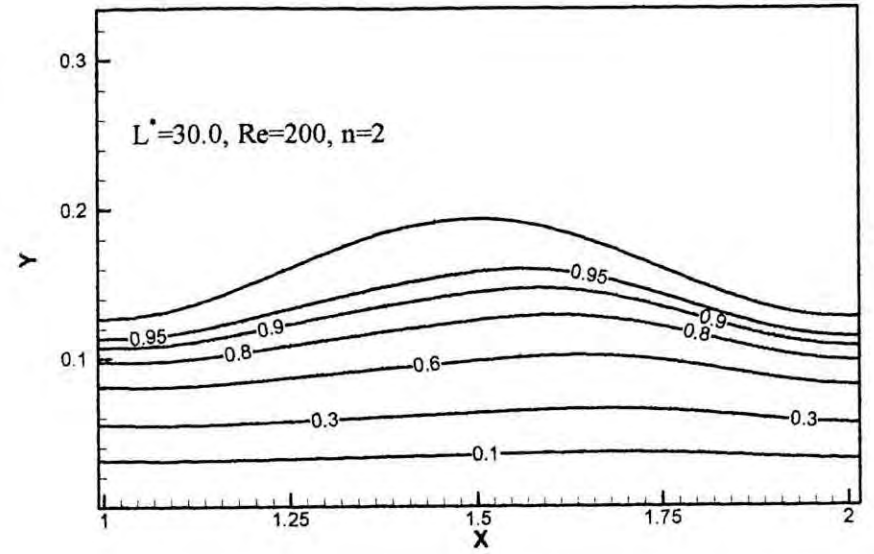
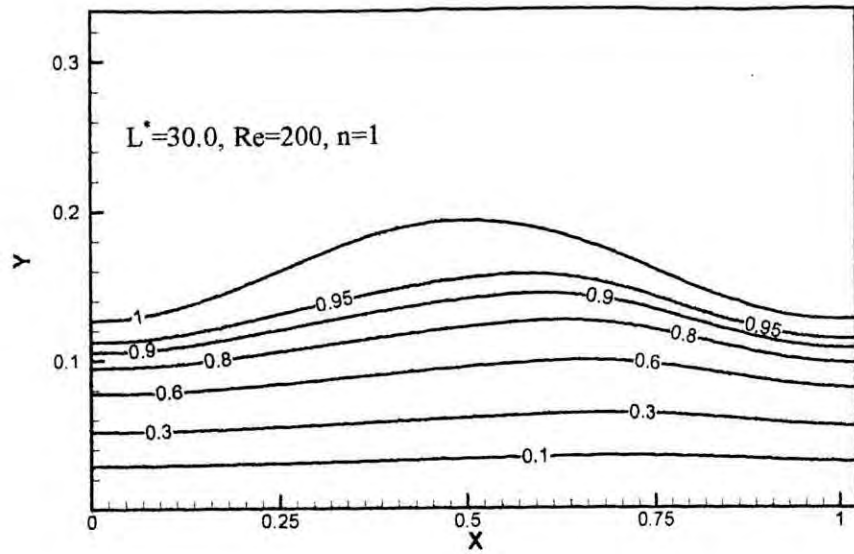


Fig.4.10 (b) Streamlines for $L^* = 30.0$, $Re = 150$, $n = 1-4$



64

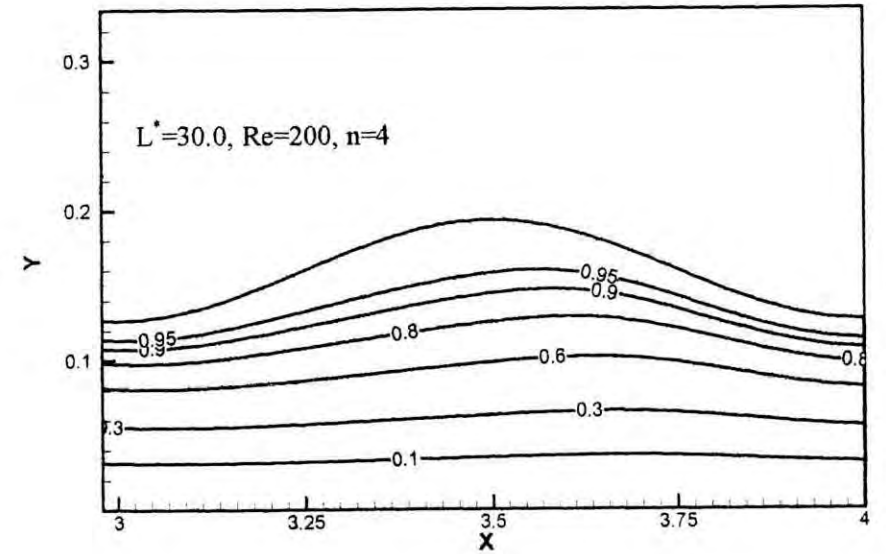
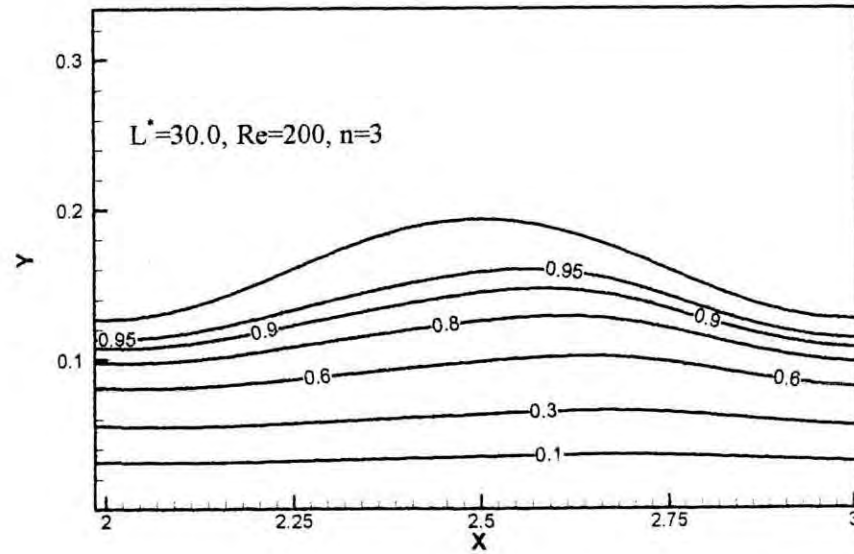
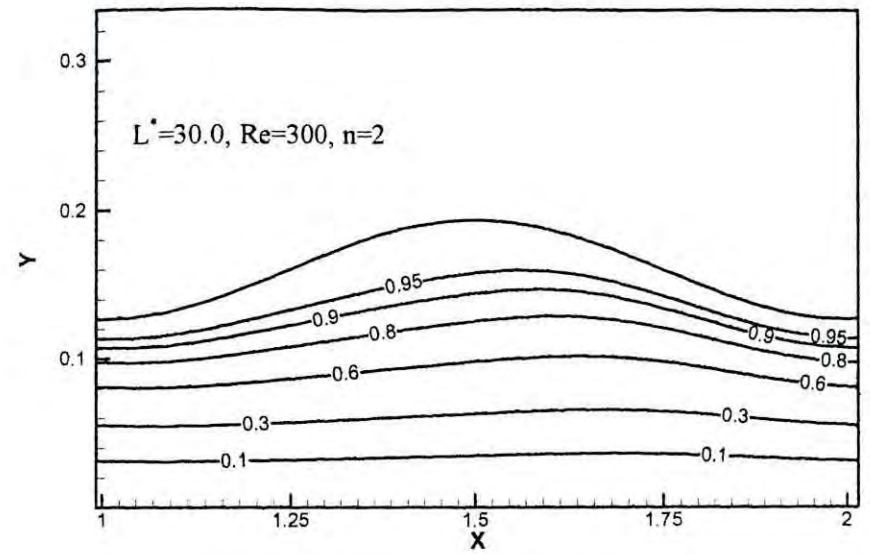
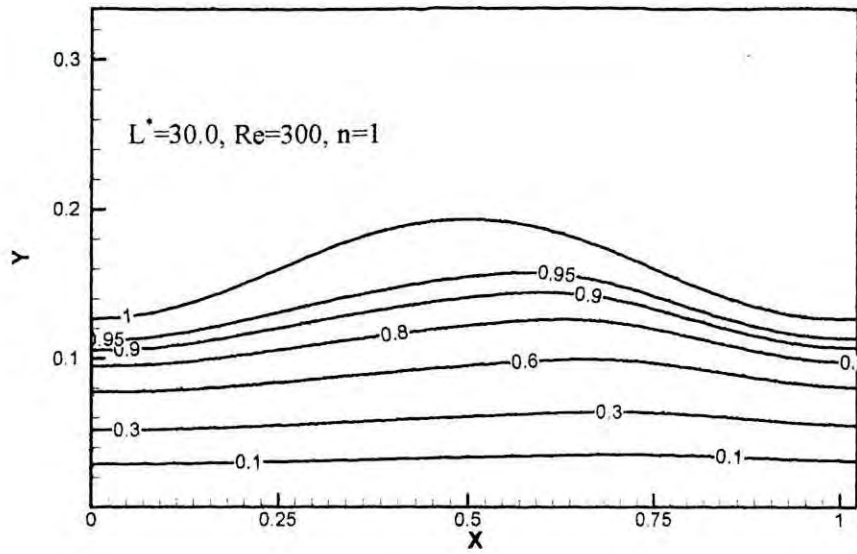


Fig.4.10 (c) Streamlines for $L^* = 30.0, Re = 200, n = 1-4$



59

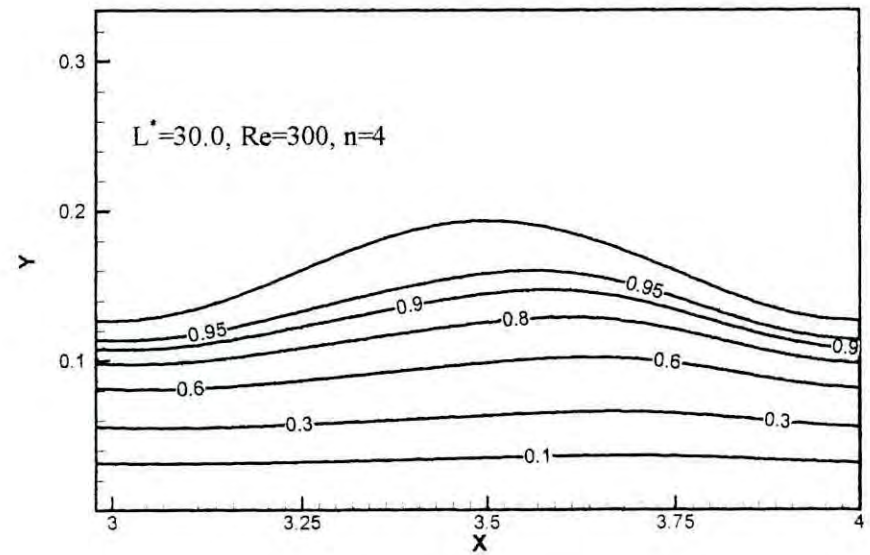
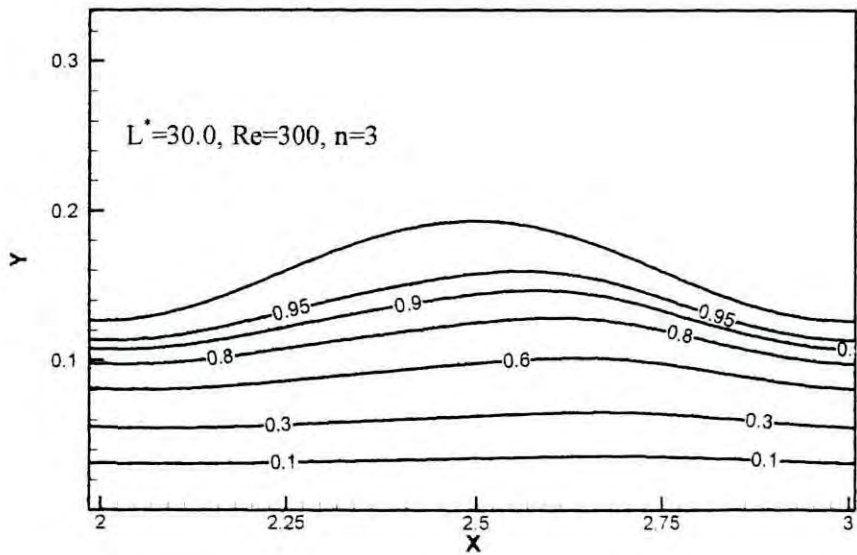
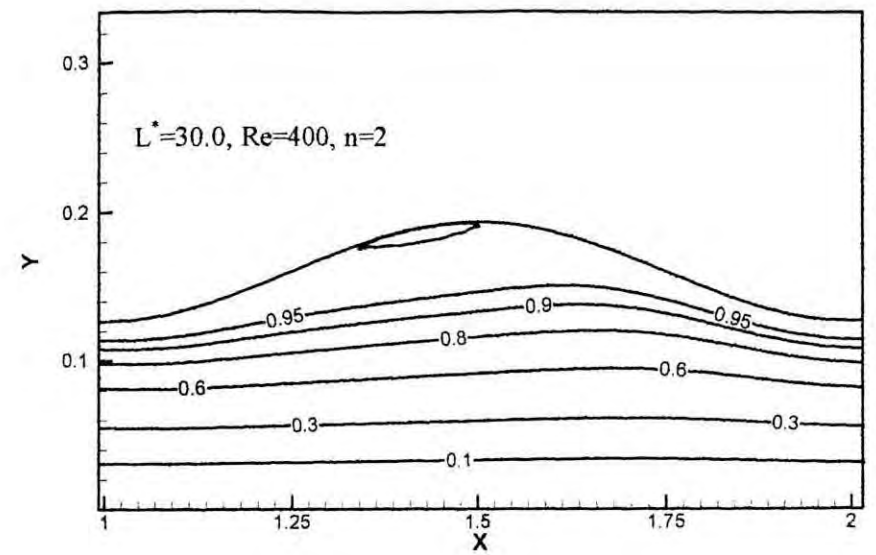
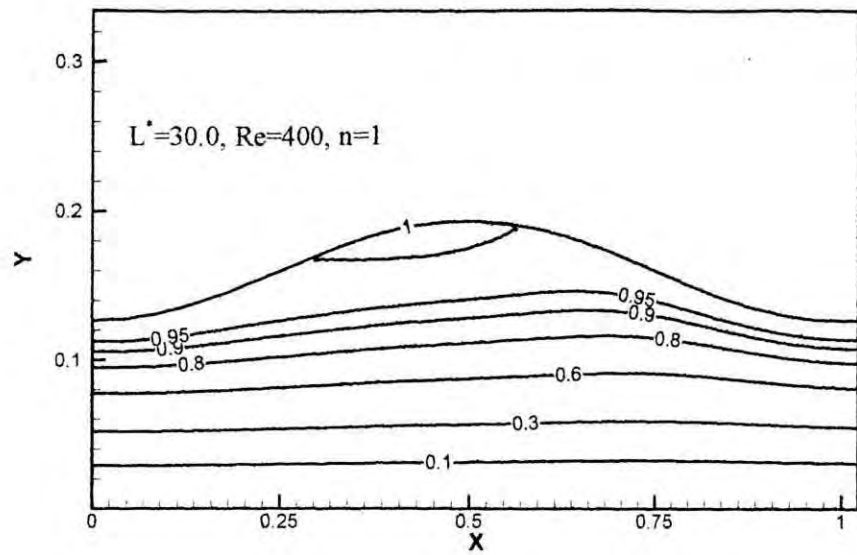


Fig.4.10 (d) Streamlines for $L^* = 30.0, Re = 300, n = 1-4$



99

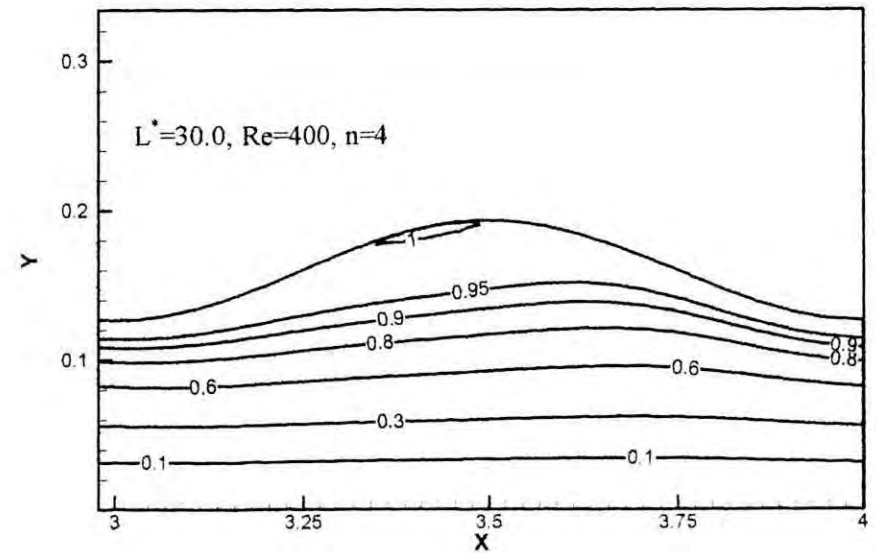
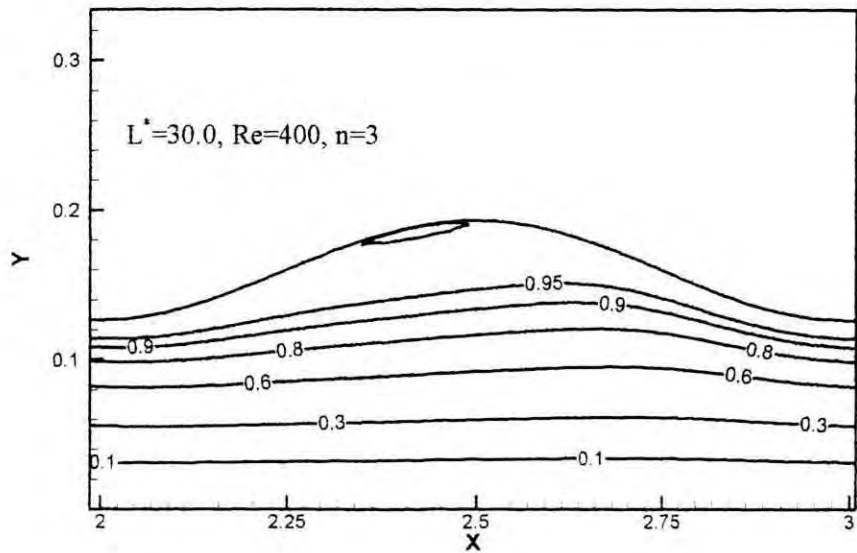
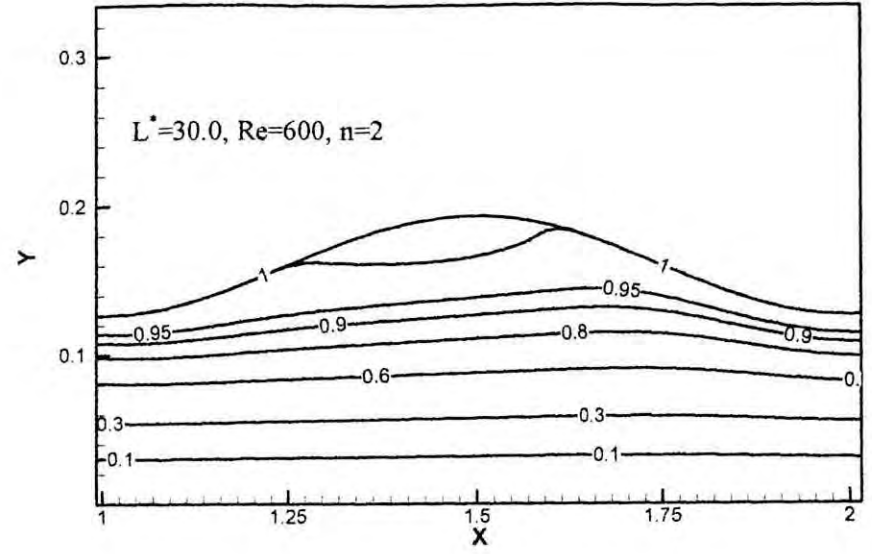
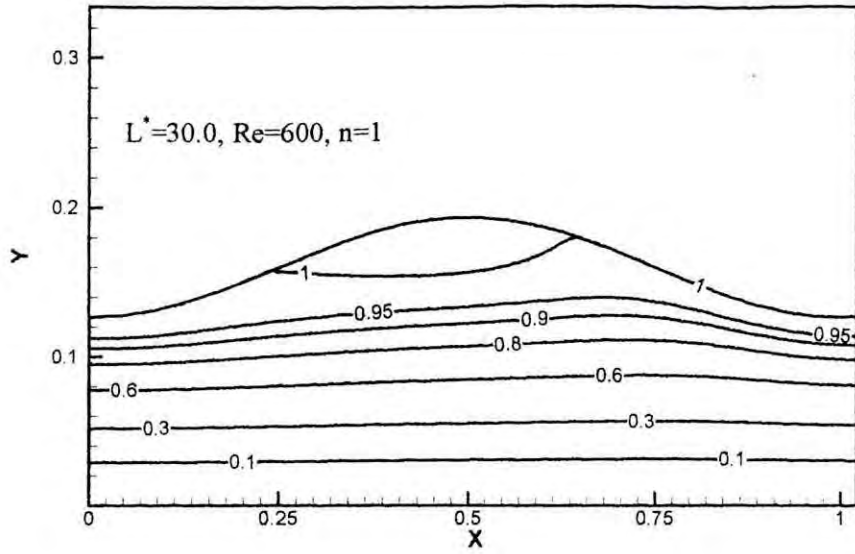


Fig.4.10 (e) Streamlines for $L^* = 30.0, Re = 400, n = 1-4$



67

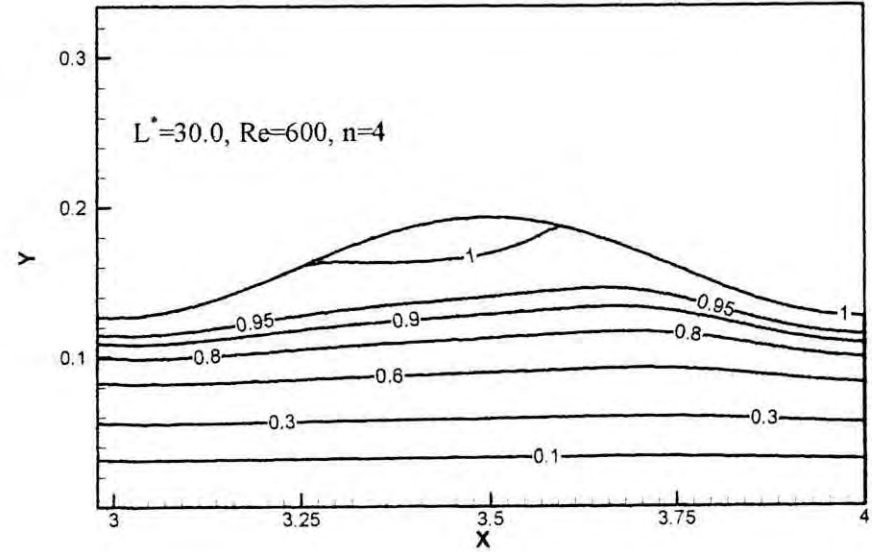
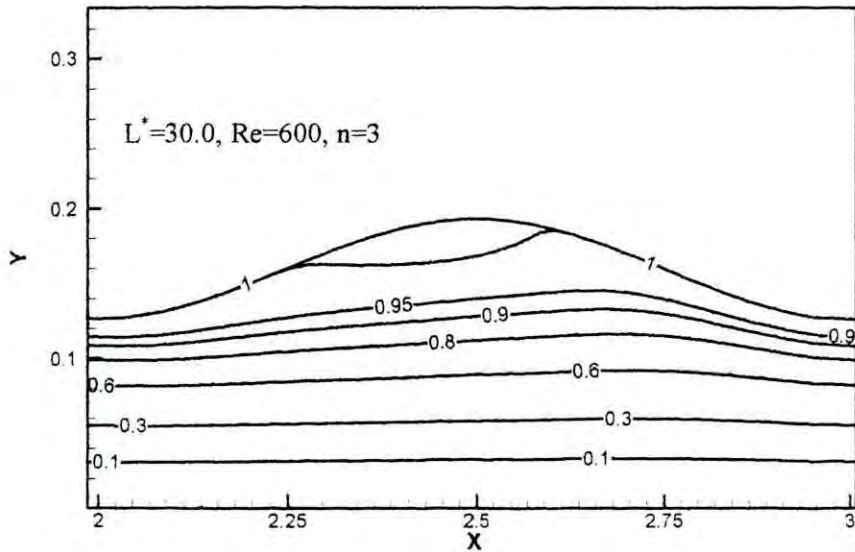
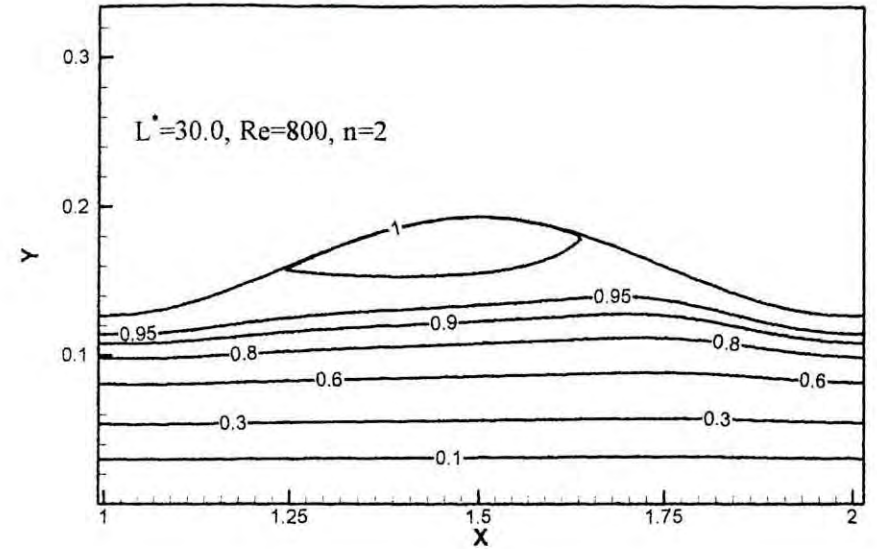
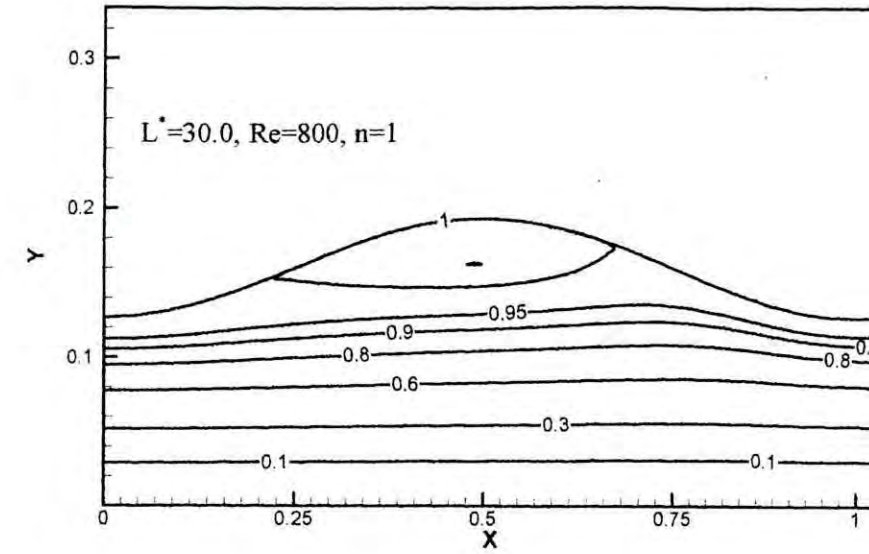


Fig.4.10 (f) Streamlines for $L^*=30.0, Re=600, n=1-4$



89

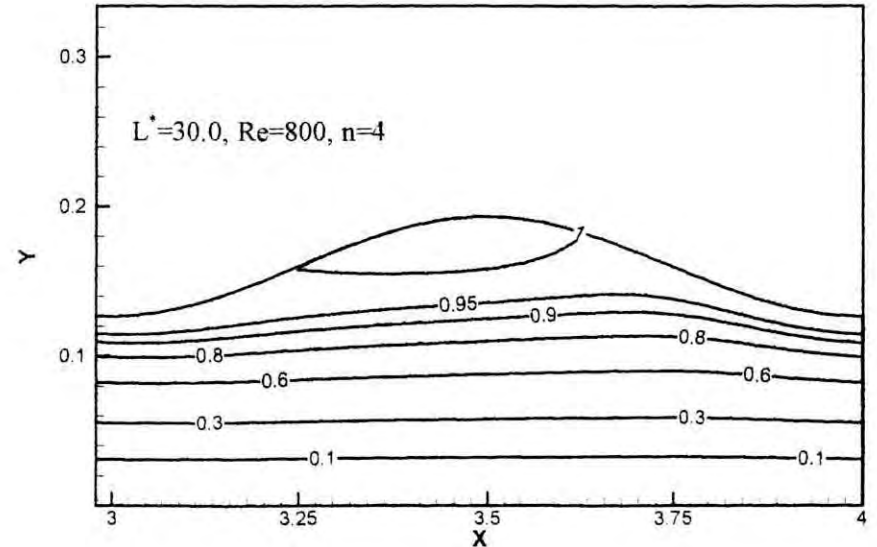
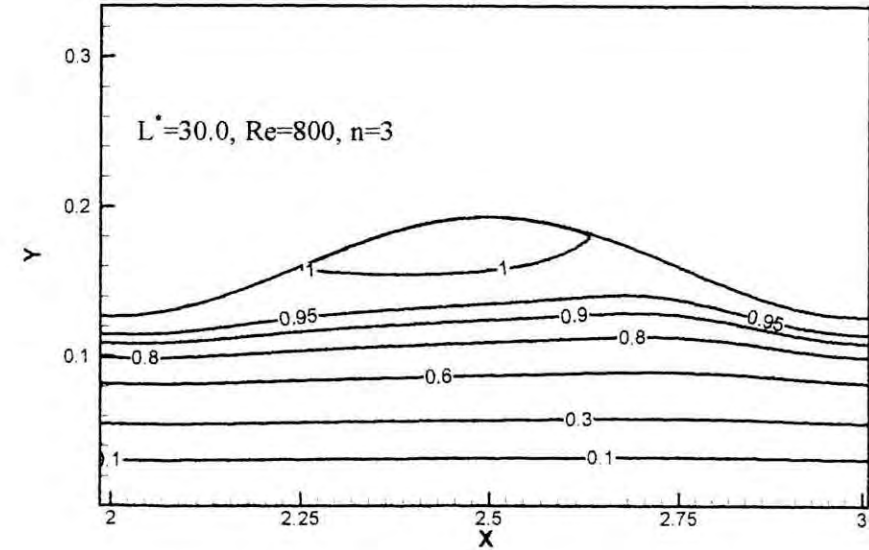
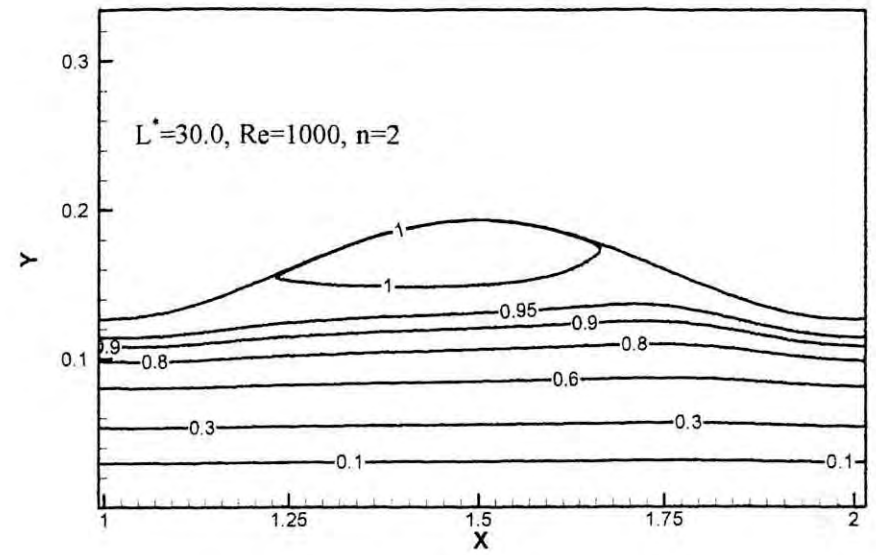
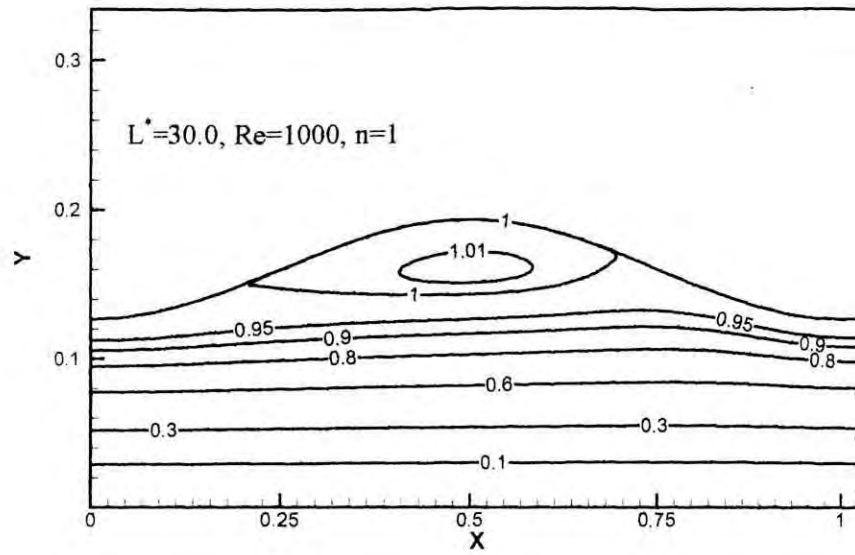


Fig.4.10 (g) Streamlines for $L^* = 30.0, Re = 800, n = 1-4$



69

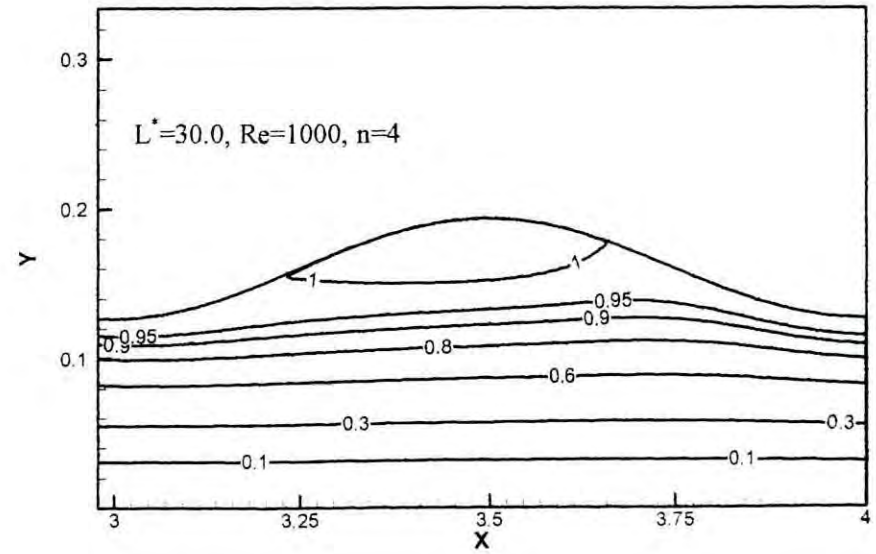
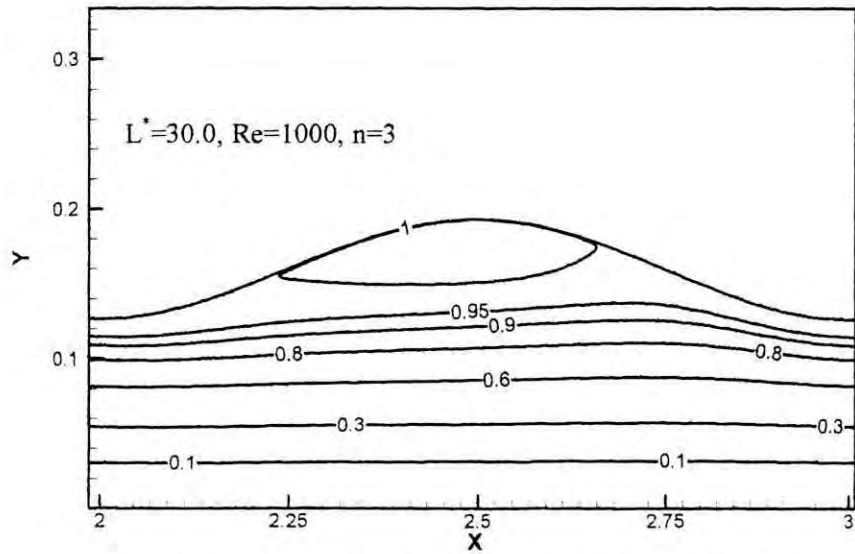
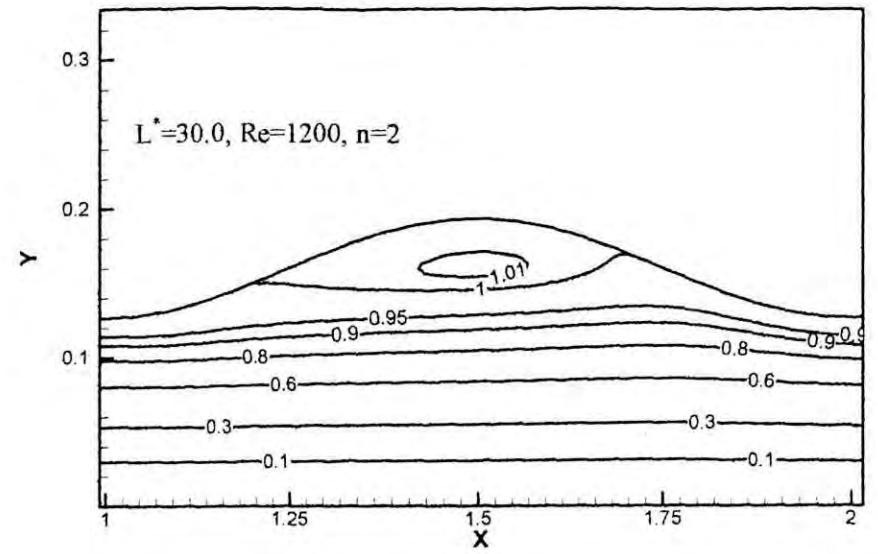
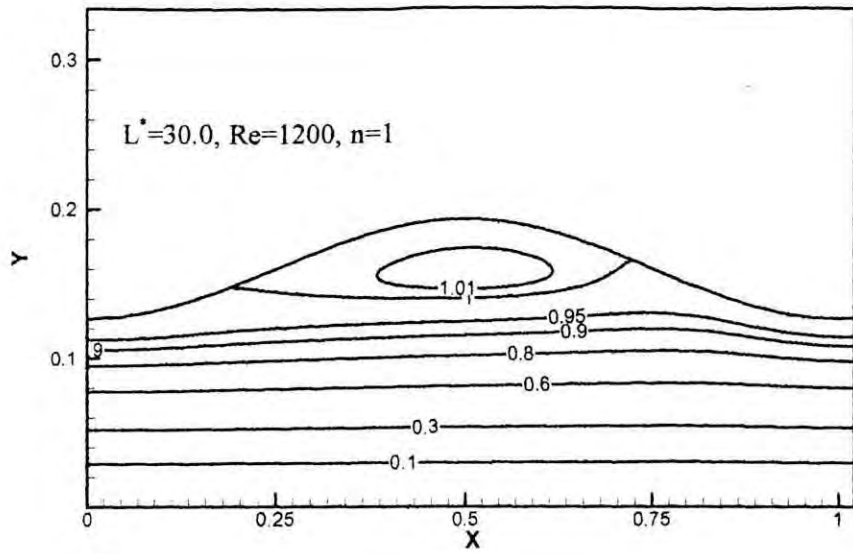


Fig.4.10 (h) Streamlines for $L^* = 30.0, Re = 1000, n = 1-4$



70

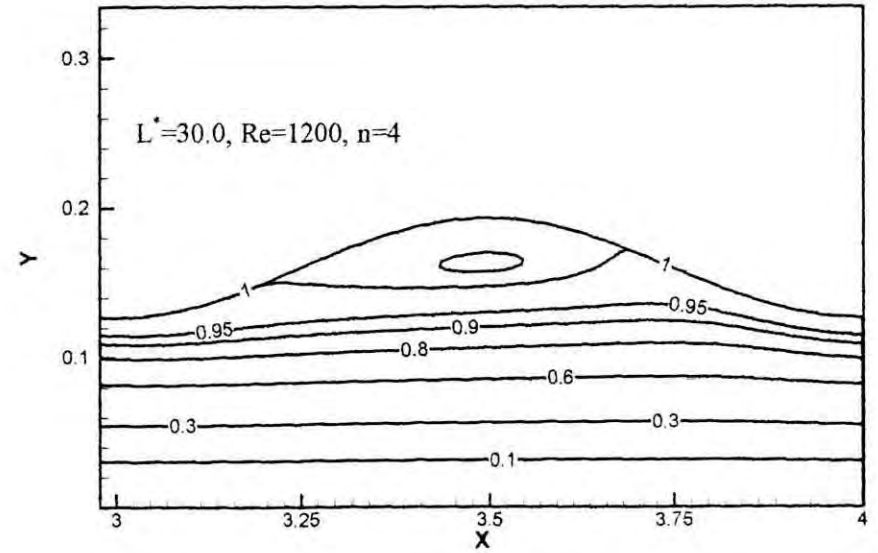
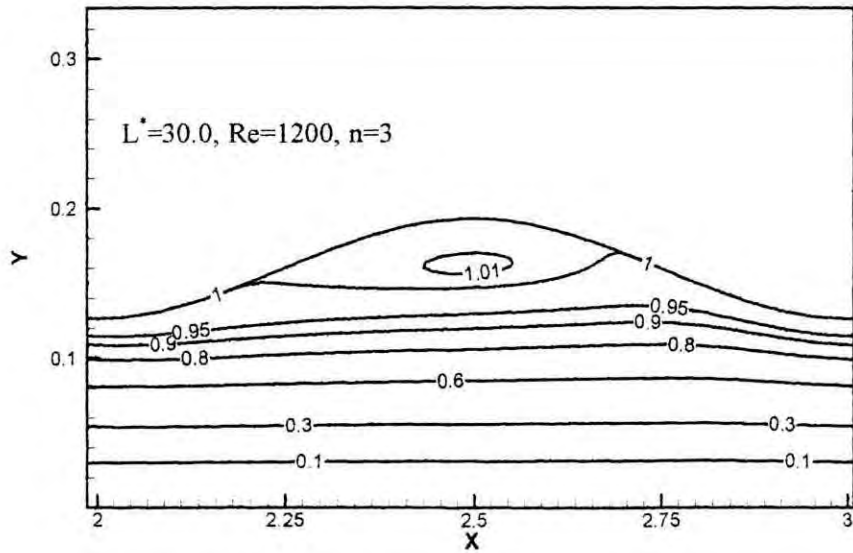
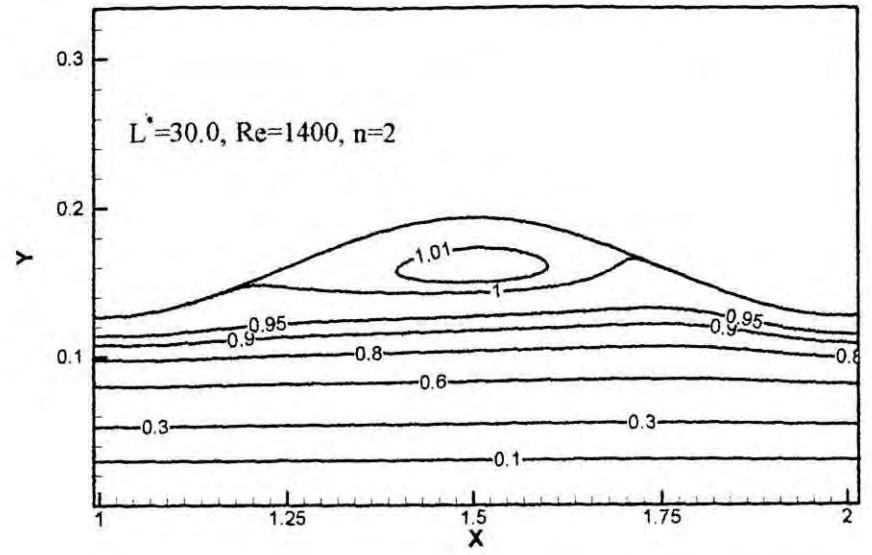
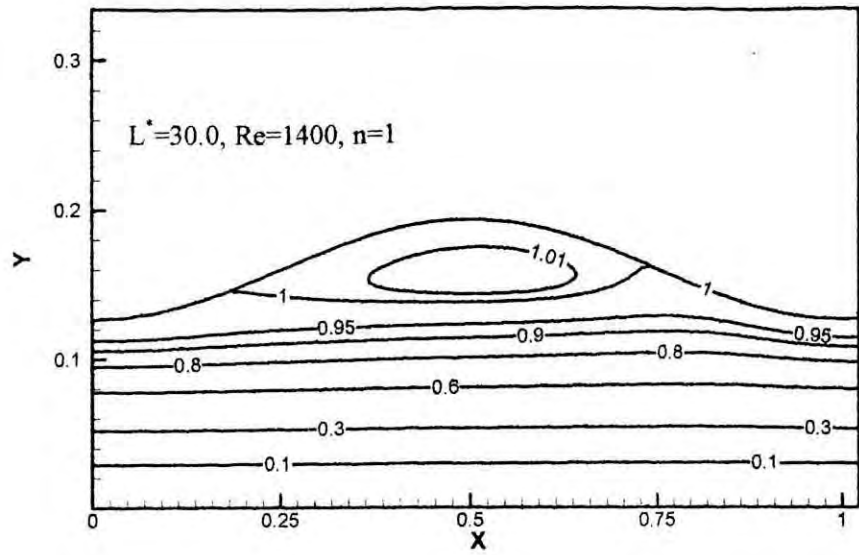


Fig.4.10 (i) Streamlines for $L^* = 30.0, Re = 1200, n = 1-4$



71

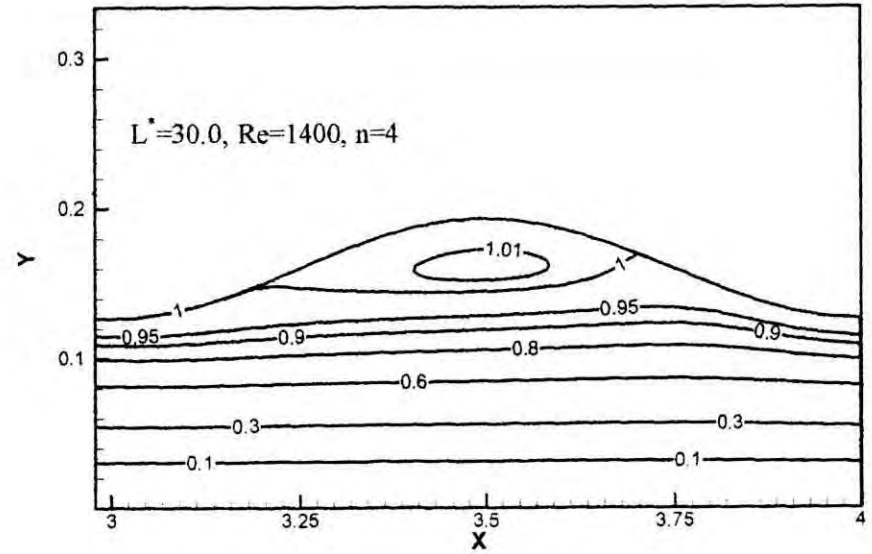
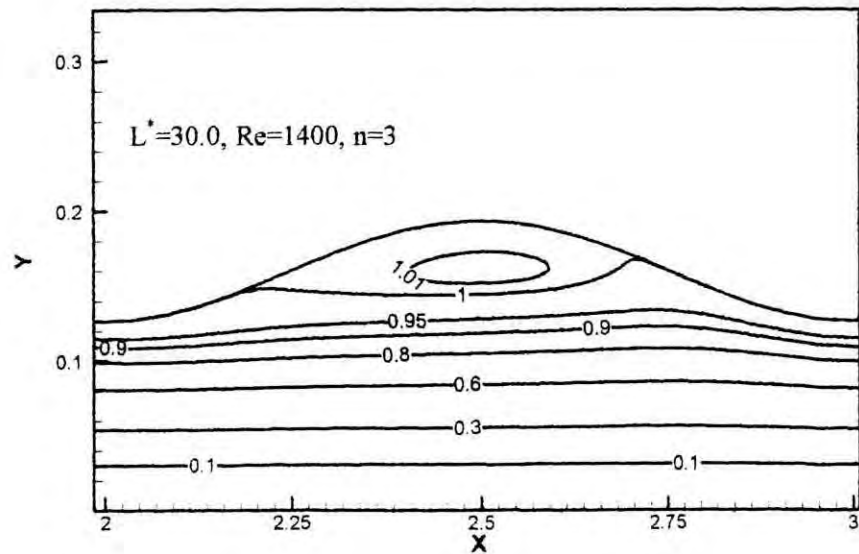
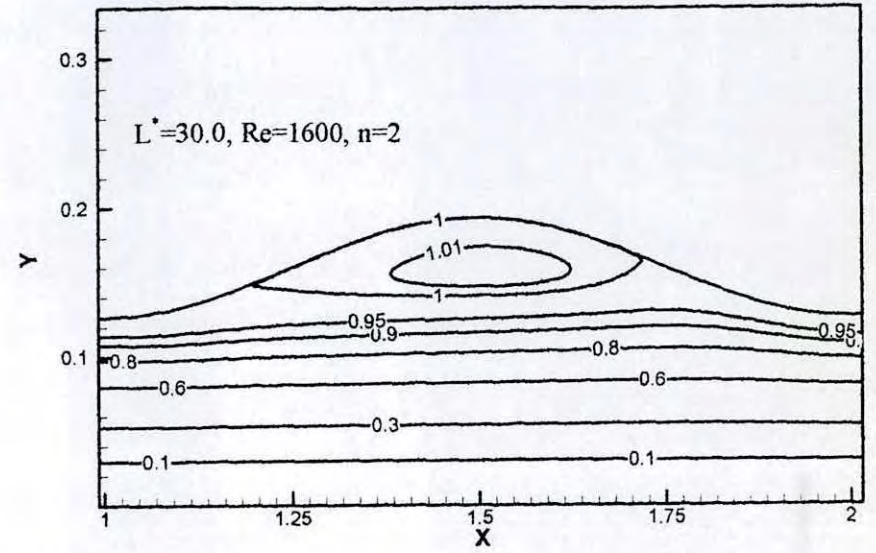
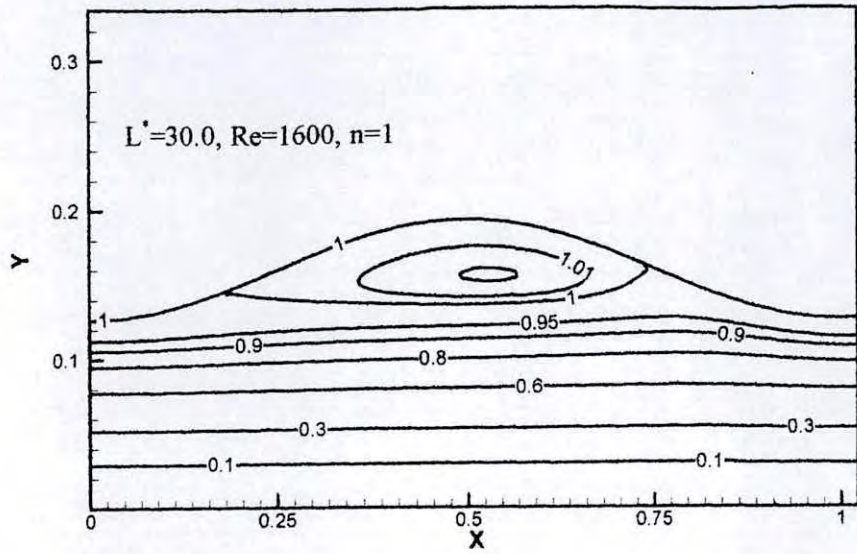


Fig.4.10 (j) Streamlines for $L^* = 30.0, Re = 1400, n = 1-4$



72

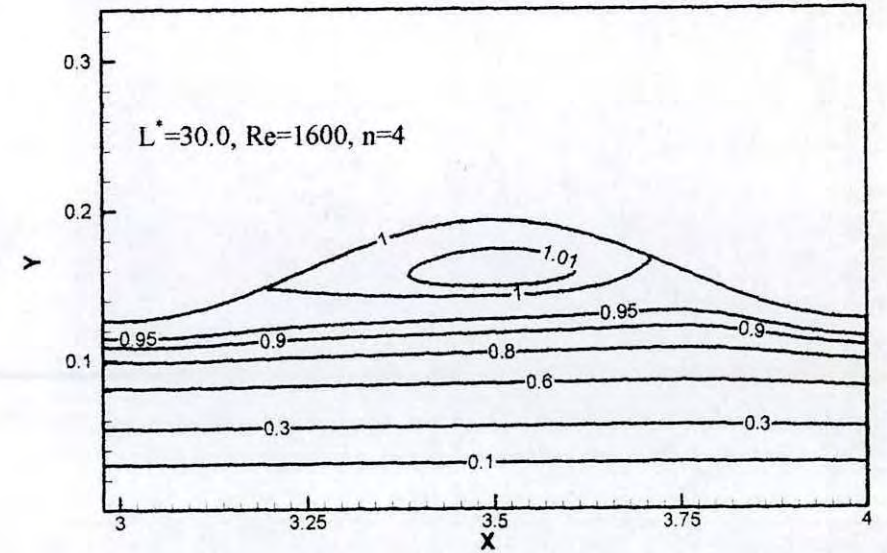
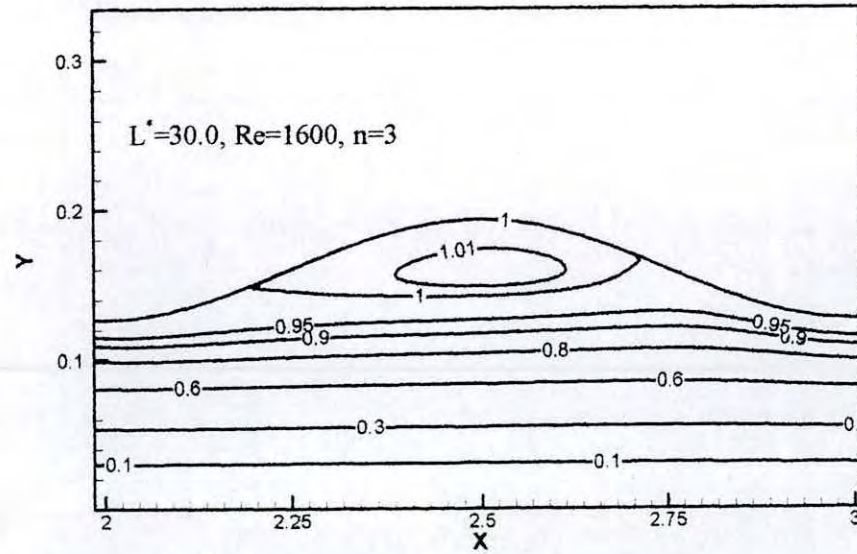
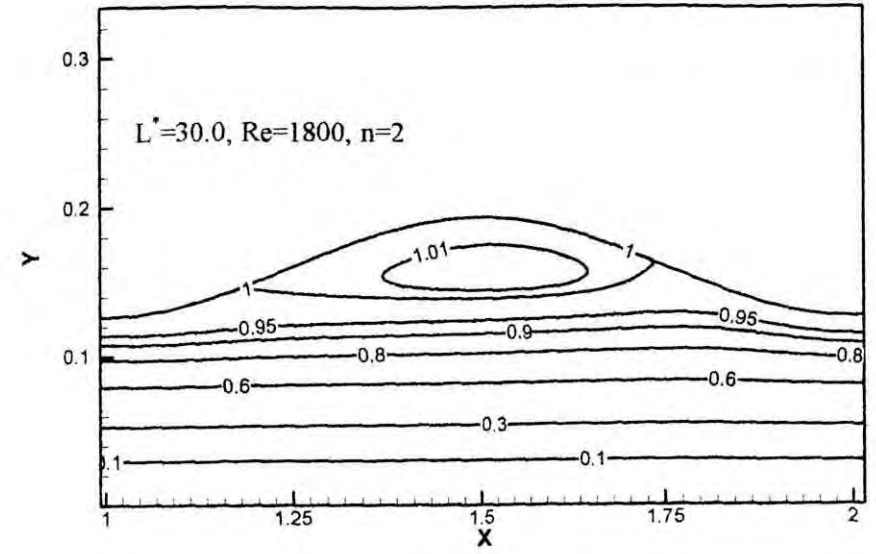
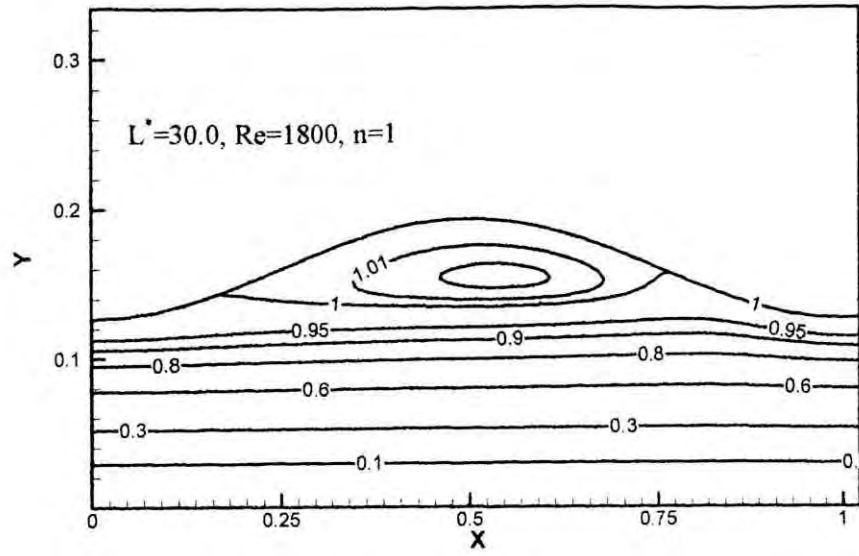


Fig.4.10 (k) Streamlines for $L^* = 30.0, Re = 1600, n = 1-4$



73

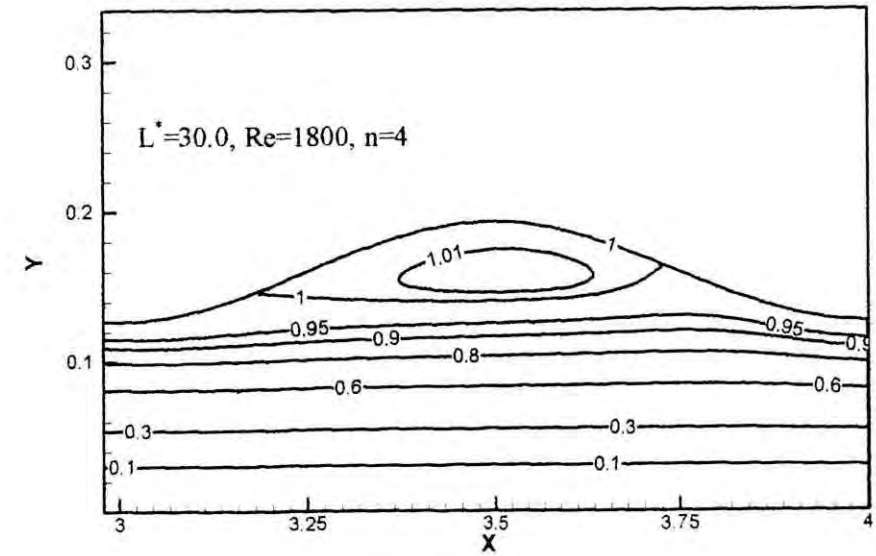
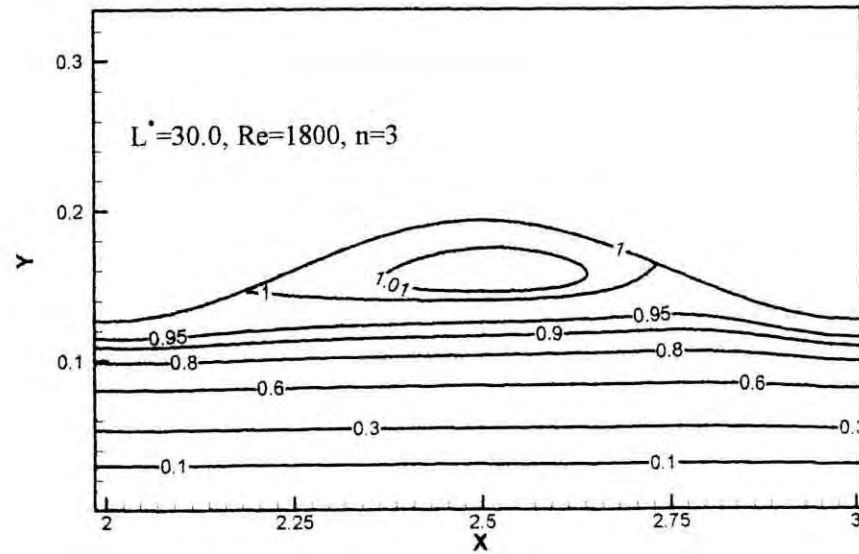
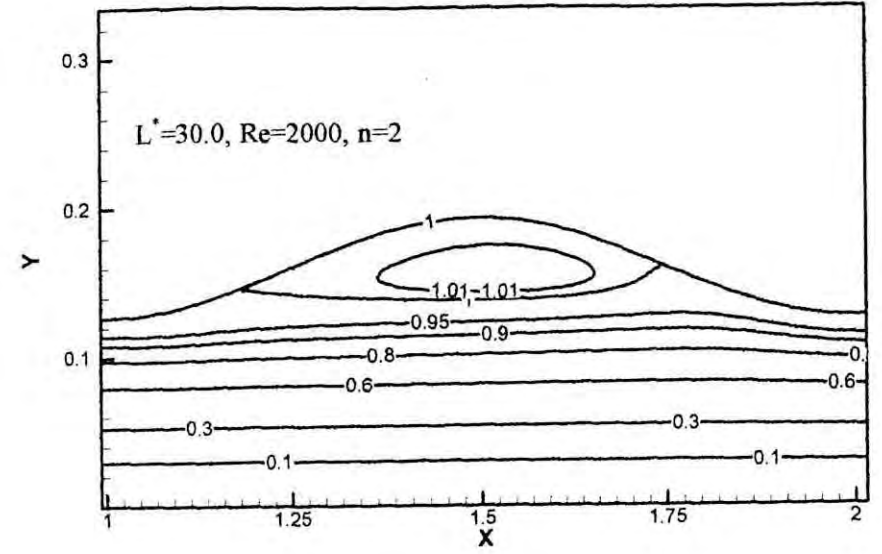
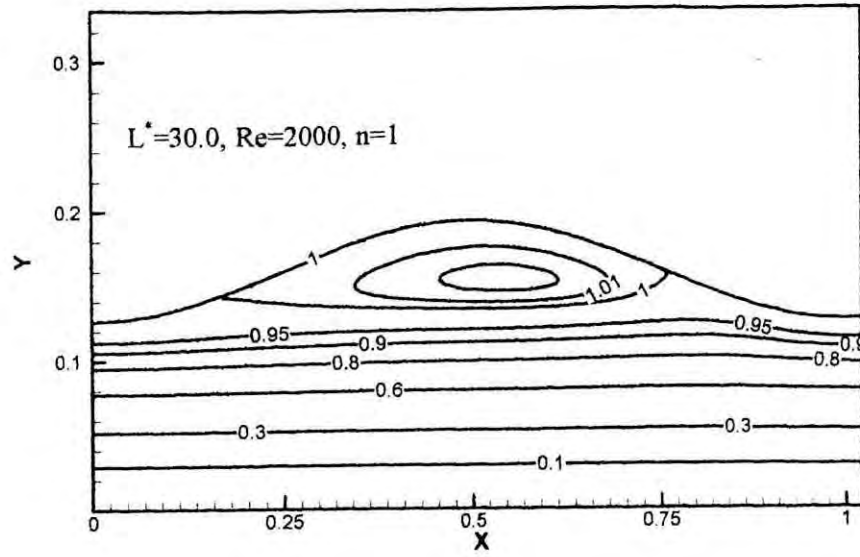


Fig.4.10 (l) Streamlines for $L^* = 30.0, Re = 1800, n = 1-4$



74

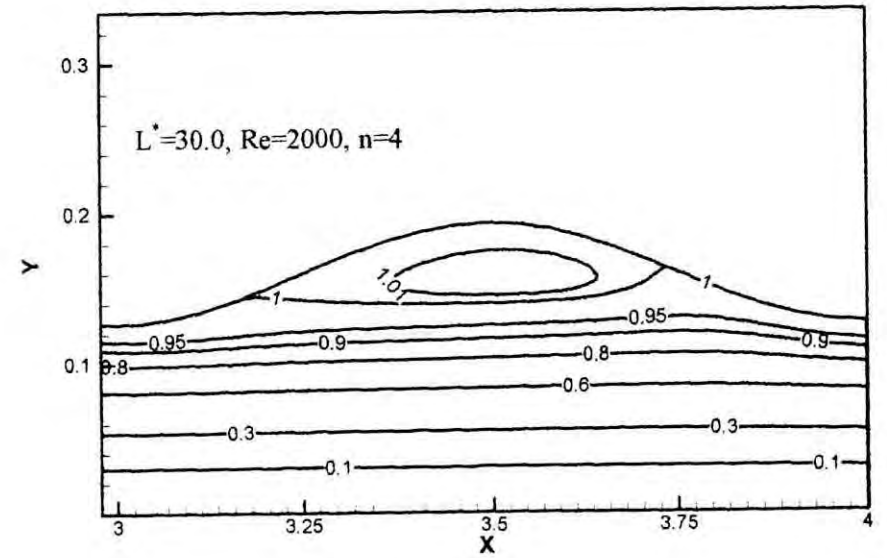
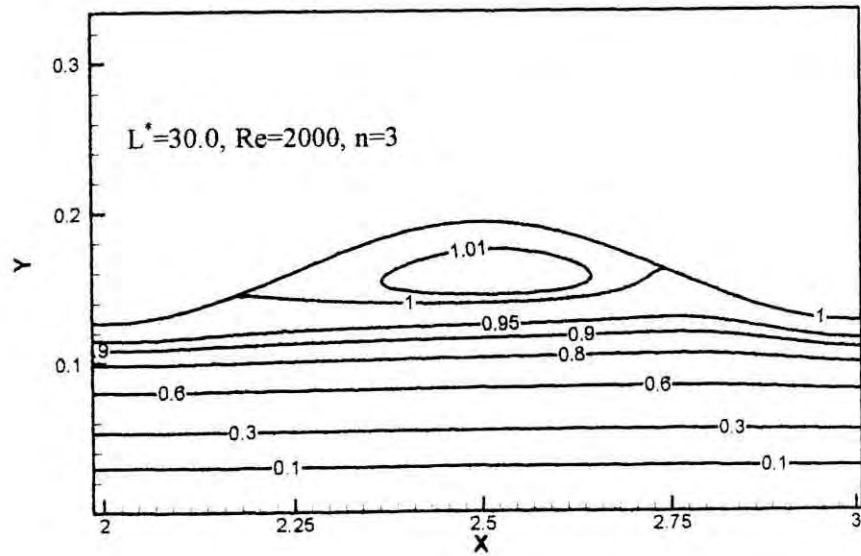
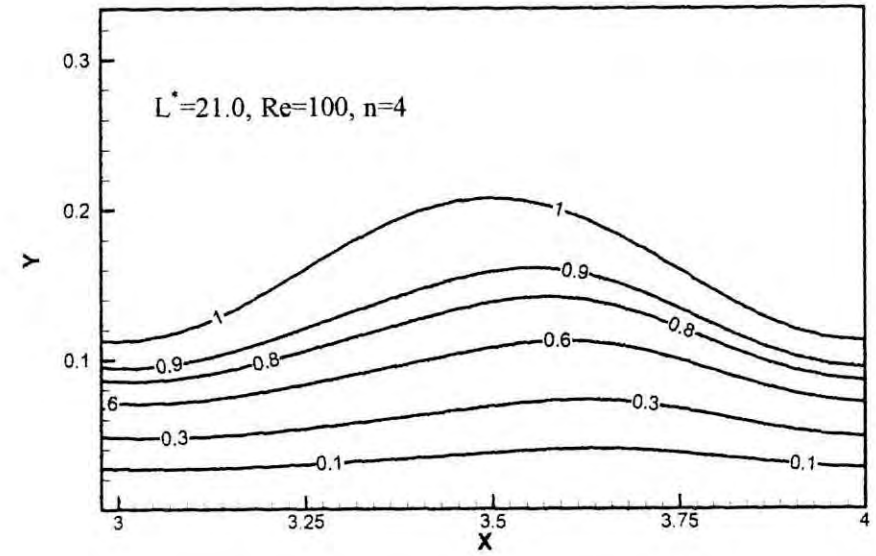
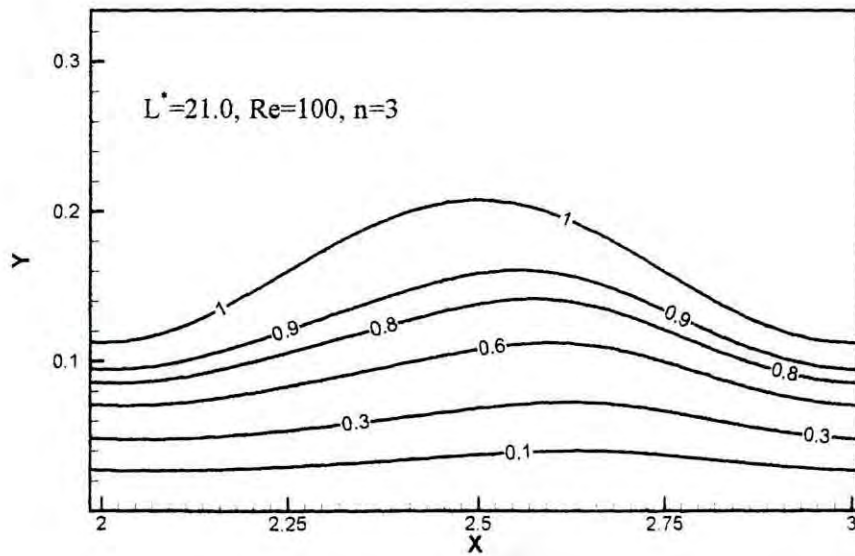
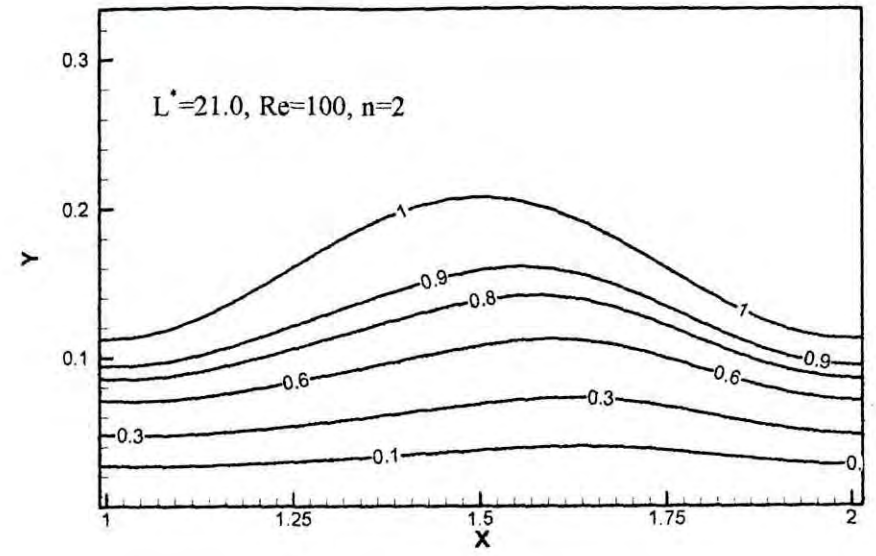
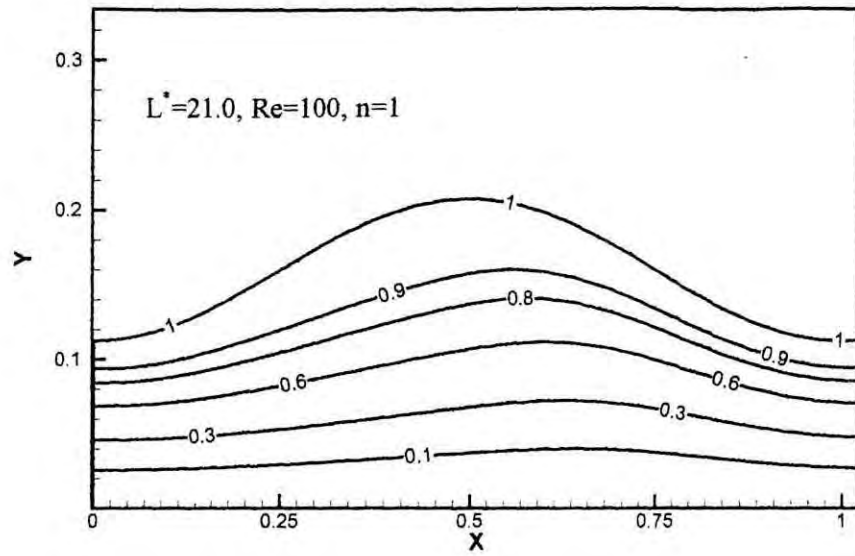
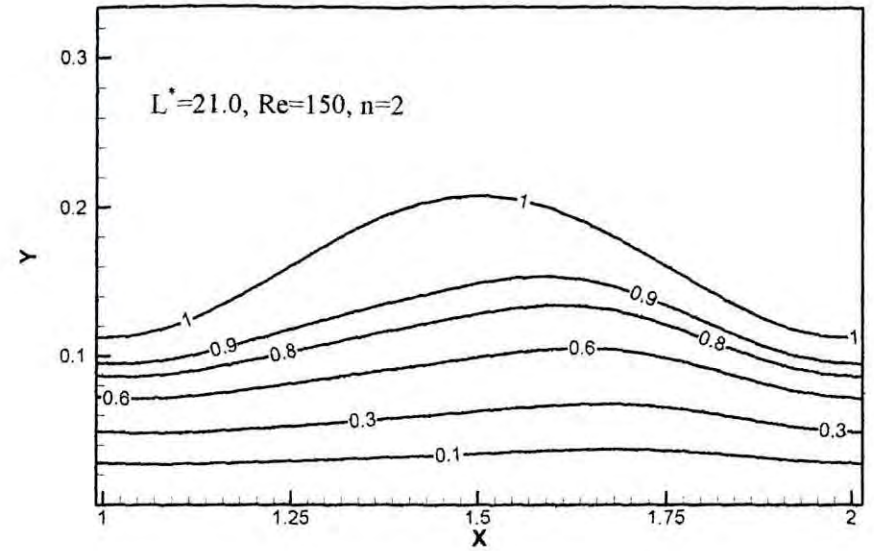
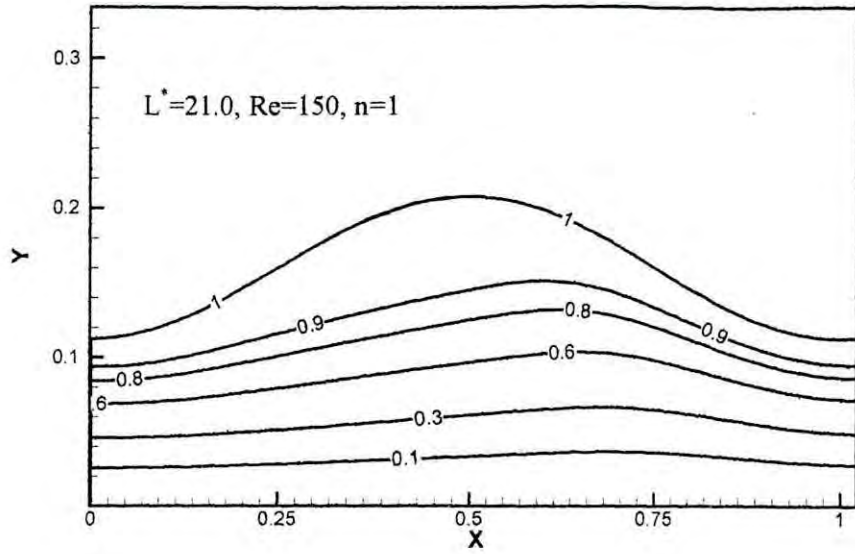


Fig.4.10 (m) Streamlines for $L^* = 30.0, Re = 2000, n = 1-4$



75

Fig.4.11 (a) Streamlines for $L^* = 21.0, Re = 100, n = 1-4$



76

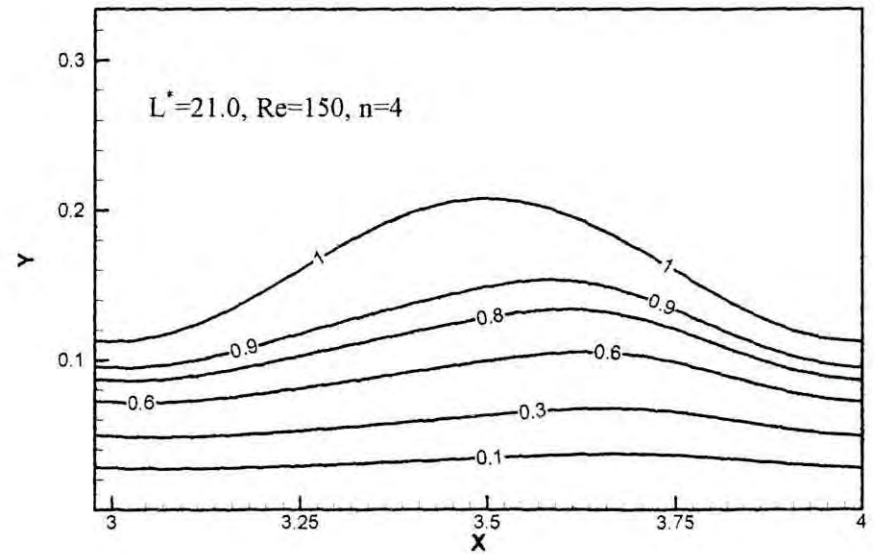
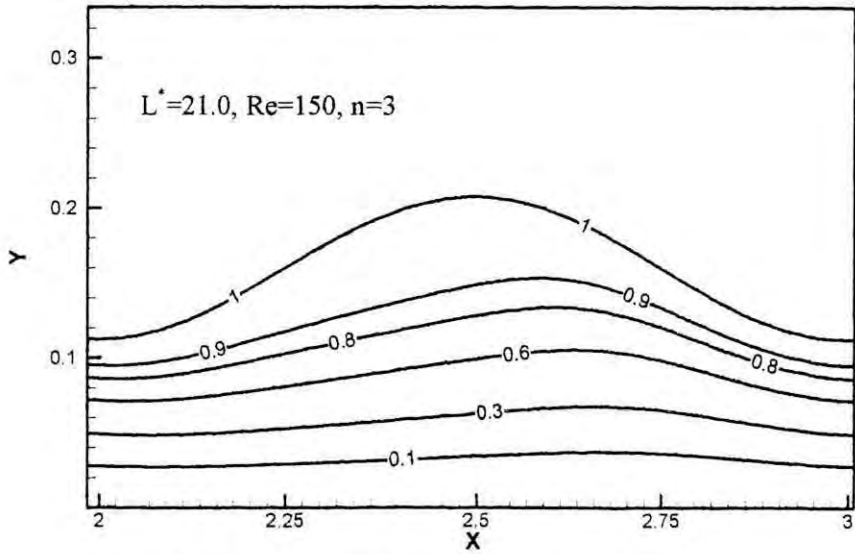


Fig.4.11 (b) Streamlines for $L^* = 21.0, Re = 150, n = 1-4$

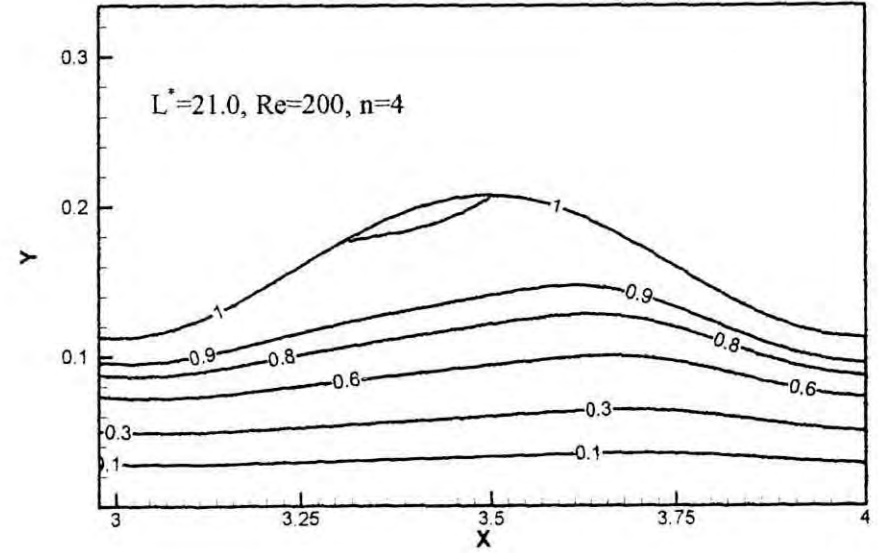
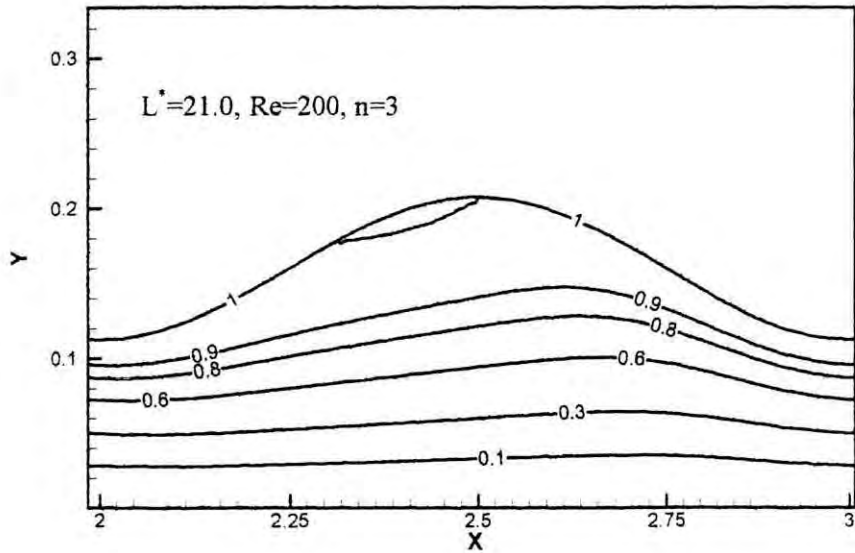
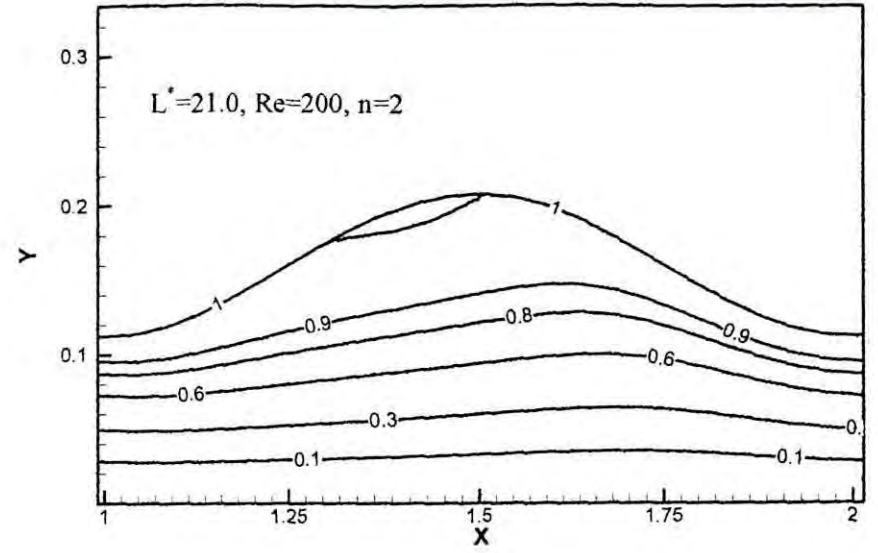
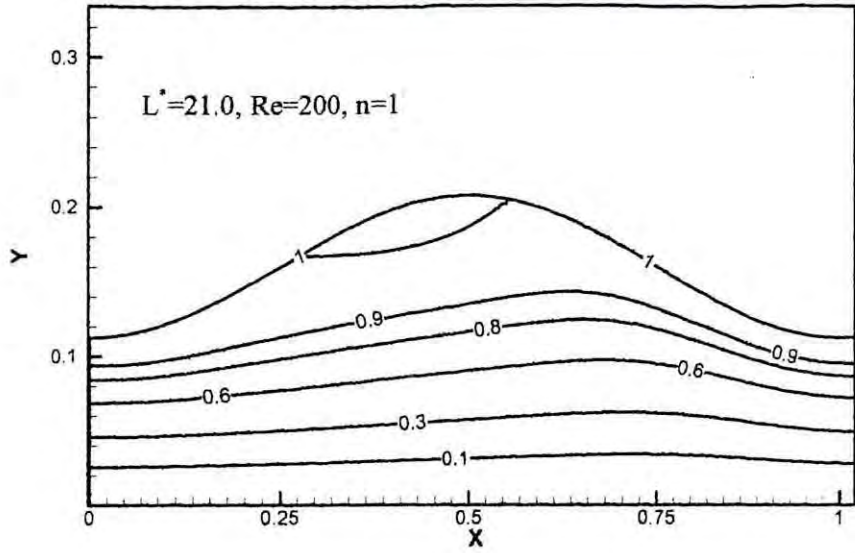
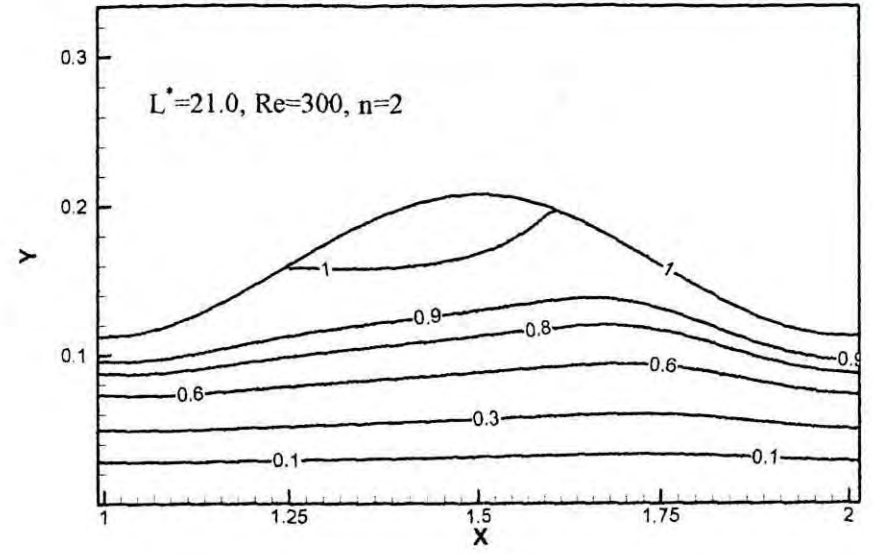
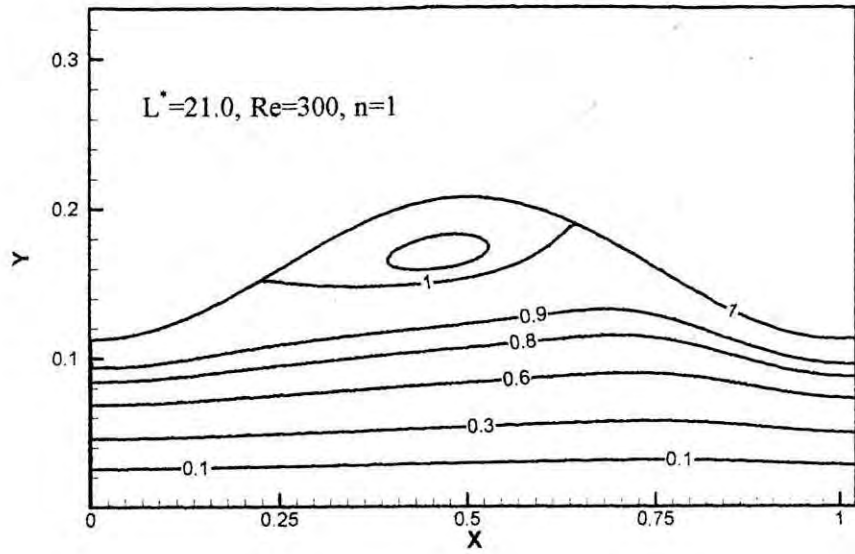


Fig.4.11 (c) Streamlines for $L^* = 21.0, Re = 200, n = 1-4$



88

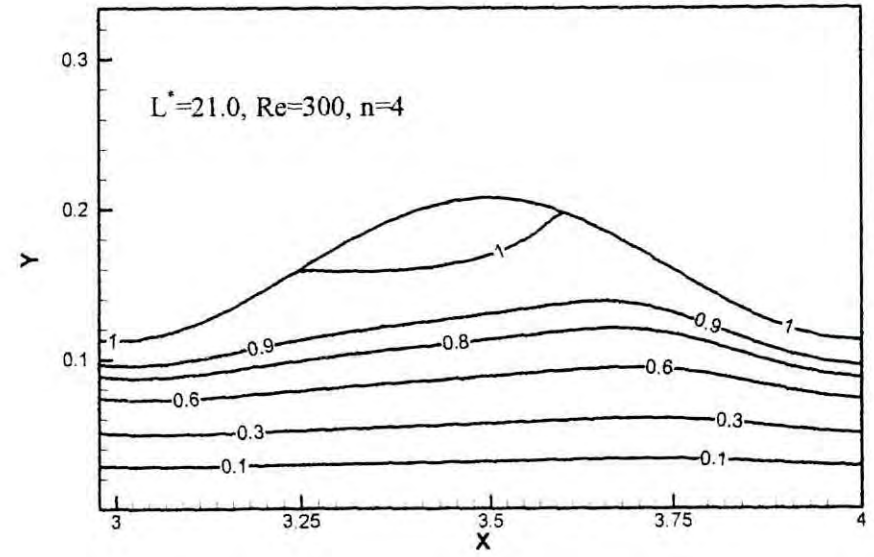
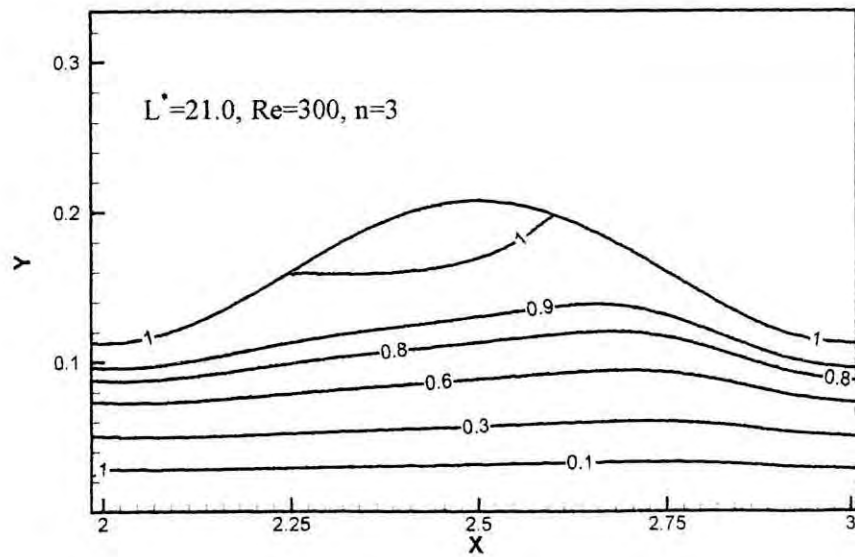
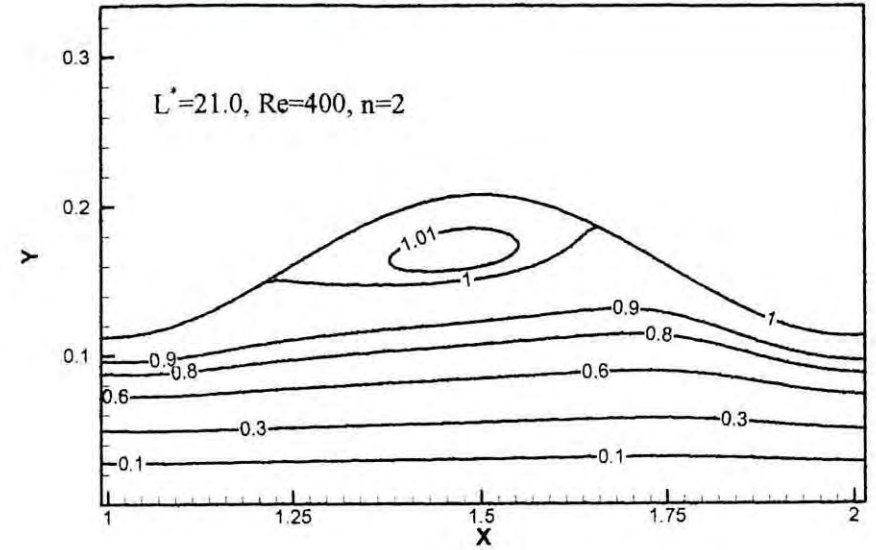
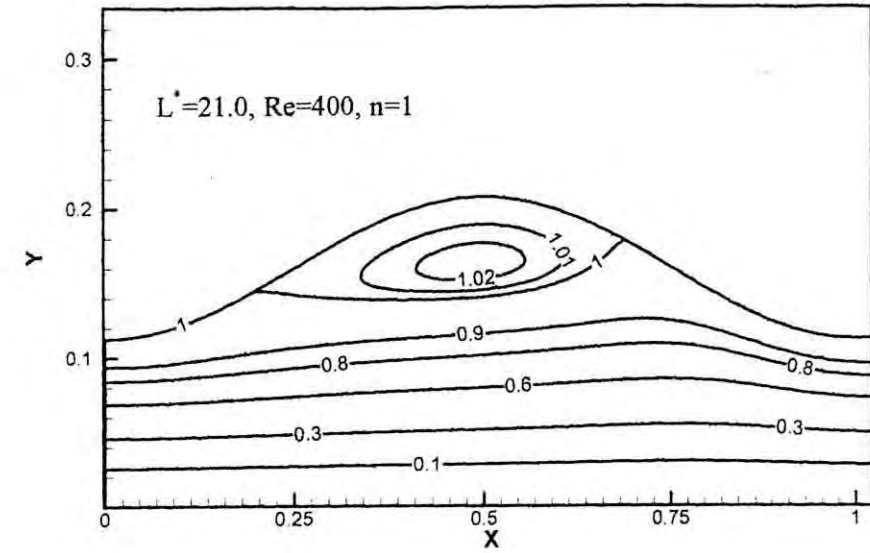


Fig.4.11 (d) Streamlines for $L^* = 21.0, Re = 300, n = 1-4$



79

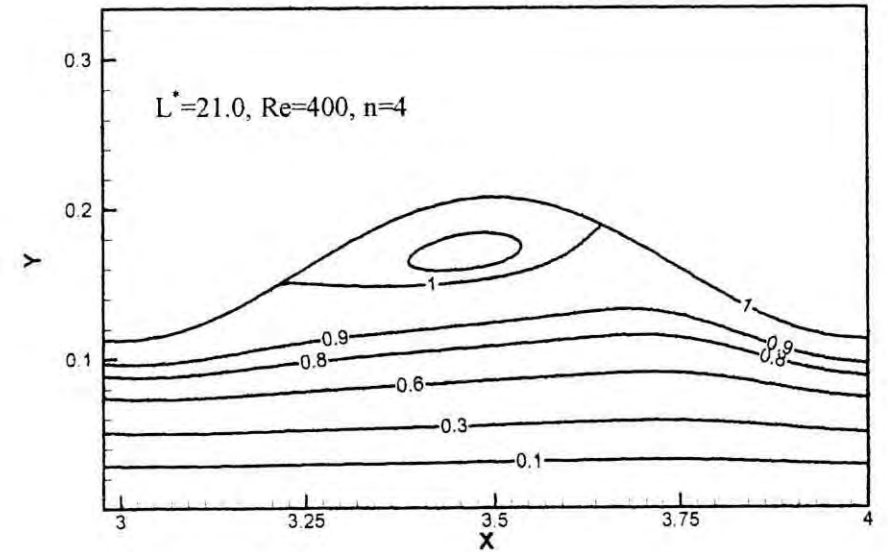
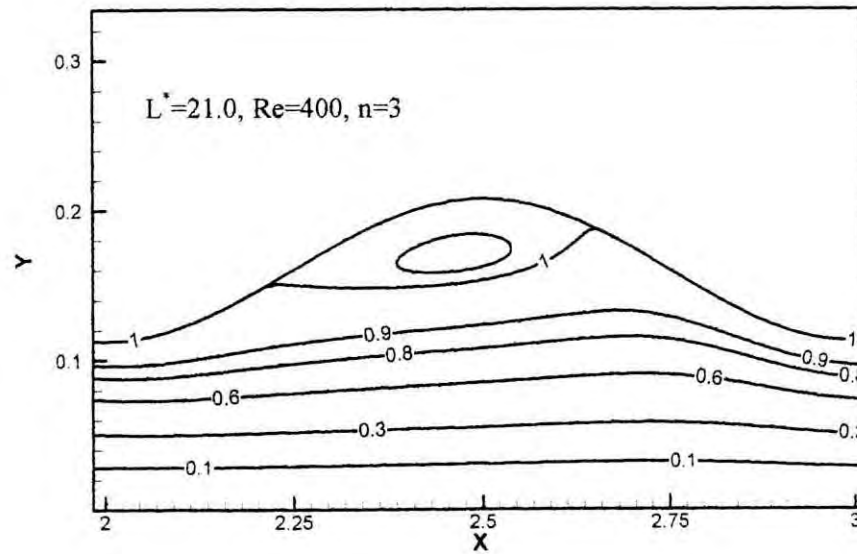


Fig.4.11 (e) Streamlines for $L^* = 21.0, Re = 400, n = 1-4$

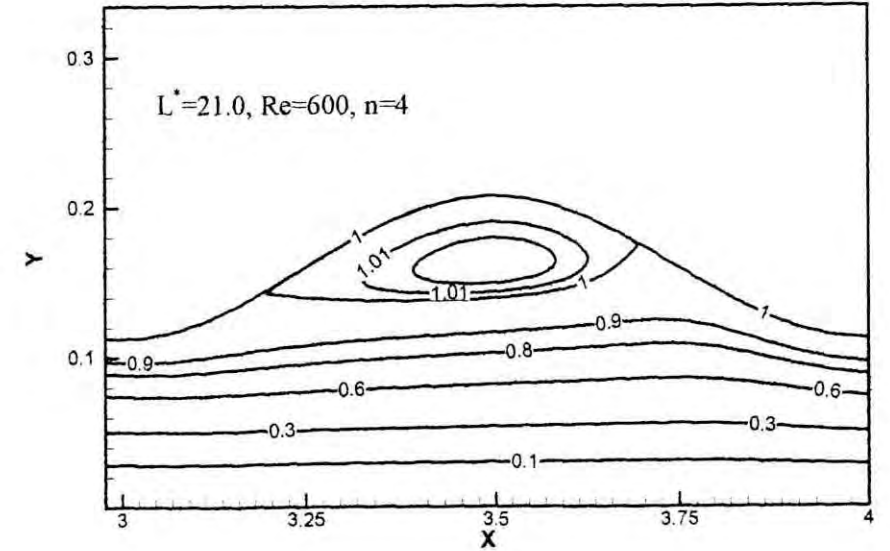
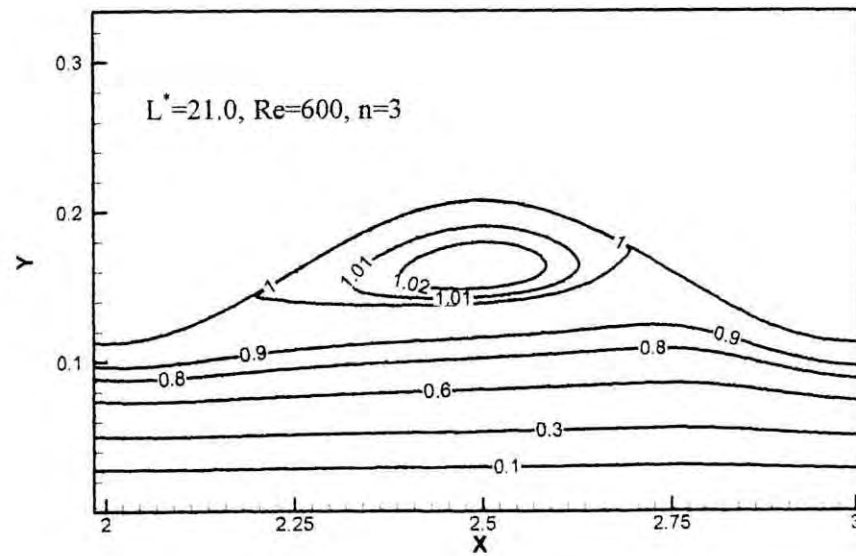
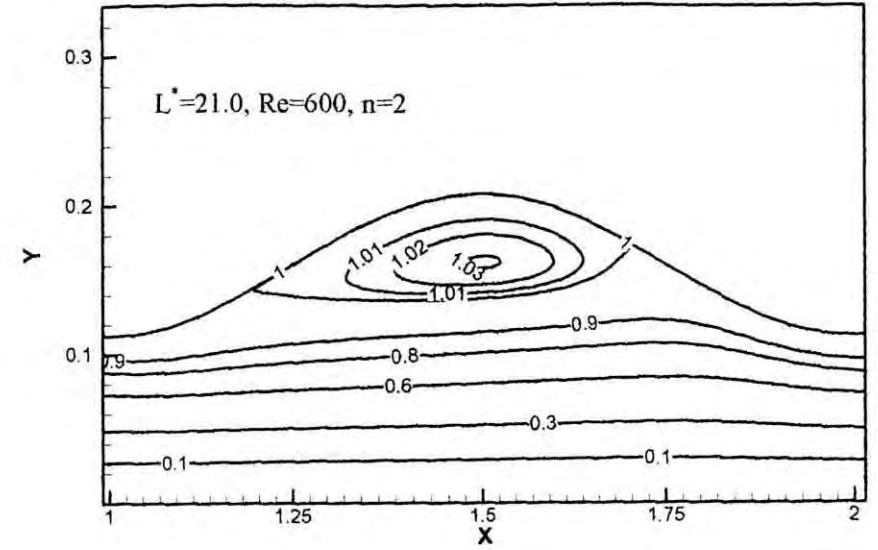
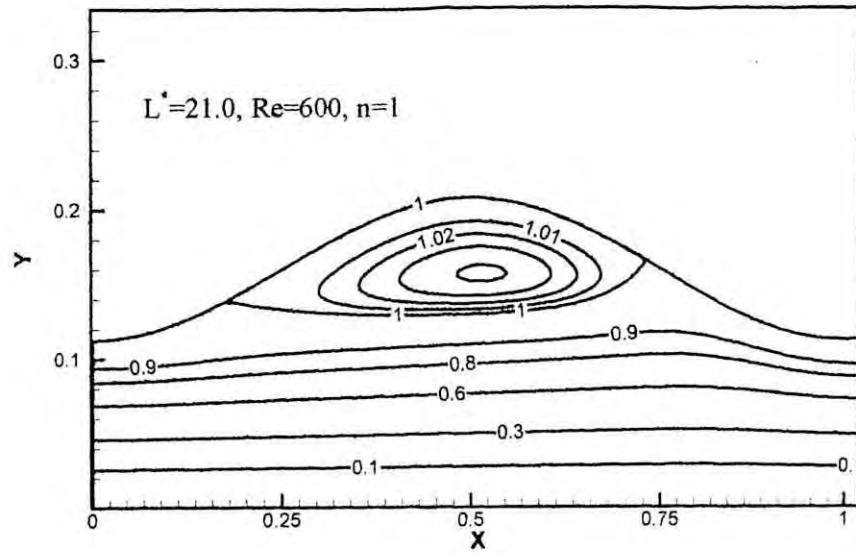


Fig.4.11 (f) Streamlines for $L^* = 21.0, Re = 600, n = 1-4$

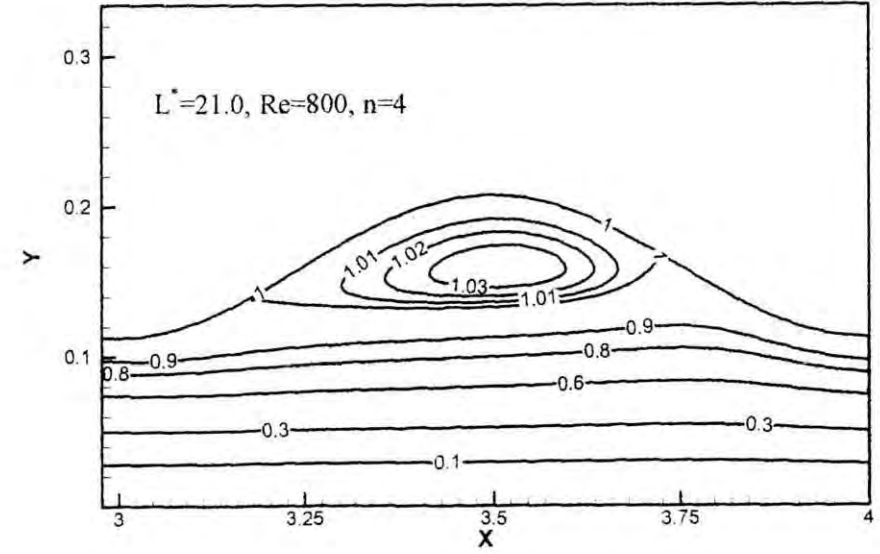
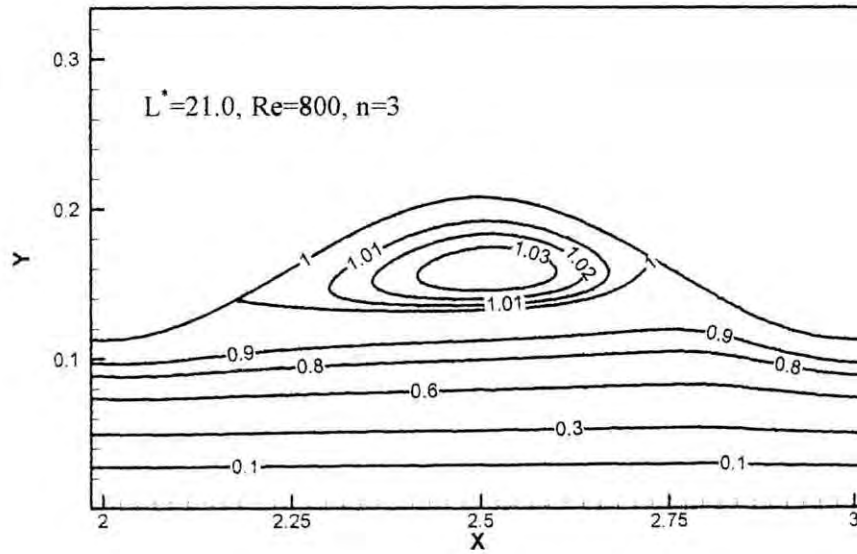
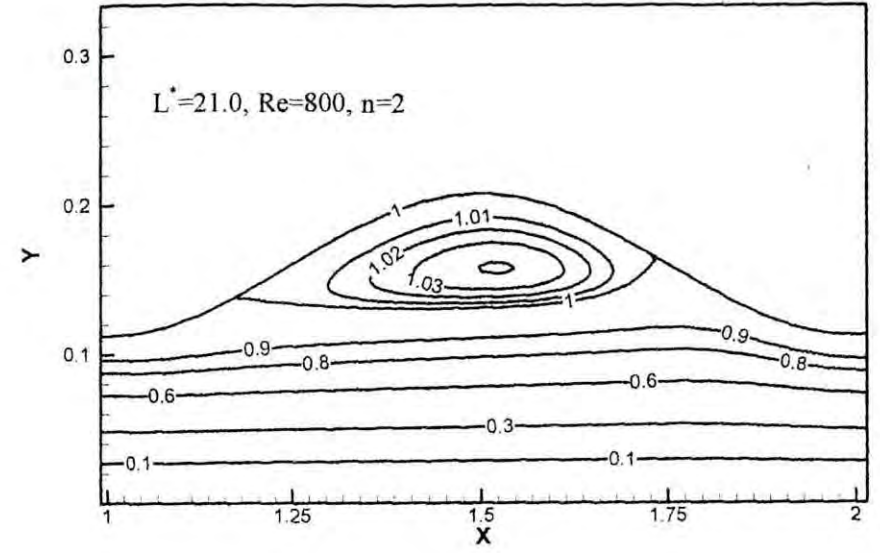
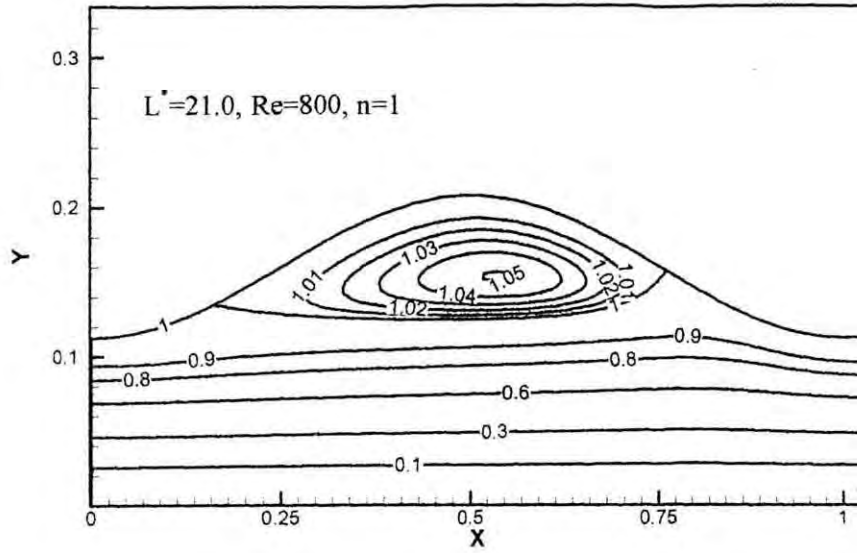


Fig.4.11 (g) Streamlines for $L^* = 21.0$, $Re = 800$, $n = 1-4$

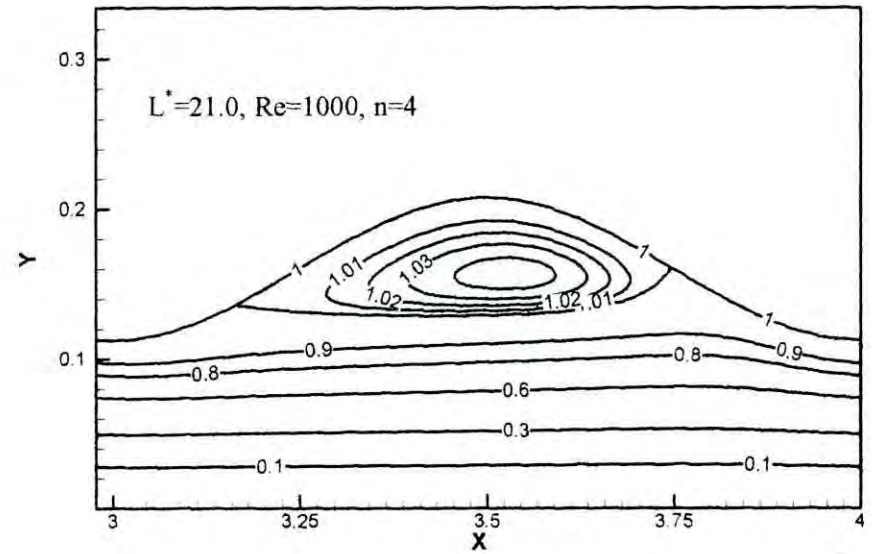
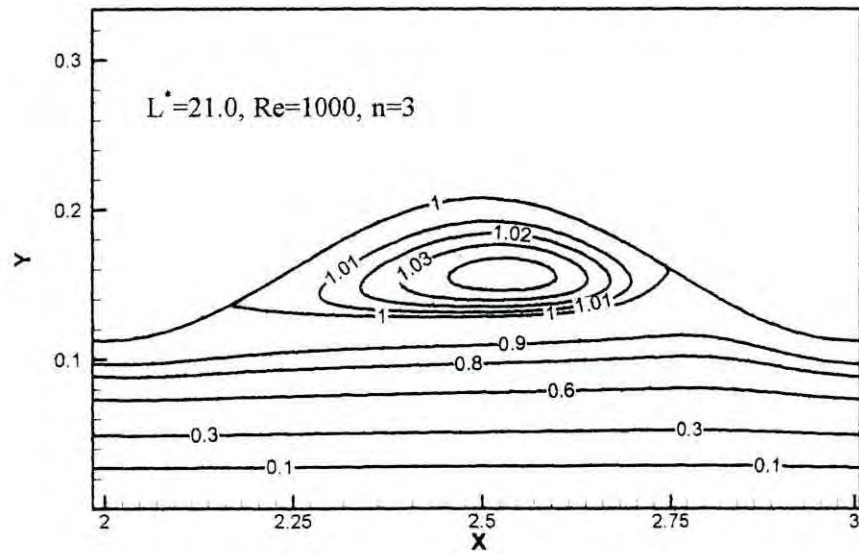
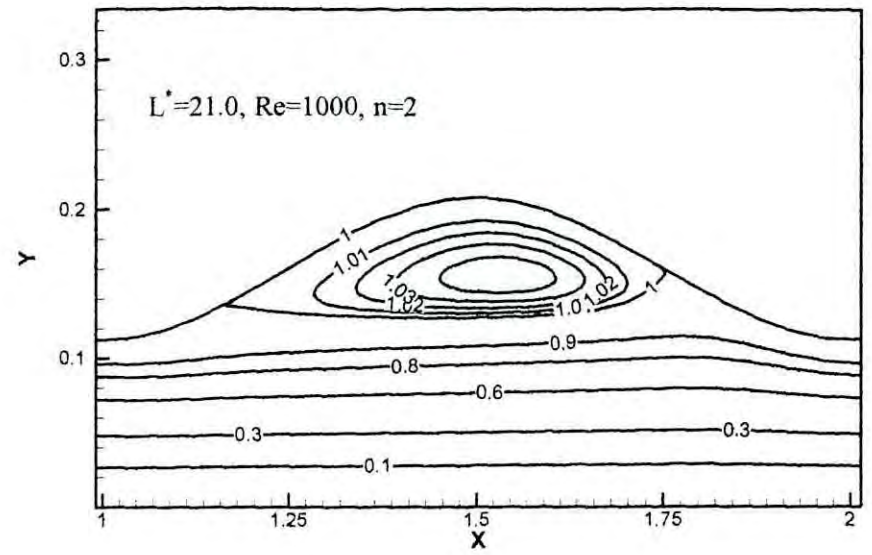
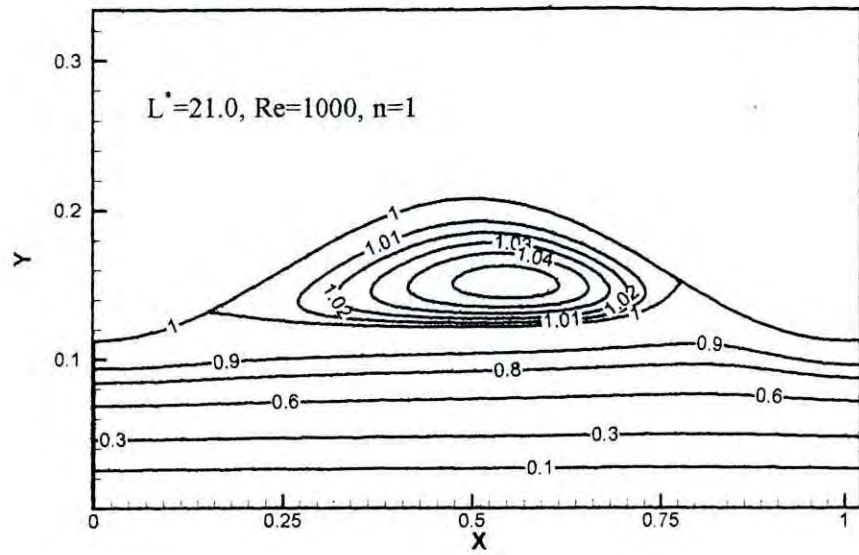
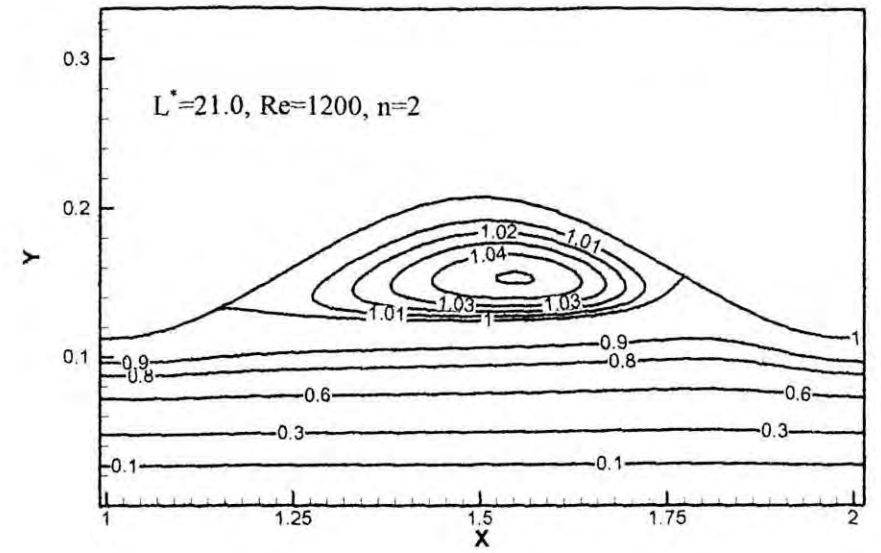
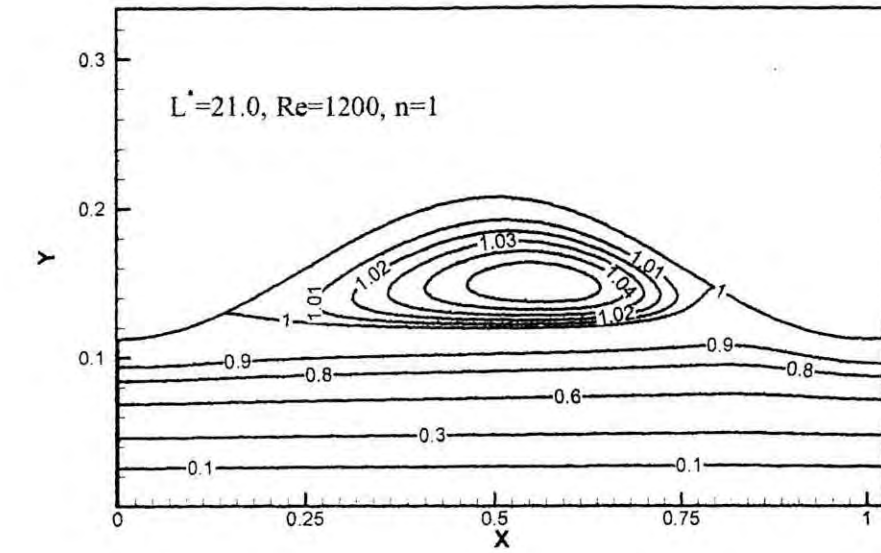


Fig.4.11 (h) Streamlines for $L^* = 21.0, Re = 1000, n = 1-4$



83

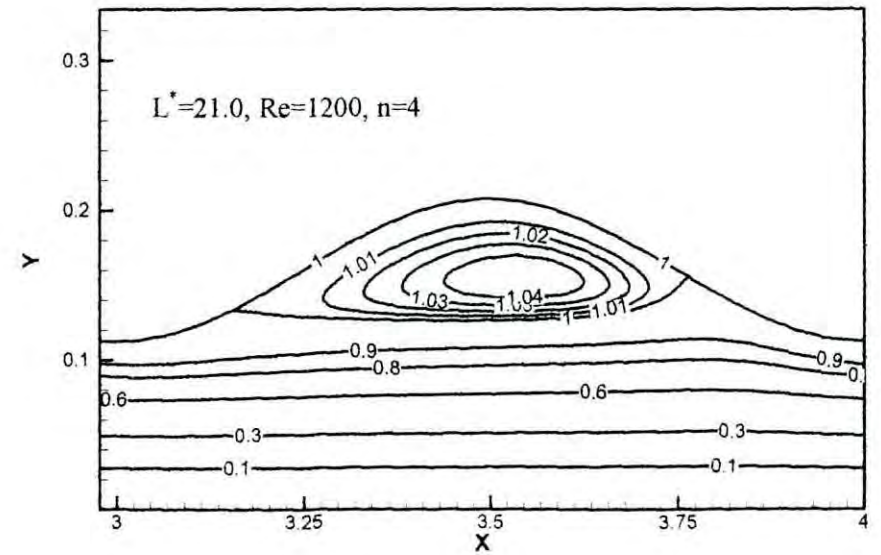
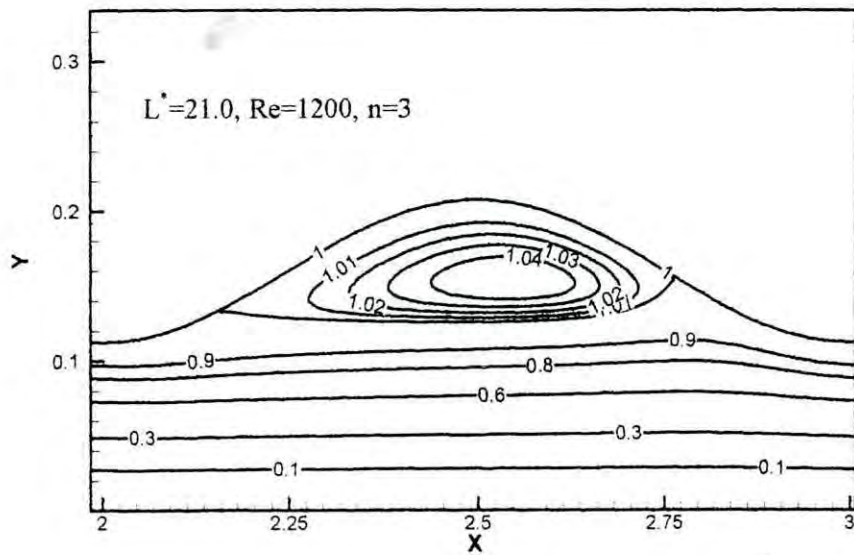
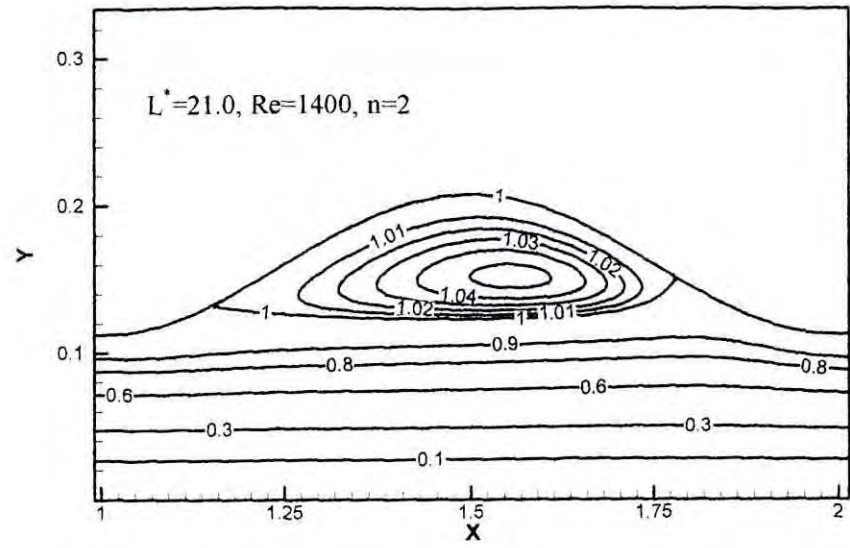
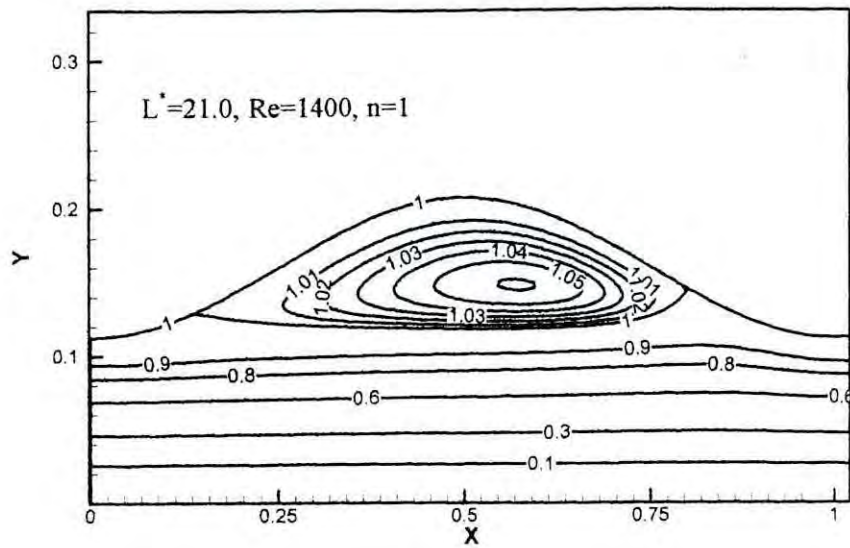


Fig.4.11 (i) Streamlines for $L^* = 21.0, Re = 1200, n = 1-4$



84

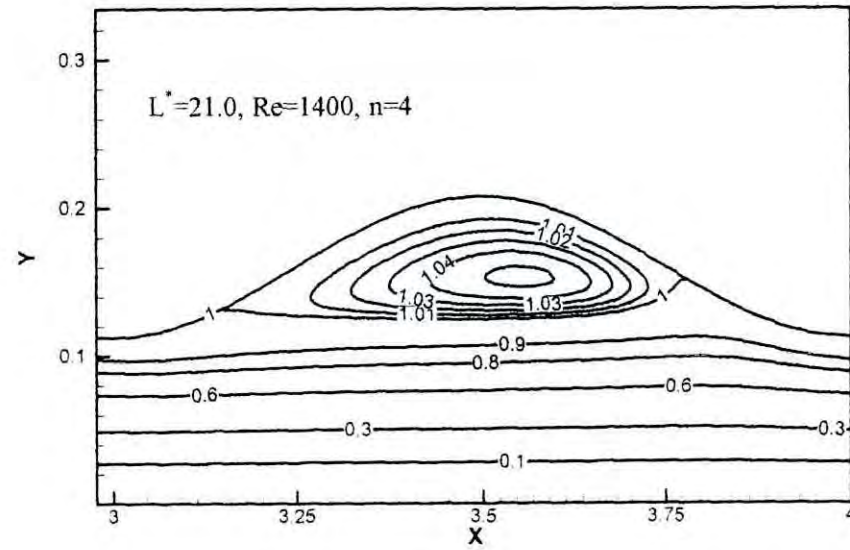
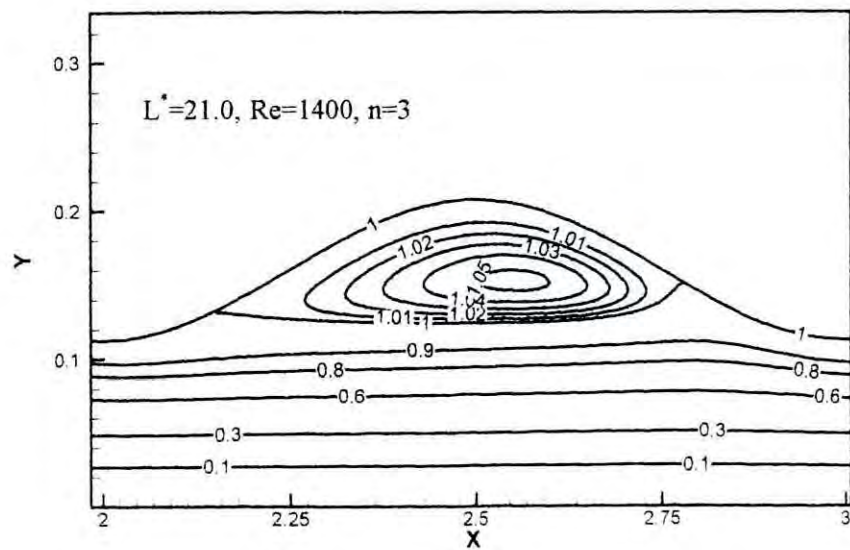


Fig.4.11 (j) Streamlines for $L^* = 21.0, Re = 1400, n = 1-4$

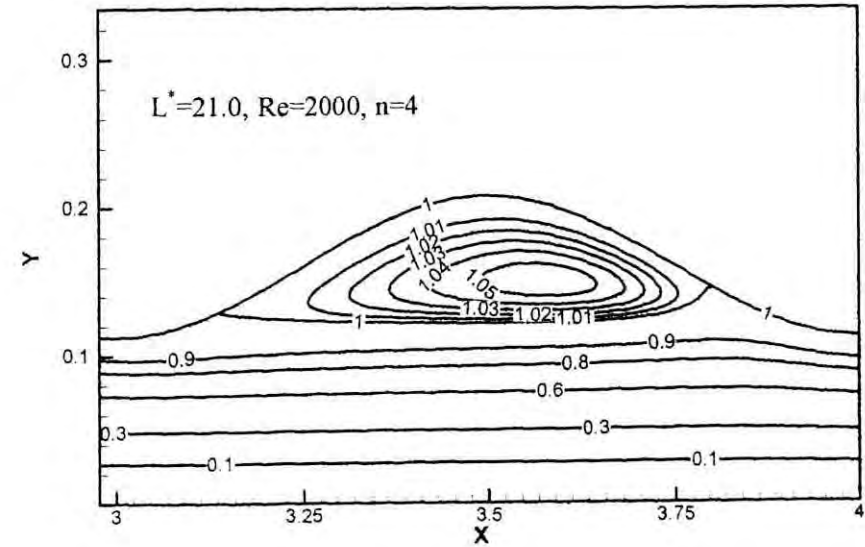
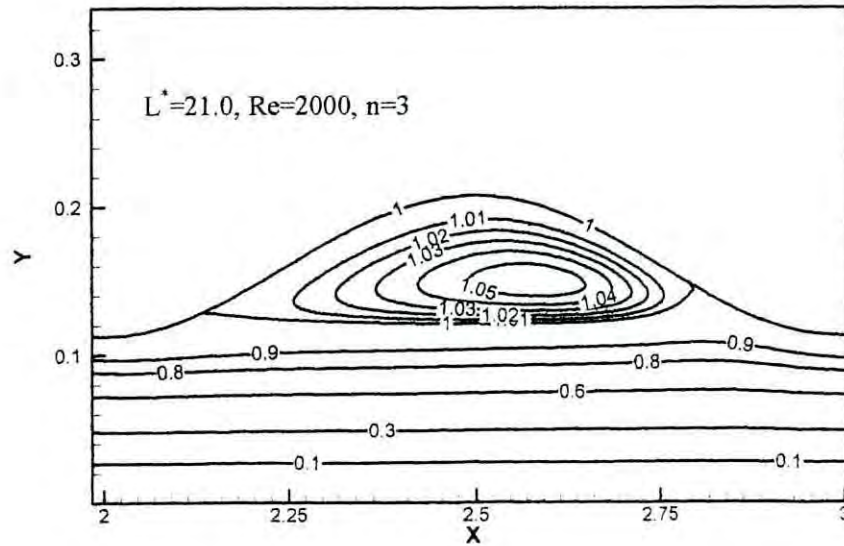
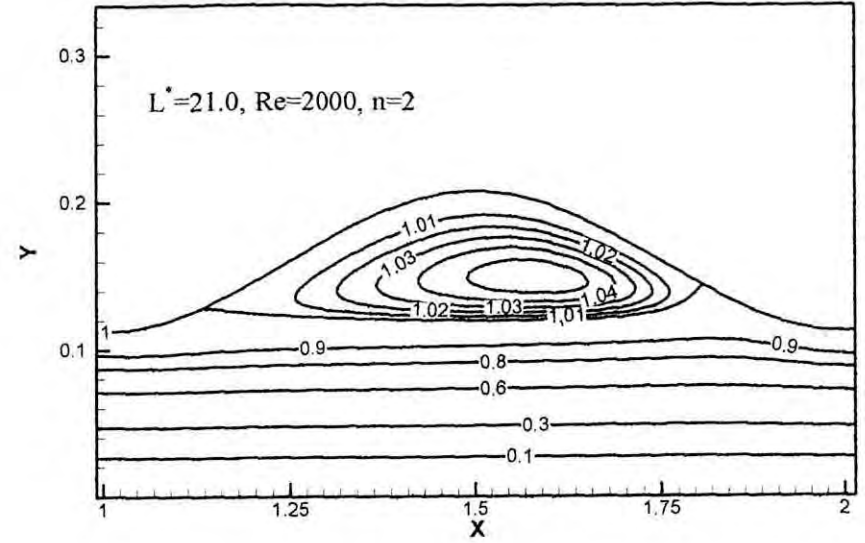
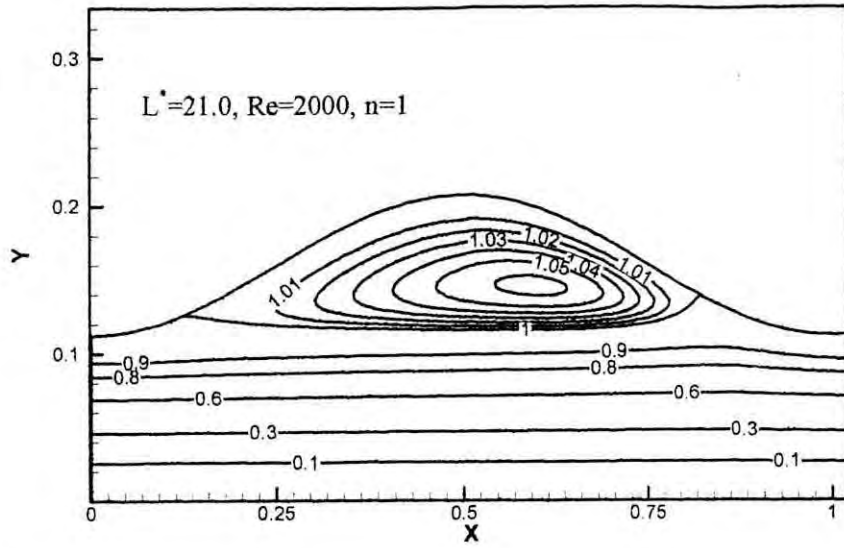


Fig.4.11 (k) Streamlines for $L^* = 21.0$, $Re = 2000$, $n = 1-4$

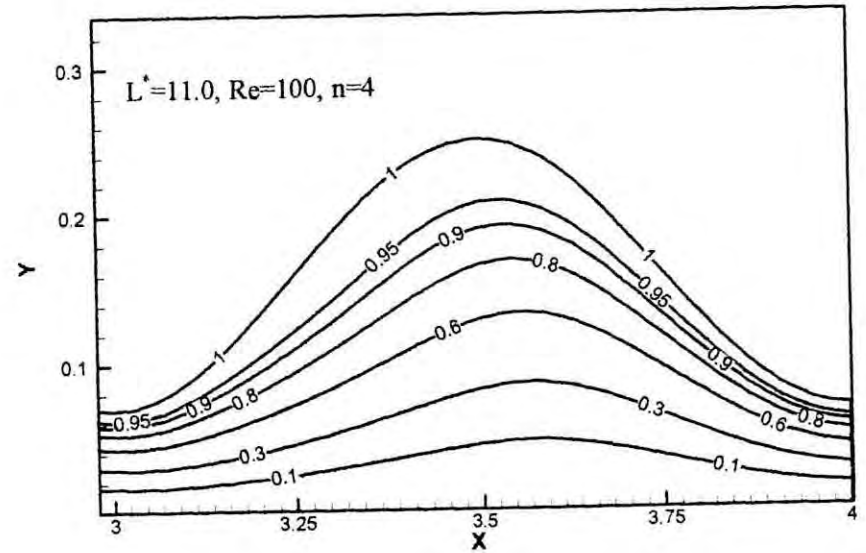
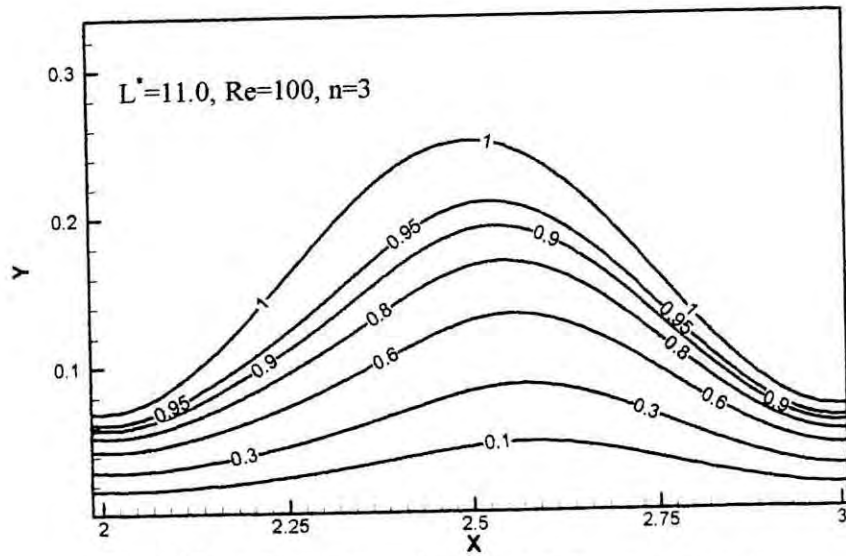
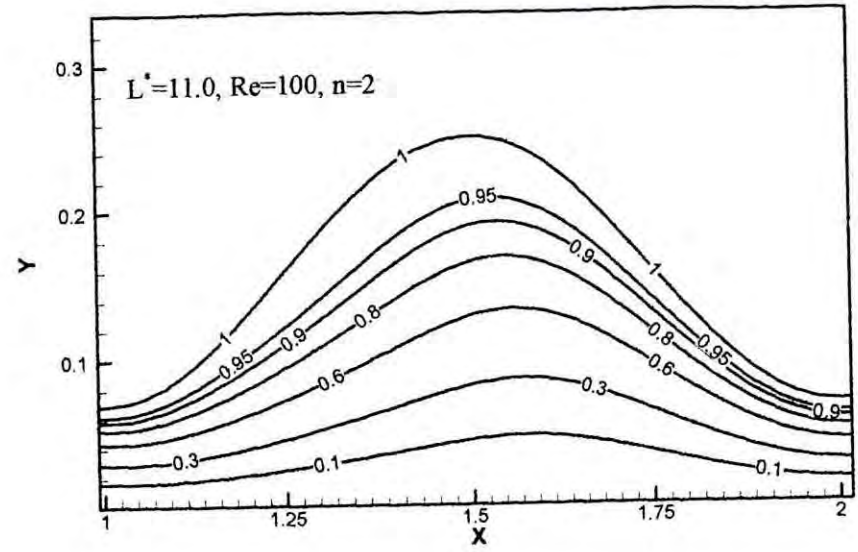
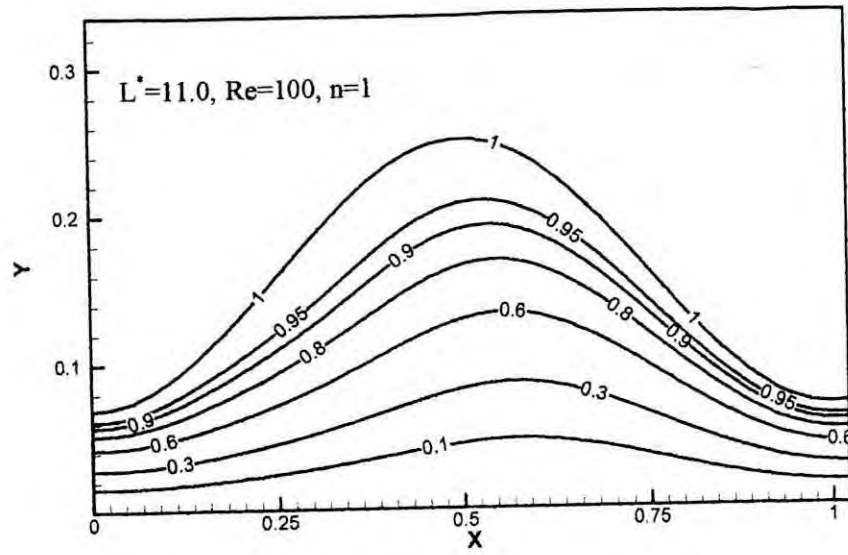


Fig.4.12 (a) Streamlines for $L^* = 11.0, Re = 100, n = 1-4$

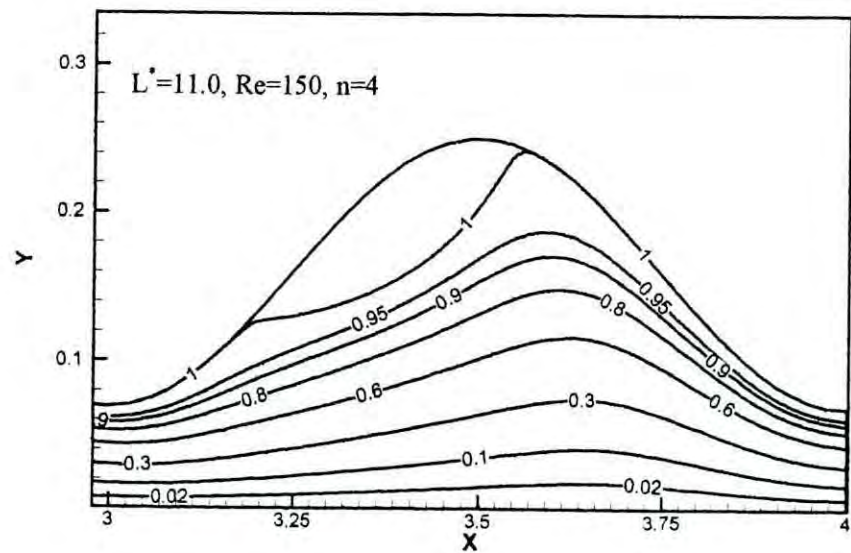
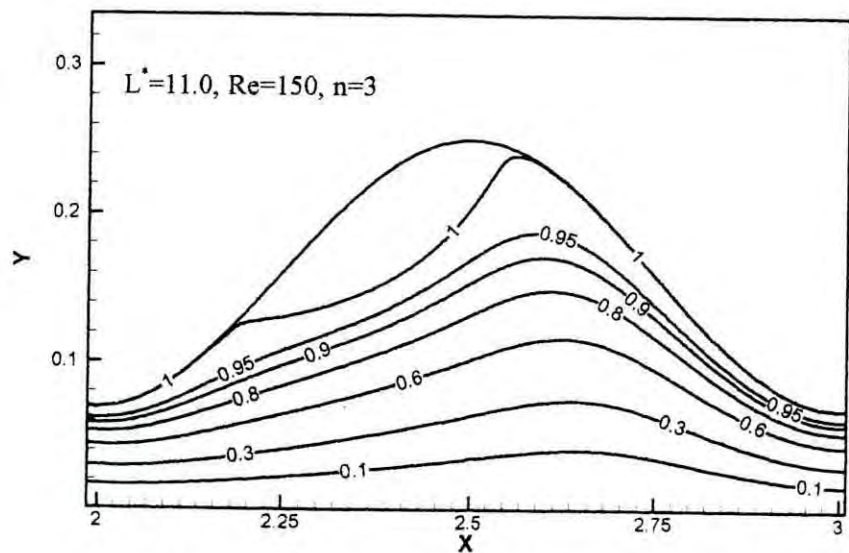
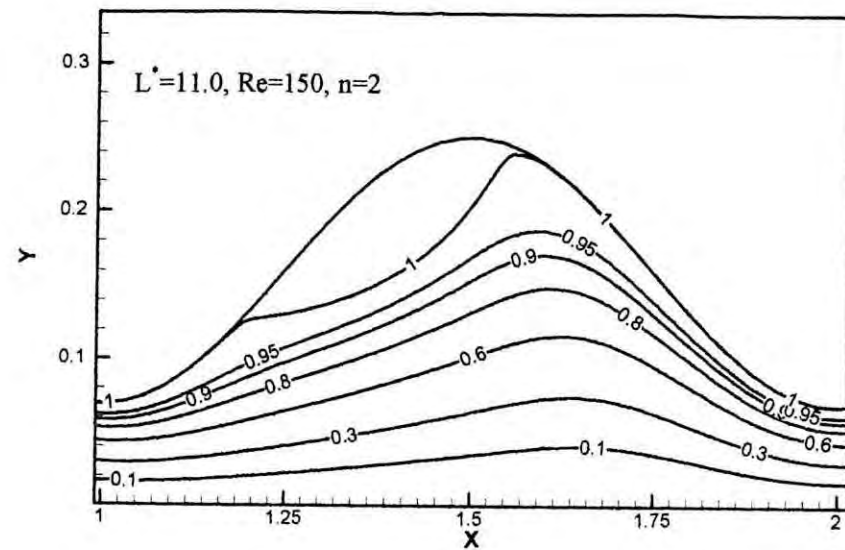
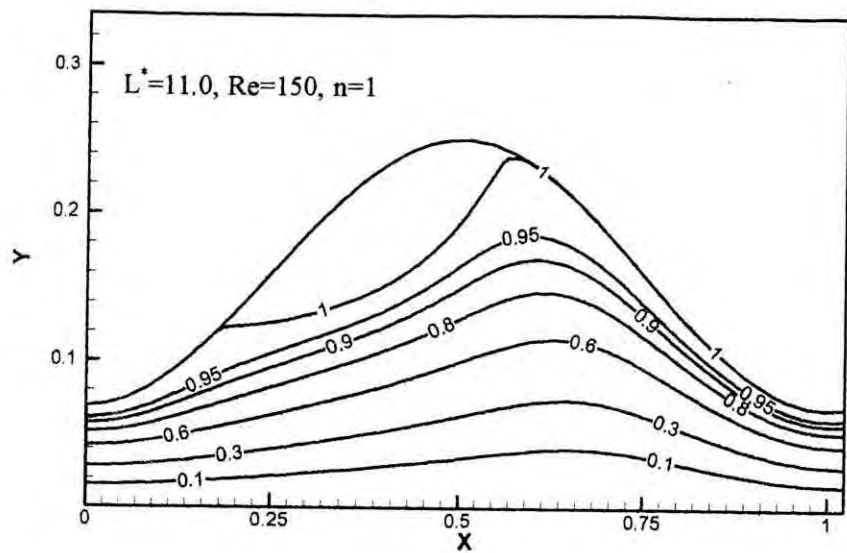


Fig.4.12 (b) Streamlines for $L^* = 11.0$, $Re = 150$, $n = 1-4$

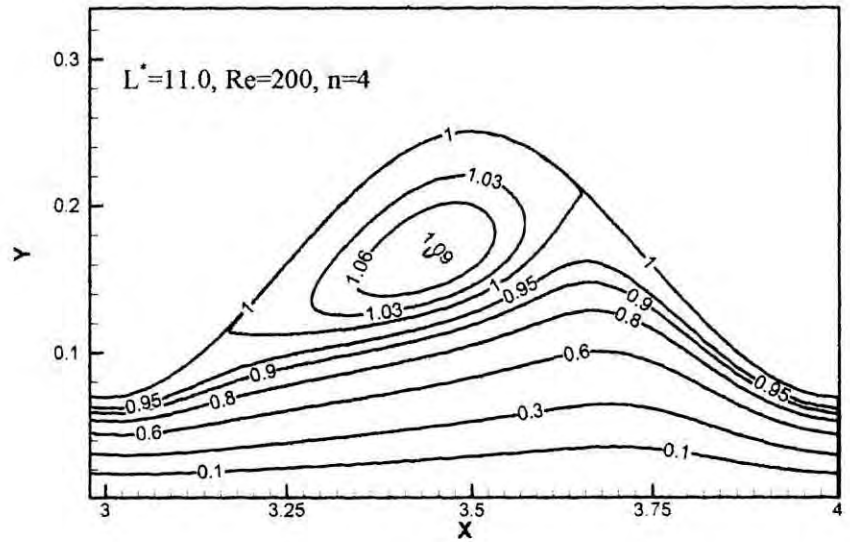
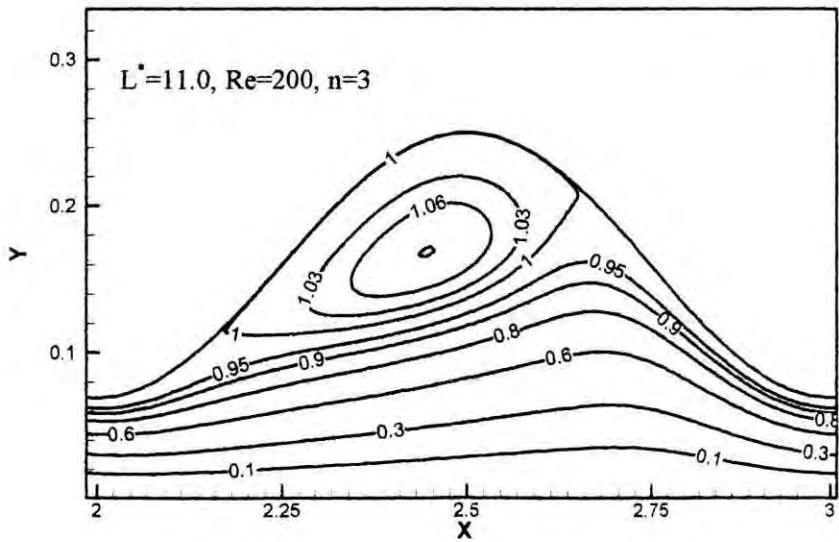
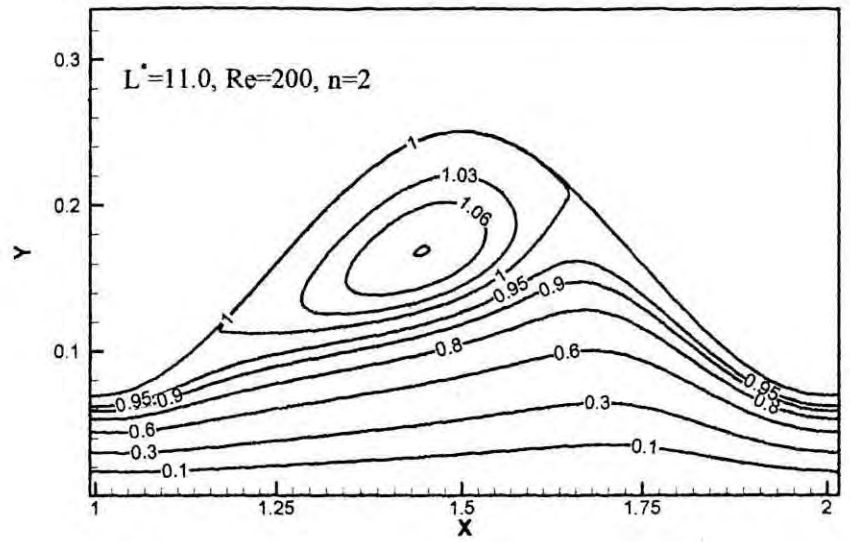
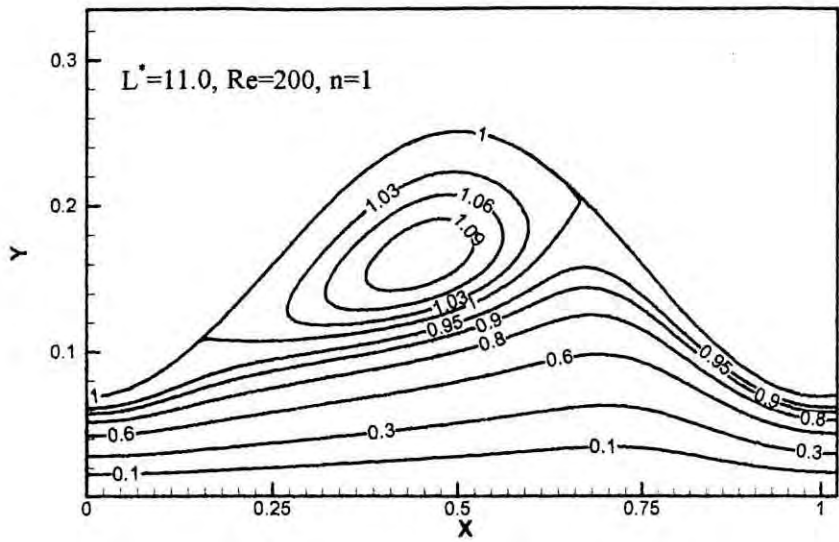


Fig.4.12 (c) Streamlines for $L^* = 11.0, Re = 200, n = 1-4$

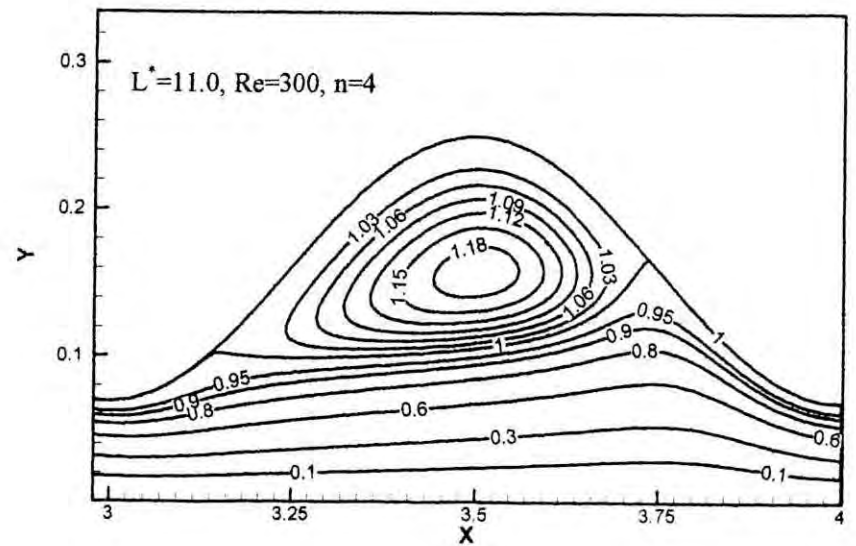
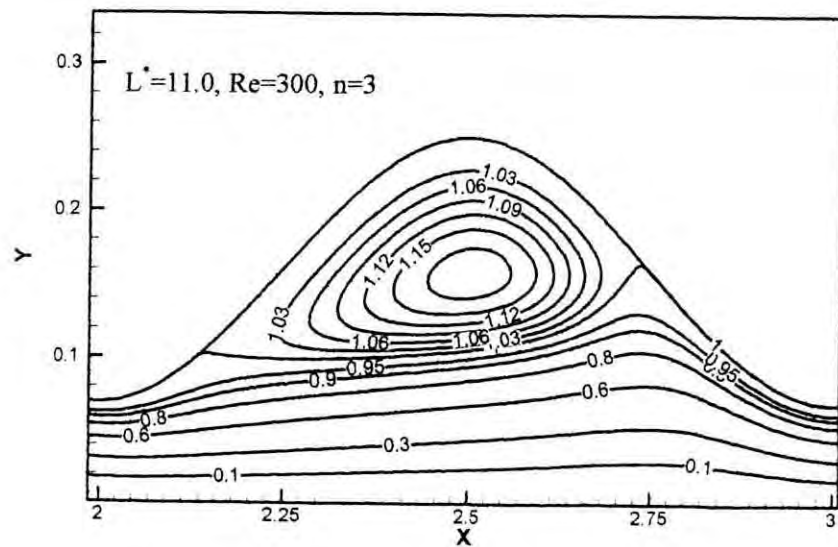
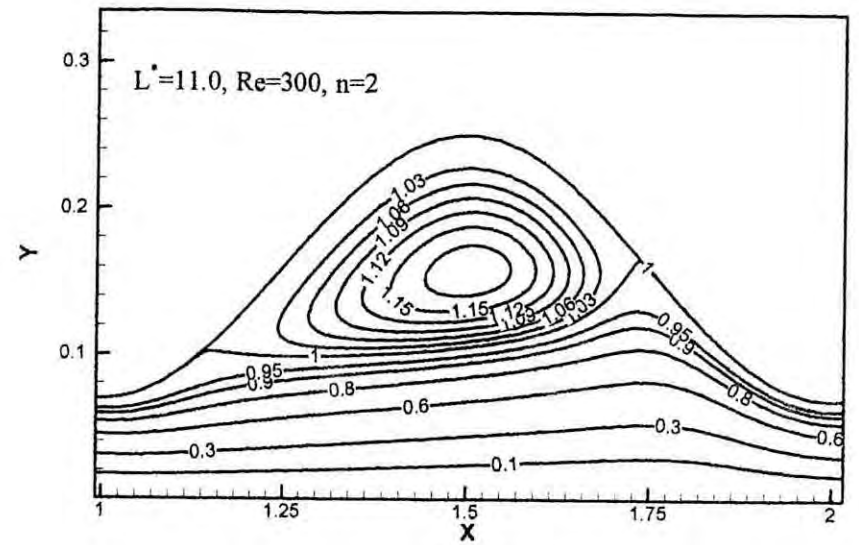
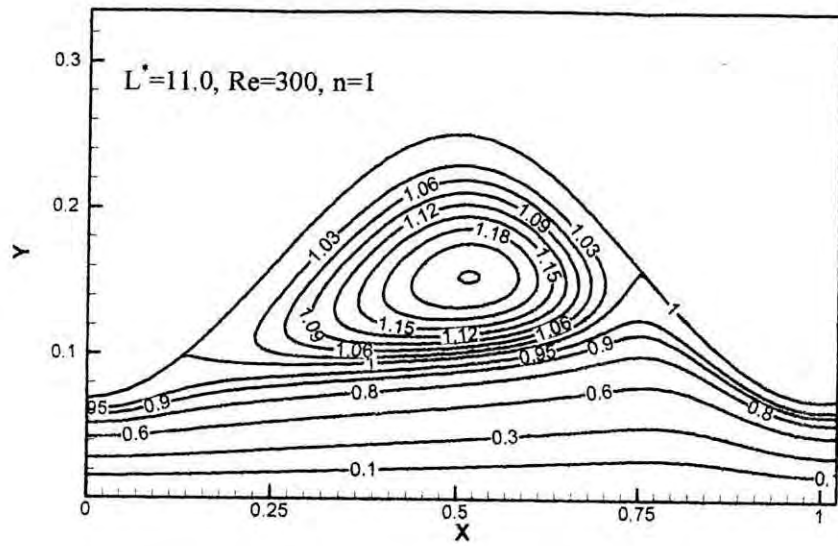


Fig.4.12 (d) Streamlines for $L^* = 11.0$, $Re = 300$, $n = 1-4$

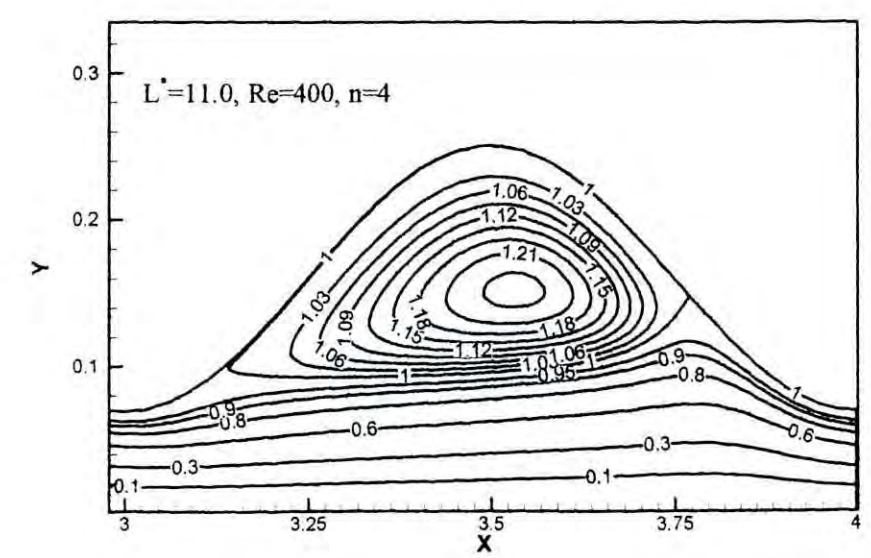
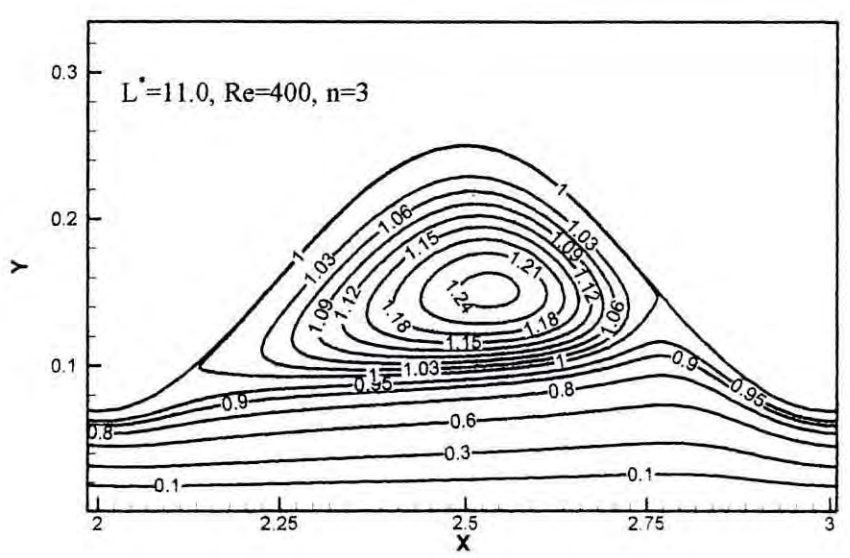
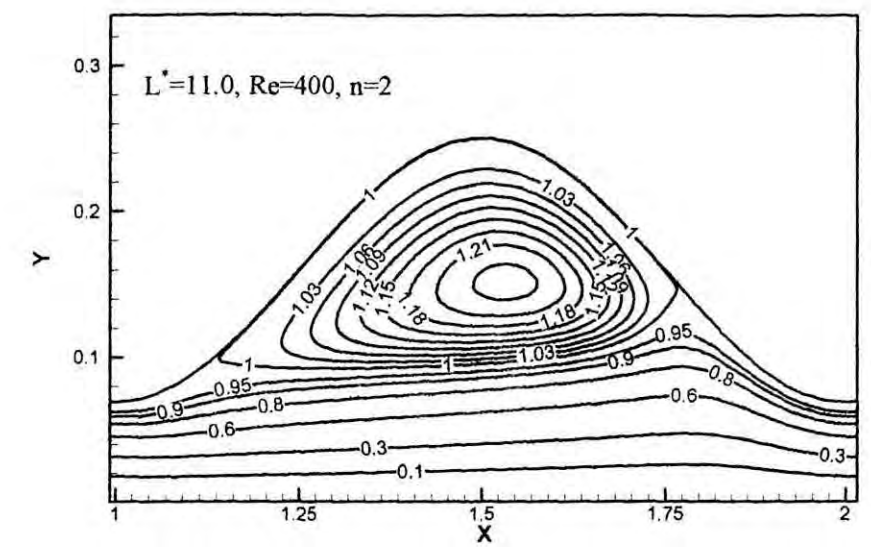
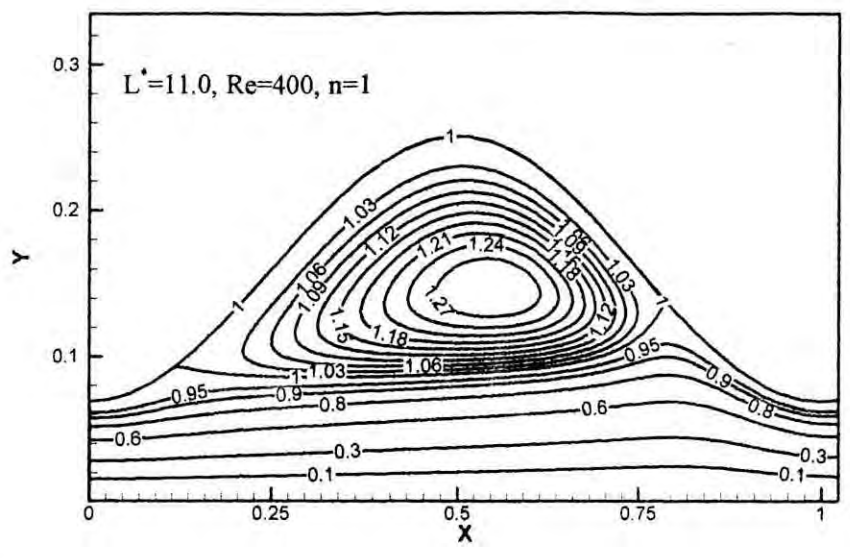
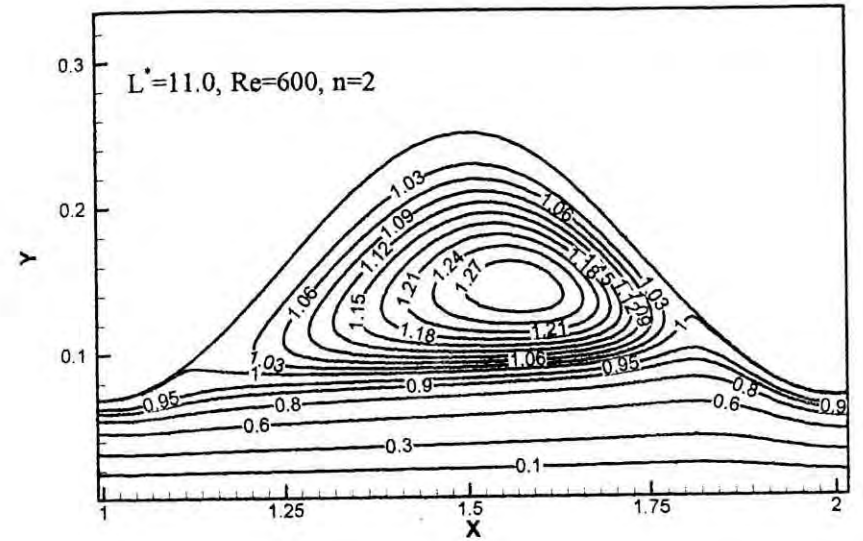
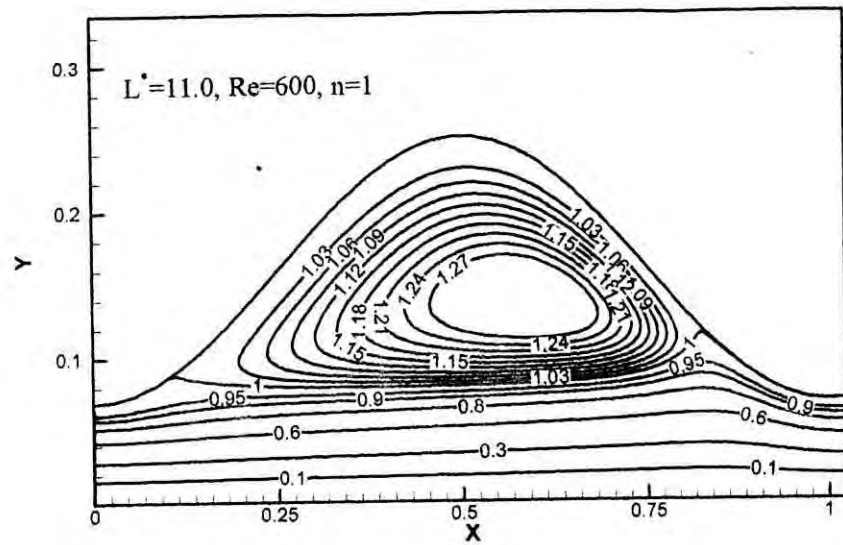


Fig.4.12 (e) Streamlines for $L^* = 11.0, Re = 400, n = 1-4$



16

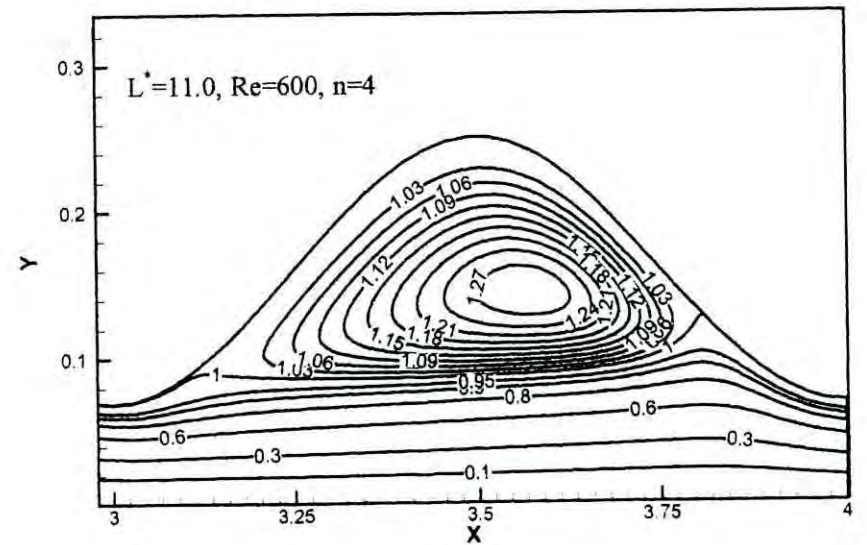
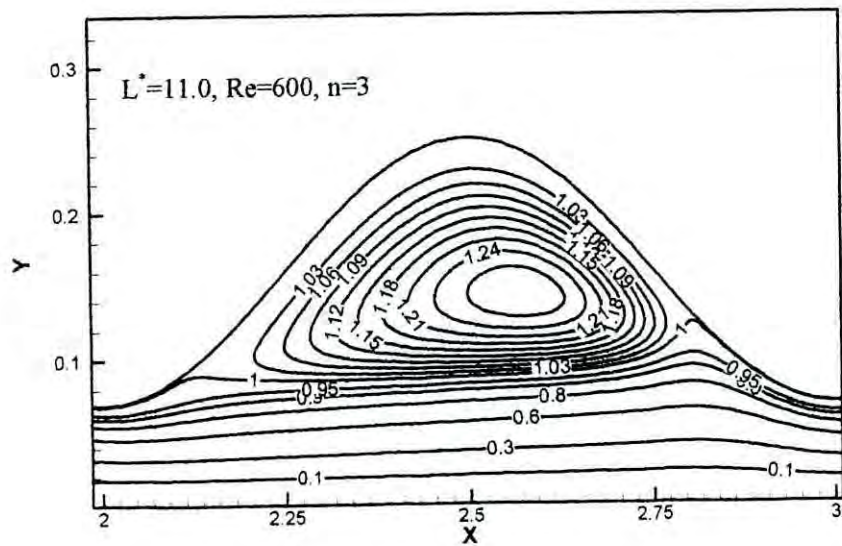


Fig.4.12 (f) Streamlines for $L^* = 11.0$, $Re = 600$, $n = 1-4$

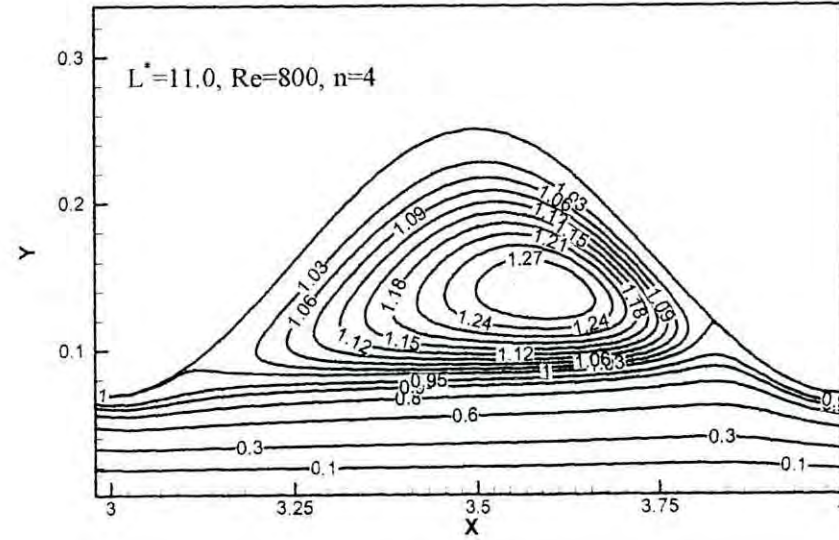
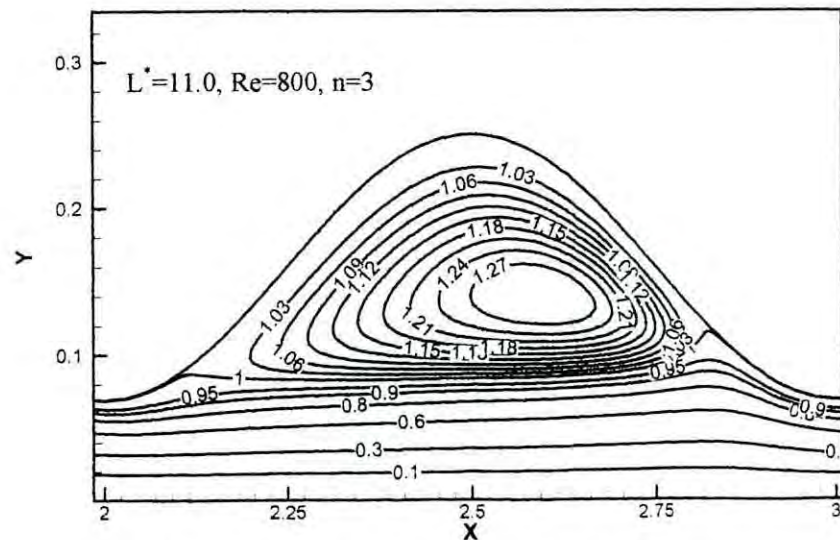
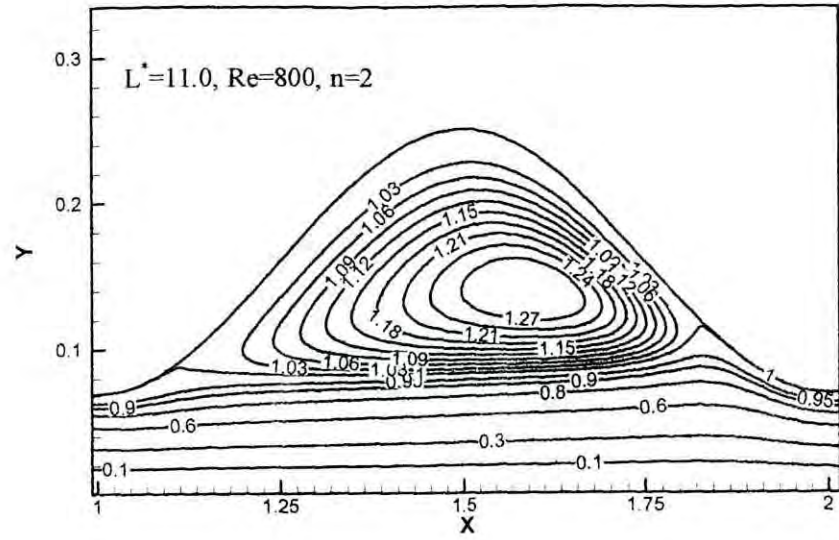
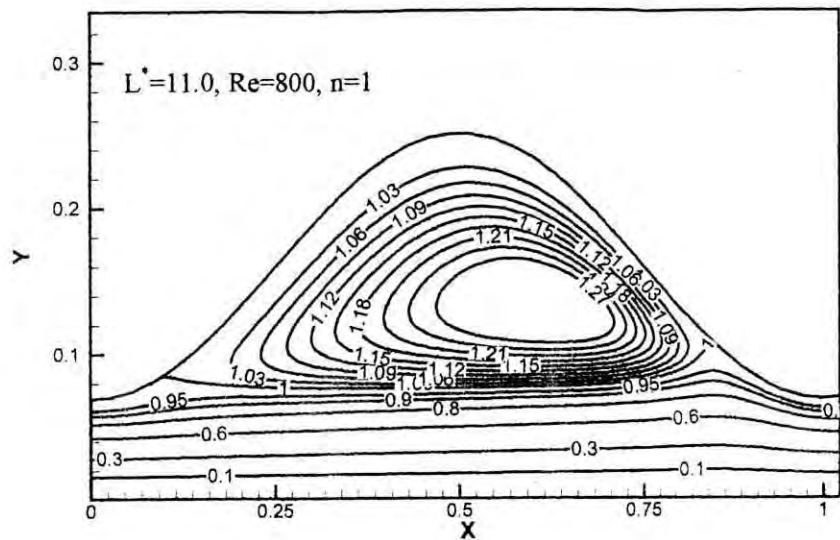
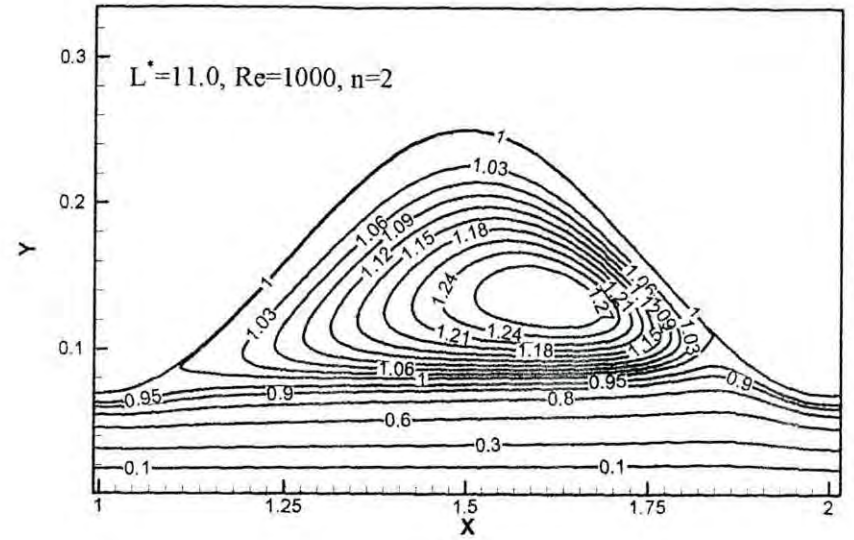
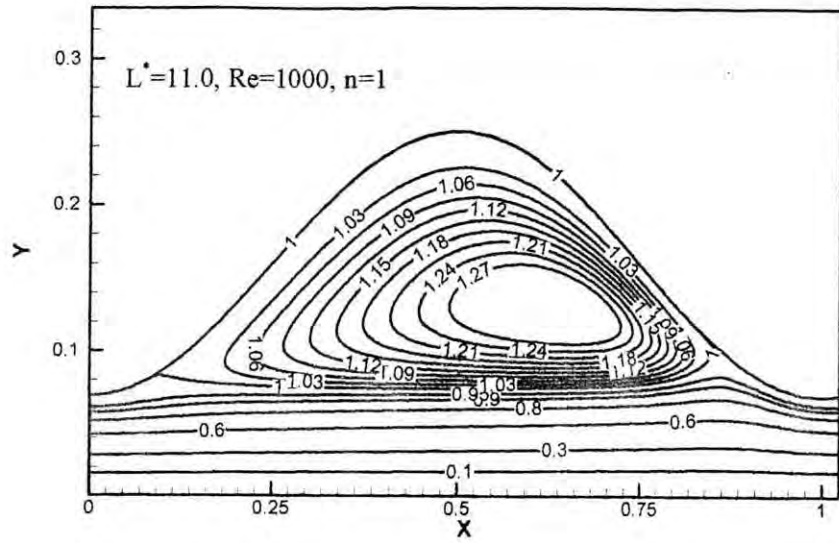


Fig.4.12 (g) Streamlines for $L^* = 11.0$, $Re = 800$, $n = 1-4$



93

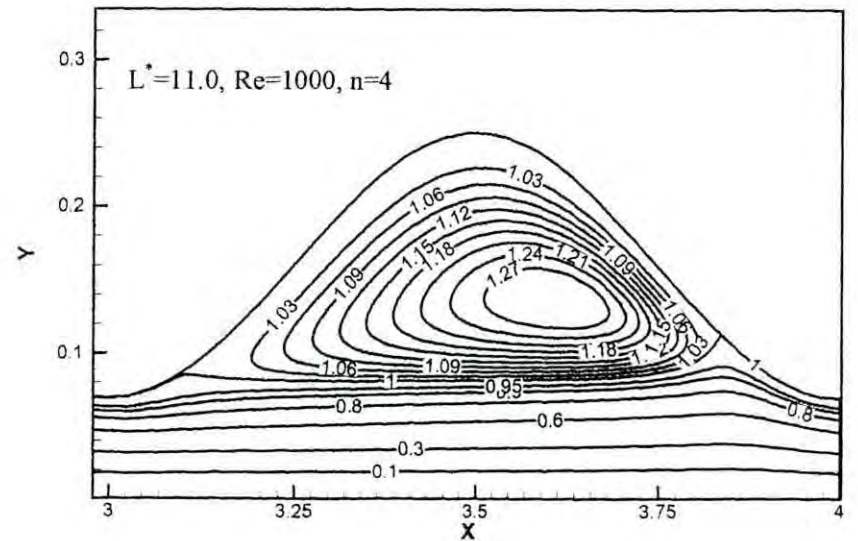
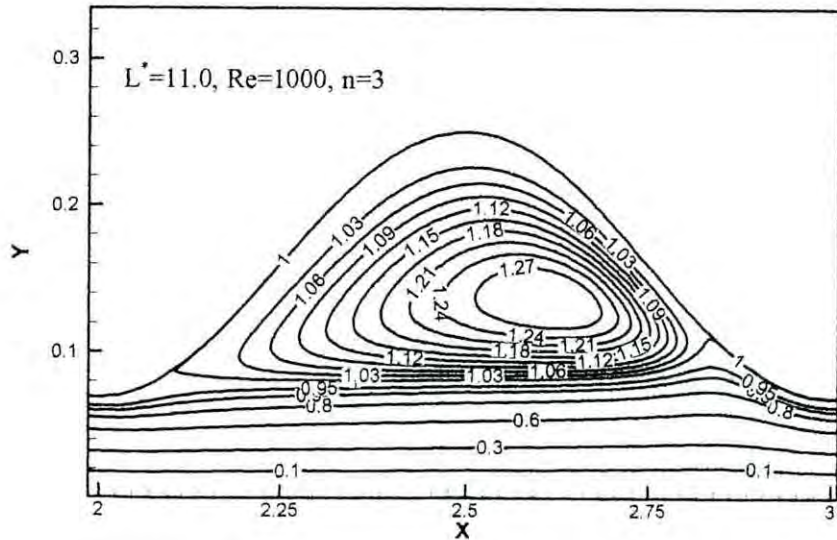
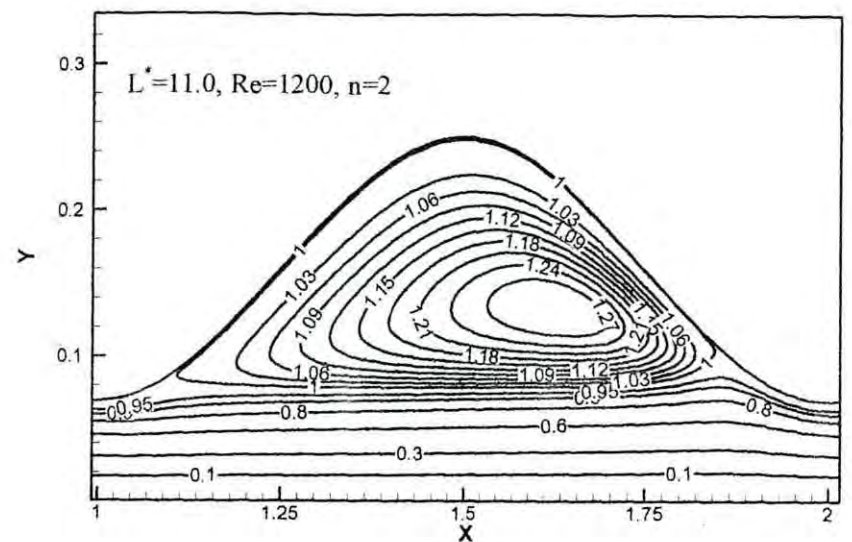
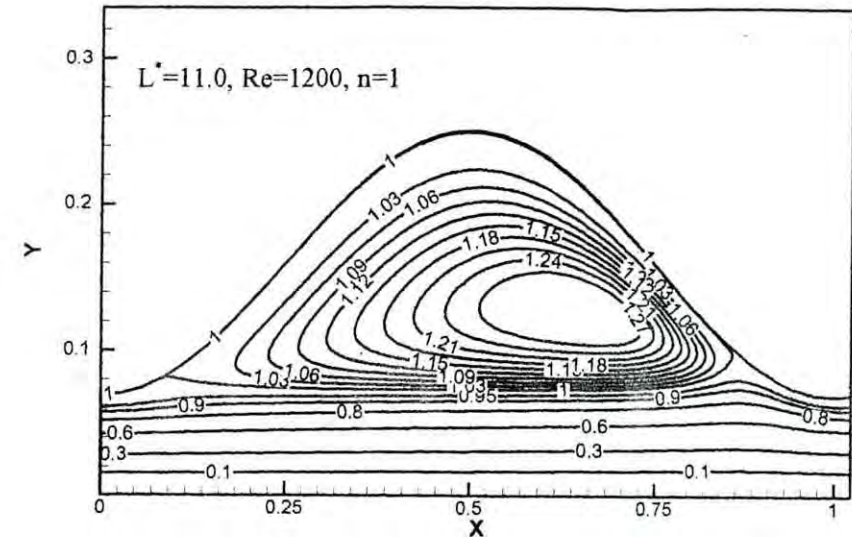


Fig.4.12 (h) Streamlines for $L^* = 11.0, Re = 1000, n = 1-4$



94

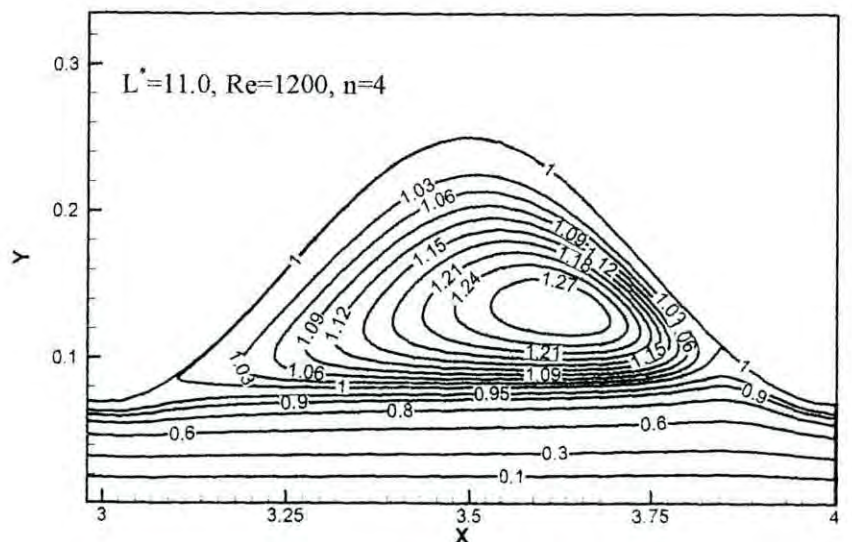
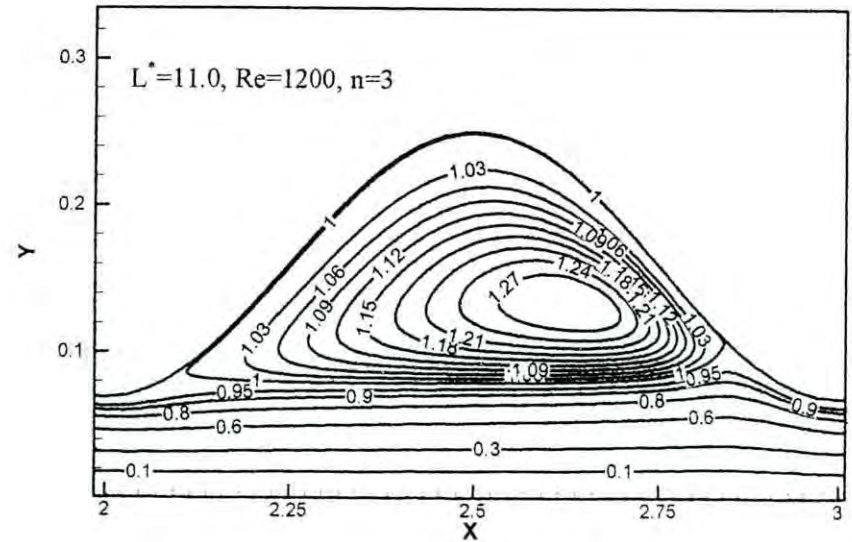


Fig.4.12 (i) Streamlines for $L^* = 11.0, Re = 1200, n = 1-4$

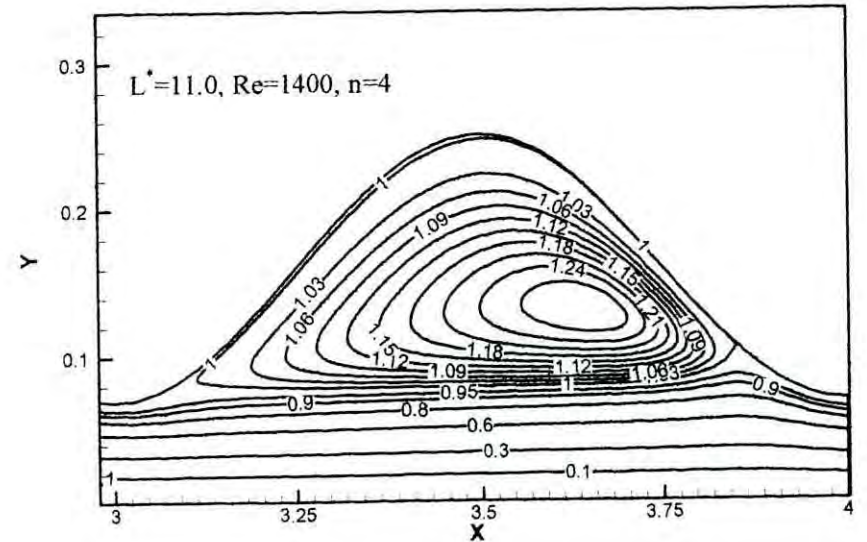
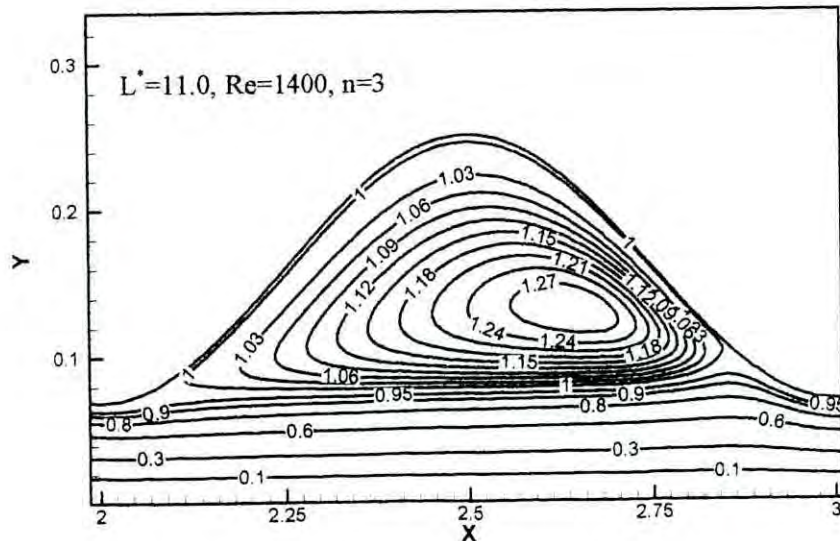
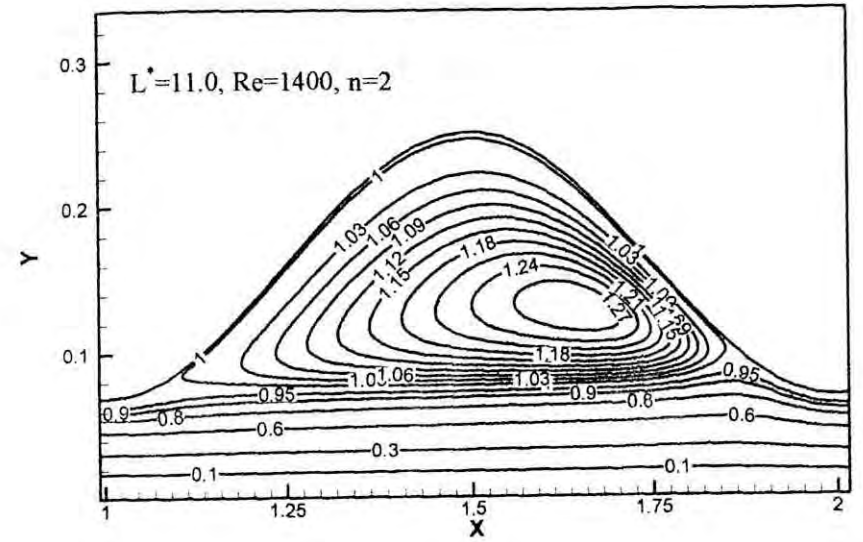
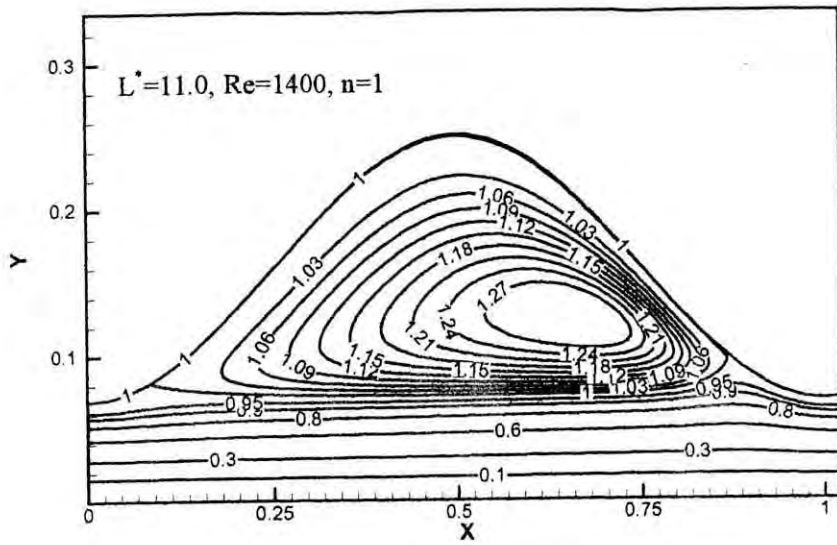


Fig.4.12 (j) Streamlines for $L^* = 11.0, Re = 1400, n = 1-4$

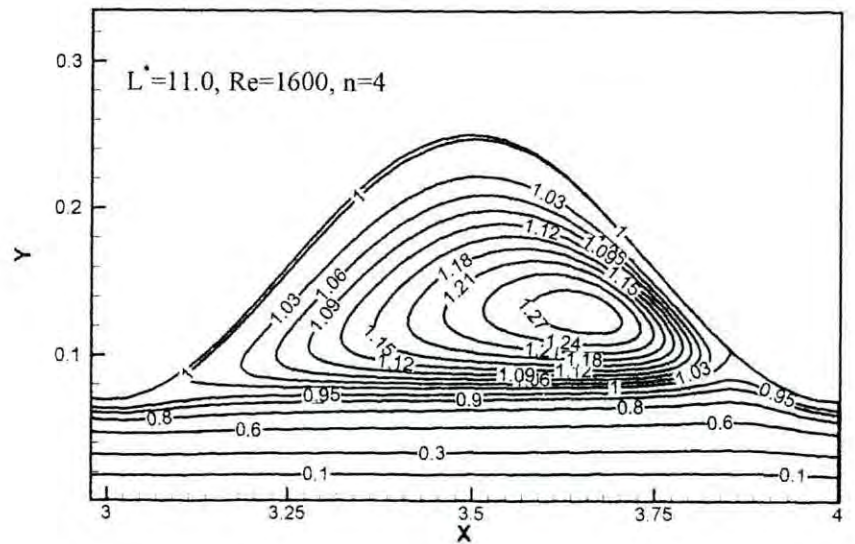
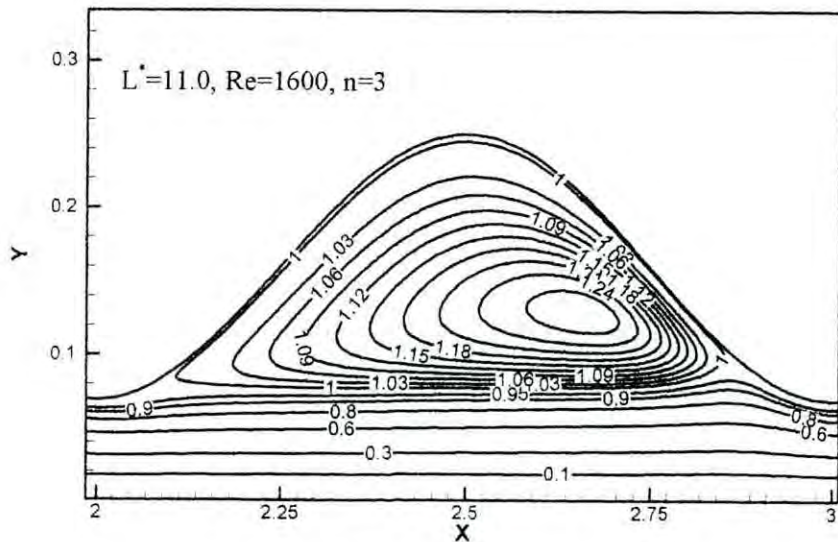
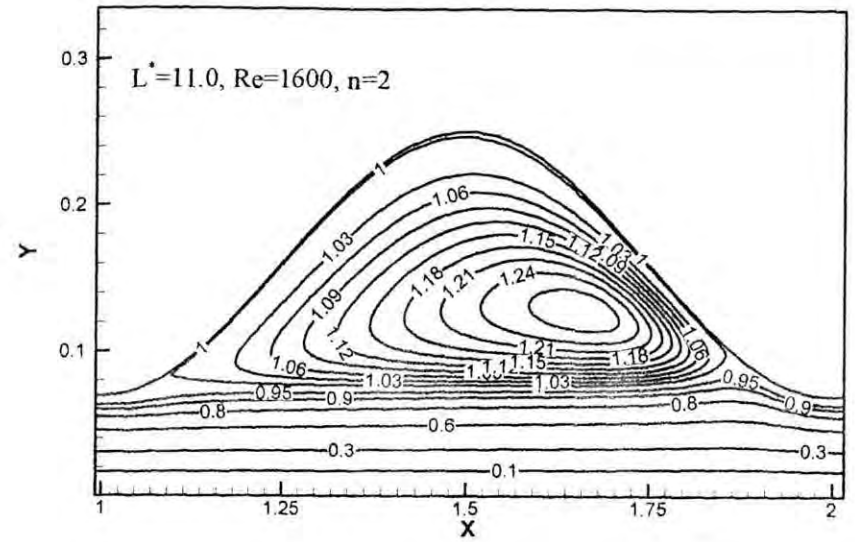
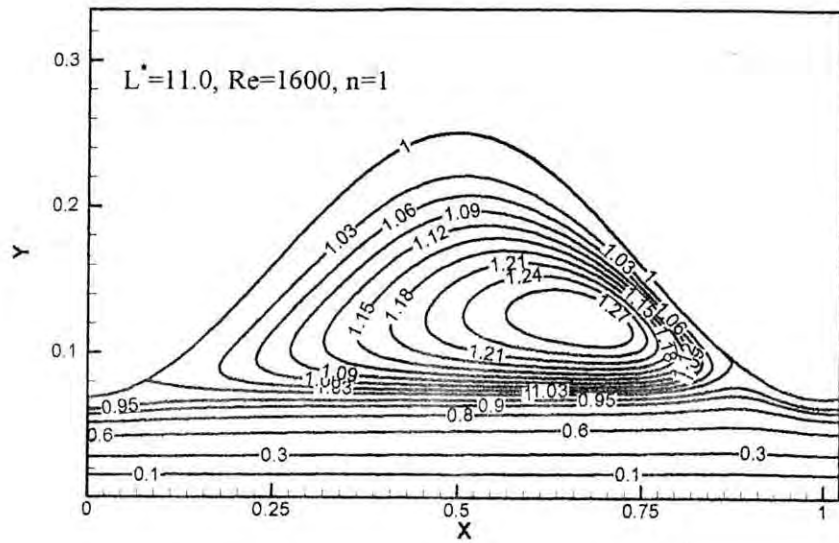
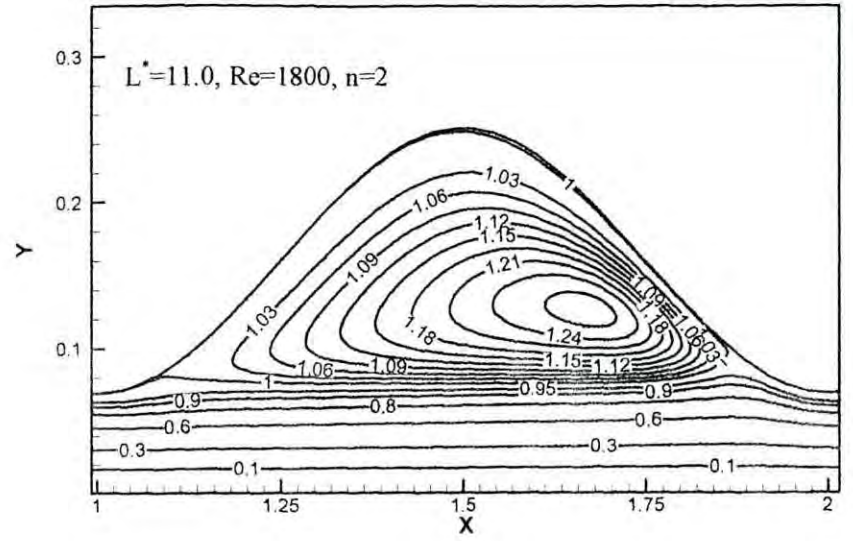
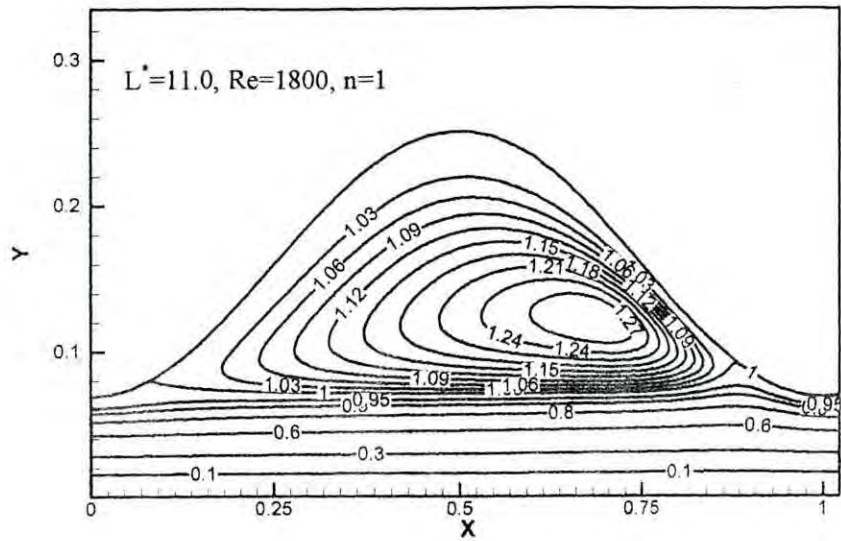


Fig.4.12 (k) Streamlines for $L^* = 11.0, Re = 1600, n = 1-4$



97

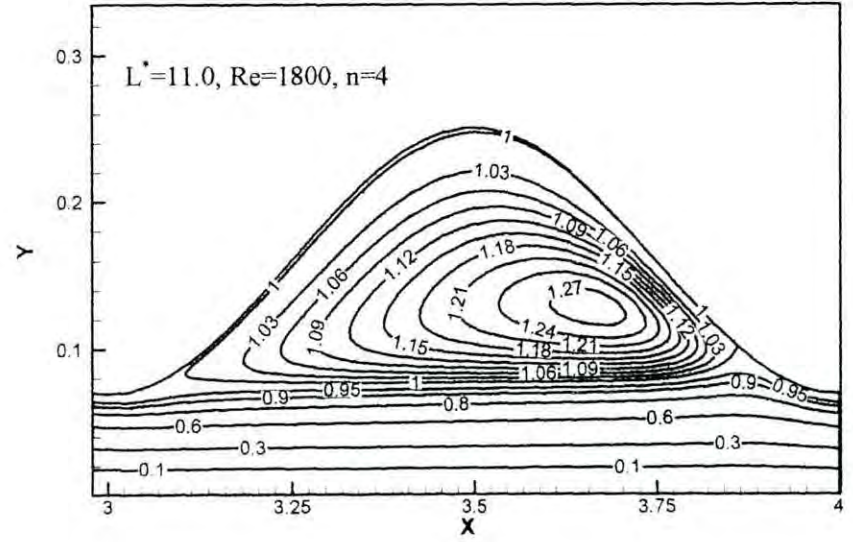
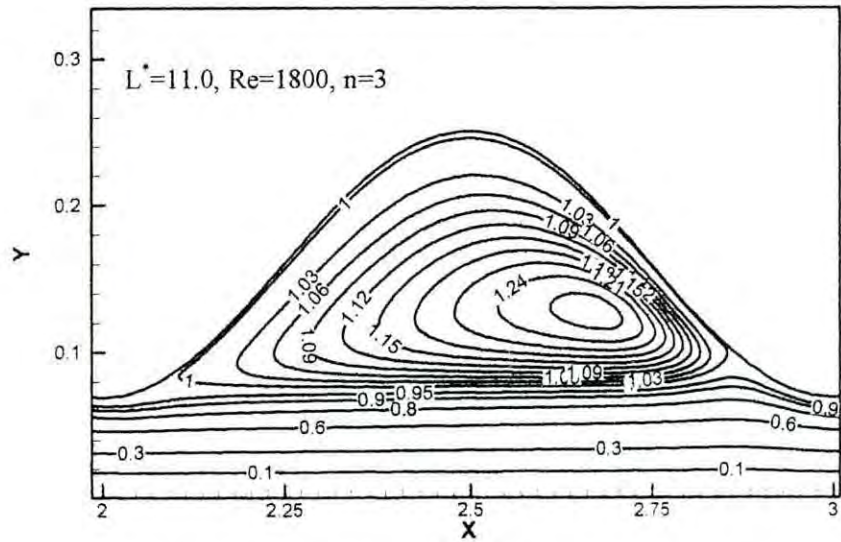
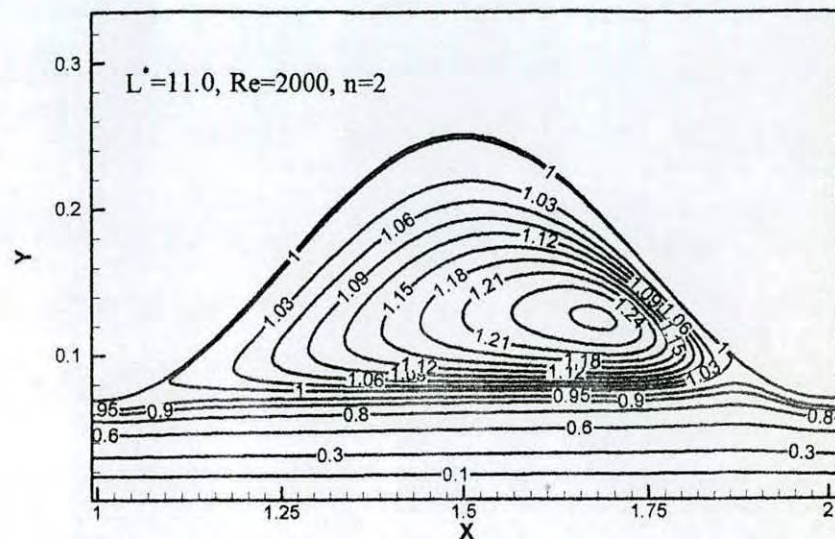
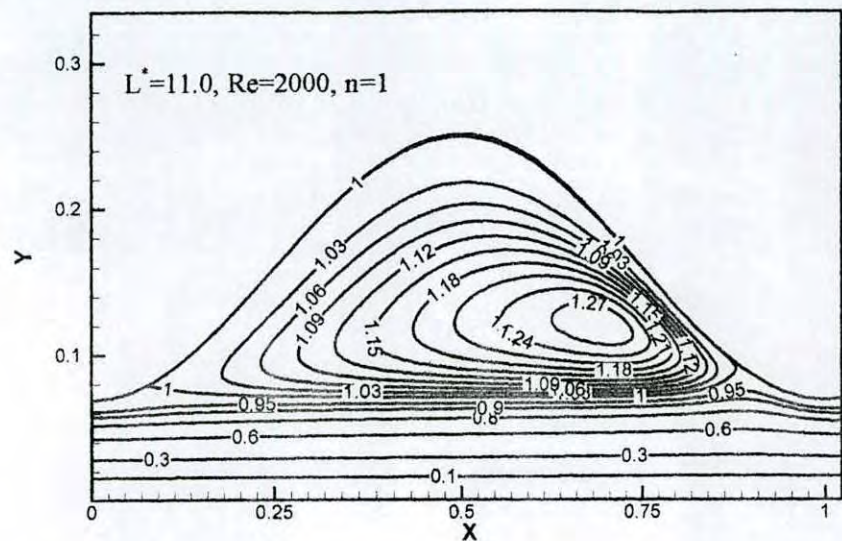


Fig.4.12 (l) Streamlines for $L^* = 11.0, Re = 1800, n = 1-4$



86

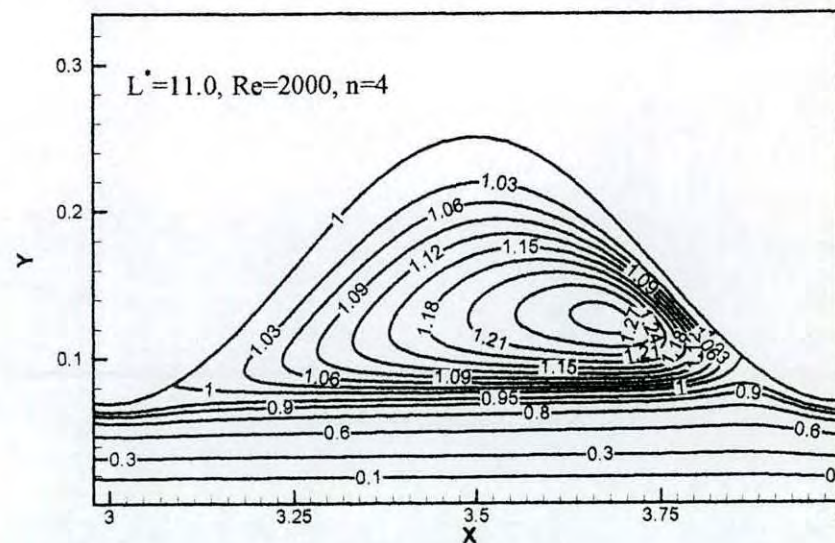
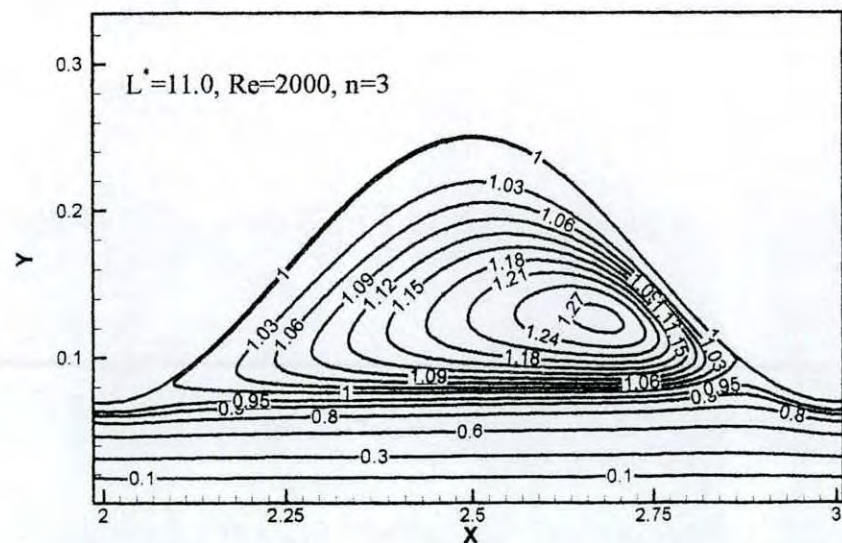


Fig.4.12 (m) Streamlines for $L^* = 11.0$, $Re = 2000$, $n = 1-4$

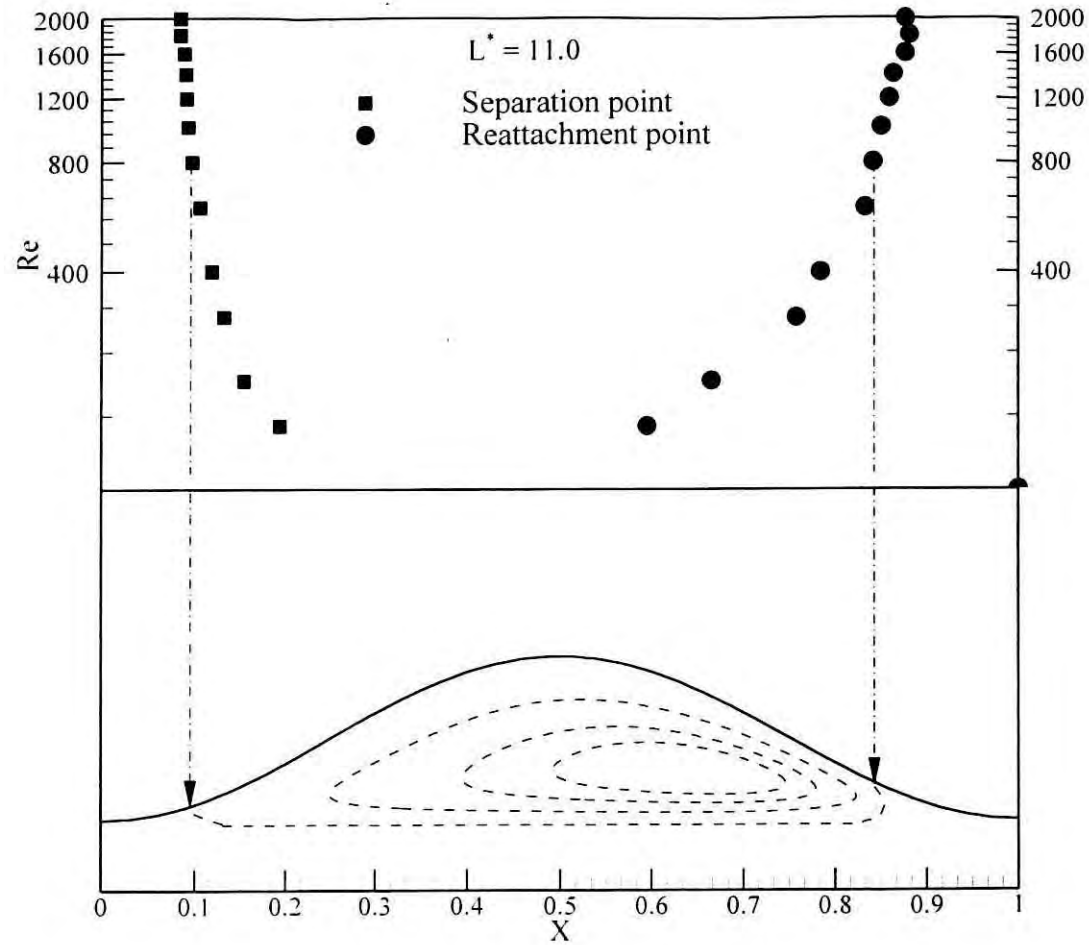


Fig. 4.13 Variation of location of separation and reattachment points on wavy wall with Reynolds number for $L^* = 11.0$

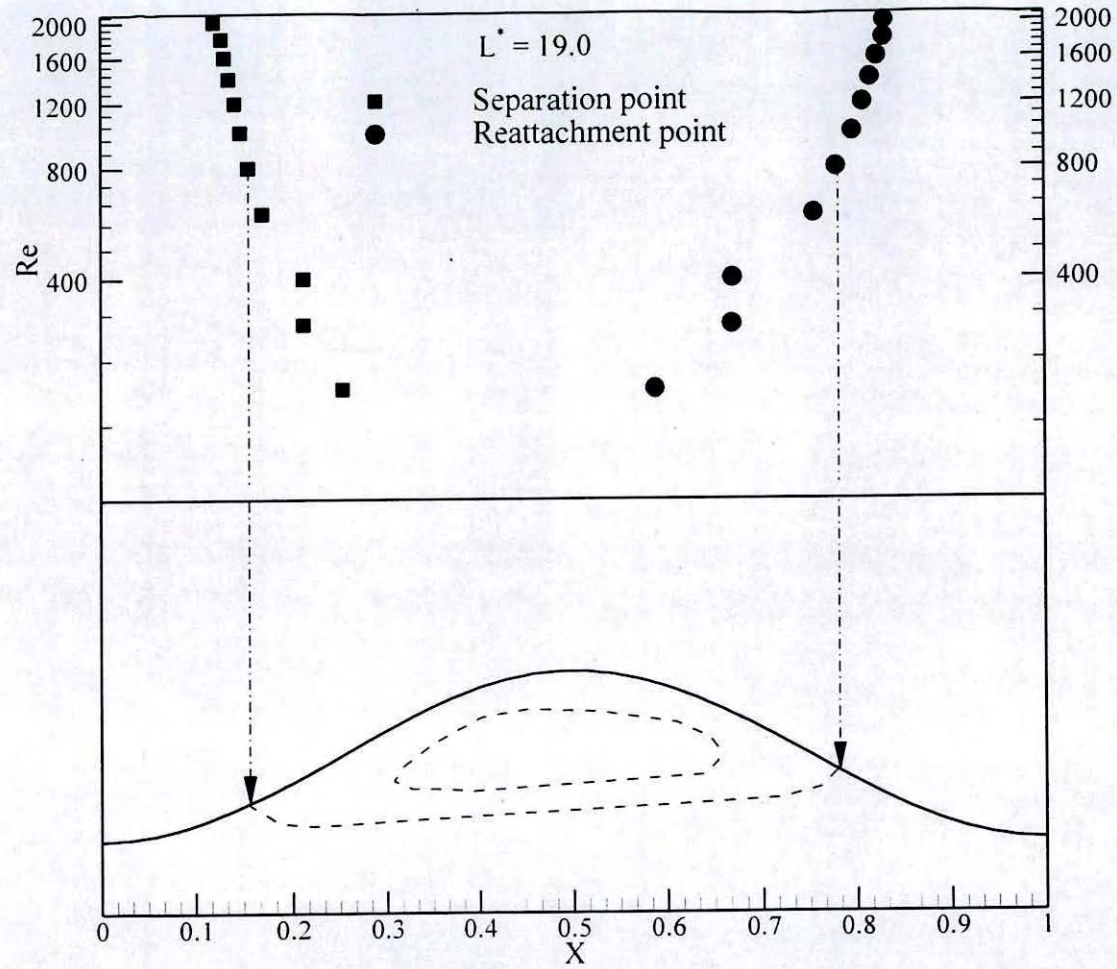


Fig. 4.14 Variation of location of separation and reattachment points on wavy wall with Reynolds number for $L^* = 19.0$

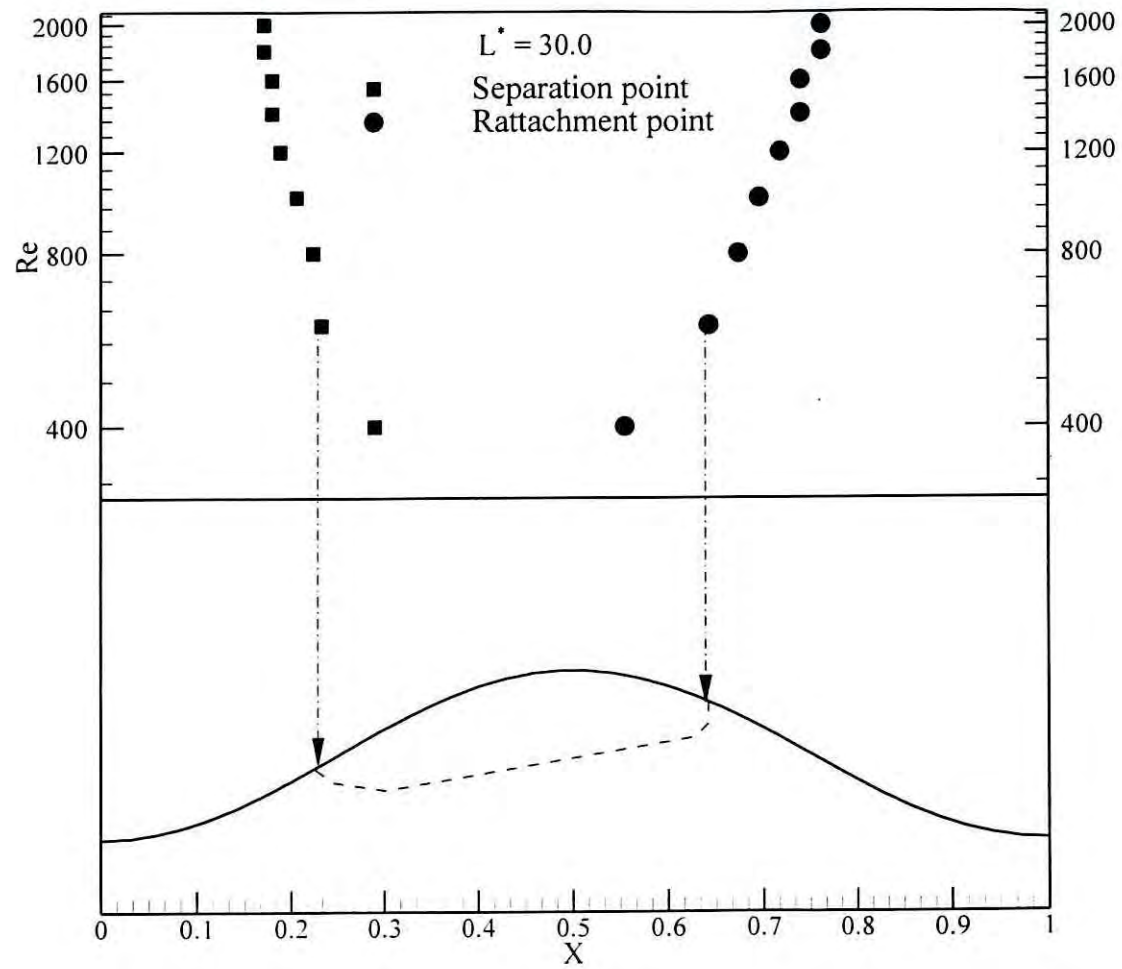


Fig. 4.15 Variation of location of separation and reattachment points on wavy wall with Reynolds number for $L^* = 30.0$

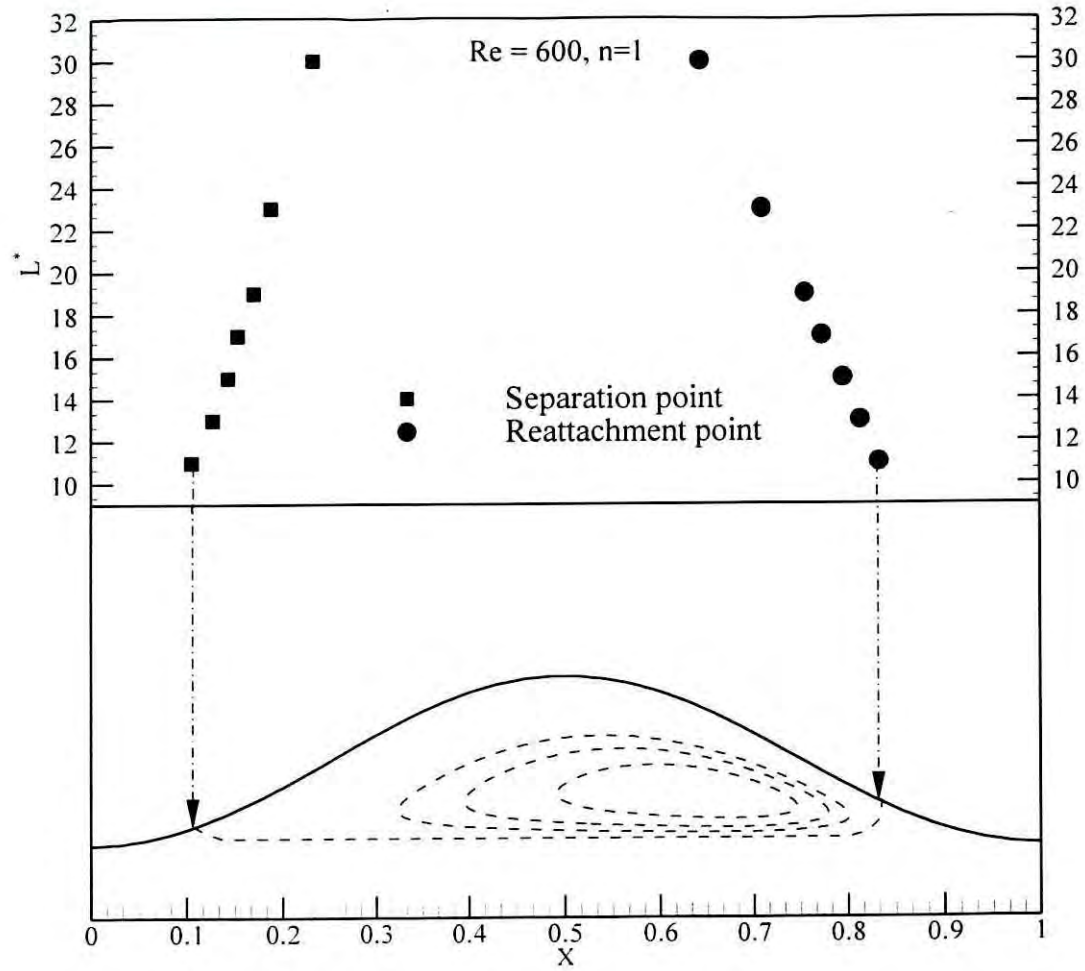


Fig. 4.16 Variation of location of separation and reattachment points on wavy wall with L^* at $Re=600$

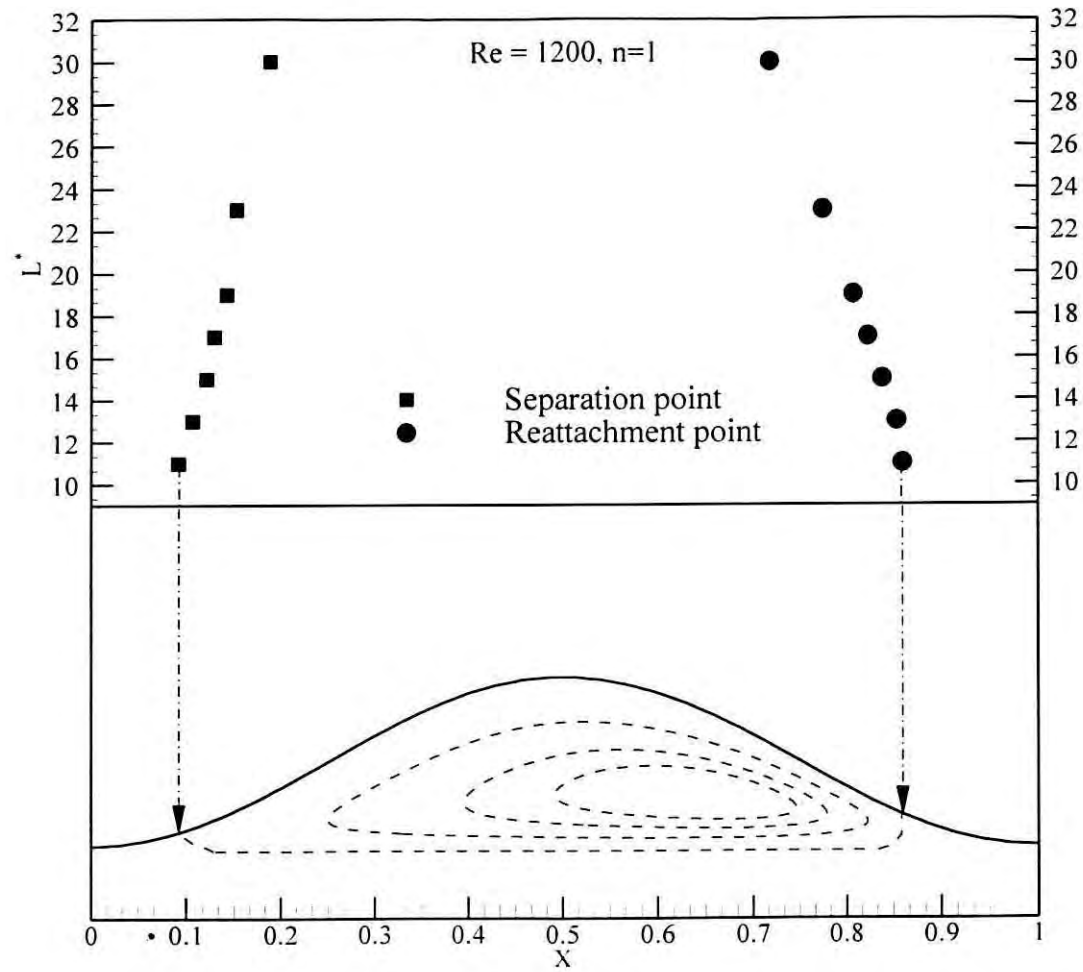


Fig. 4.17 Variation of location of separation and reattachment points on wavy wall with L^* at $Re=1200$

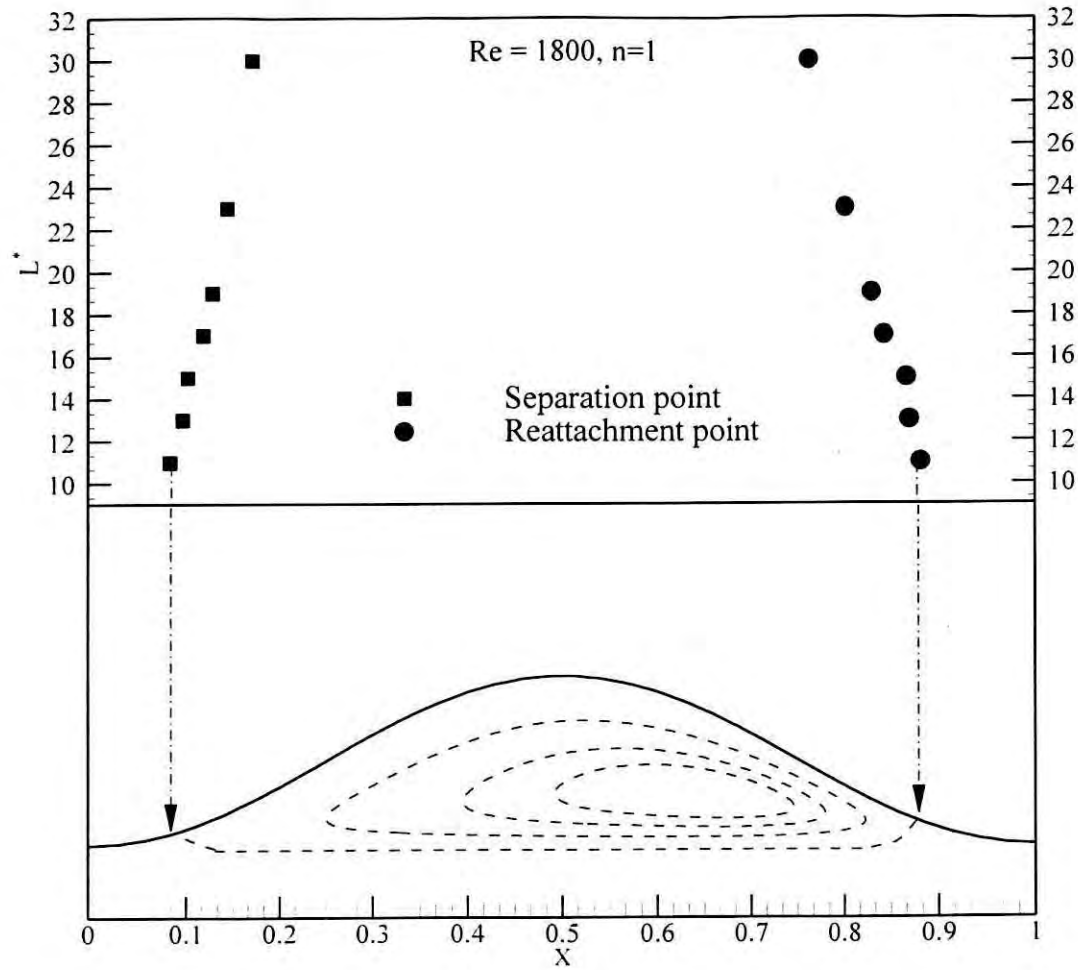


Fig. 4.18 Variation of location of separation and reattachment points on wavy wall with L^* at $Re=1800$

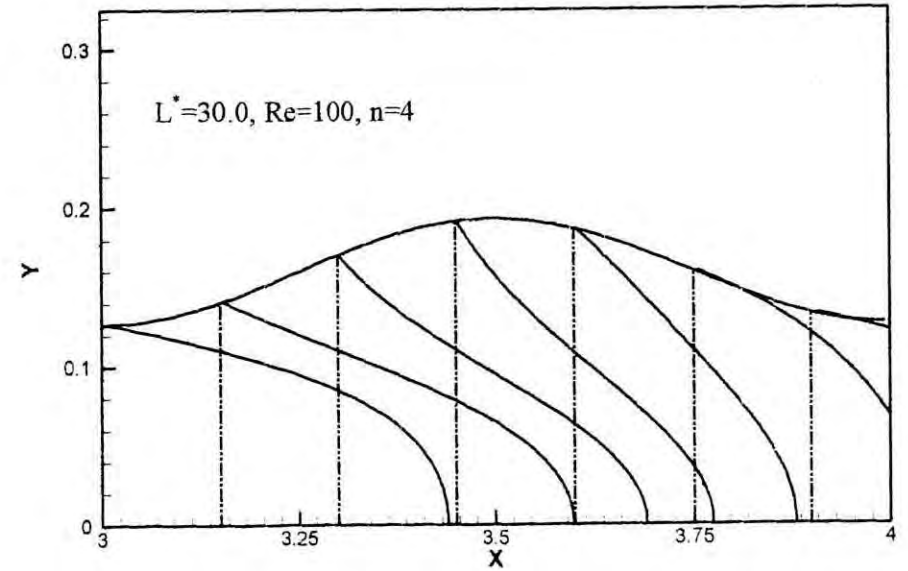
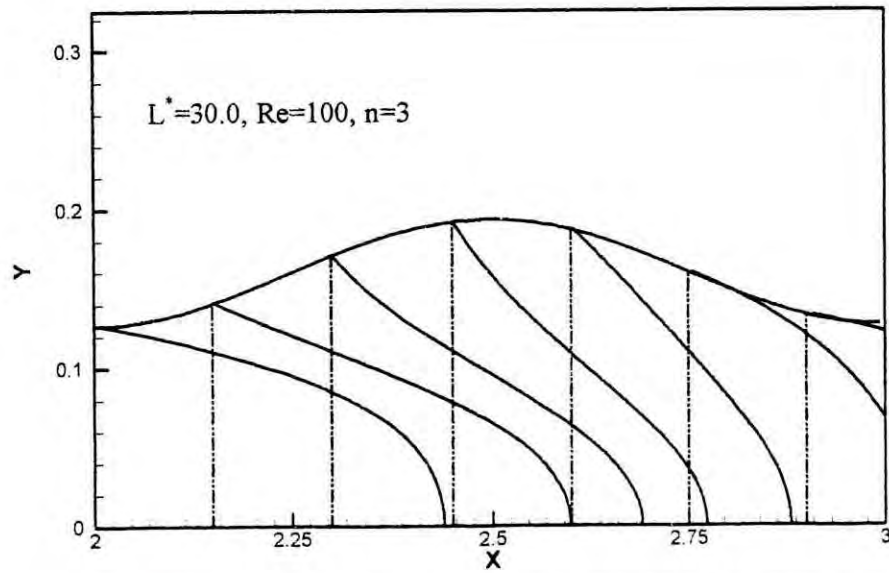
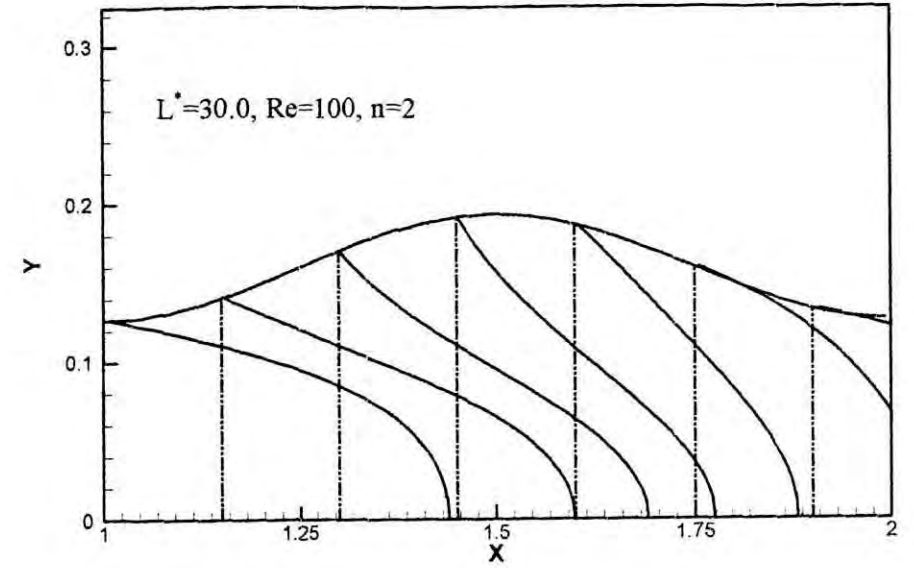
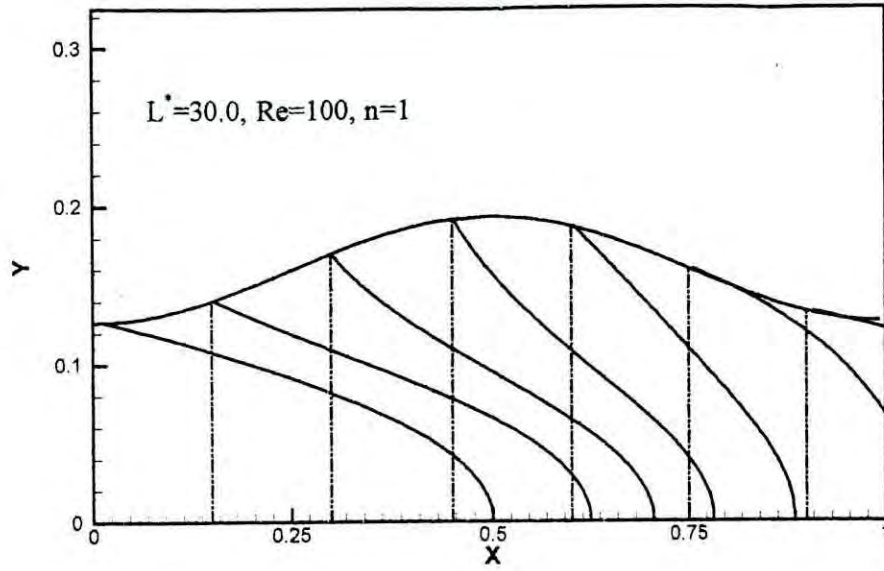
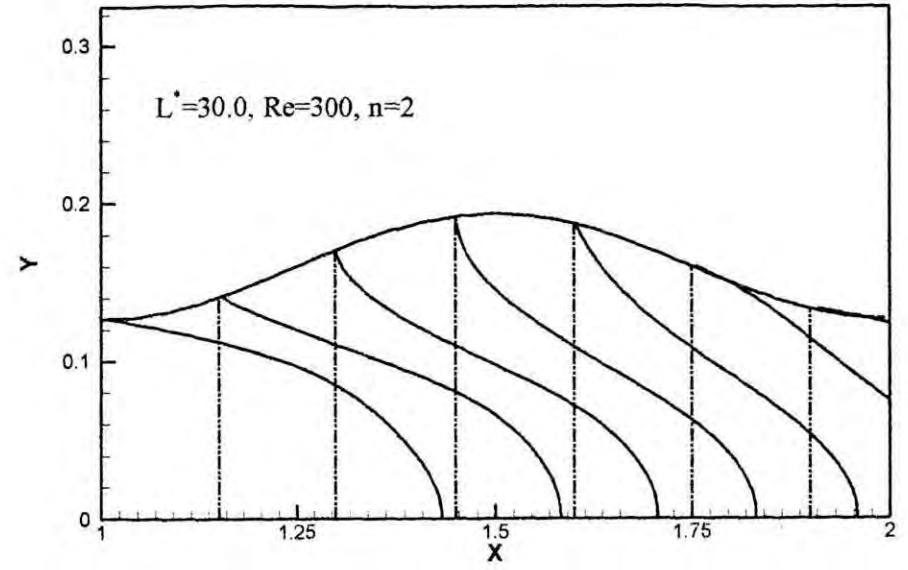
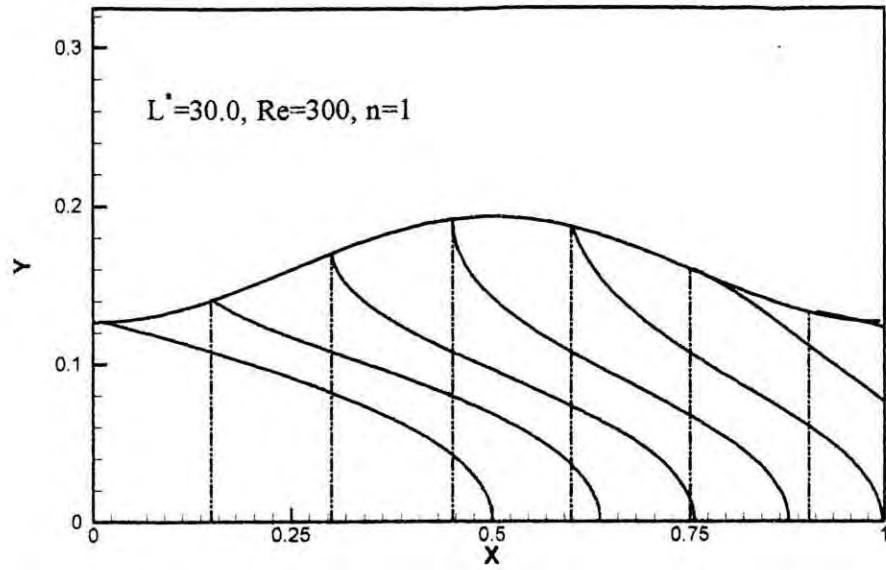


Fig.4.19 (a) Axial velocity profiles for $L^* = 30.0$, $Re = 100$, $n = 1-4$



106

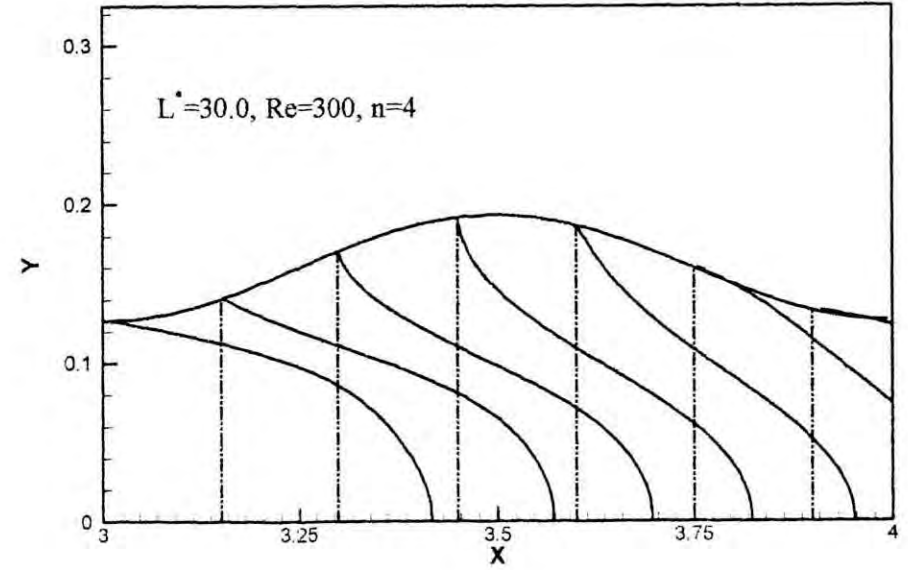
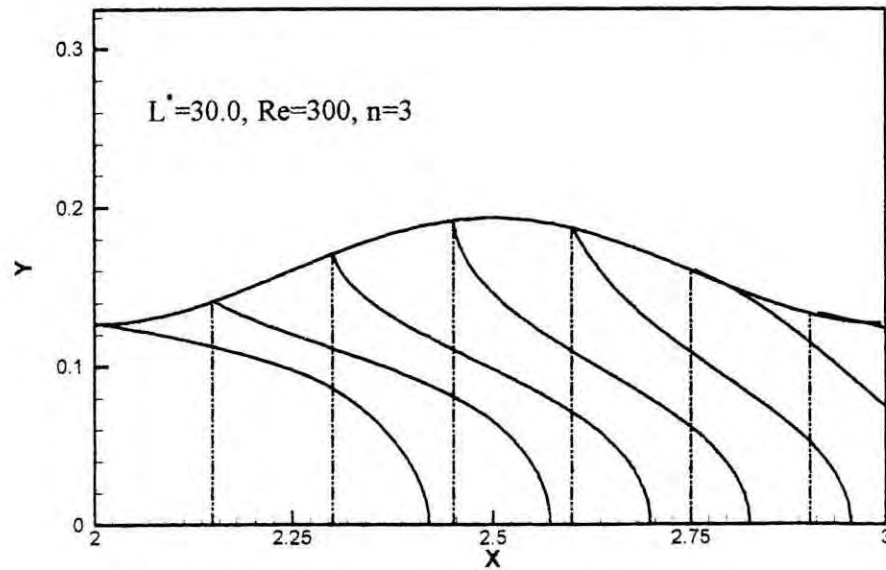


Fig.4.19 (b) Axial velocity profiles for $L^*=30.0, Re=300, n=1-4$

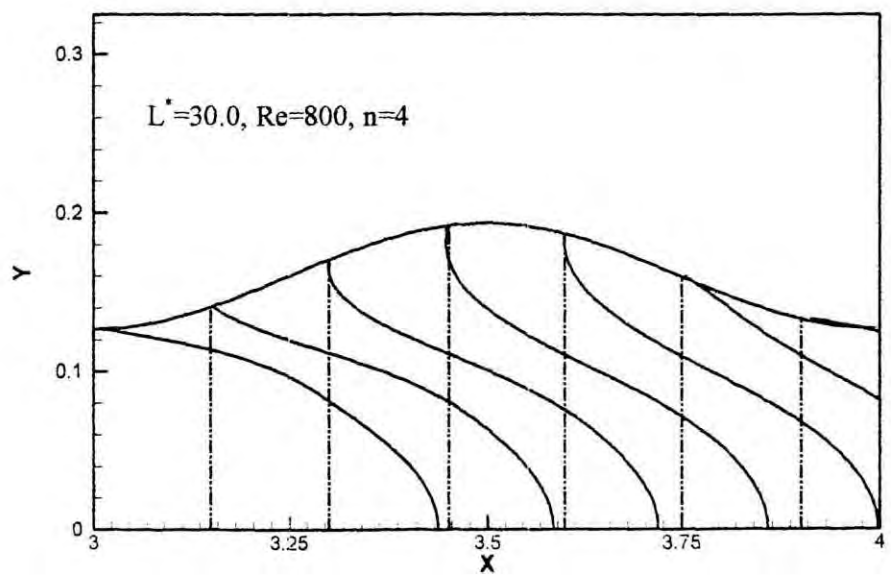
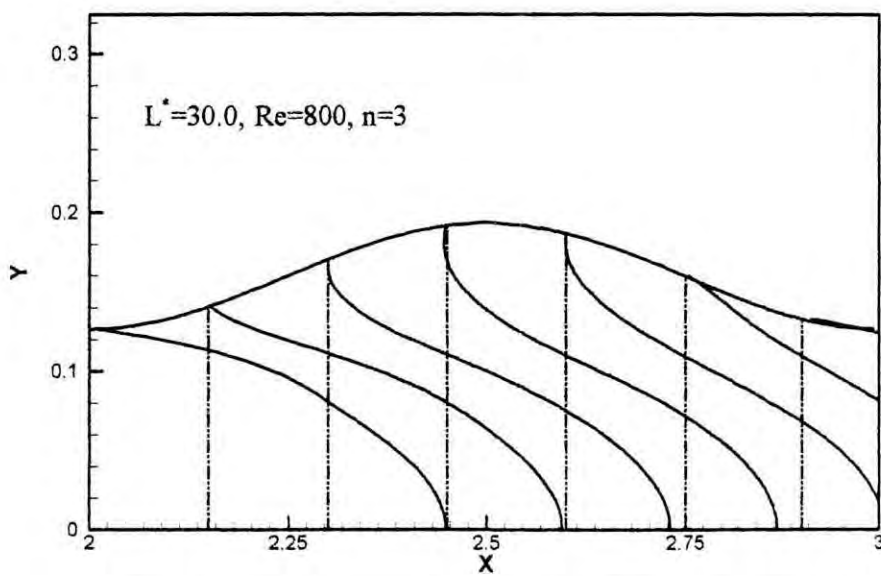
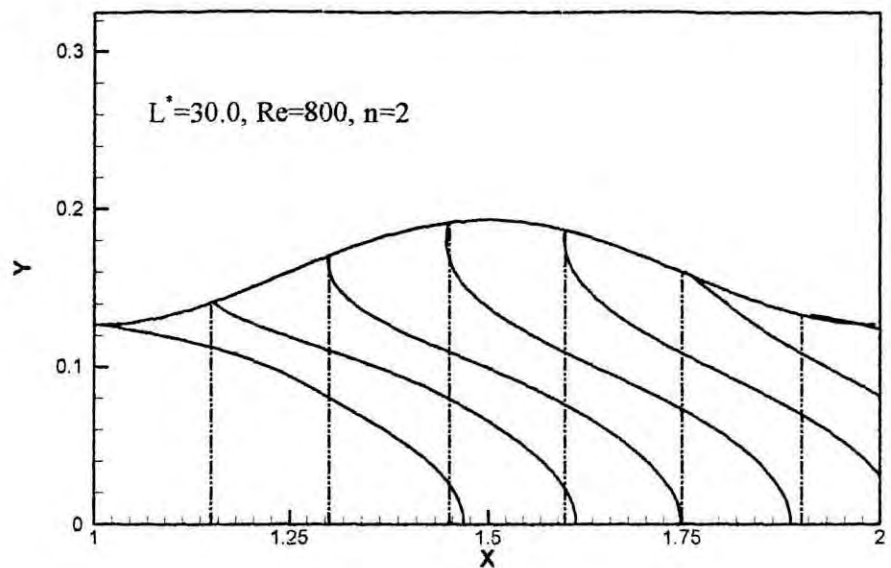
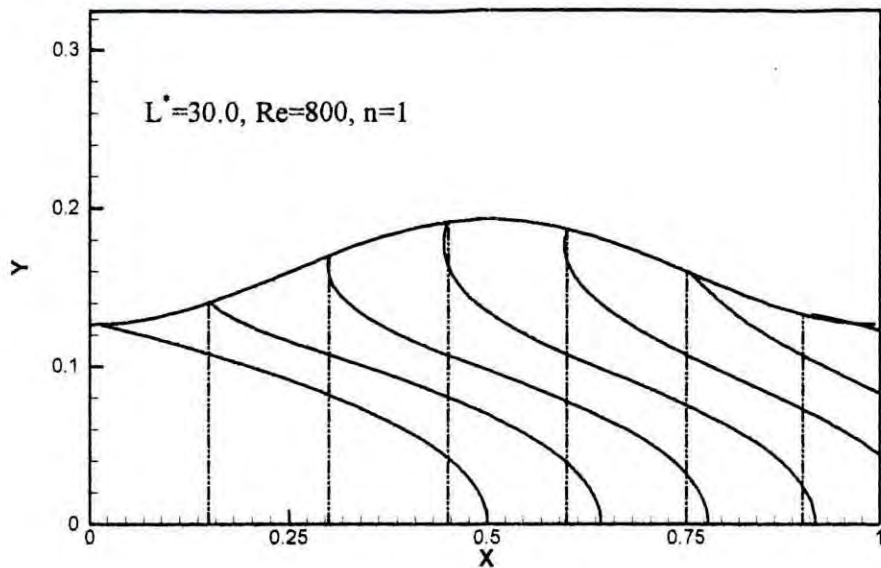


Fig.4.19 (c) Axial velocity profiles for $L^*=30.0$, $Re=800$, $n=1-4$

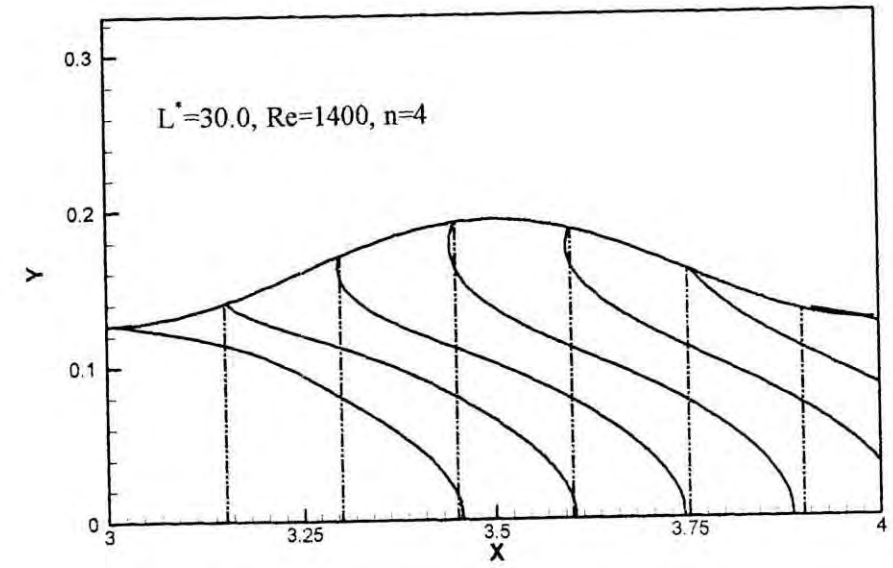
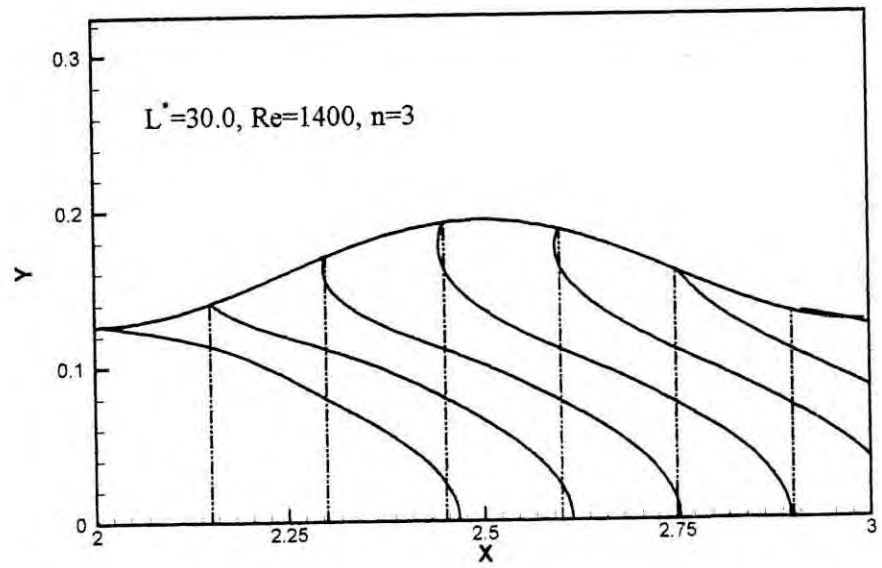
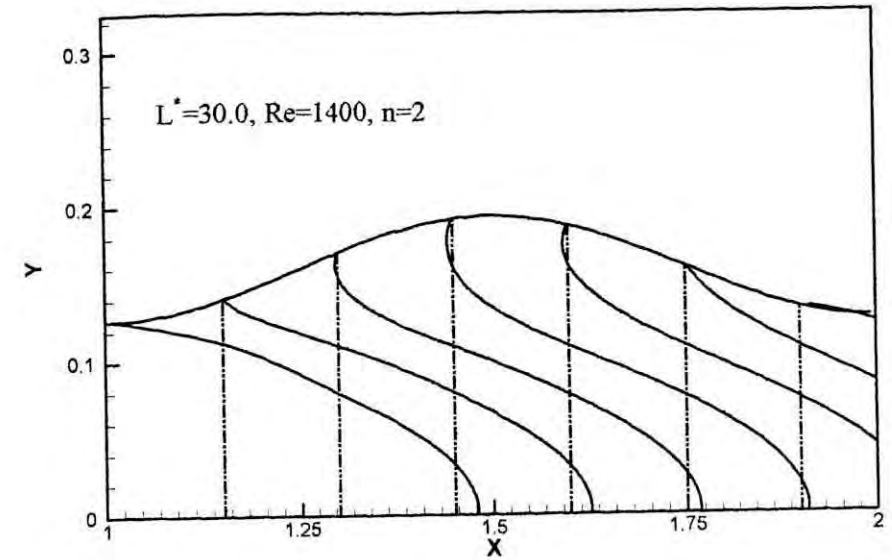
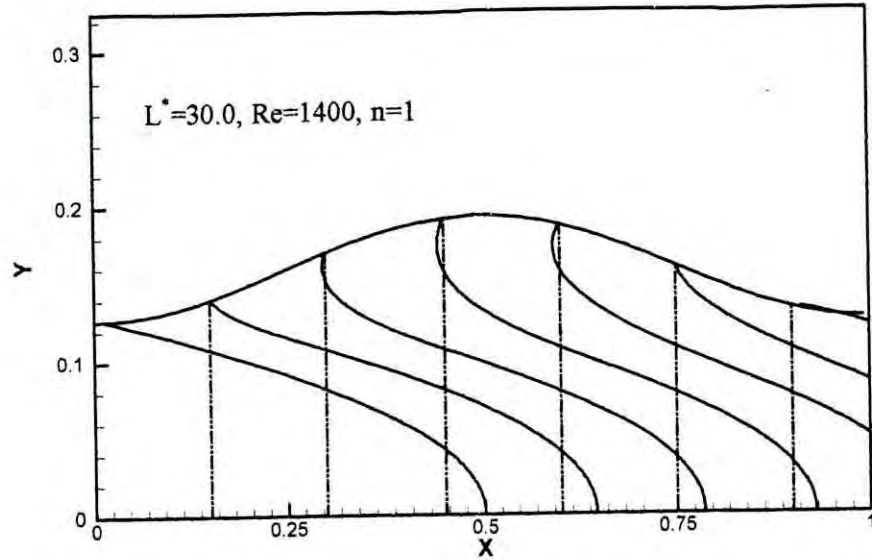
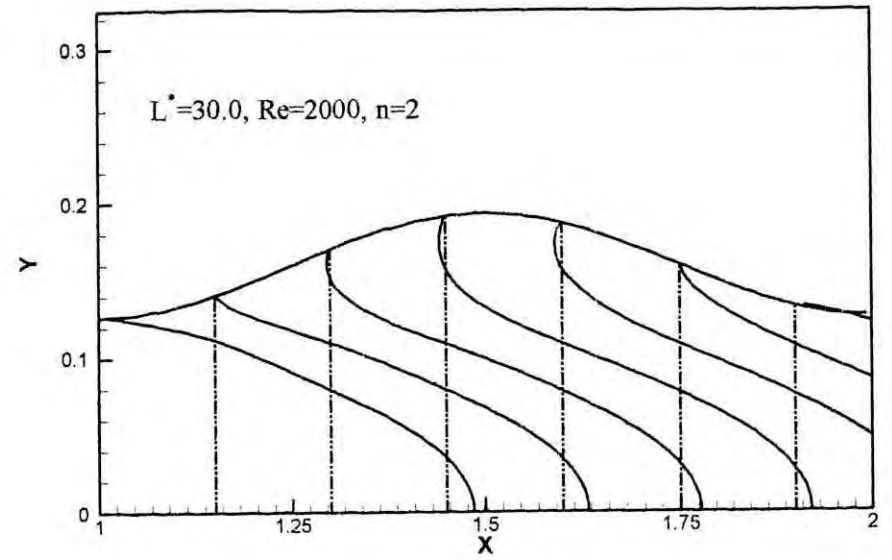
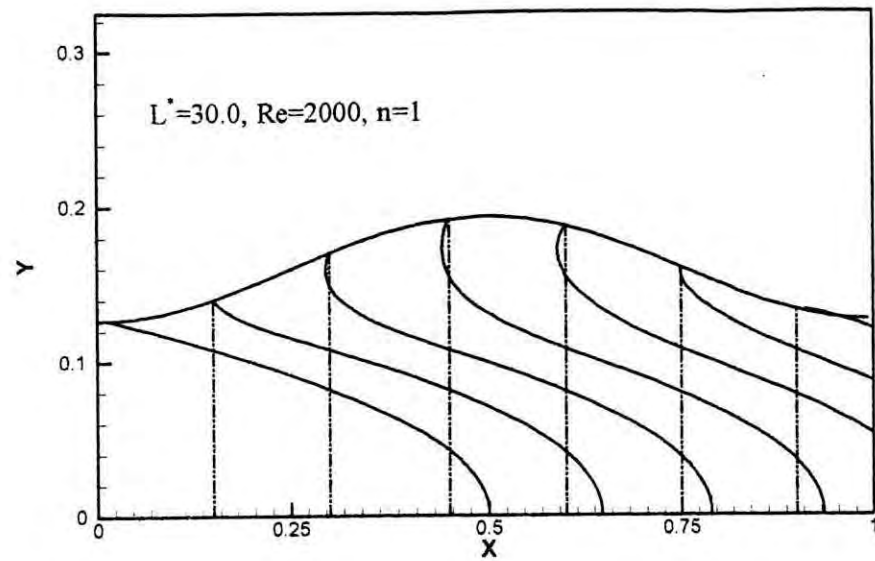


Fig.4.19 (d) Axial velocity profiles for $L^* = 30.0, Re = 1400, n = 1-4$



109

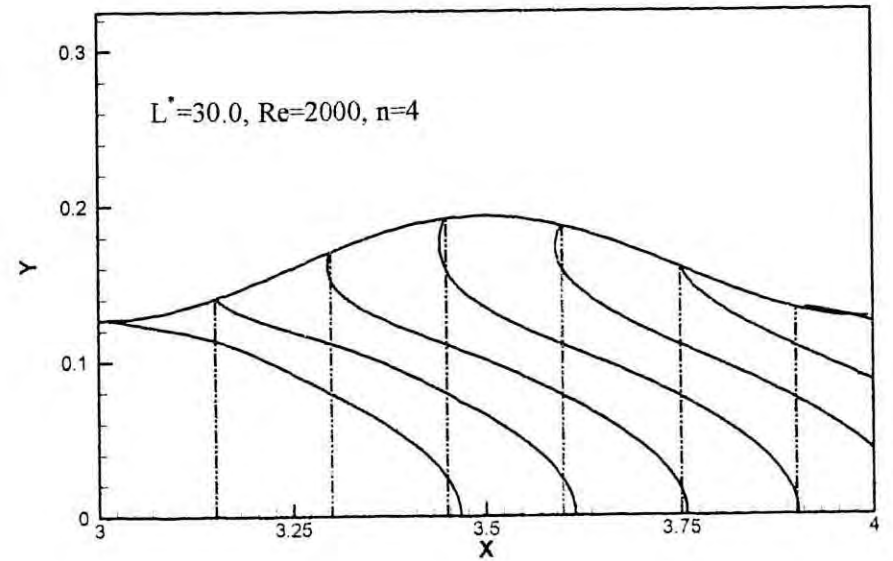
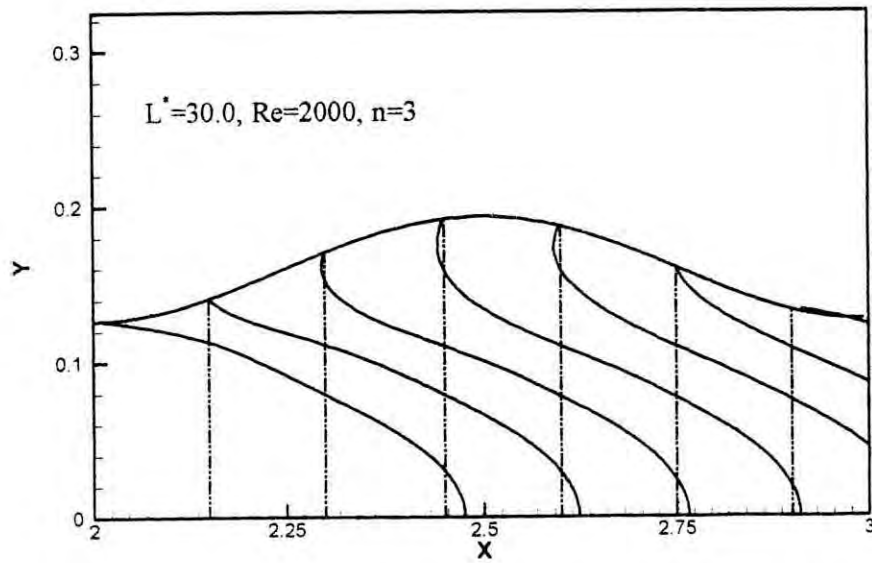
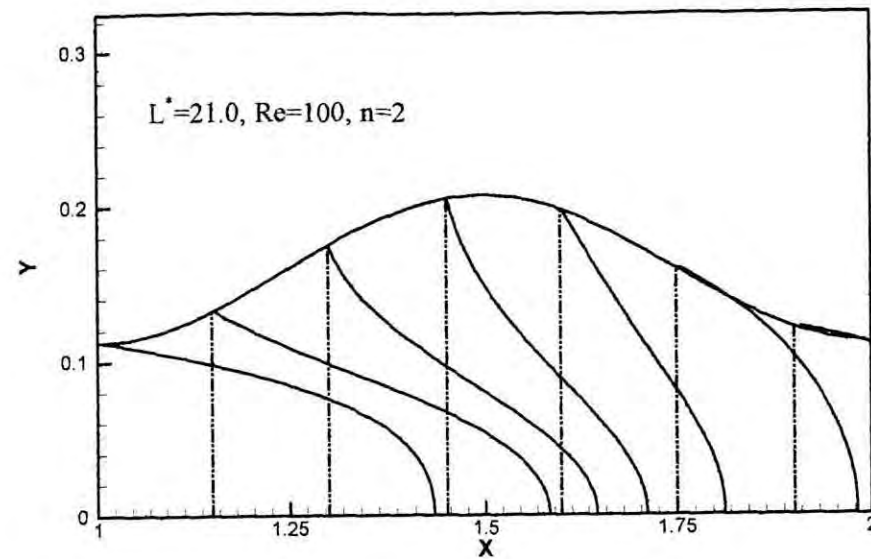
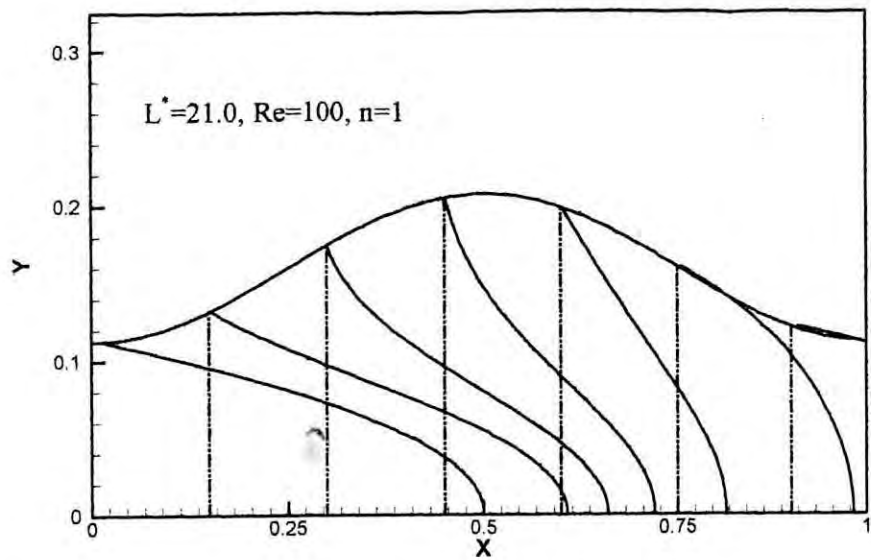


Fig.4.19 (e) Axial velocity profiles for $L^*=30.0, Re=2000, n=1-4$



011

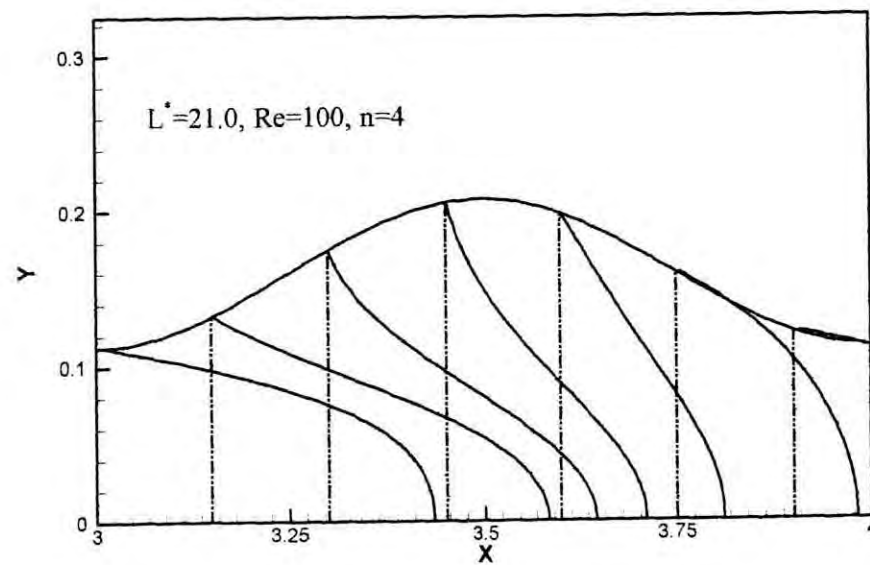
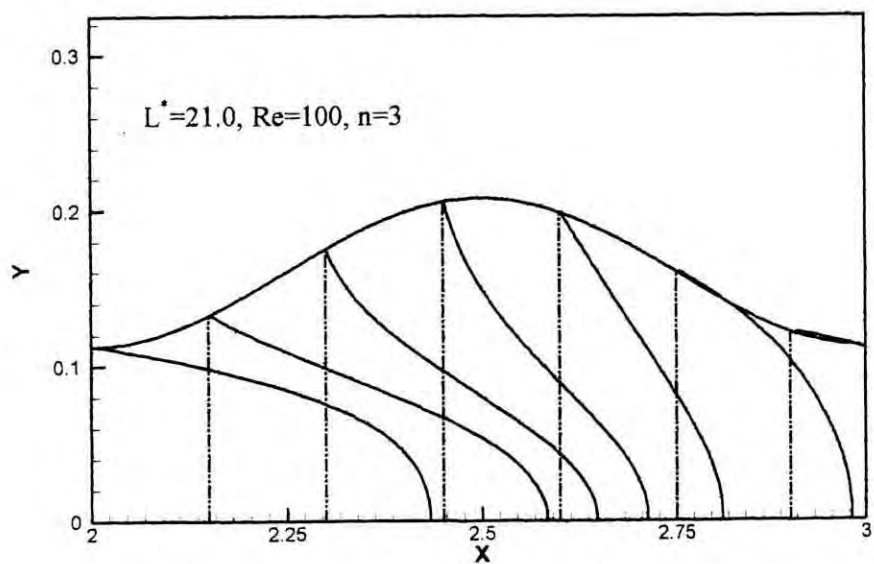
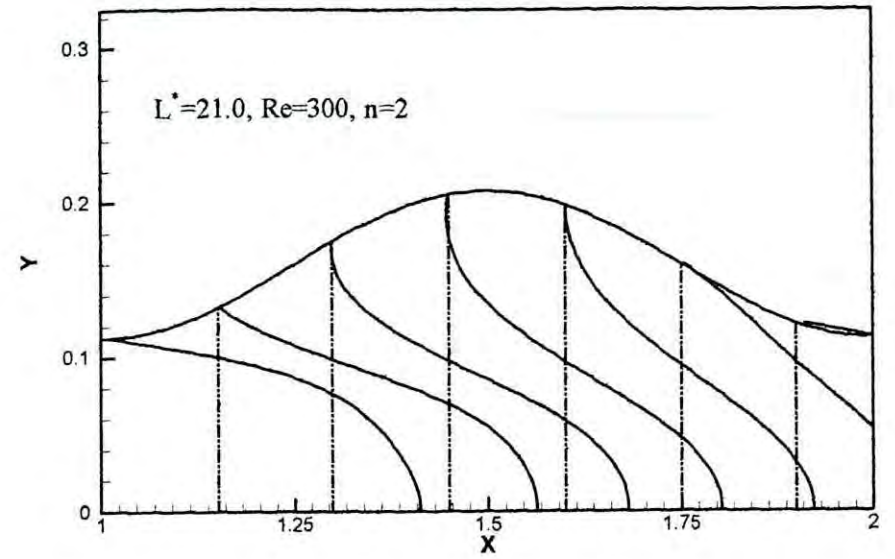
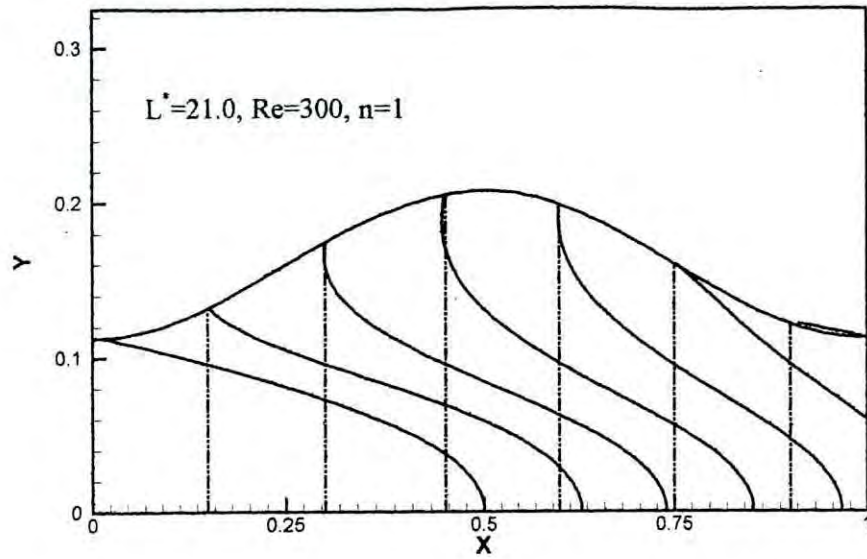


Fig.4.20 (a) Axial velocity profiles for $L^* = 21.0, Re = 100, n = 1-4$



111

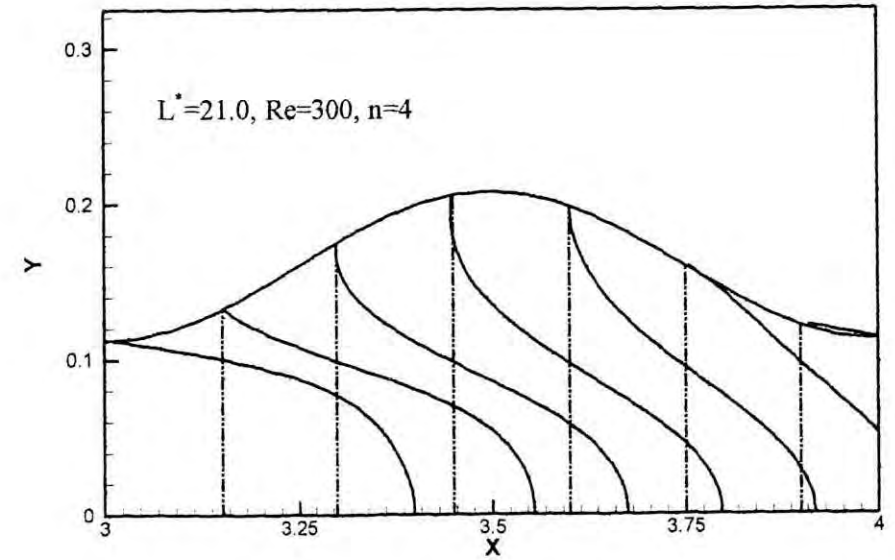
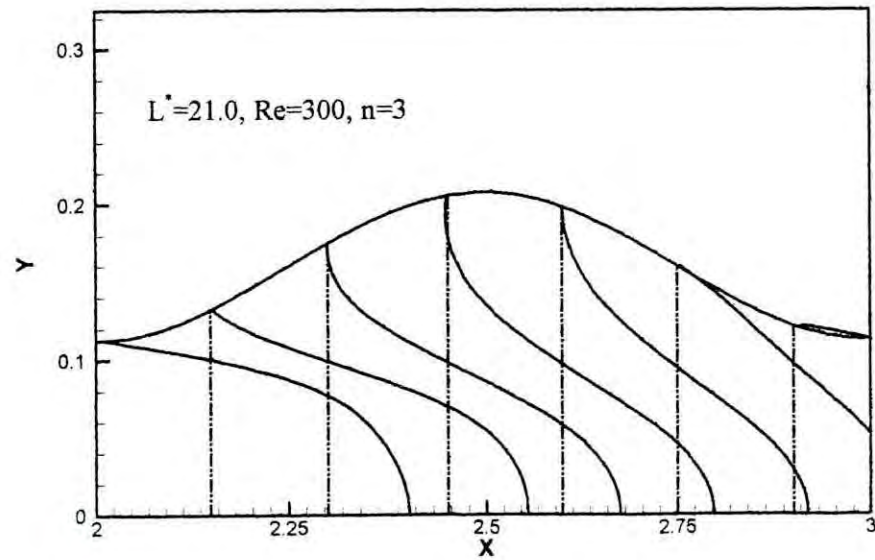
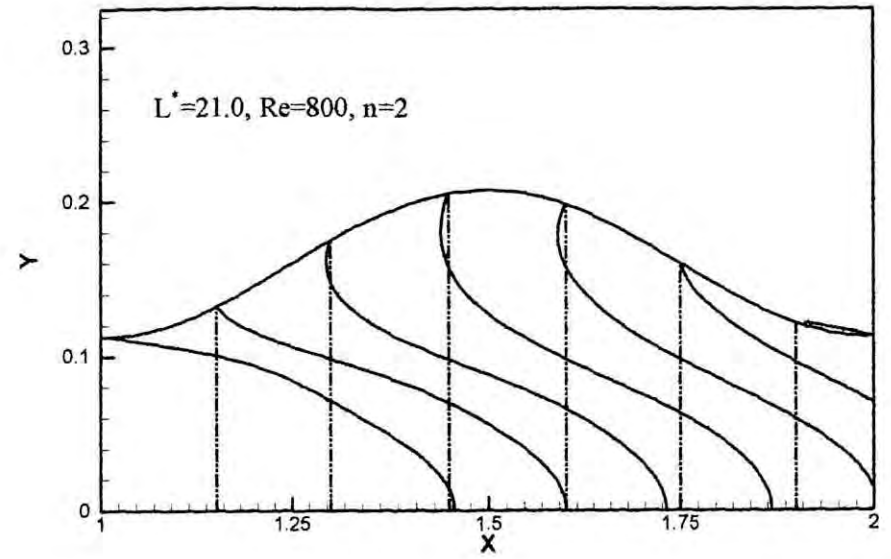
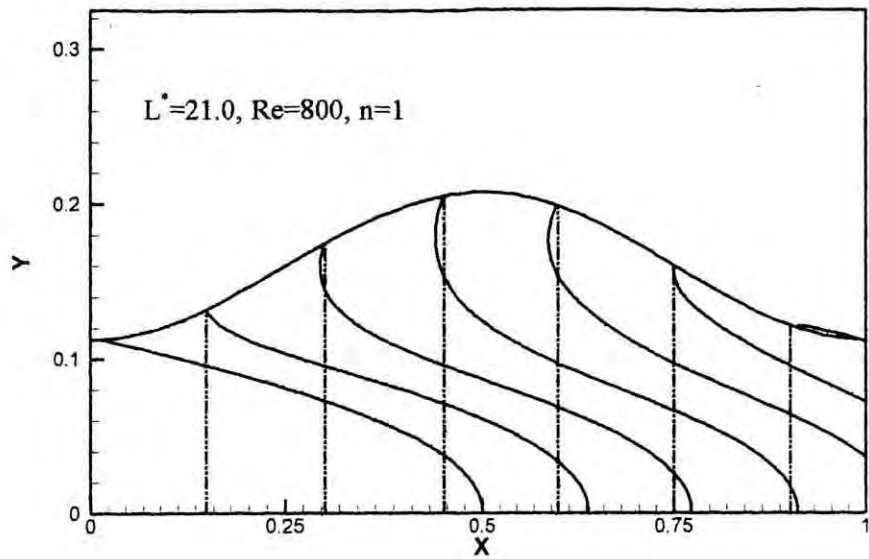


Fig.4.20 (b) Axial velocity profiles for $L^* = 21.0, Re = 300, n = 1-4$



112

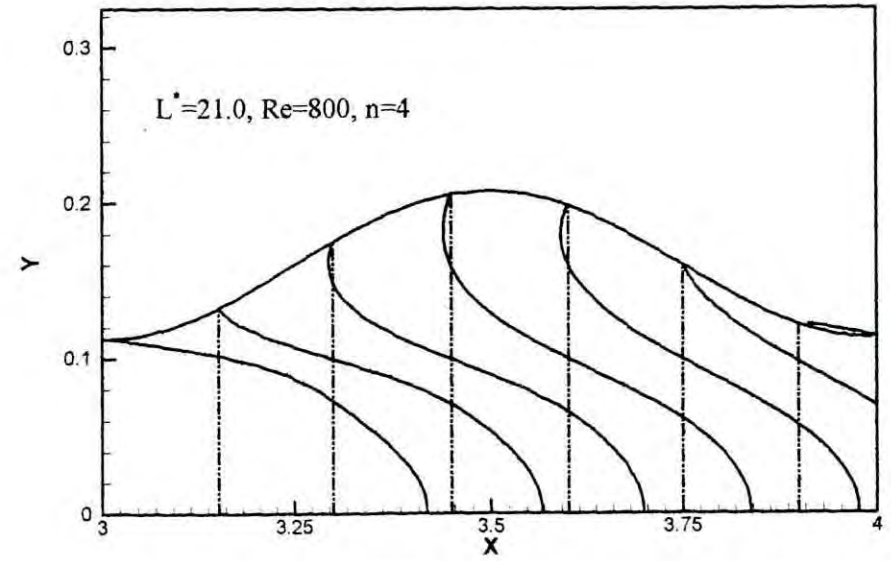
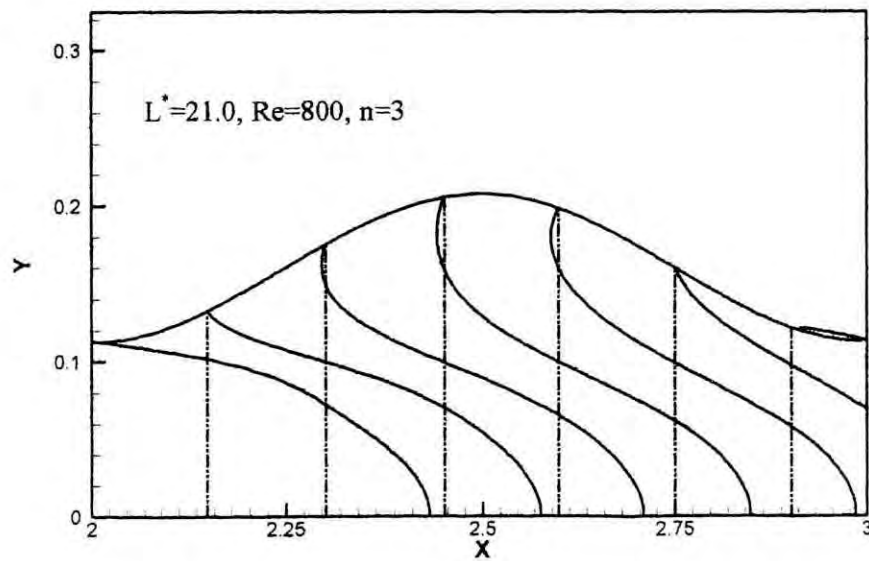
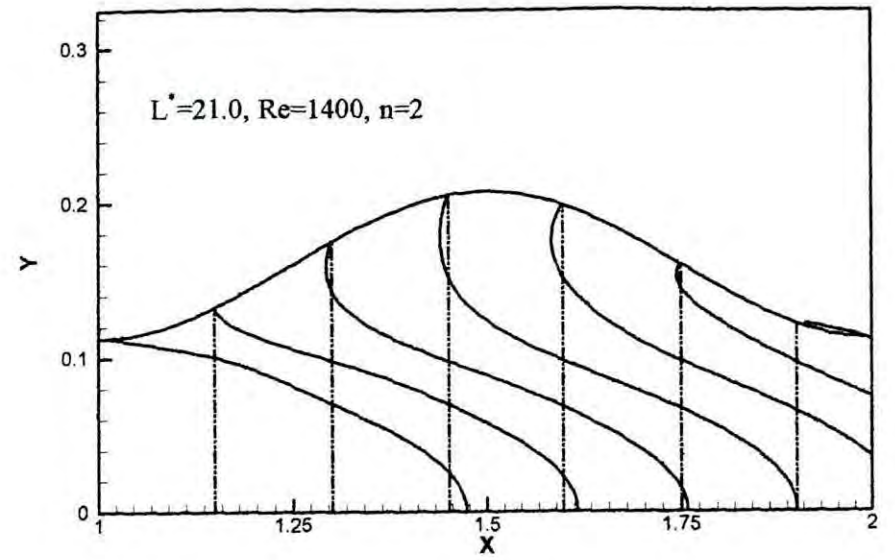
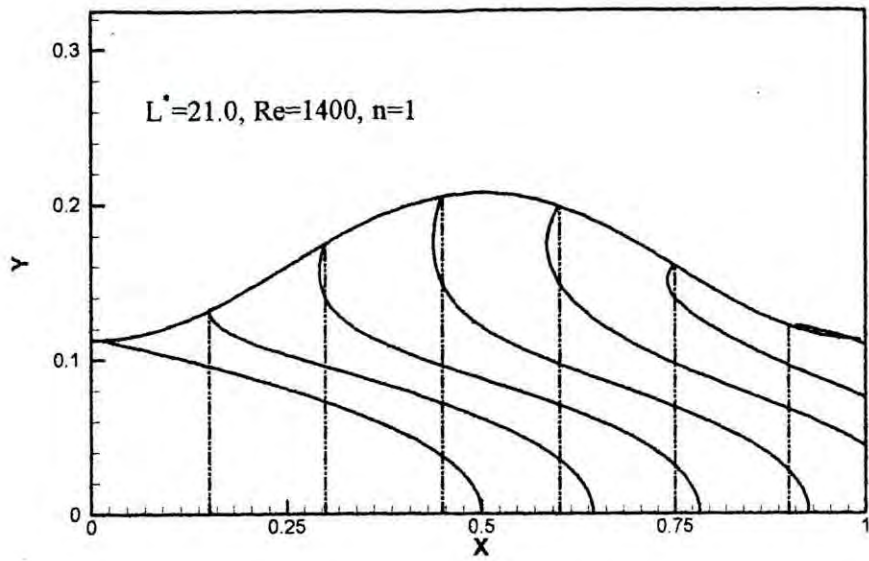


Fig.4.20 (c) Axial velocity profiles for $L^* = 21.0, Re = 800, n = 1-4$



113

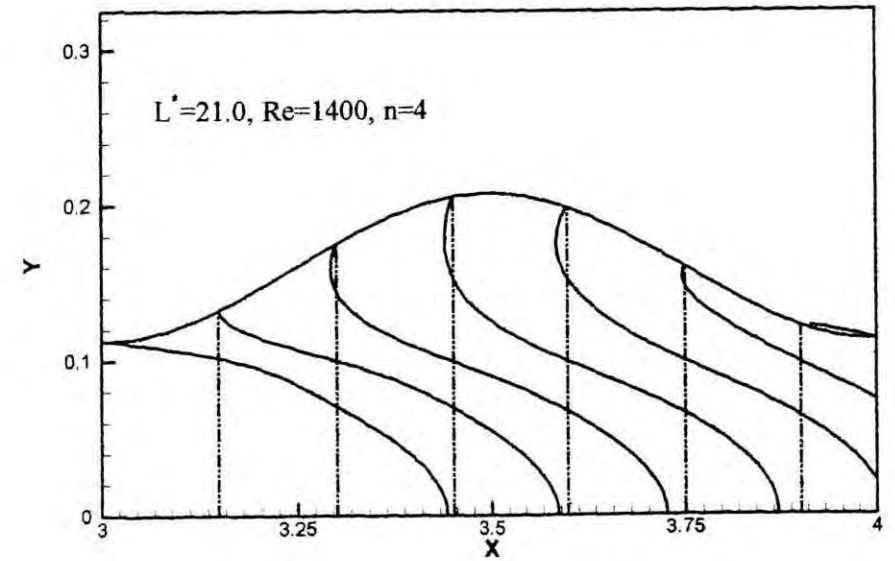
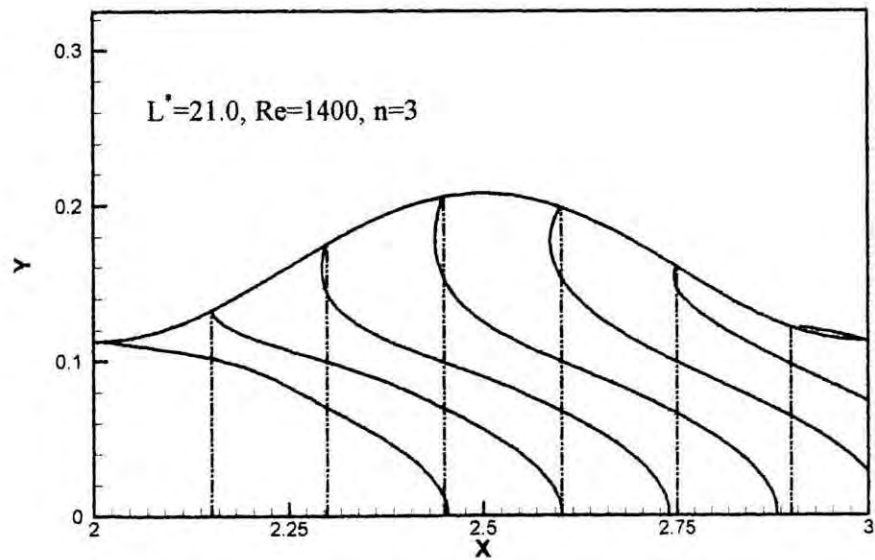


Fig.4.20 (d) Axial velocity profiles for $L^* = 21.0, Re = 1400, n = 1-4$

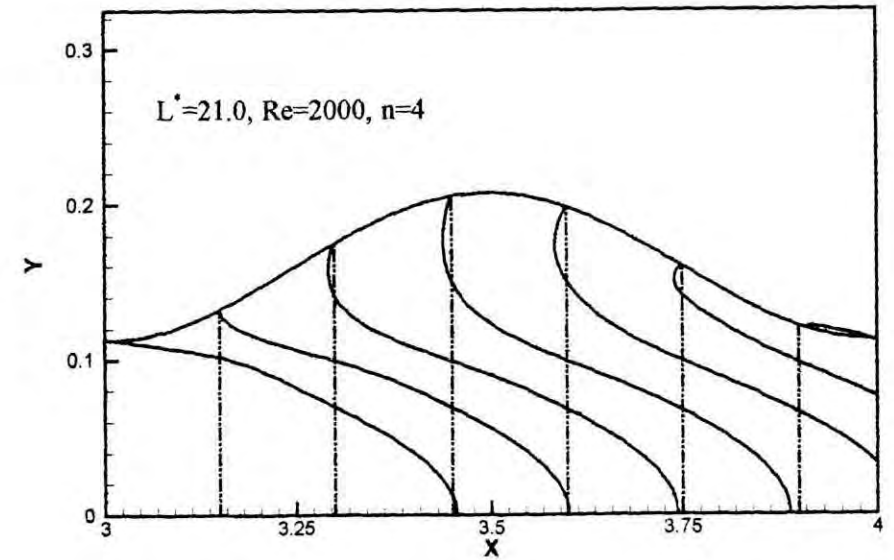
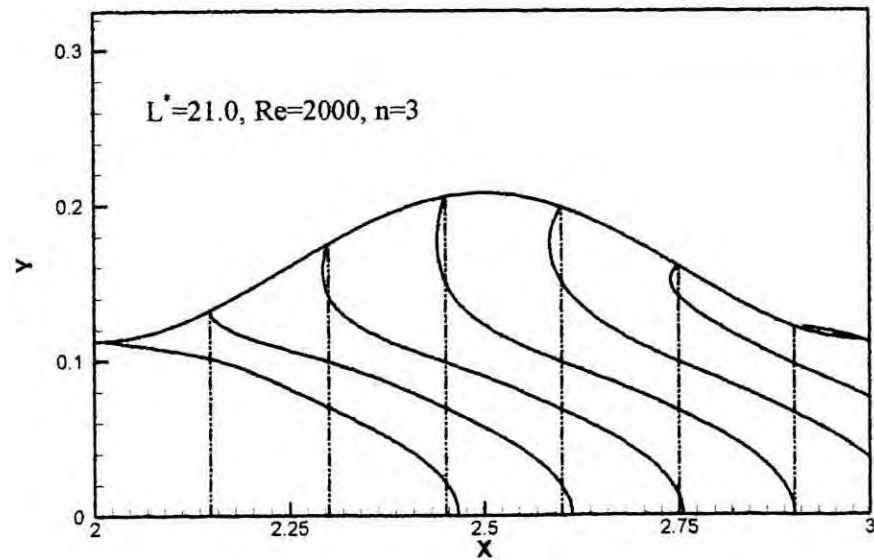
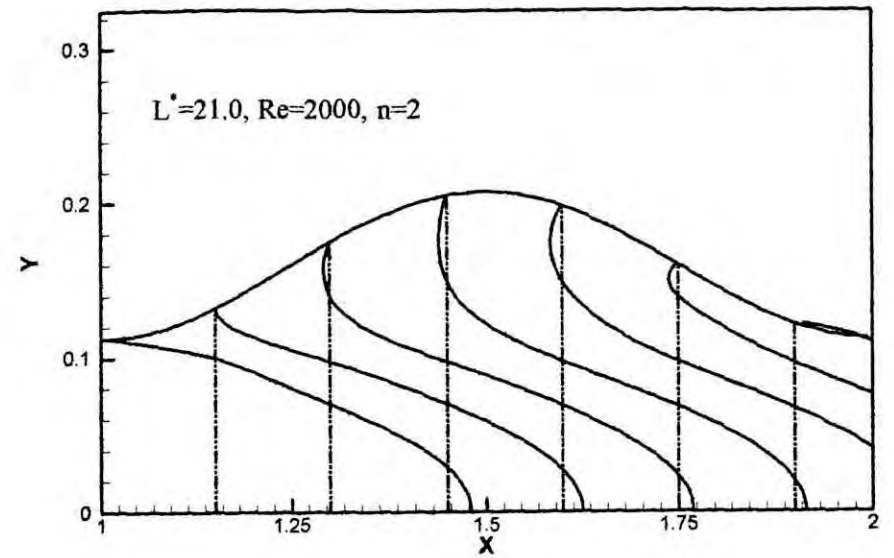
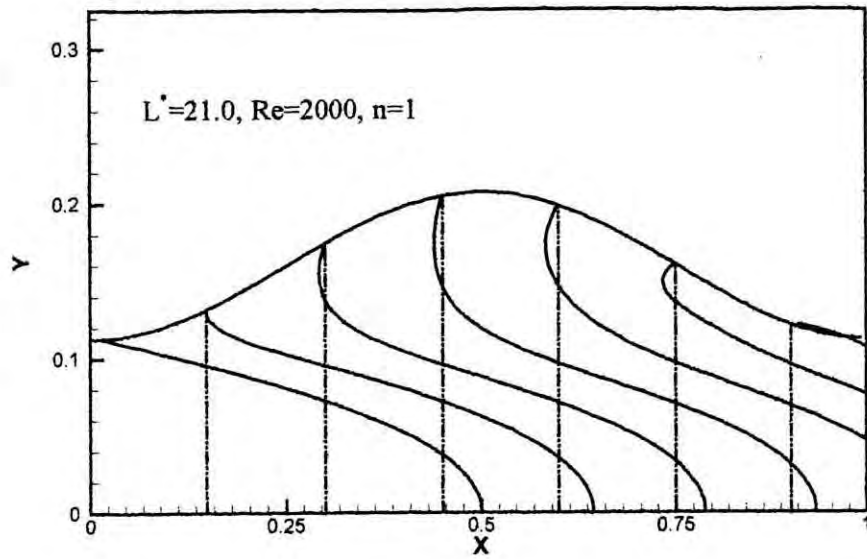


Fig.4.20 (e) Axial velocity profiles for $L^* = 21.0, Re = 2000, n = 1-4$

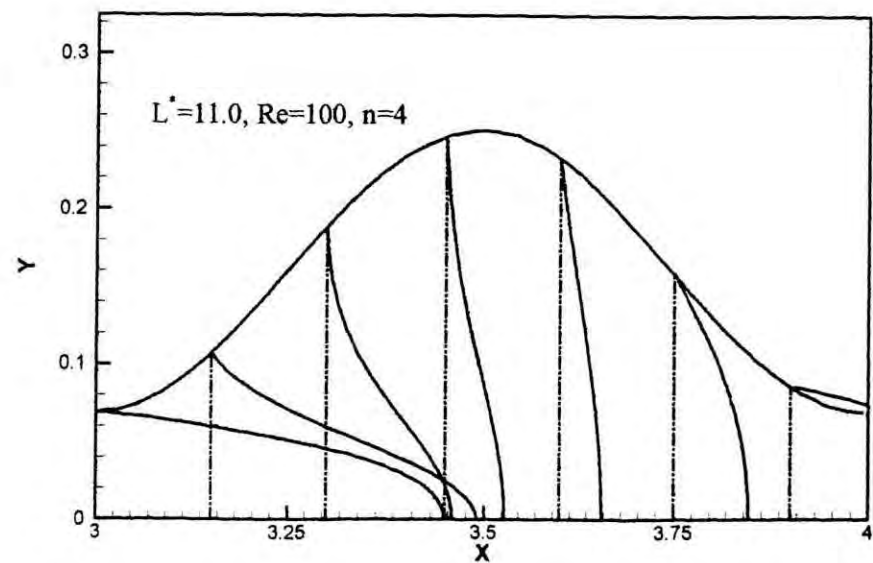
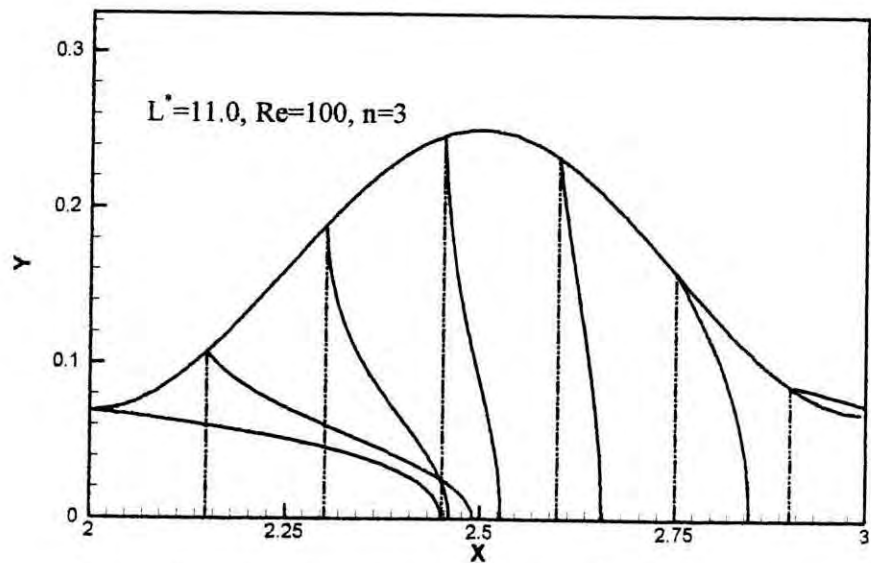
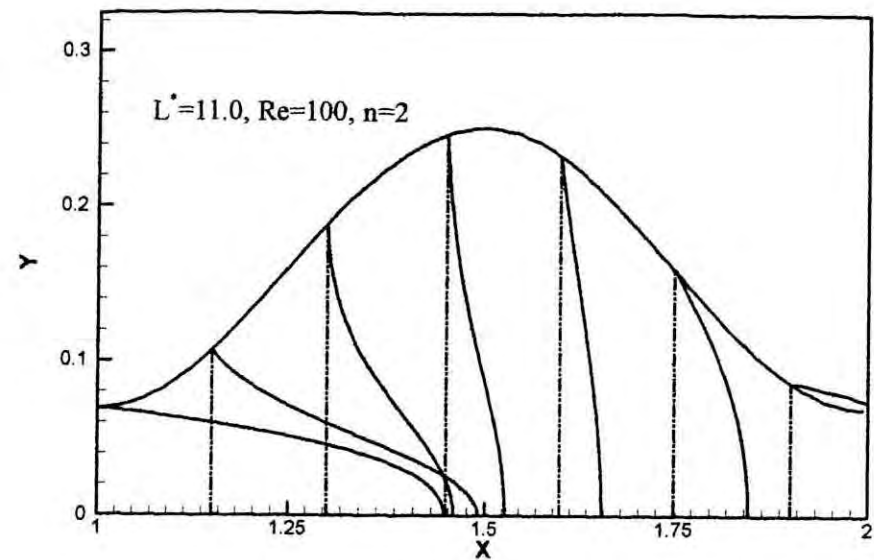
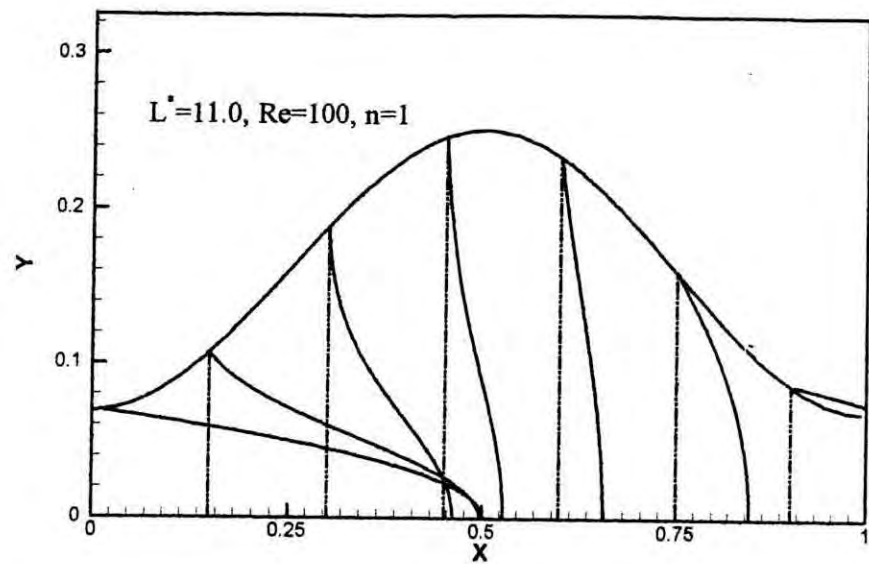
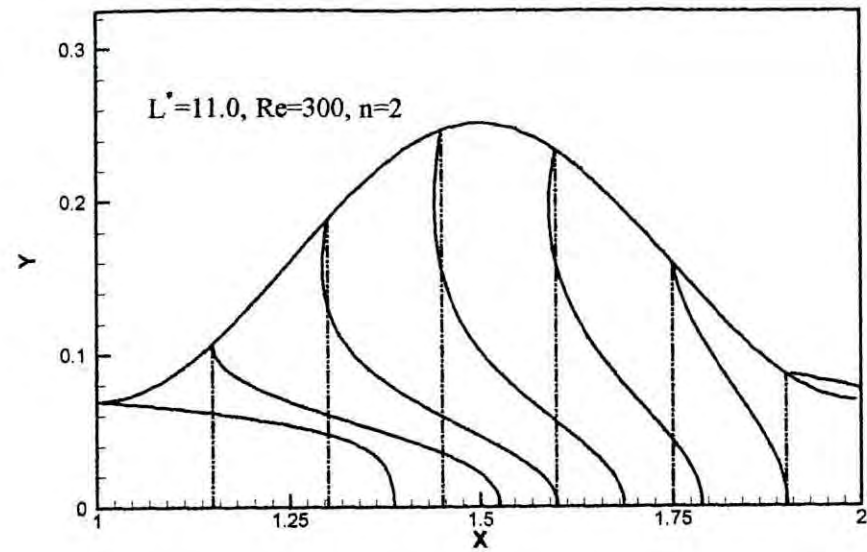
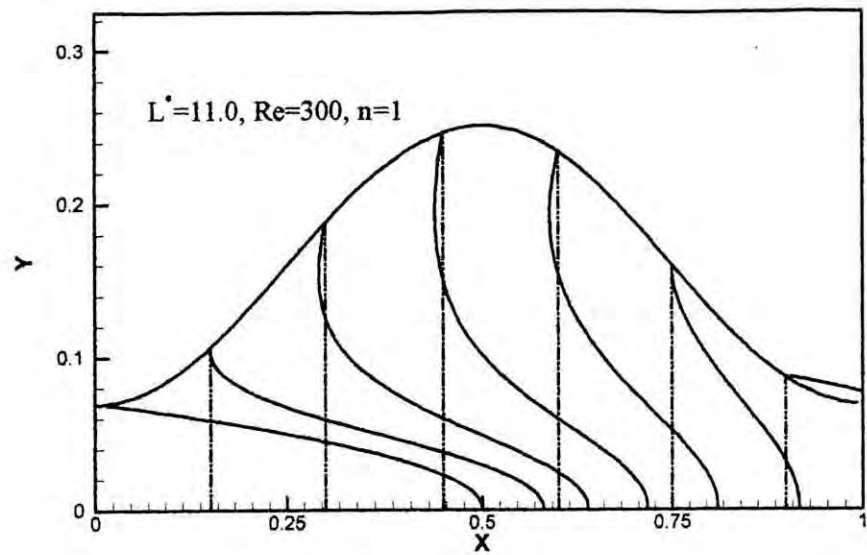


Fig.4.21 (a) Axial velocity profiles for $L^* = 11.0$, $Re = 100$, $n = 1-4$



916

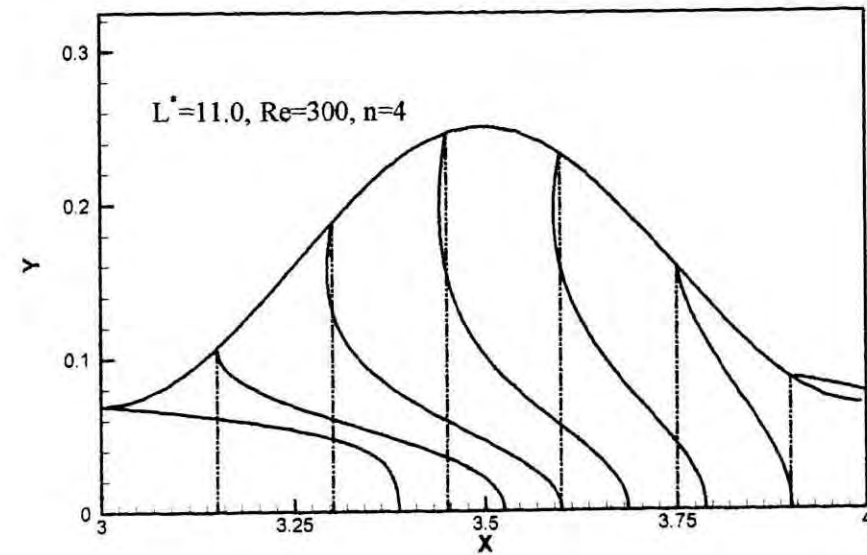
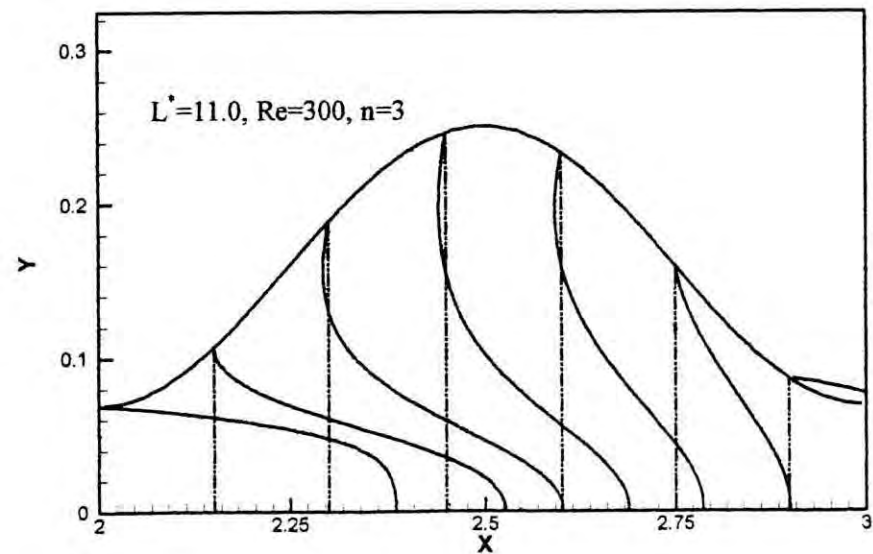


Fig.4.21 (b) Axial velocity profiles for $L^* = 11.0, Re = 300, n = 1-4$

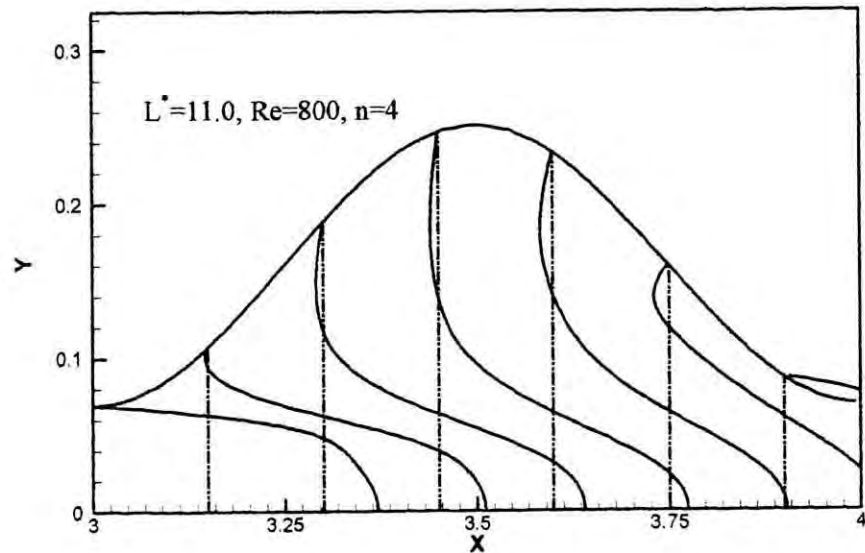
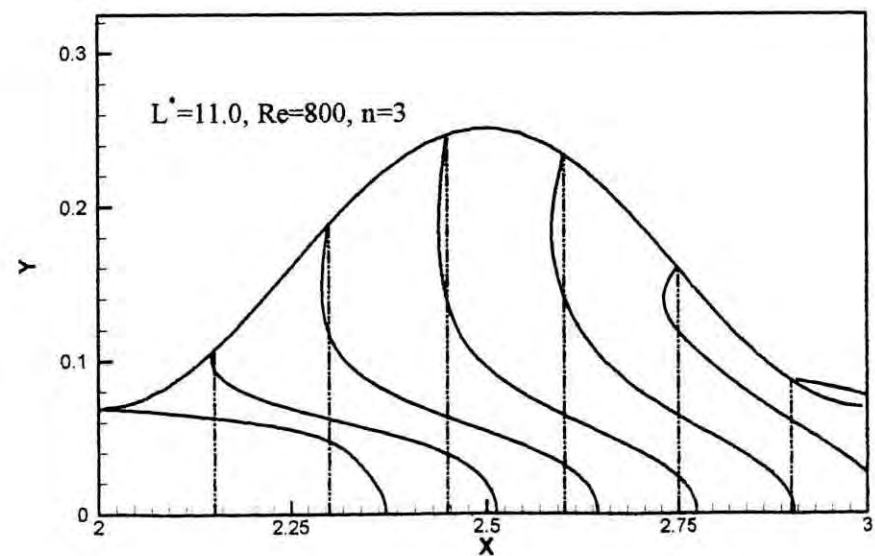
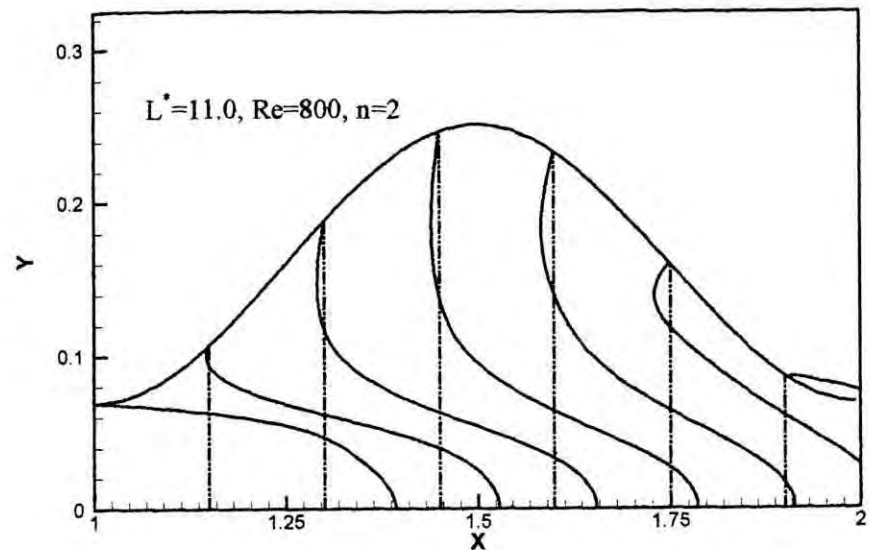
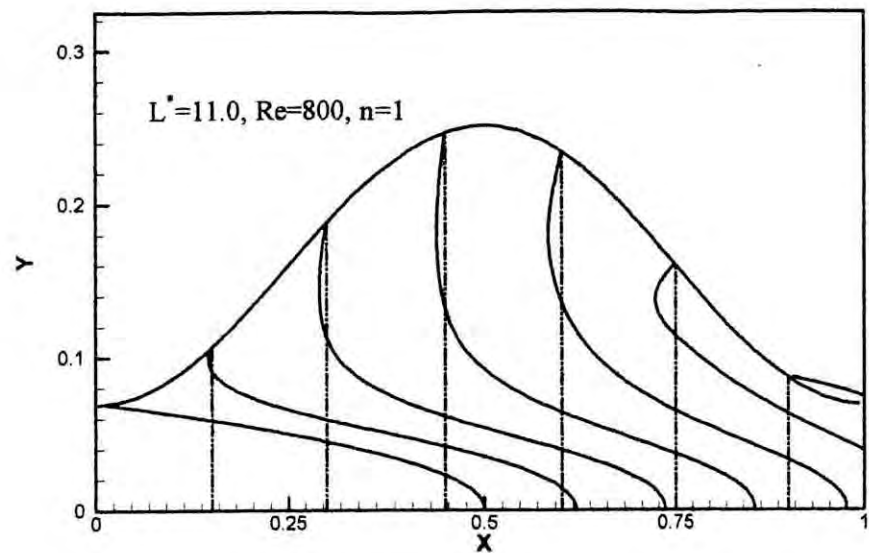
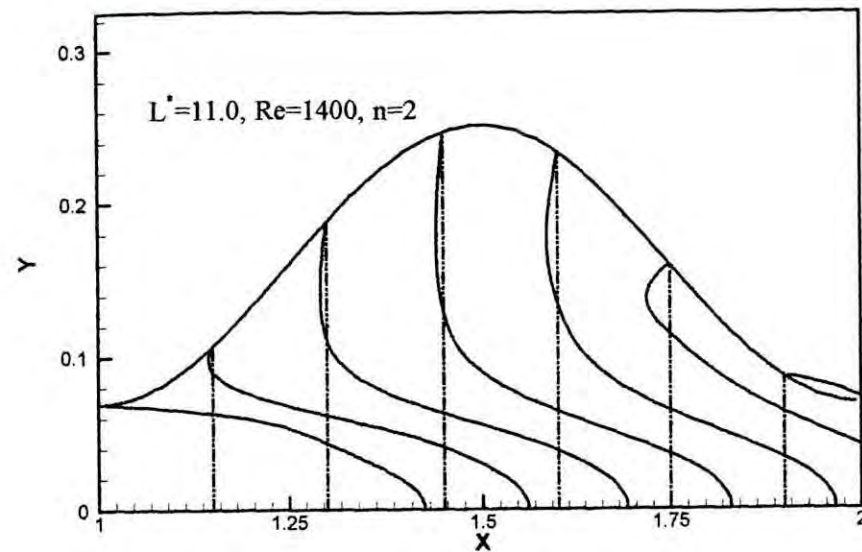
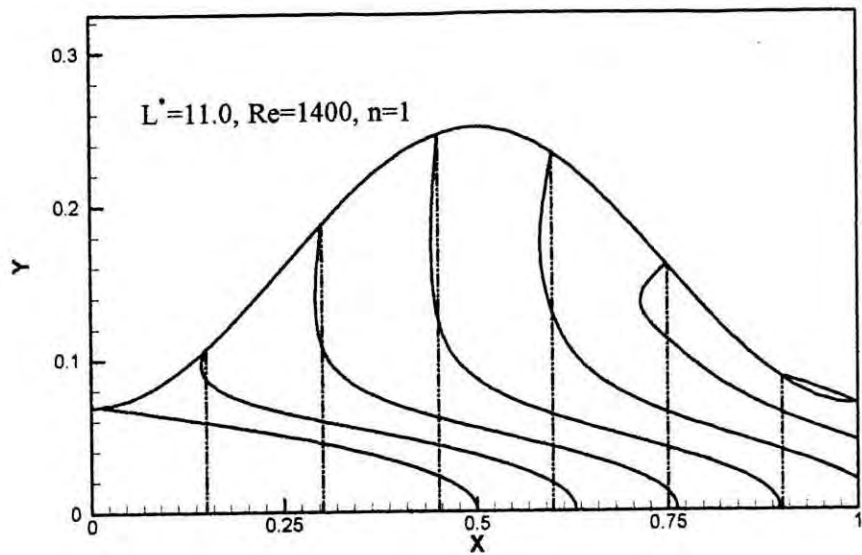


Fig.4.21 (c) Axial velocity profiles for $L^* = 11.0, Re = 800, n = 1-4$



811

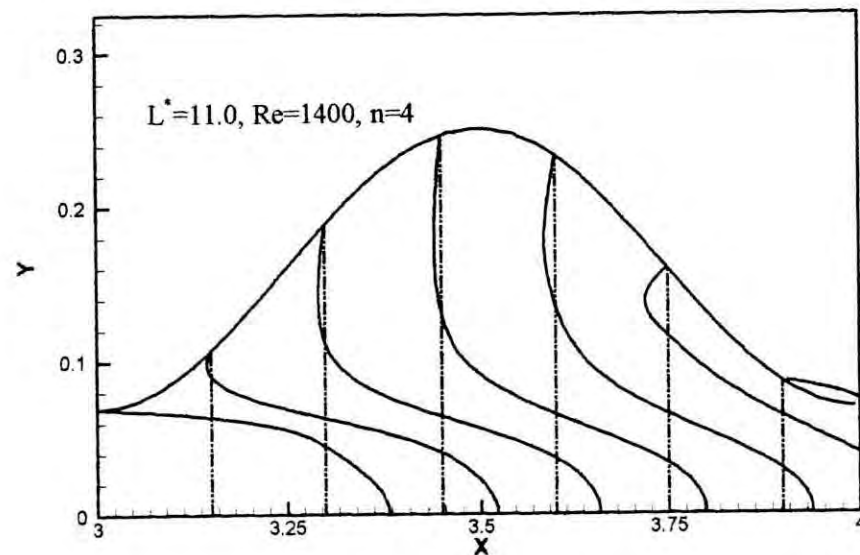
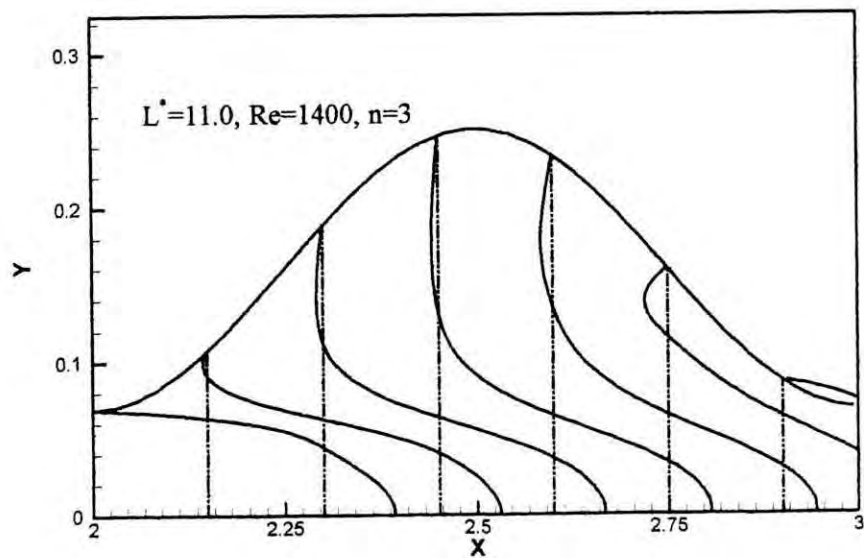
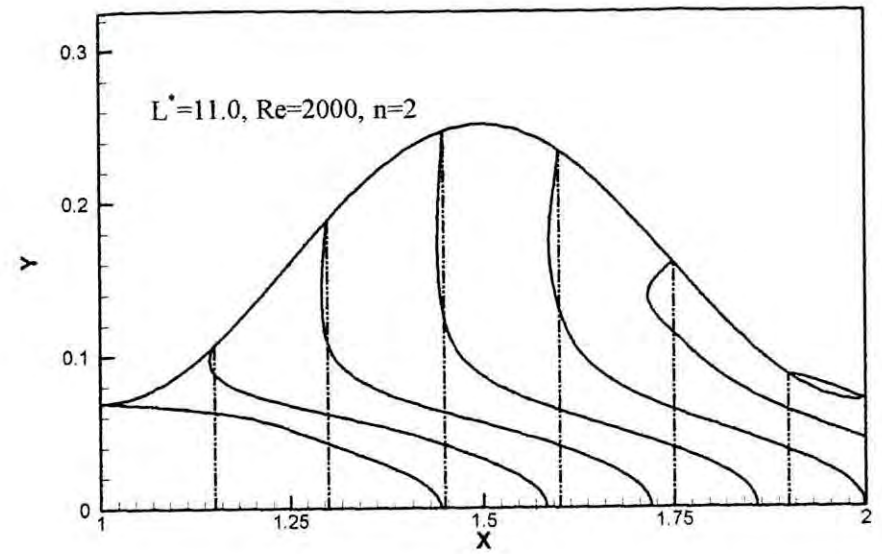
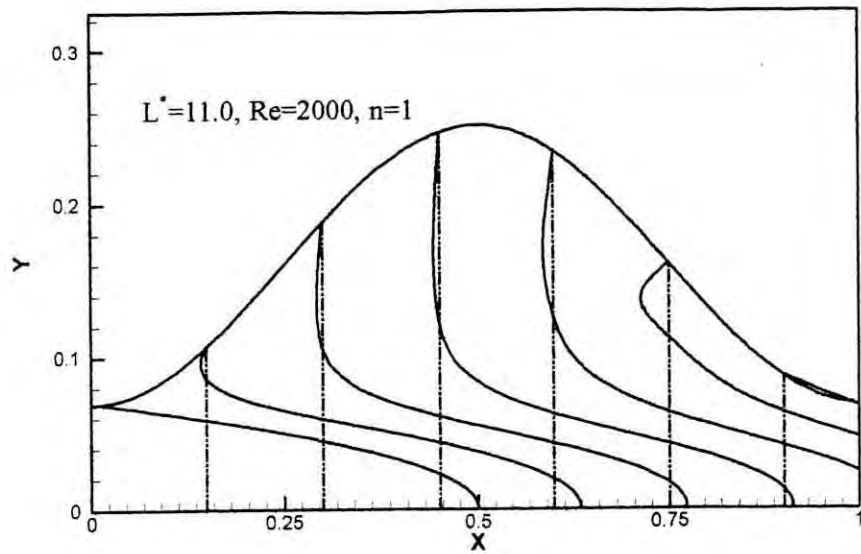


Fig.4.21 (d) Axial velocity profiles for $L^* = 11.0, Re = 1400, n = 1-4$



611

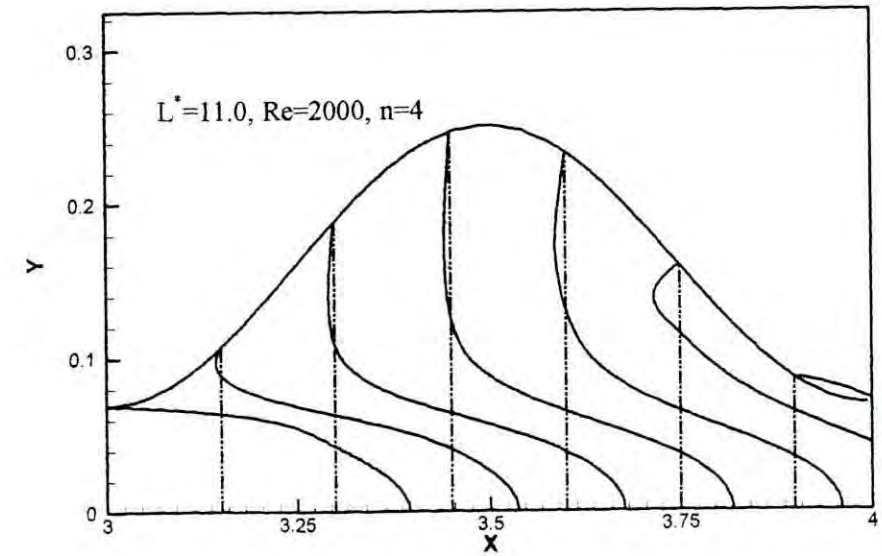
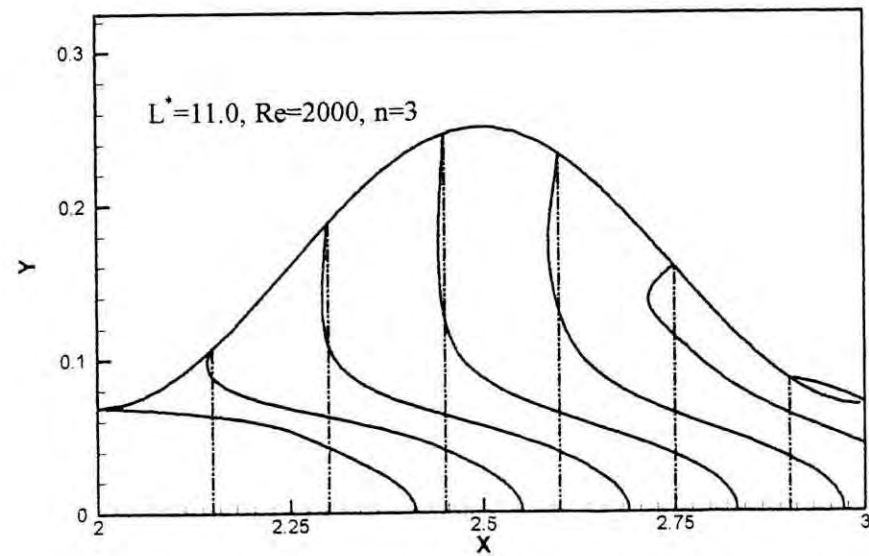


Fig.4.21 (e) Axial velocity profiles for $L^* = 11.0, Re = 2000, n = 1-4$

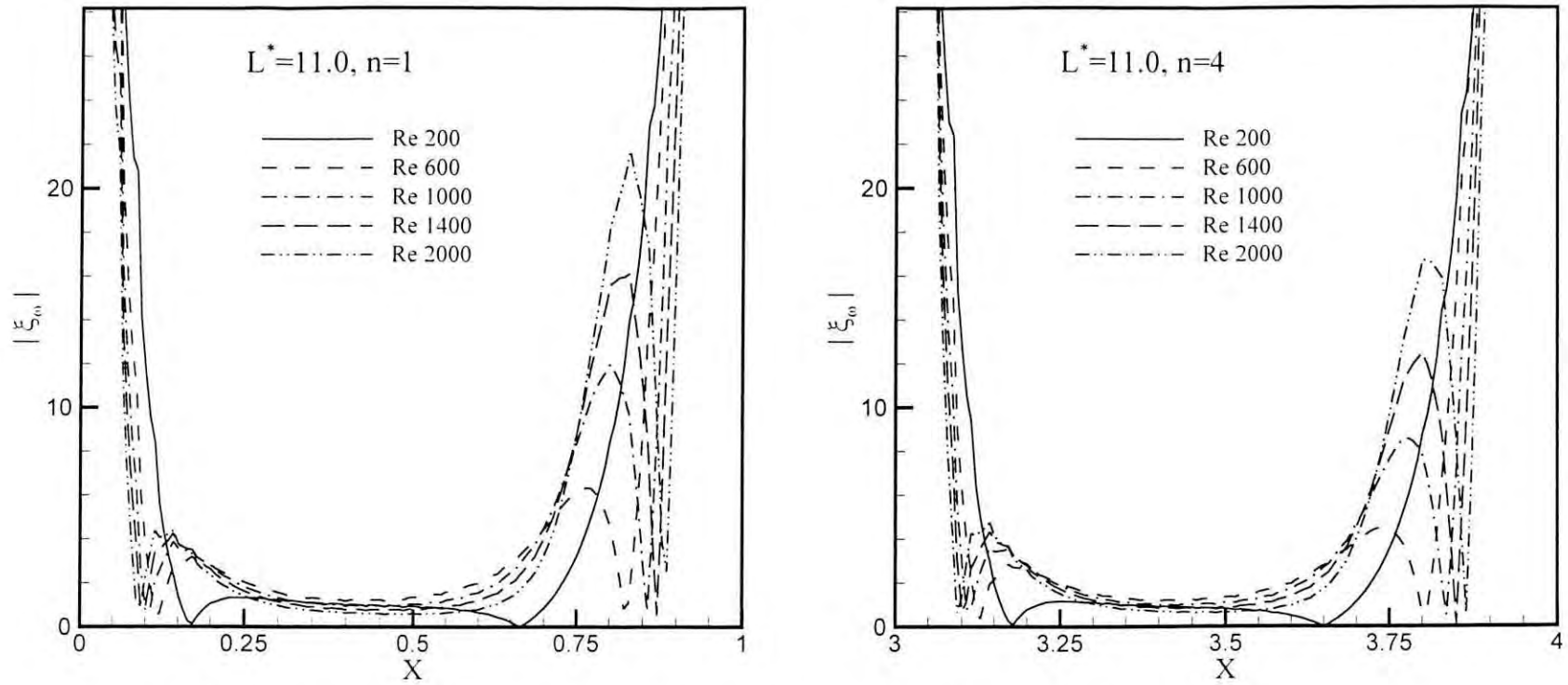


Fig. 4.22 Wall vorticity distribution along first & fourth cycle for $L^* = 11.0$ (Axisymmetric case)

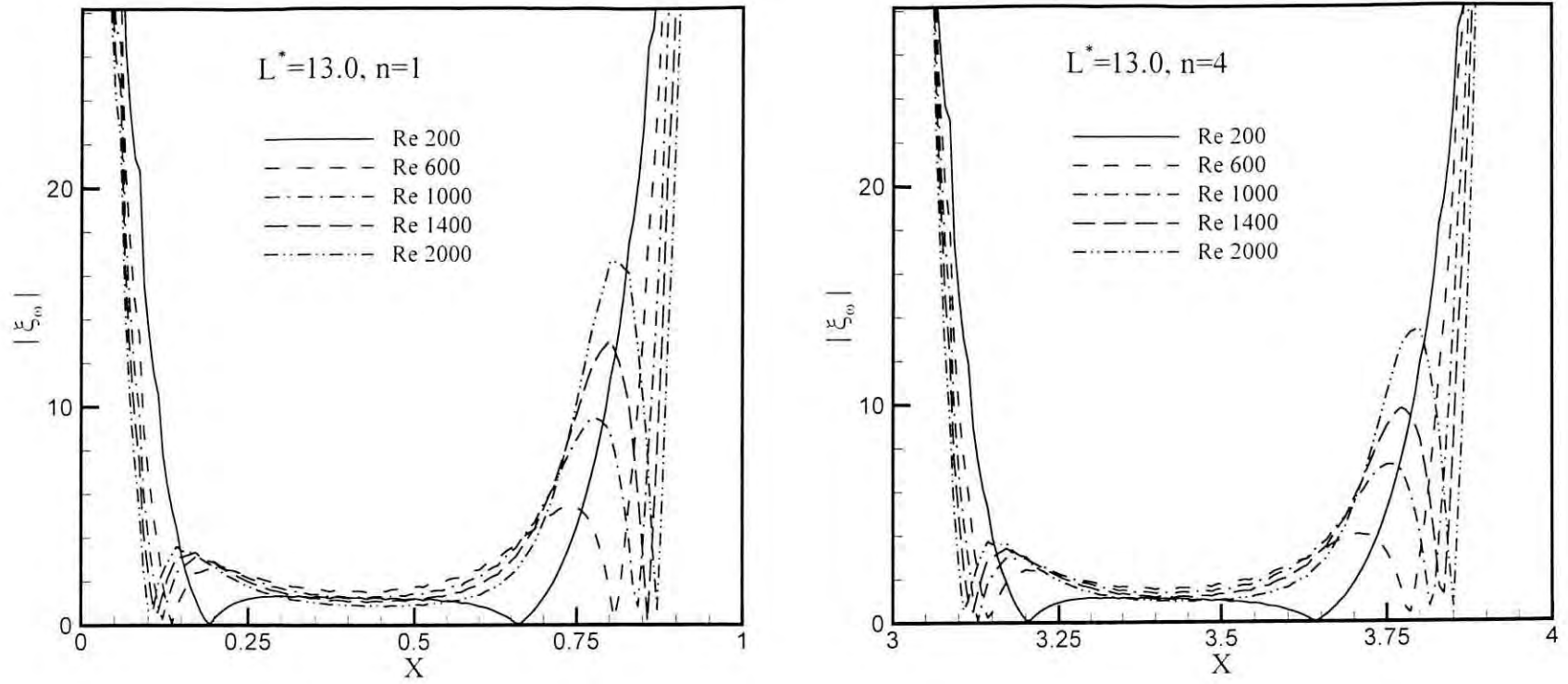


Fig. 4.23 Wall vorticity distribution along first & fourth cycle for $L^* = 13.0$ (Axisymmetric case)

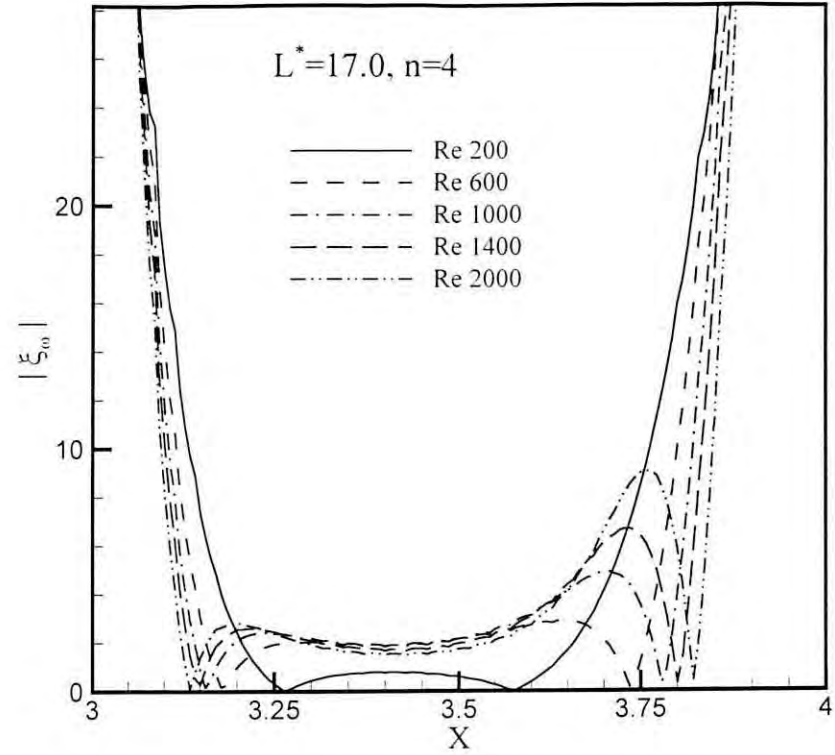
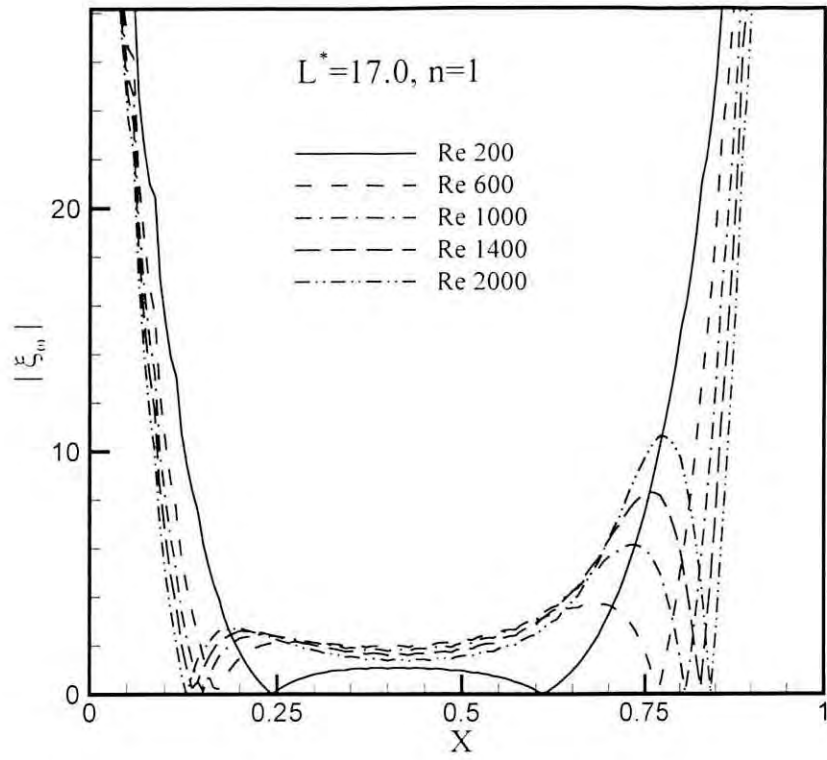


Fig. 4.24 Wall vorticity distribution along first & fourth cycle for $L^* = 17.0$ (Axisymmetric case)

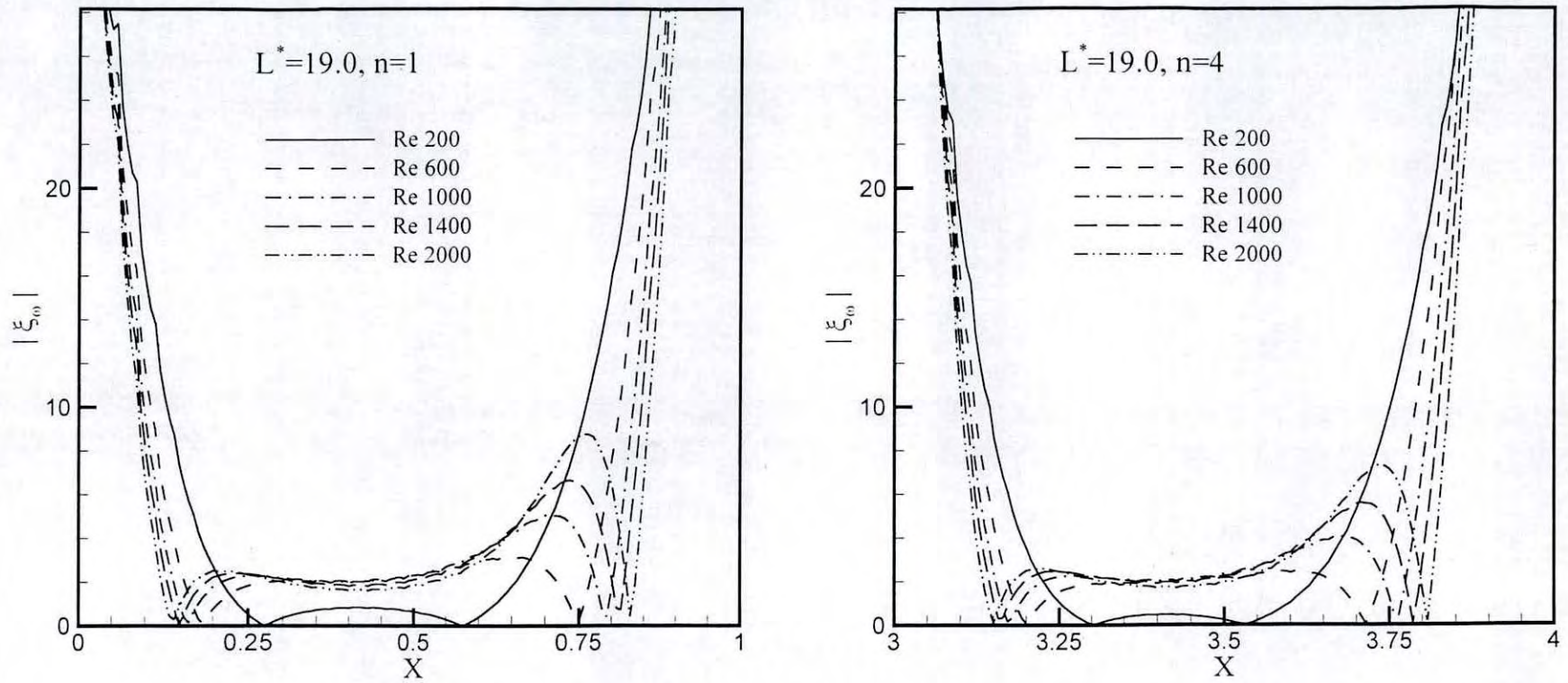


Fig. 4.25 Wall vorticity distribution along first & fourth cycle for $L^* = 19.0$ (Axisymmetric case)

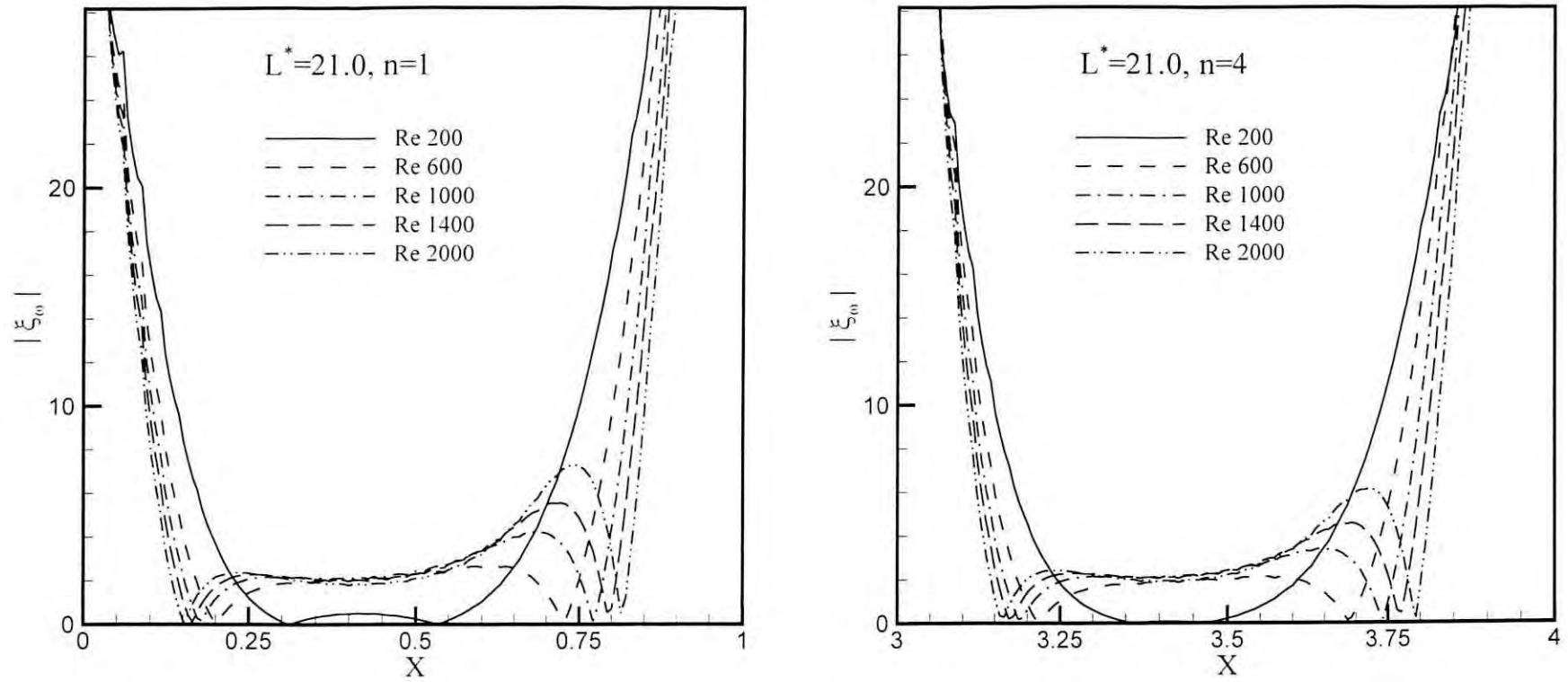


Fig. 4.26 Wall vorticity distribution along first & fourth cycle for $L^* = 21.0$ (Axisymmetric case)

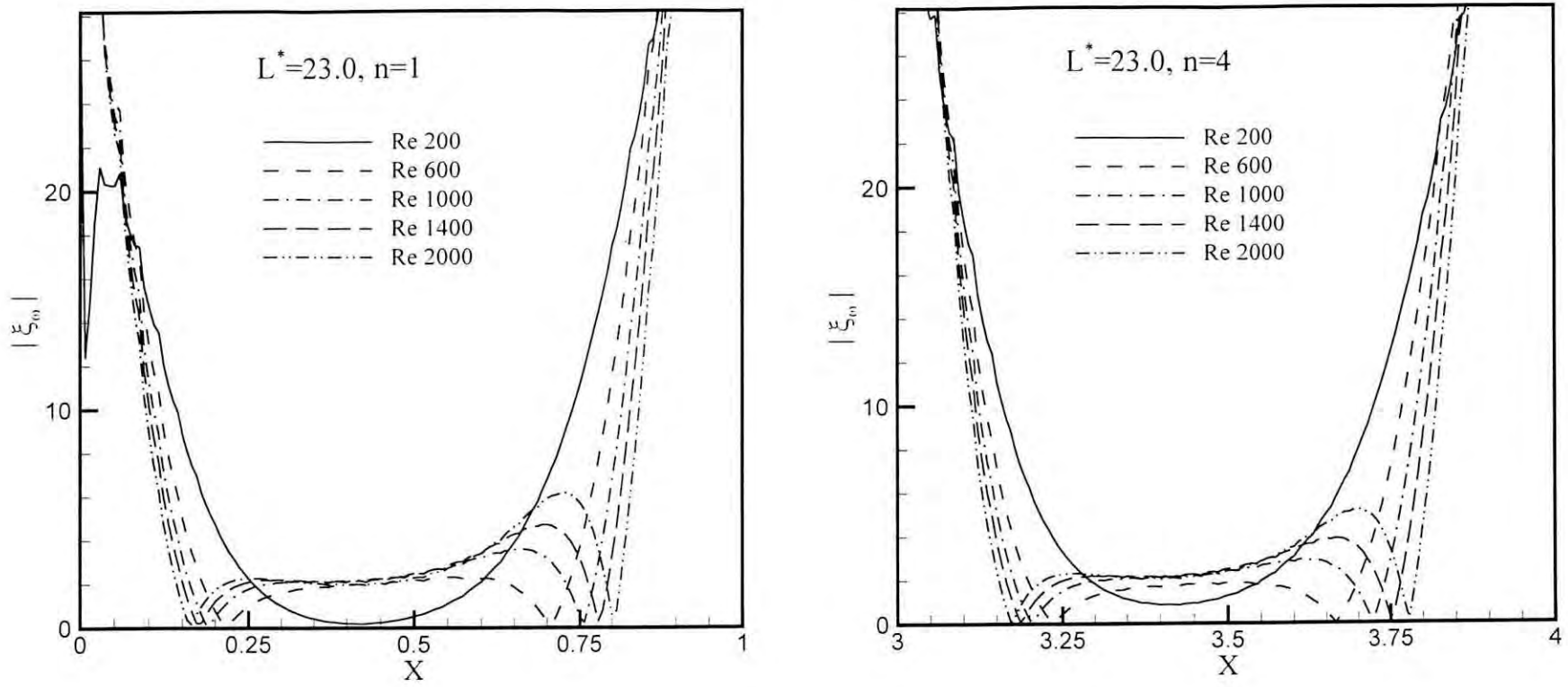


Fig. 4.27 Wall vorticity distribution along first & fourth cycle for $L^* = 23.0$ (Axisymmetric case)

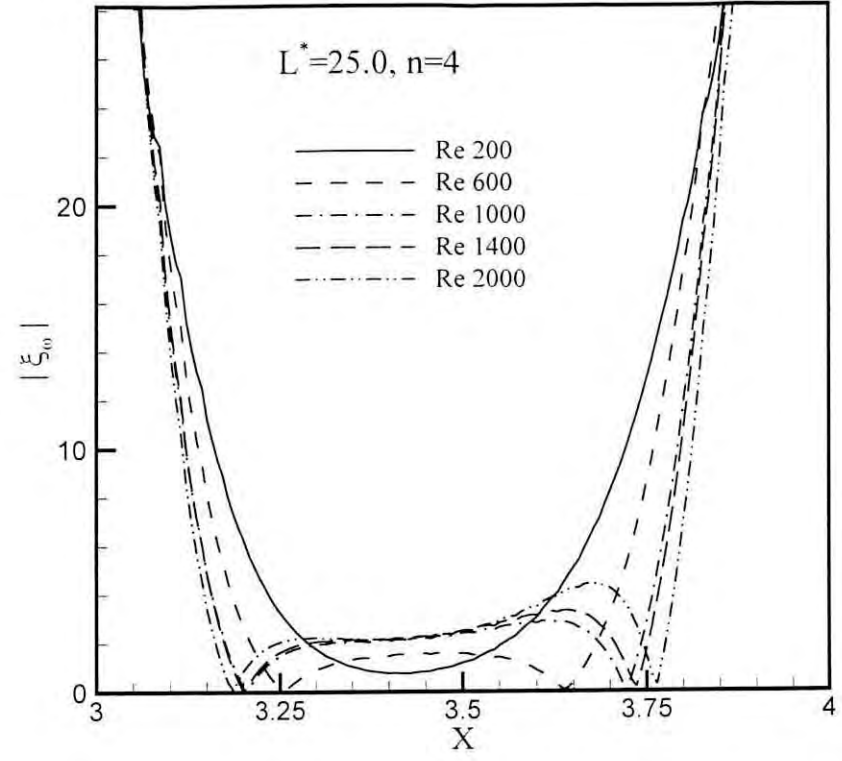
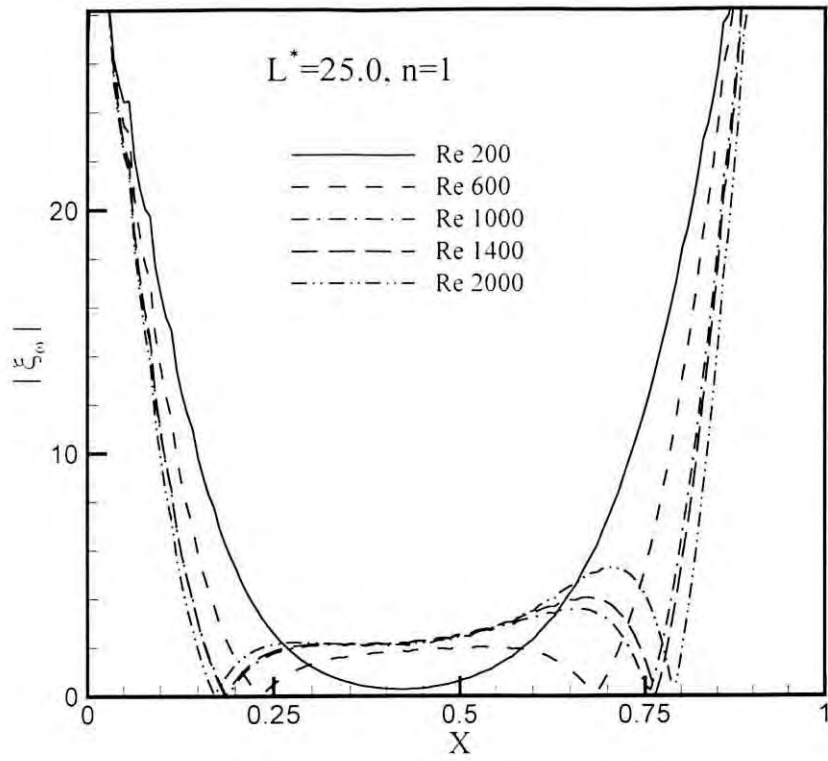


Fig. 4.28 Wall vorticity distribution along first & fourth cycle for $L^* = 25.0$ (Axisymmetric case)

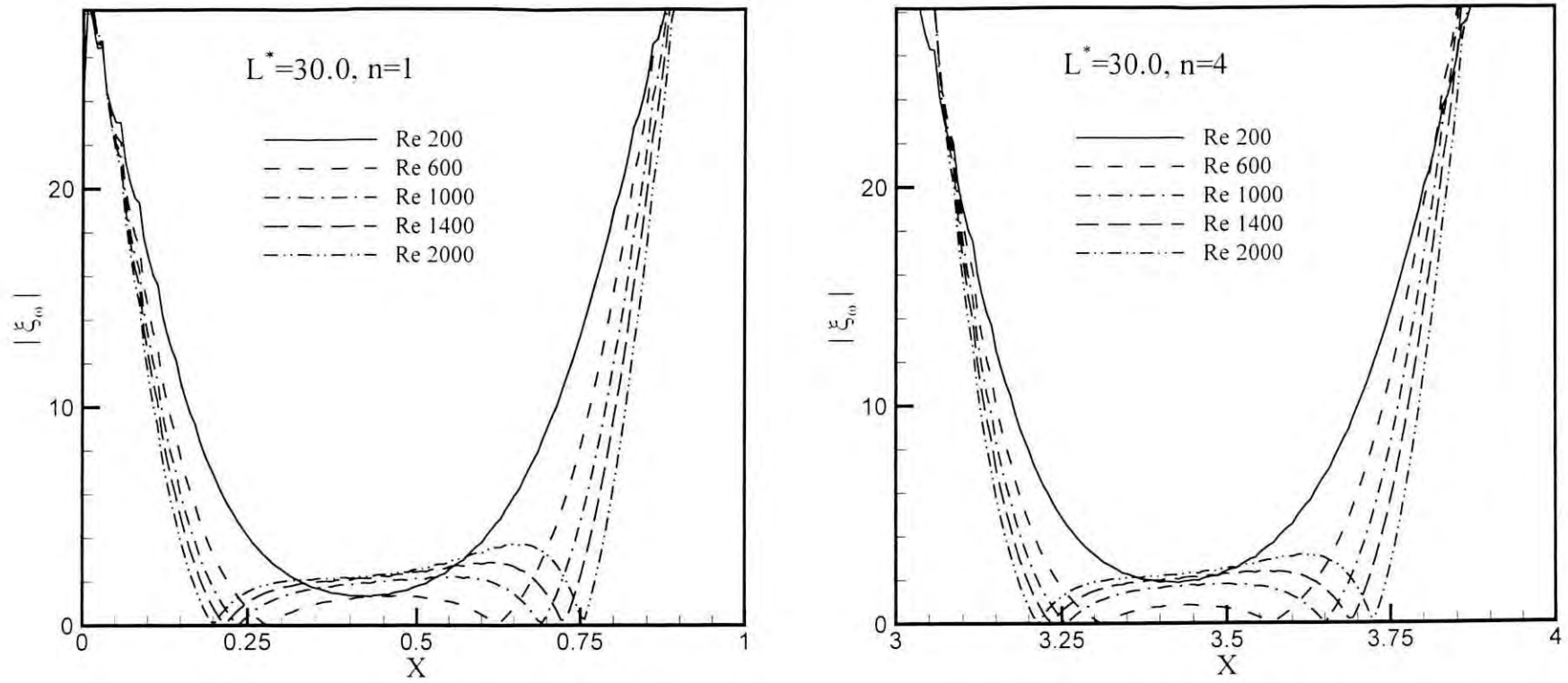


Fig.4.29 Wall vorticity distribution along first & fourth cycle for $L^* = 30.0$ (Axisymmetric case)

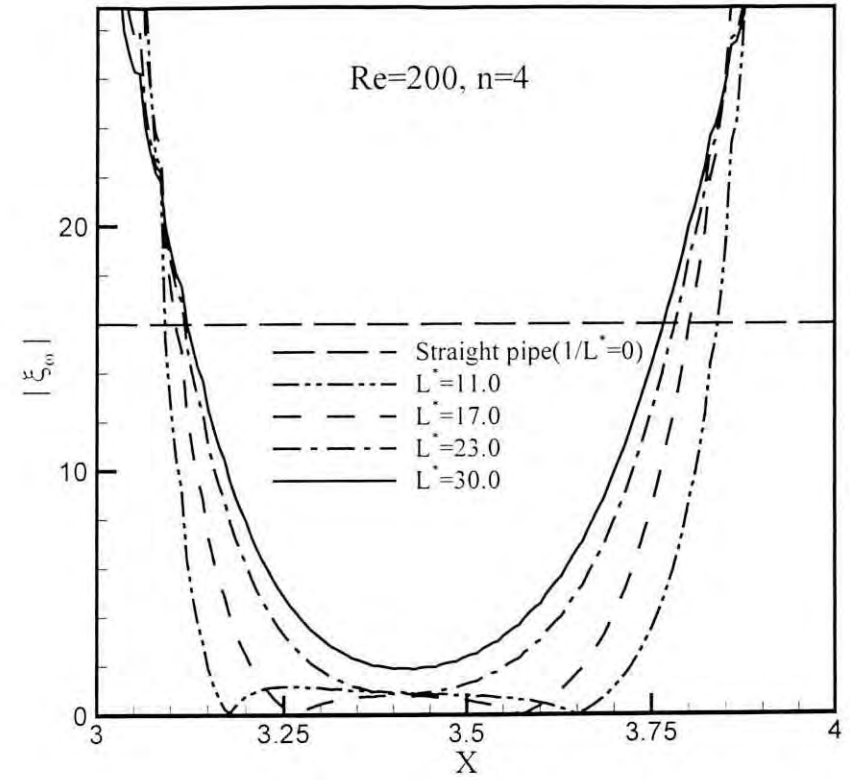
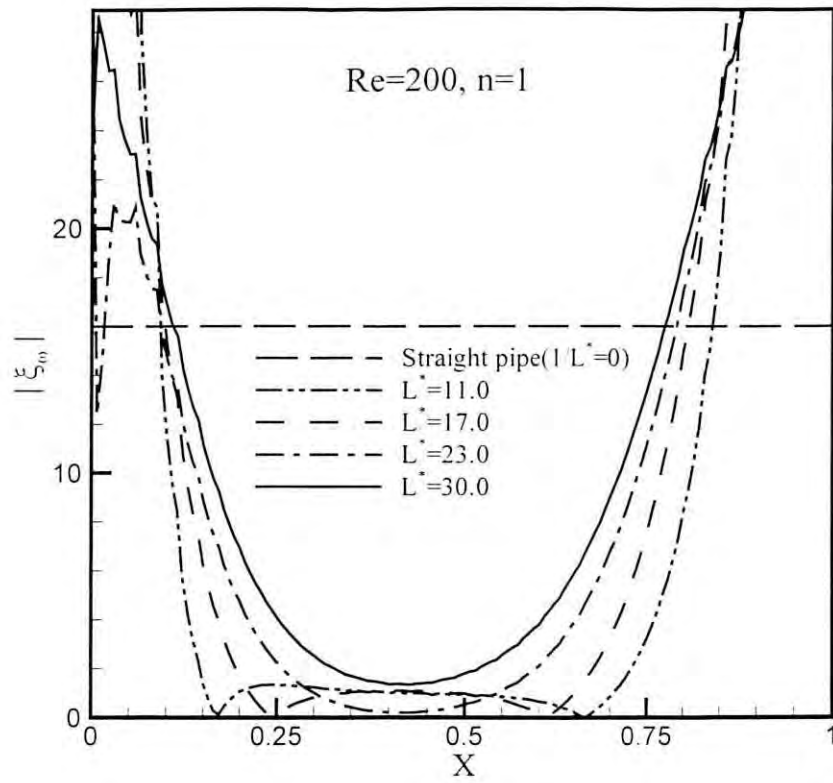


Fig. 4.30 Wall vorticity distribution along first & fourth cycle for Re=200 (Axisymmetric case)

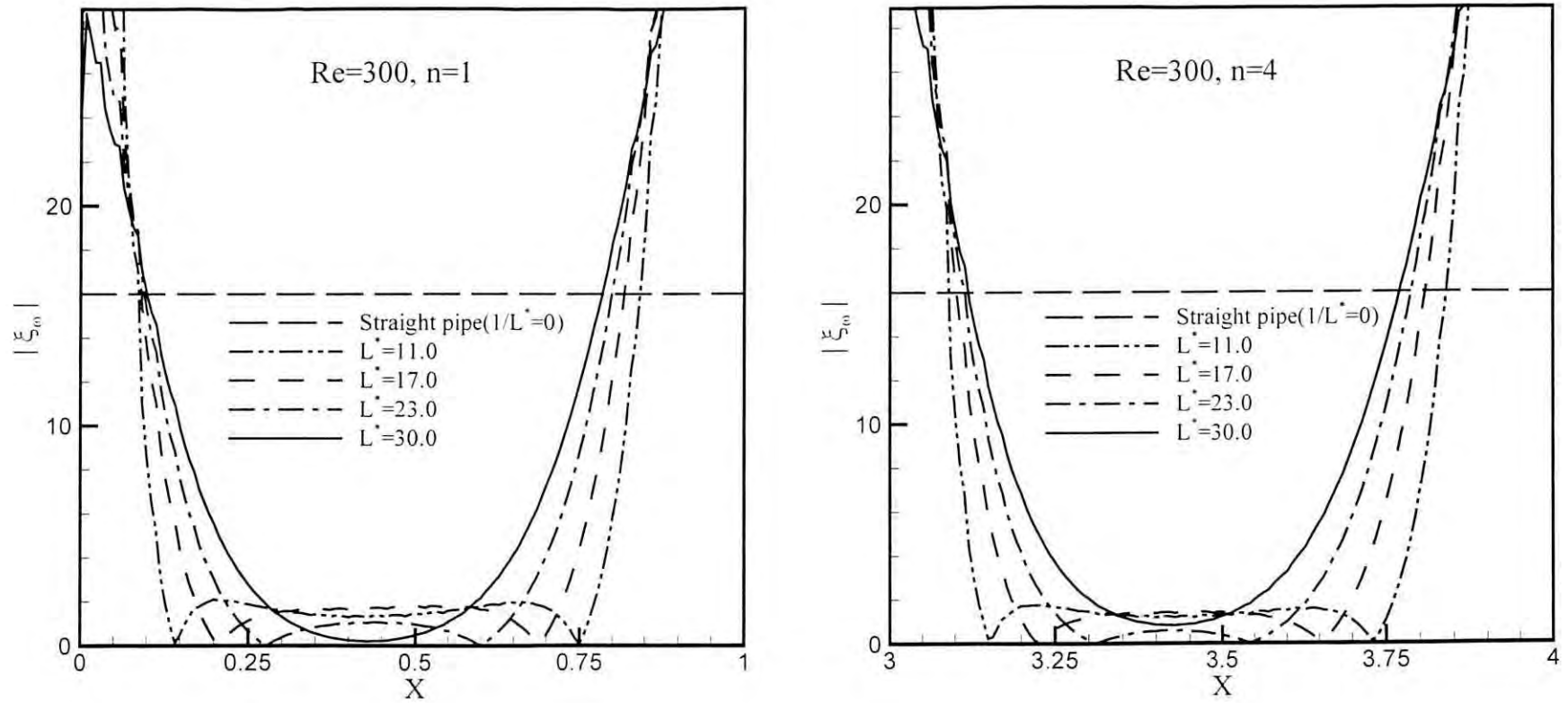


Fig. 4.31 Wall vorticity distribution along first & fourth cycle for $Re=300$ (Axisymmetric case)

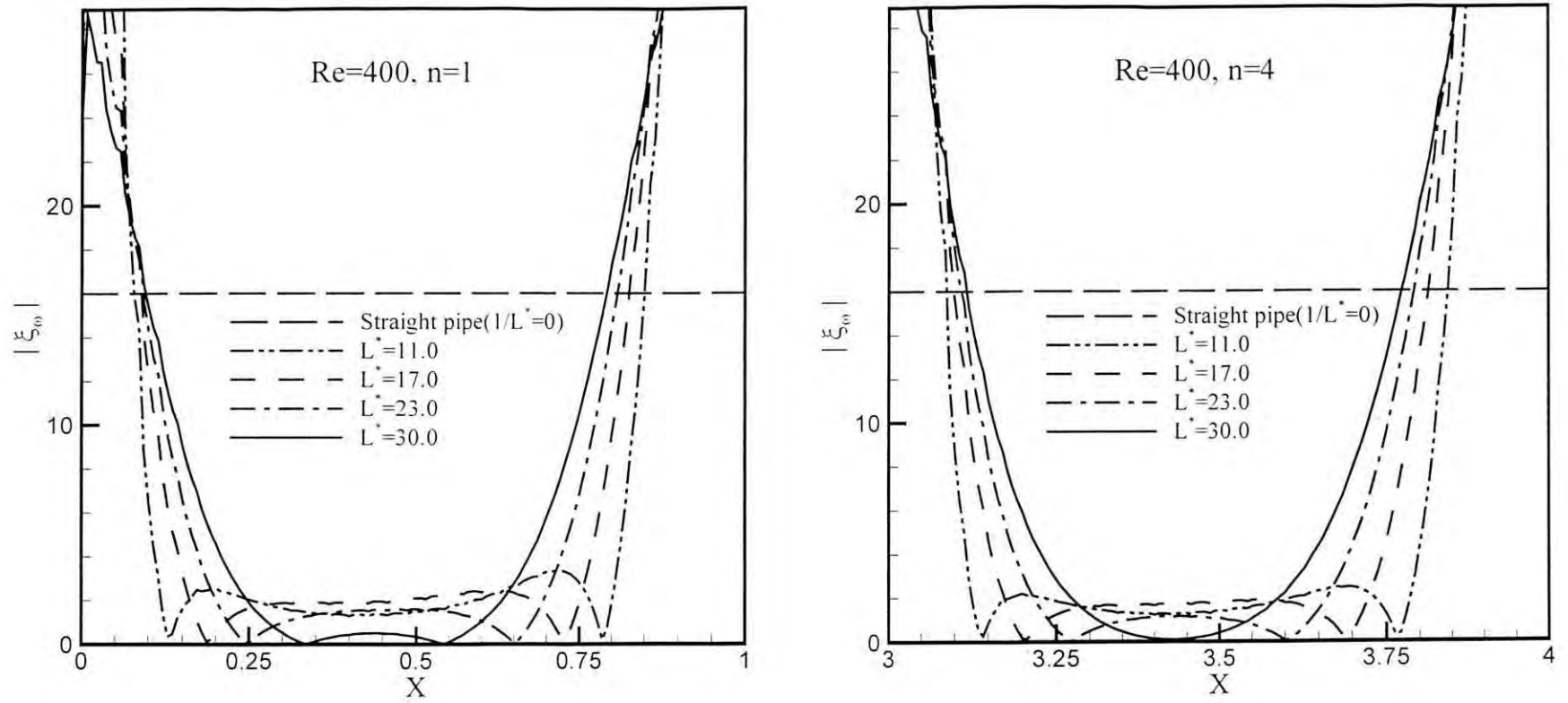


Fig. 4.32 Wall vorticity distribution along first & fourth cycle for Re=400 (Axisymmetric case)

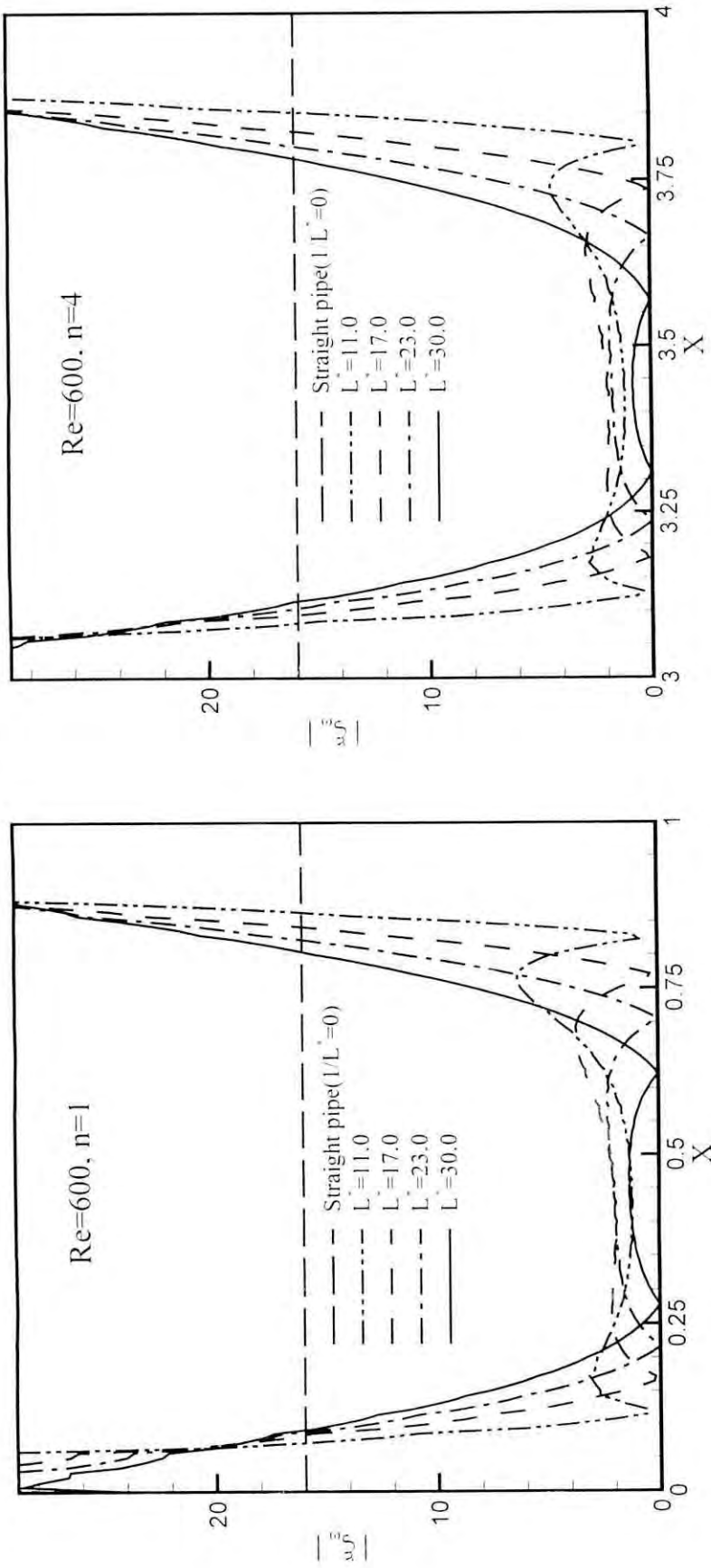


Fig. 4.33 Wall vorticity distribution along first & fourth cycle for $Re=600$ (Axisymmetric case)

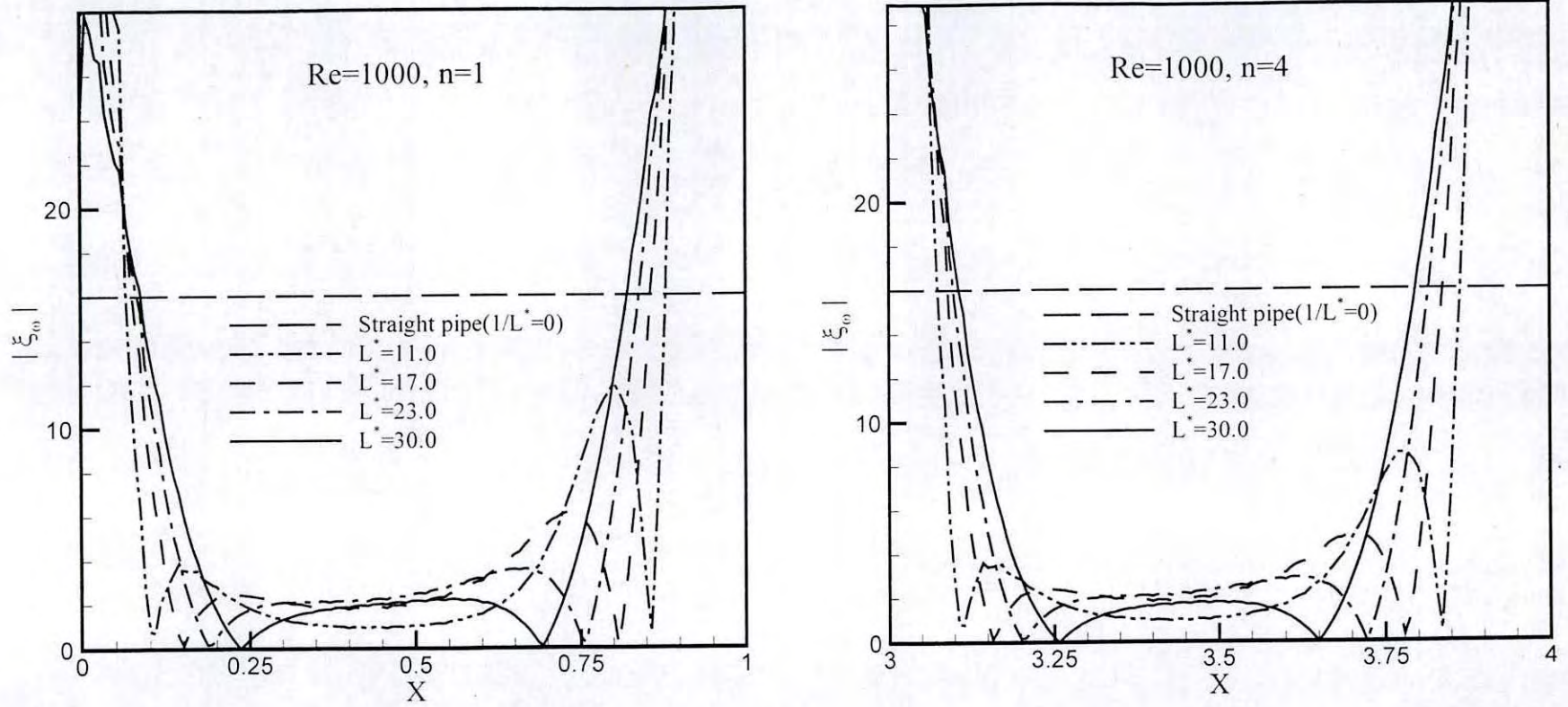


Fig. 4.34 Wall vorticity distribution along first & fourth cycle for $Re=1000$ (Axisymmetric case)

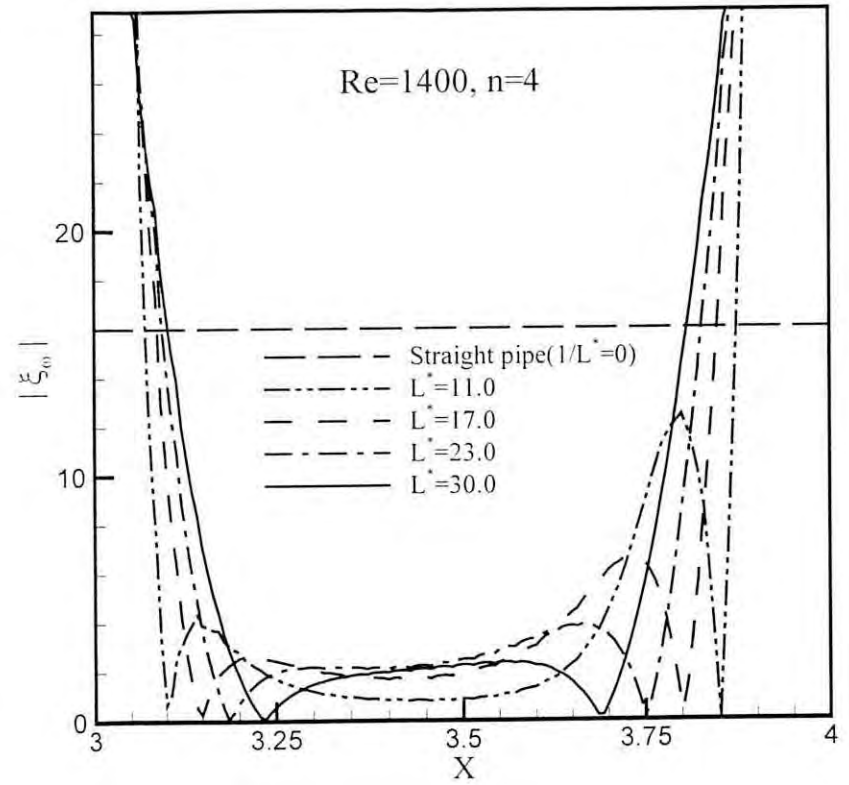
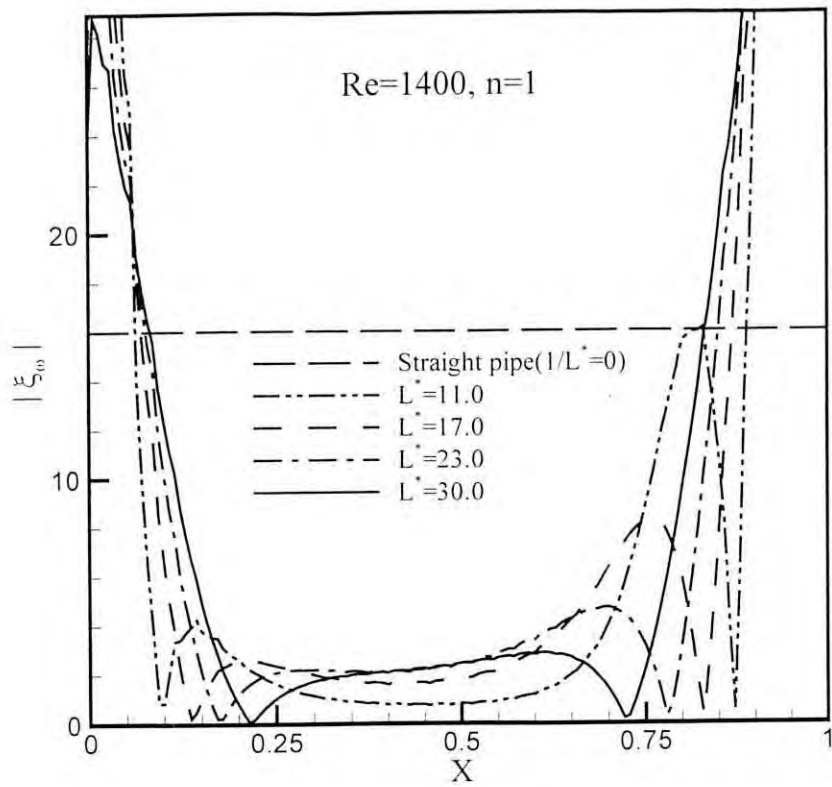


Fig. 4.35 Wall vorticity distribution along first & fourth cycle for Re=1400 (Axisymmetric case)

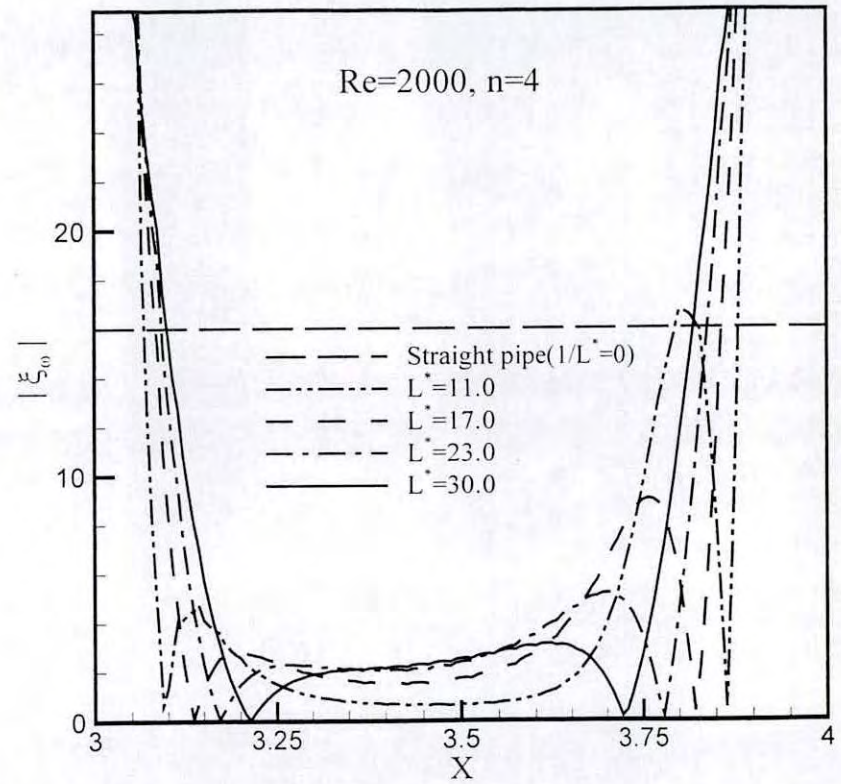
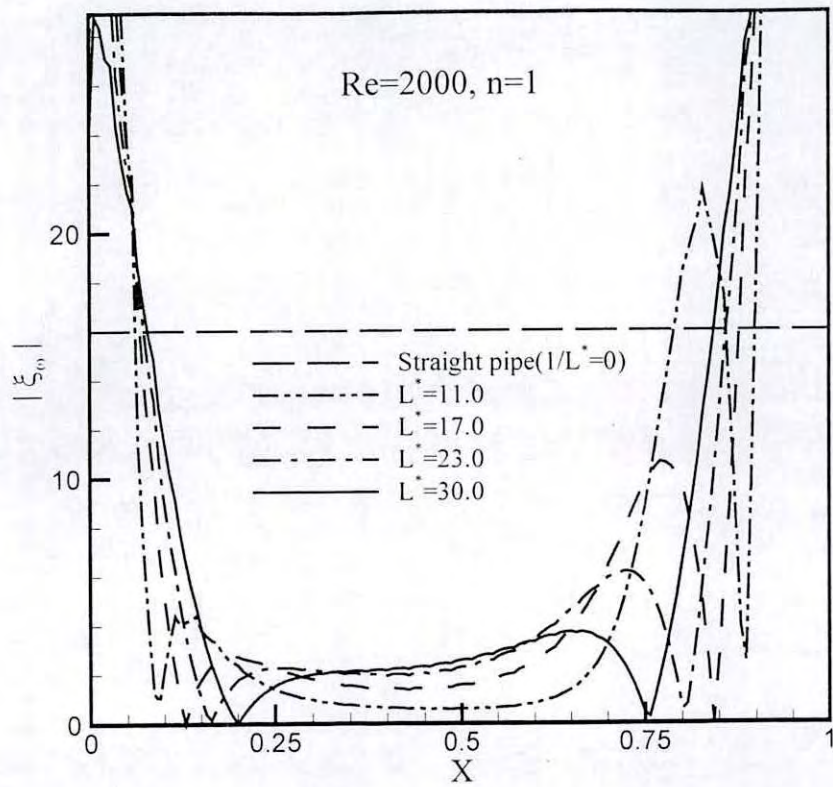


Fig. 4.36 Wall vorticity distribution along first & fourth cycle for Re=2000 (Axisymmetric case)

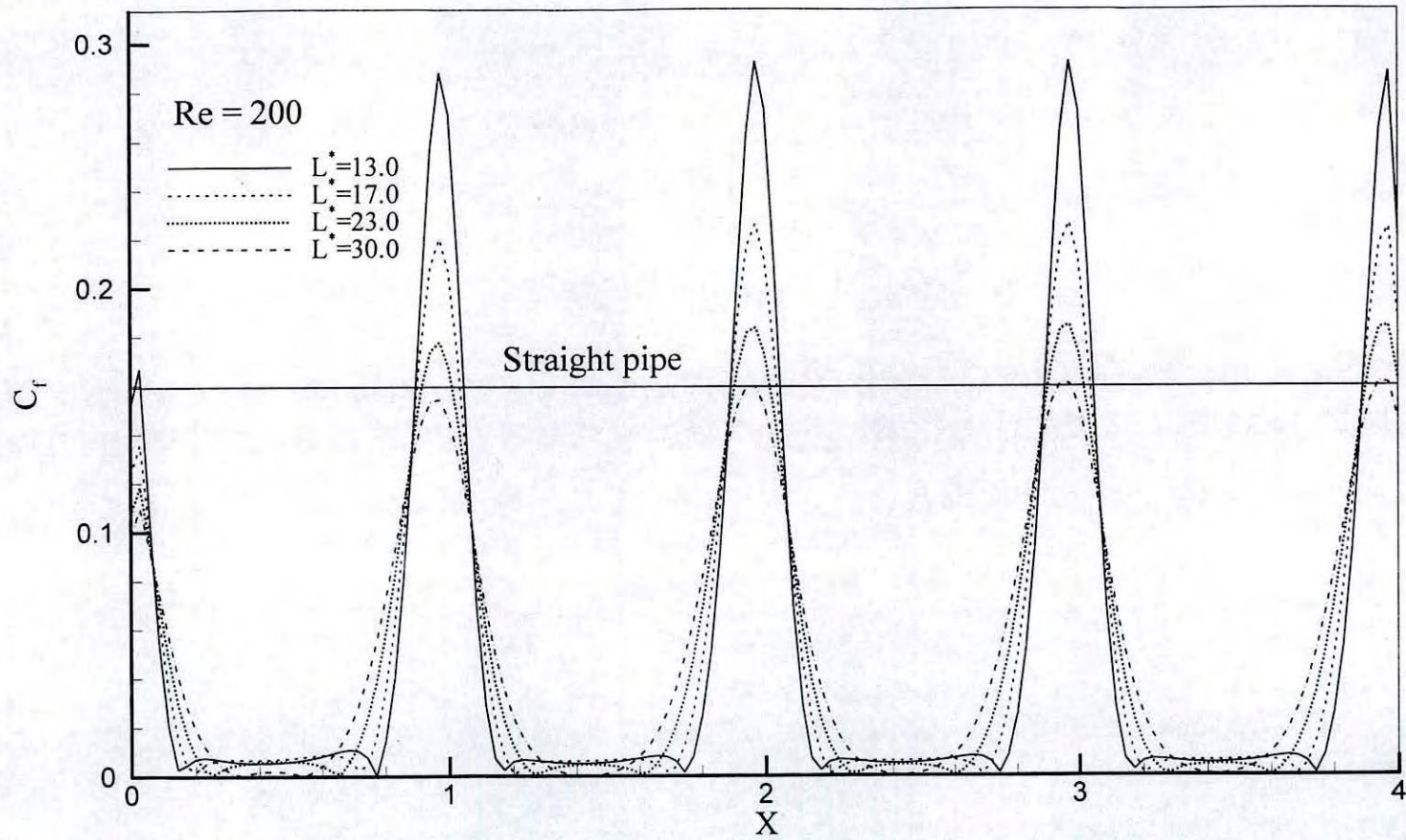


Fig. 4.37 Skin friction distribution along the wavy wall at $Re=200$ (axisymmetric case)

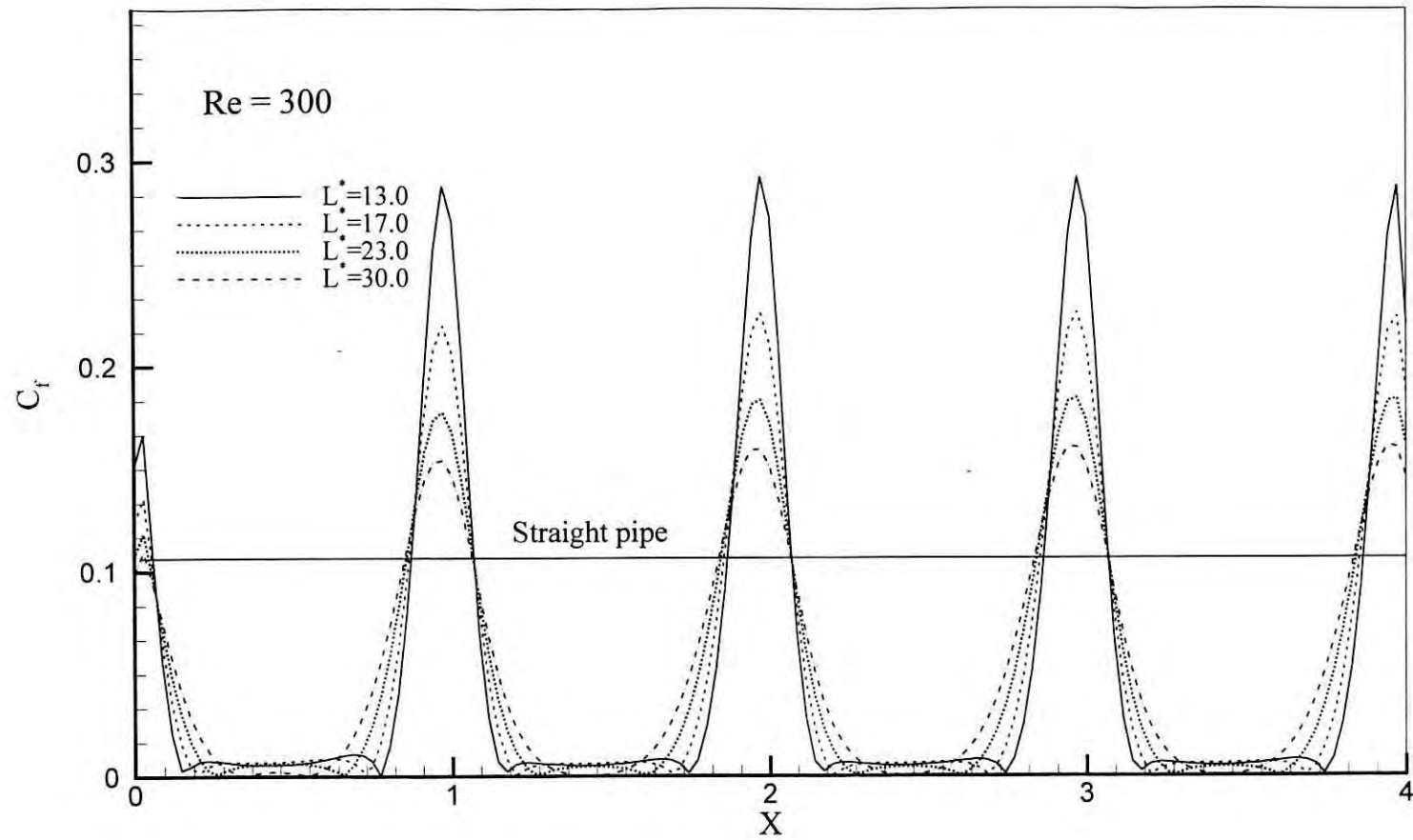


Fig. 4.38 Skin friction distribution along the wavy wall at $Re=300$ (axisymmetric case)

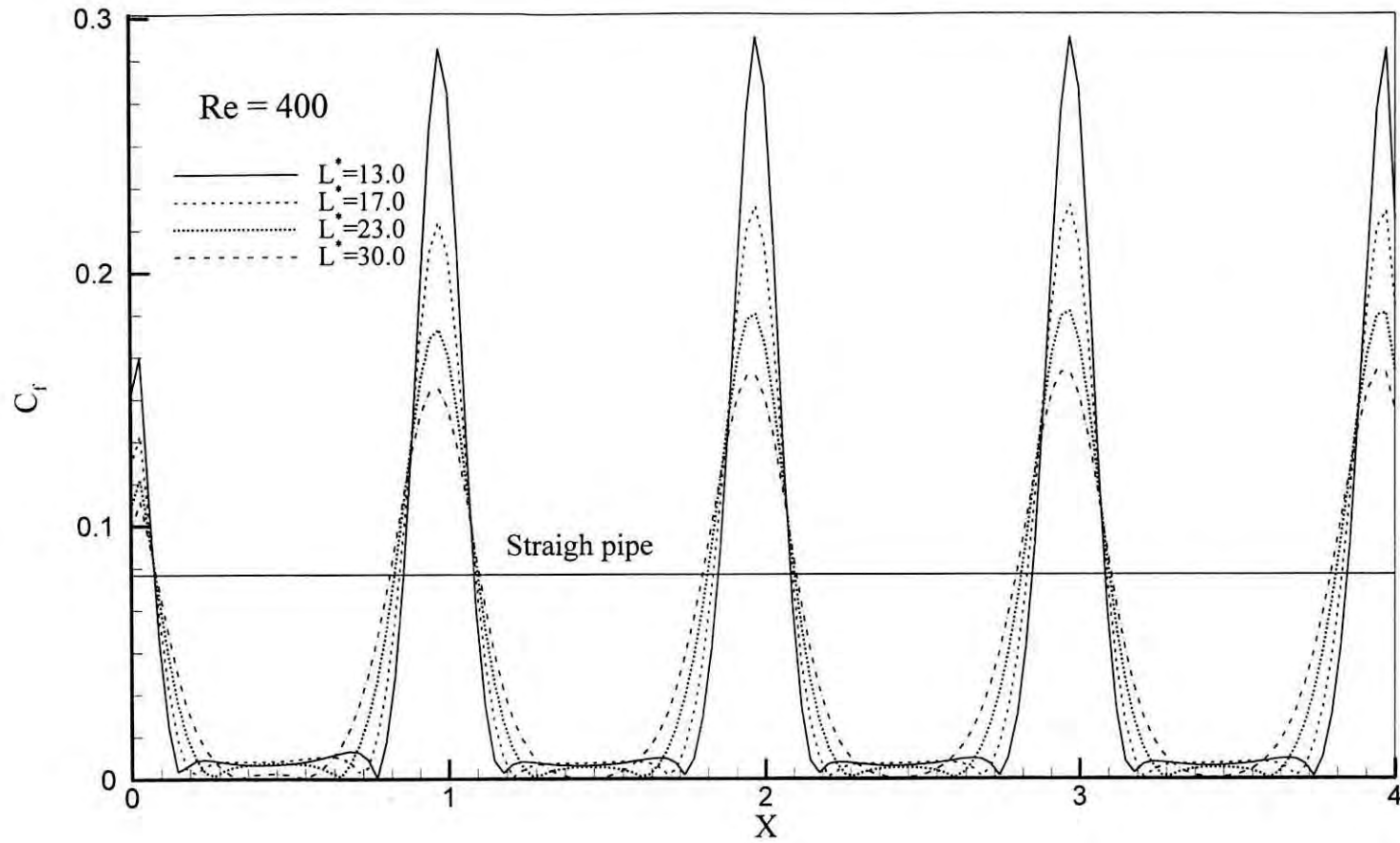


Fig. 4.39 Skin friction distribution along the wavy wall at $Re=400$ (axisymmetric case)

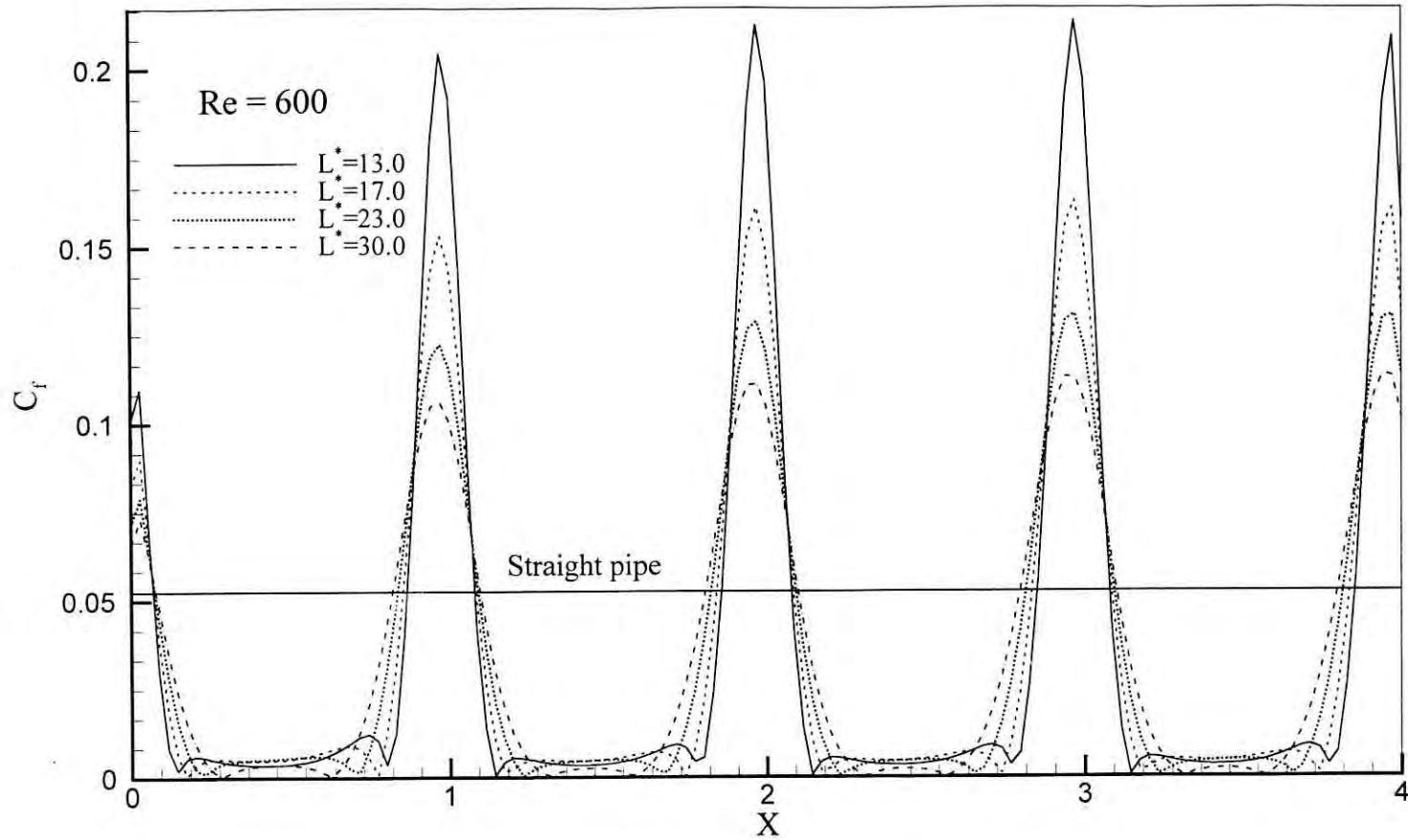


Fig. 4.40 Skin friction distribution along the wavy wall at $Re=600$ (axisymmetric case)

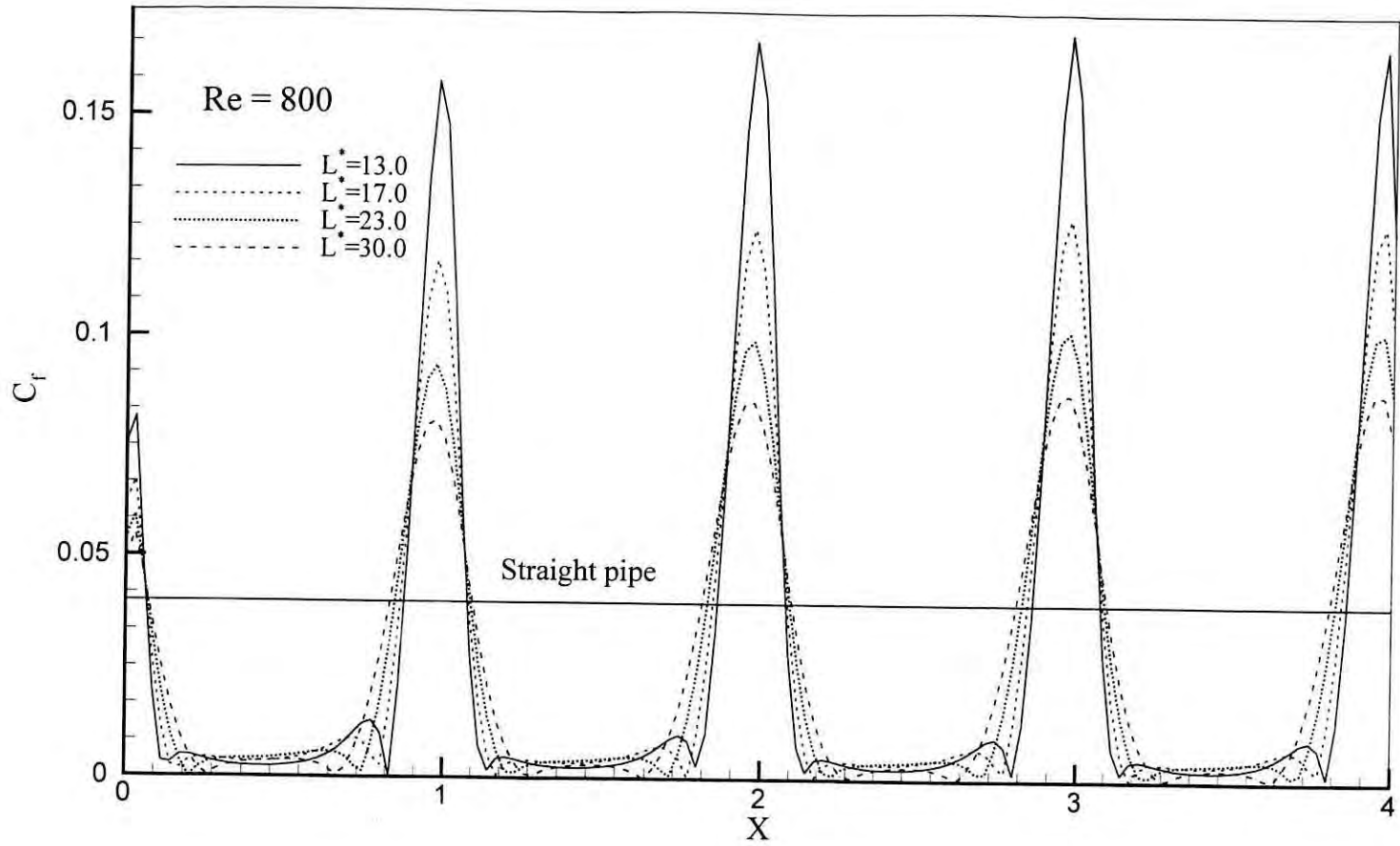


Fig. 4.41 Skin friction distribution along the wavy wall at $Re=800$ (axisymmetric case)

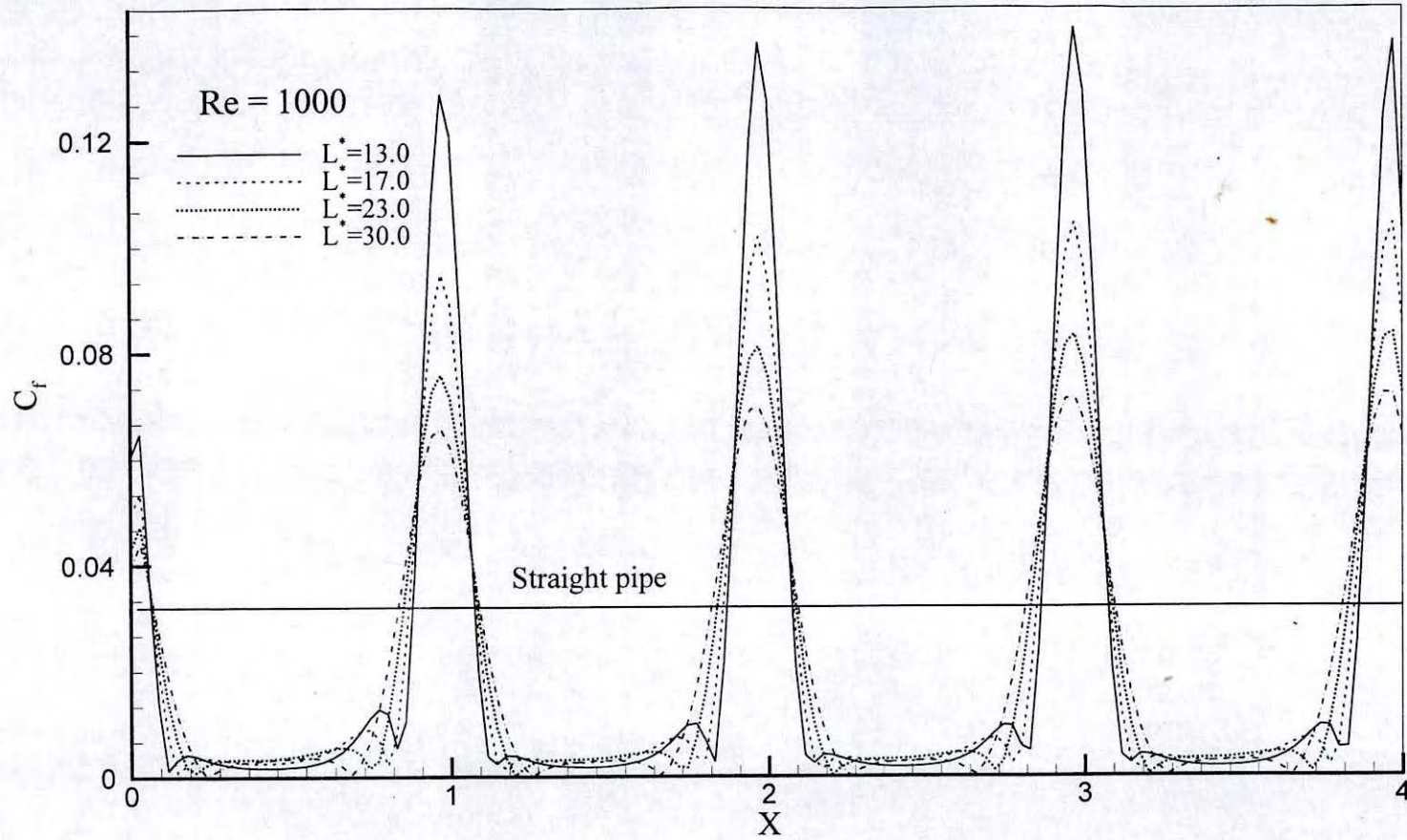


Fig. 4.42 Skin friction distribution along the wavy wall at $Re=1000$ (axisymmetric case)

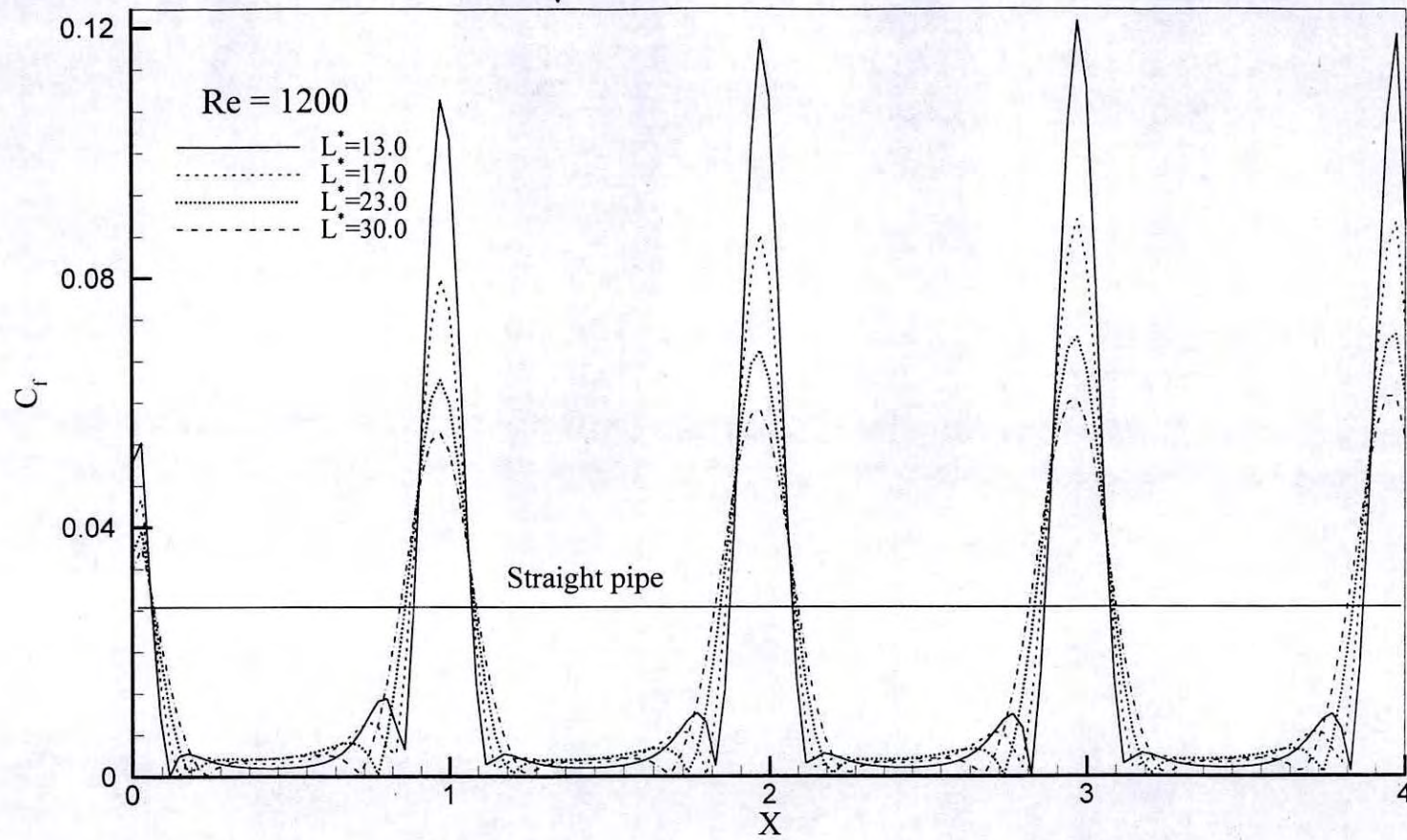


Fig. 4.43 Skin friction distribution along the wavy wall at $Re=1200$ (axisymmetric case)

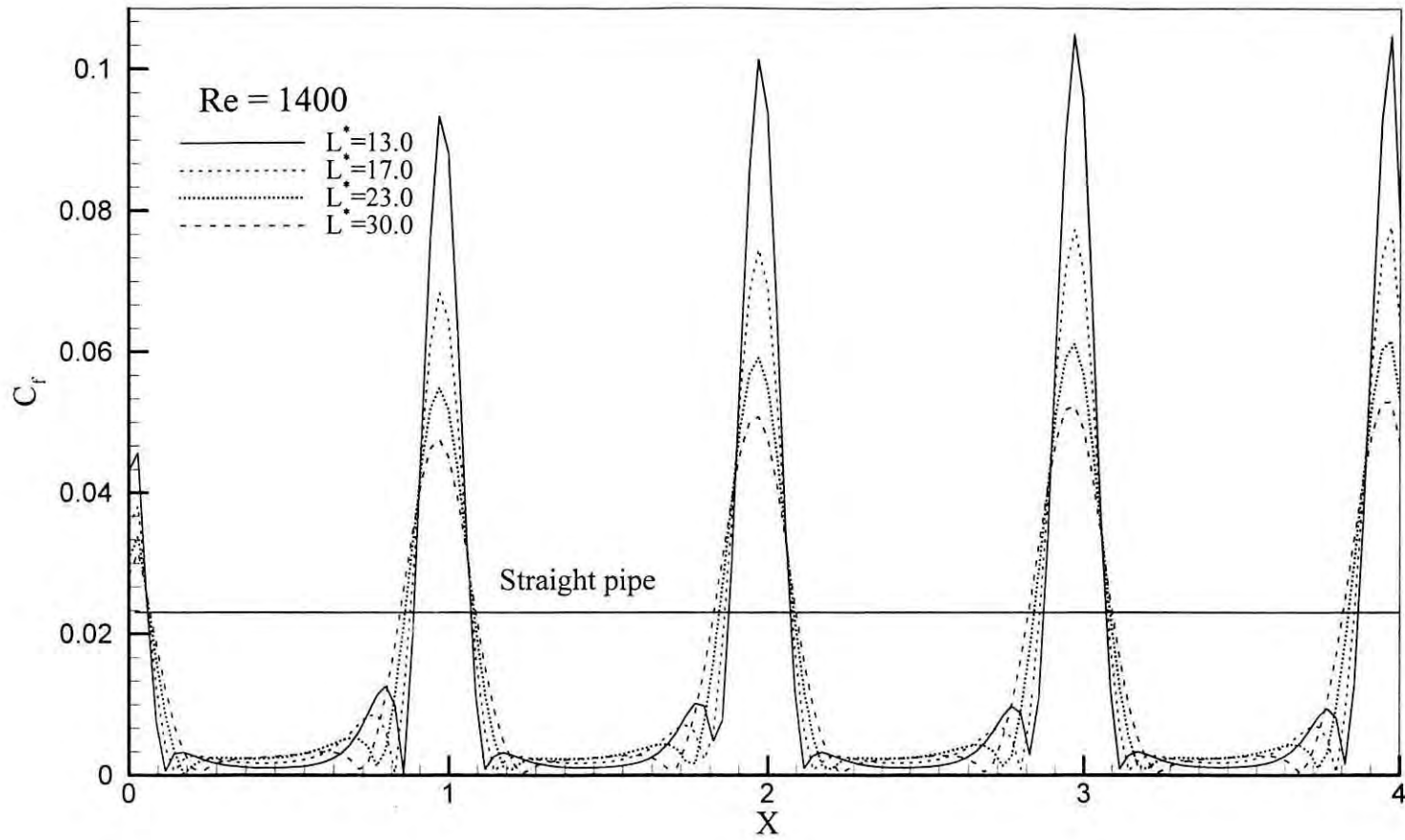


Fig. 4.44 Skin friction distribution along the wavy wall at $Re=1400$ (axisymmetric case)

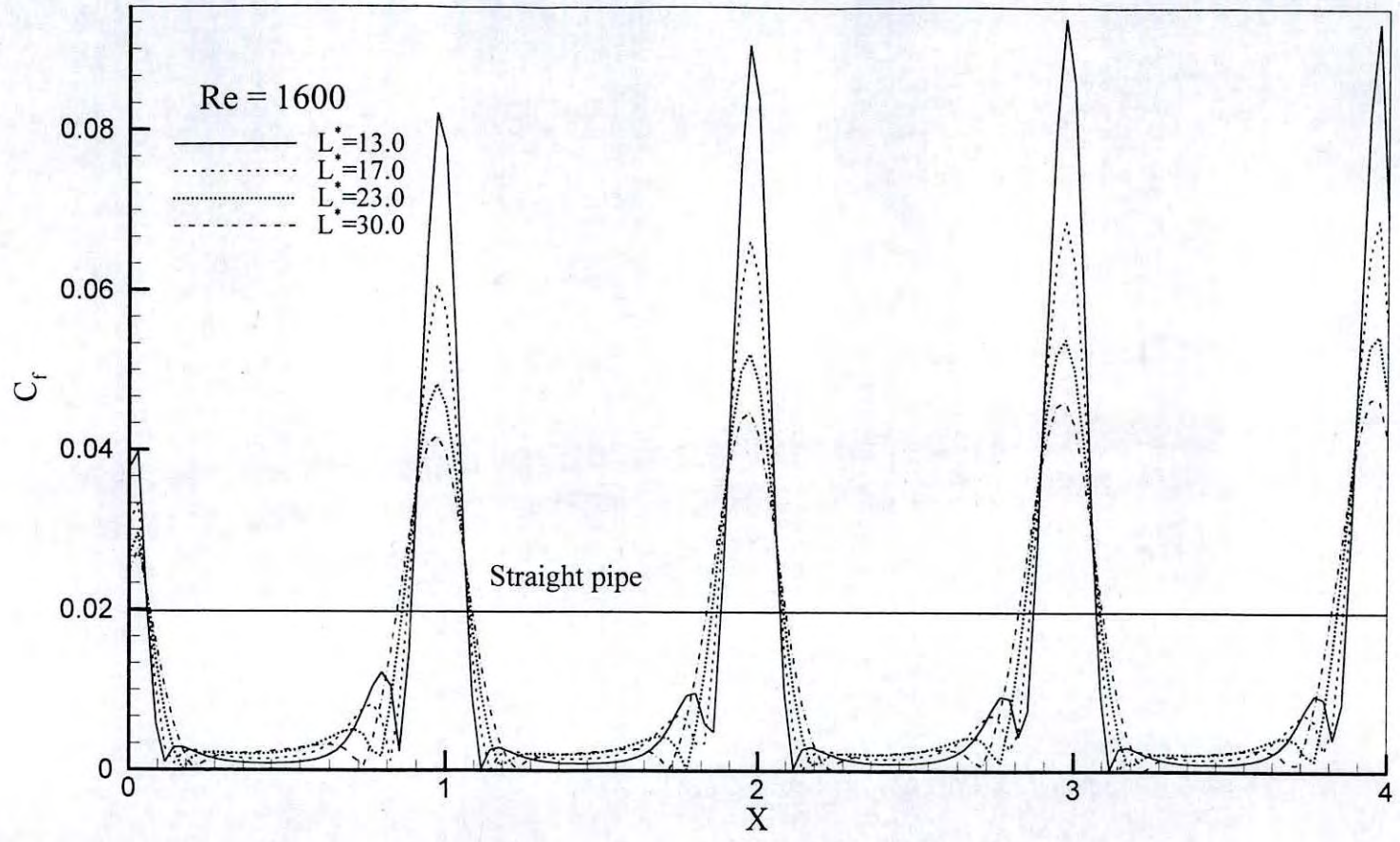


Fig. 4.45 Skin friction distribution along the wavy wall at $Re=1600$ (axisymmetric case)

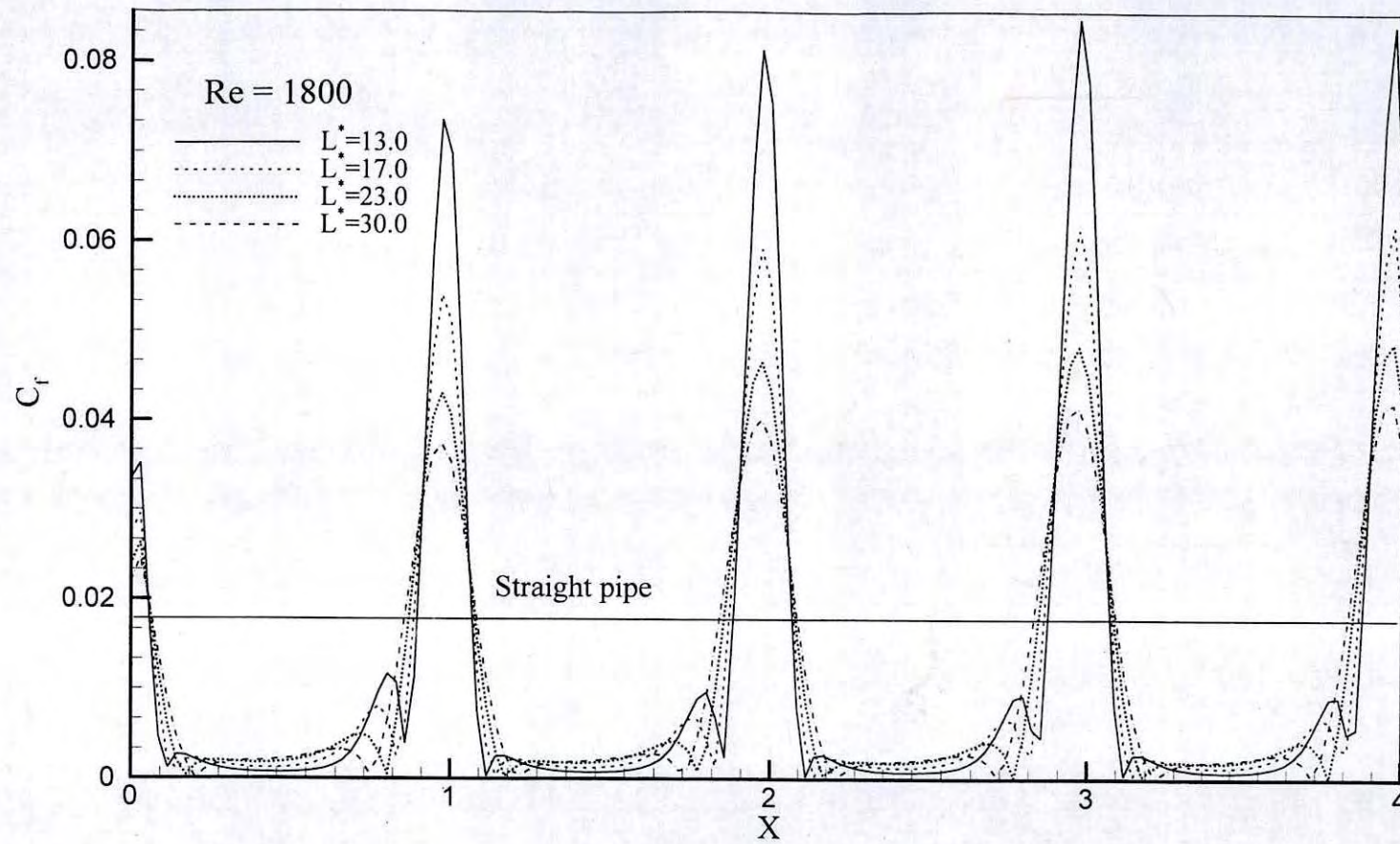


Fig. 4.46 Skin friction distribution along the wavy wall at $Re=1800$ (axisymmetric case)

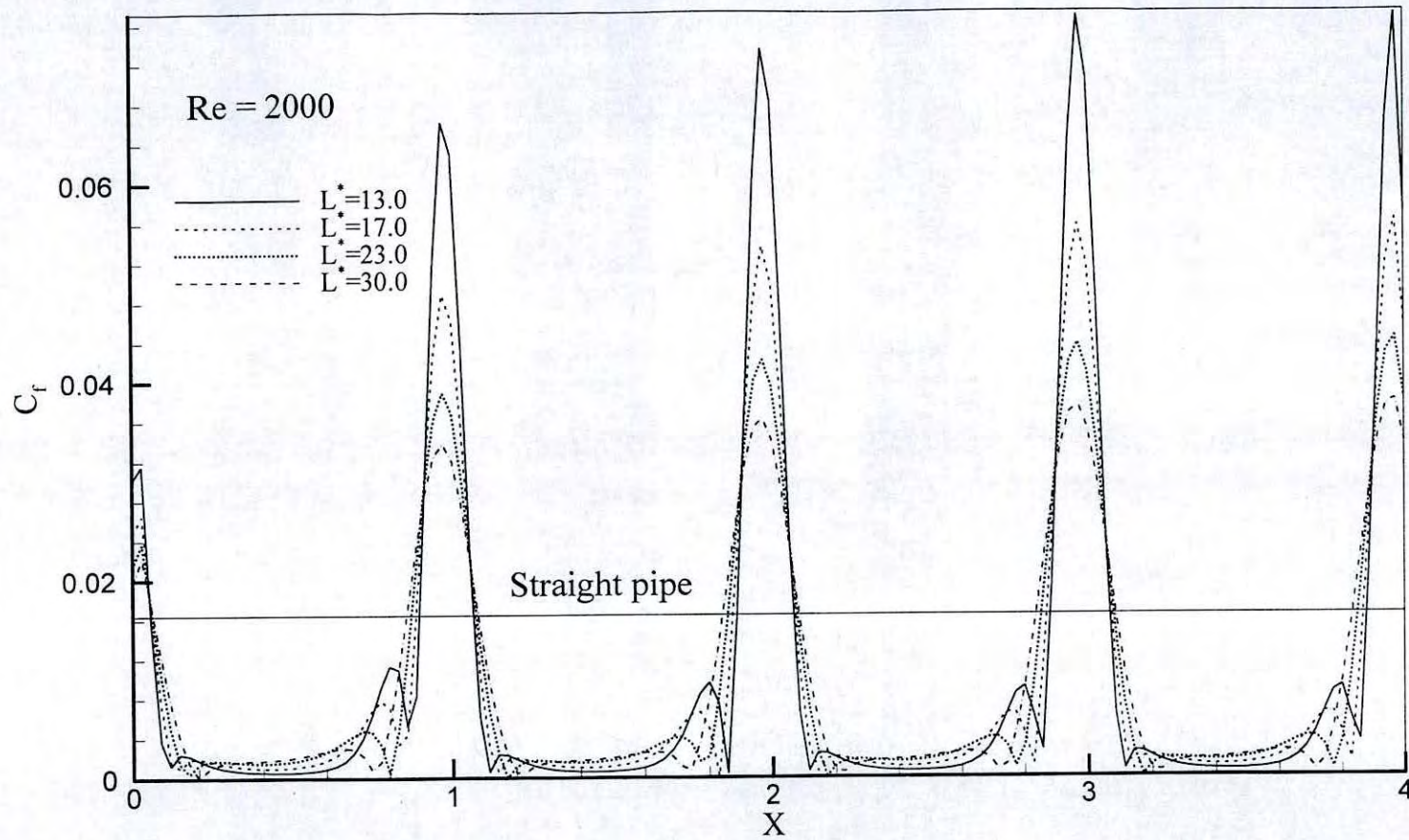


Fig. 4.47 Skin friction distribution along the wavy wall at $Re=2000$ (axisymmetric case)

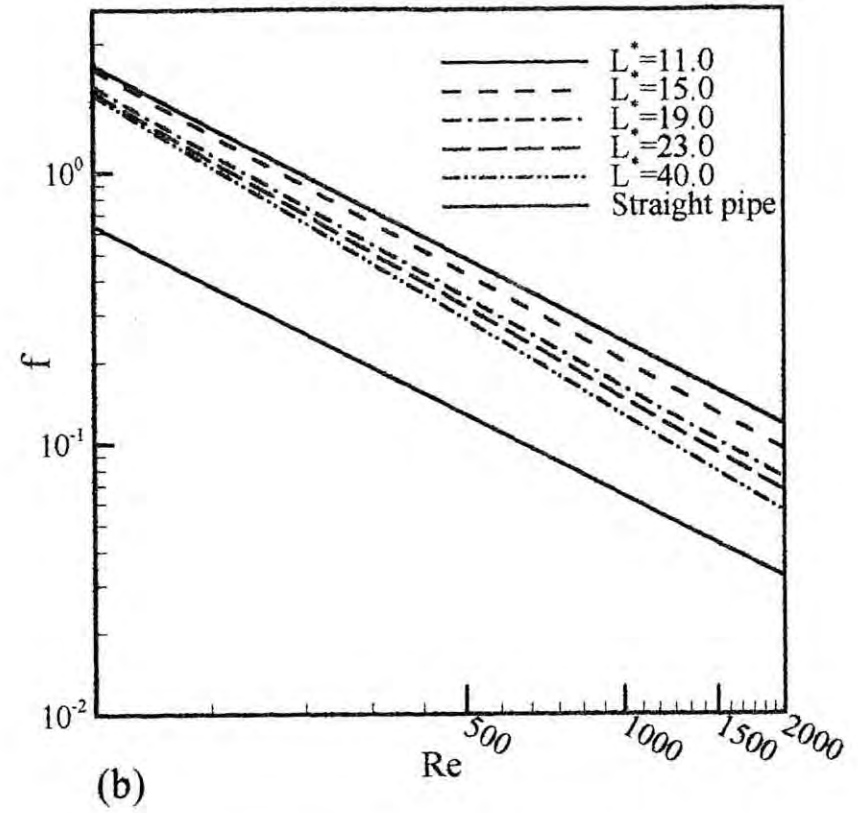
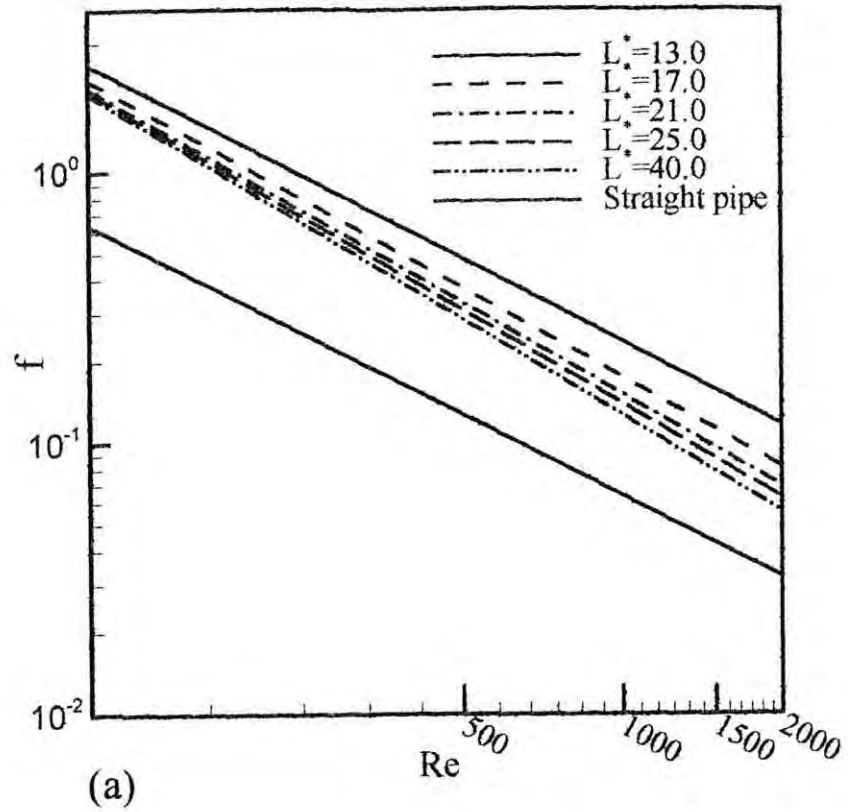


Fig.4.48 (a) & (b) Mean friction coefficient per wavelength for various geometry parameter L^* , (Axisymmetric geometry)

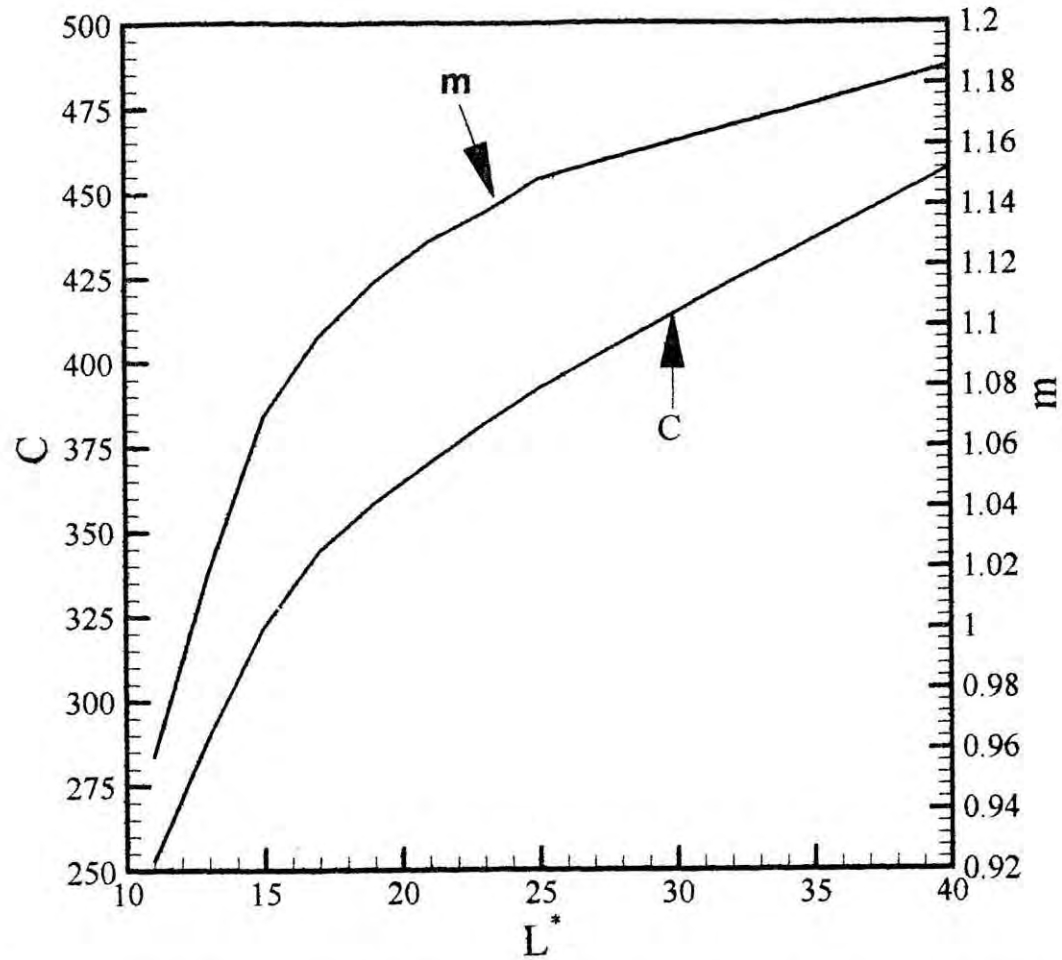


Fig.4.49 Variation of correlation constant (C) and correlation exponent (m) with L^*

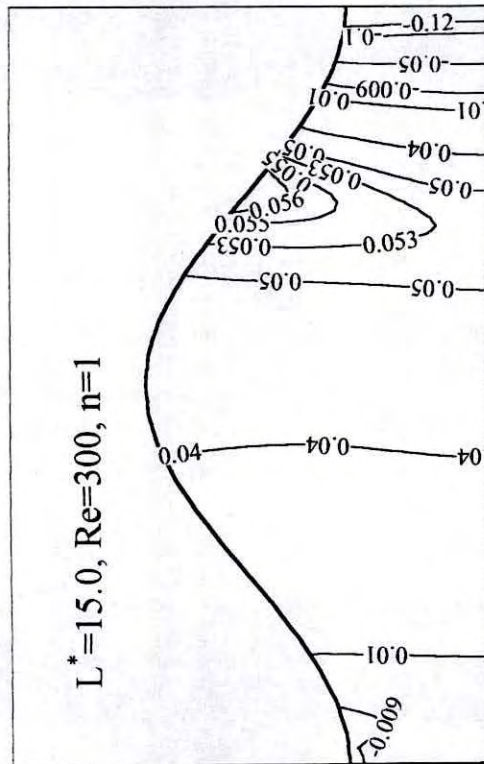
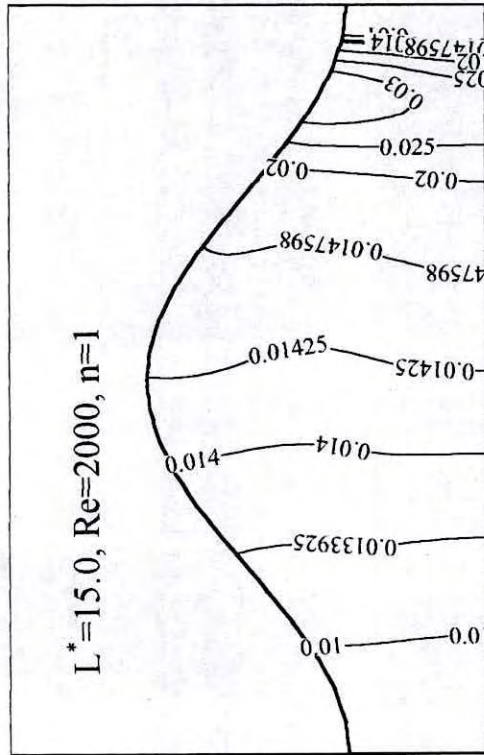


Fig.4.50 Isobars at Re=300 & 2000 for $L^* = 15.0$

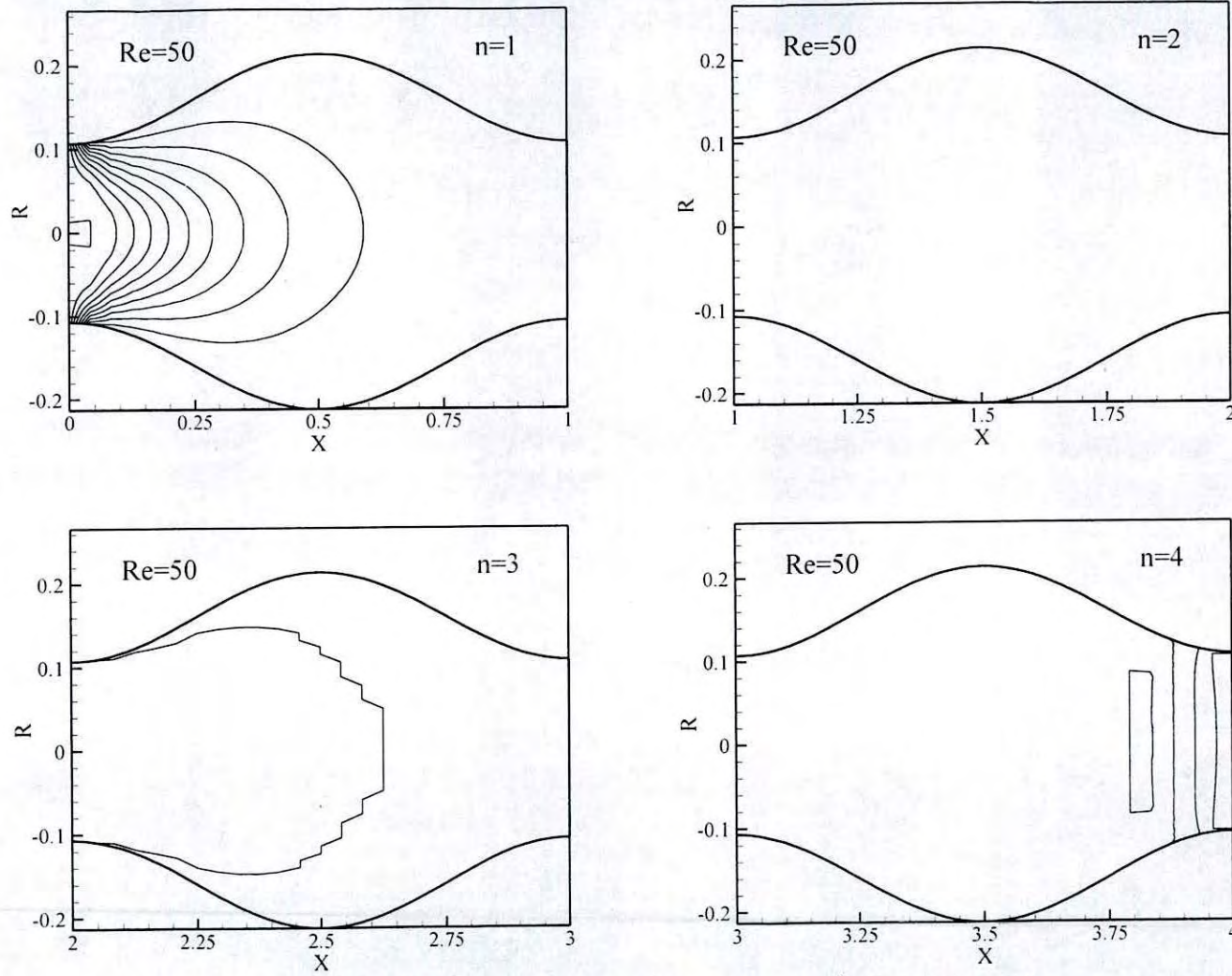


Fig. 4.51(a) Contours of normalized temperature for $n=1$ to 4, $L^*=19.0$ & $Re=50$

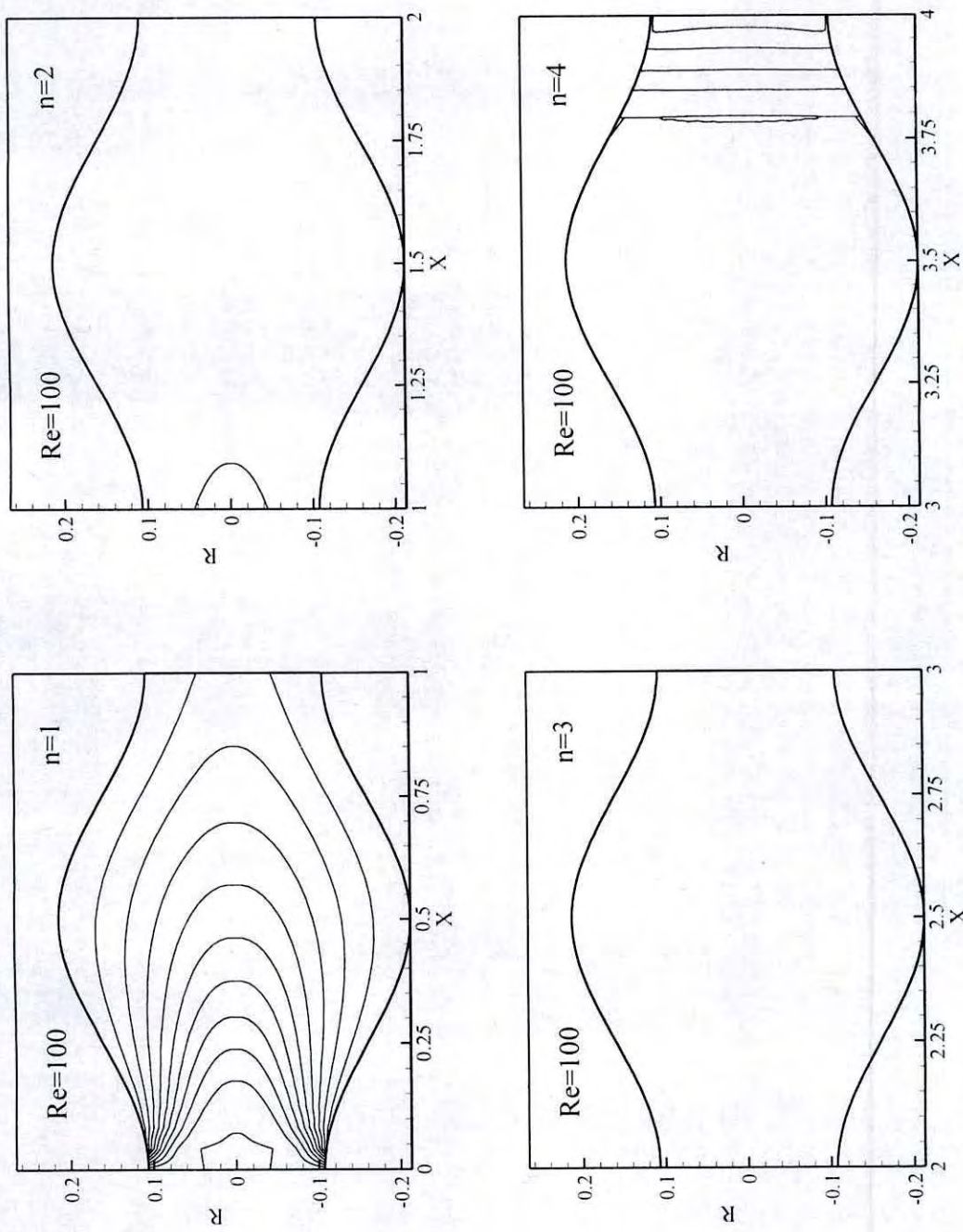


Fig. 4.51(b) Contours of normalized temperature for $n=1$ to 4 , $L^*=19.0$ & $Re=100$

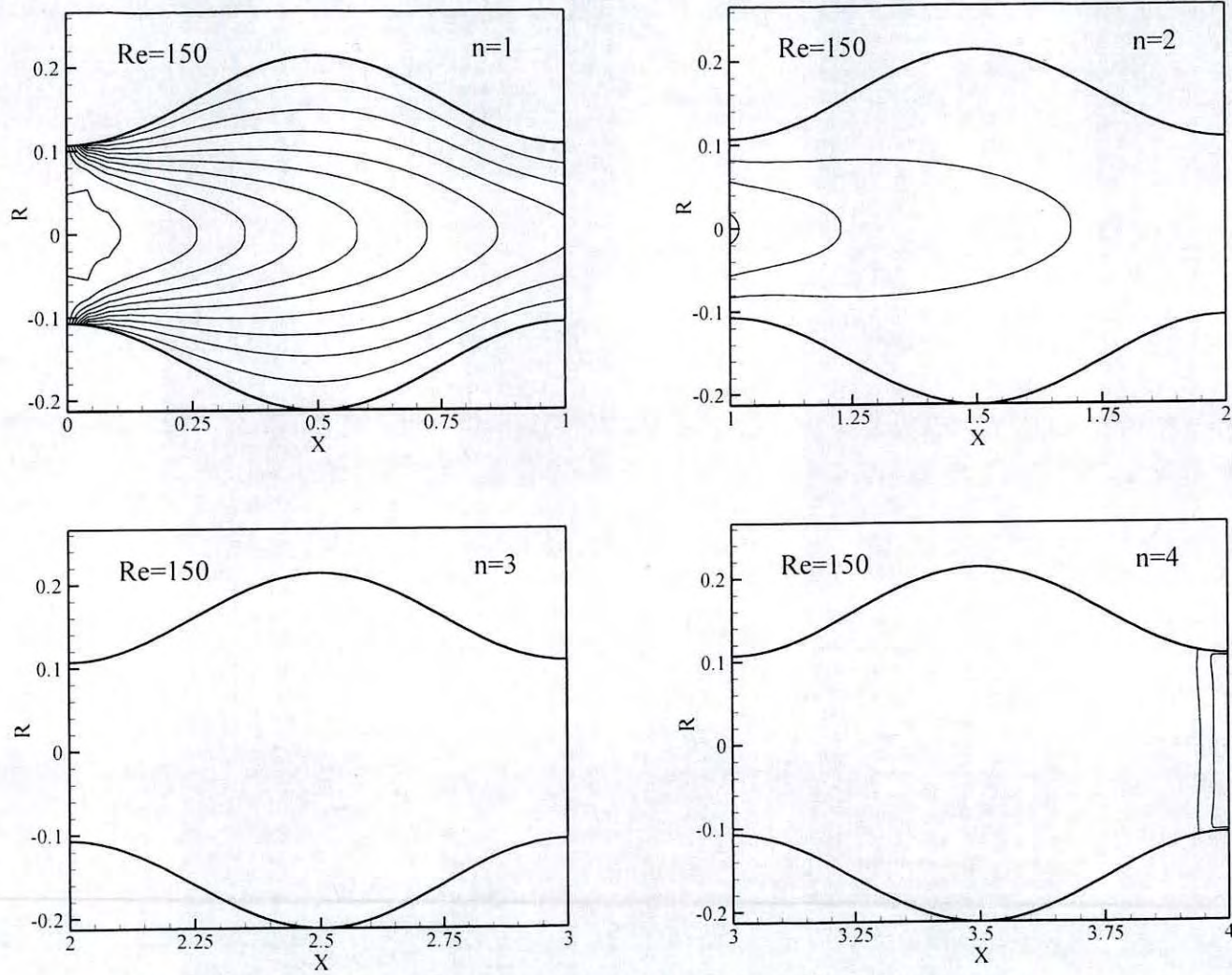


Fig. 4.51(c) Contours of normalized temperature for $n=1$ to 4, $L^*=19.0$ & $Re=150$

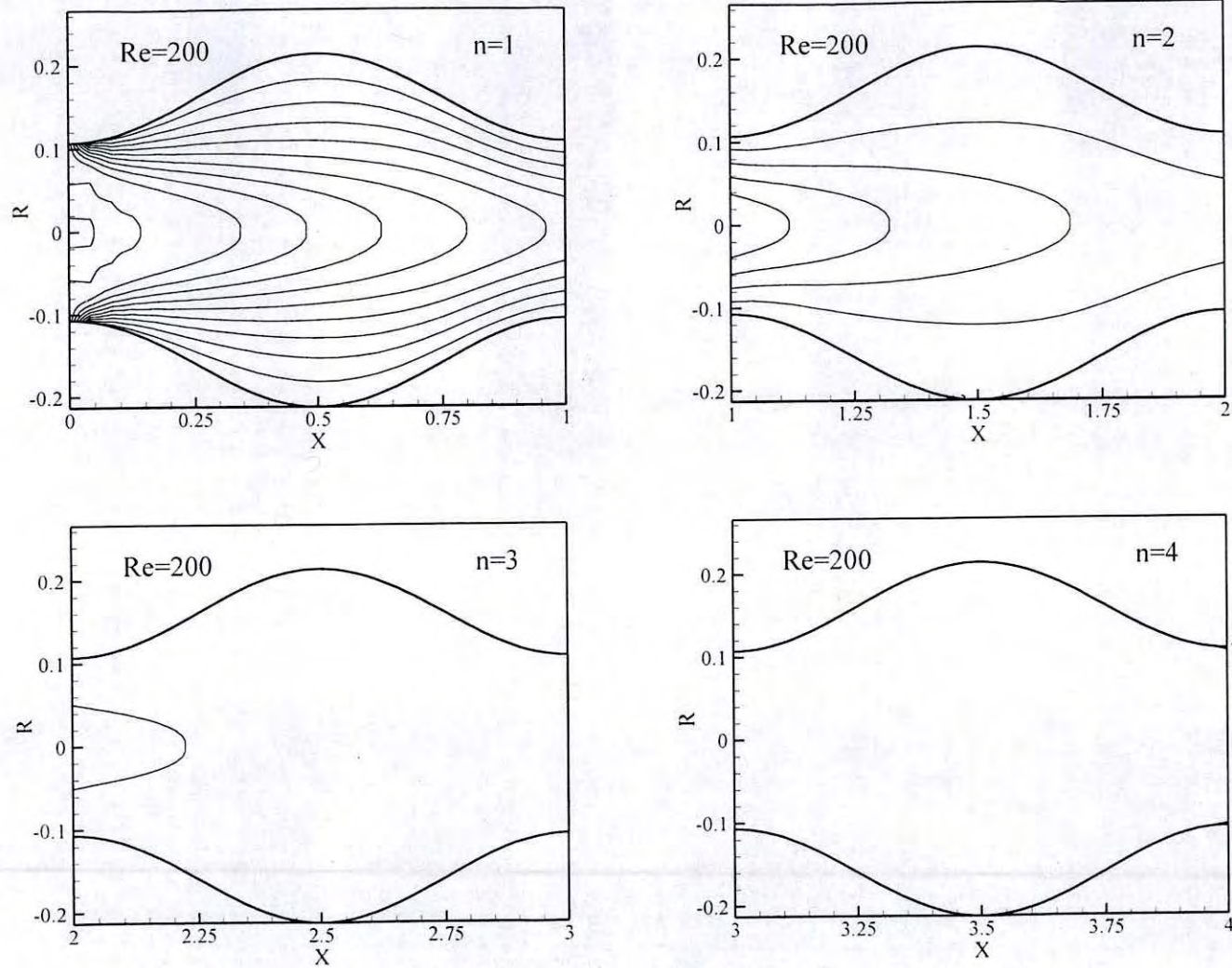


Fig. 4.51(d) Contours of normalized temperature for $n=1$ to 4, $L^*=19.0$ & $Re=200$

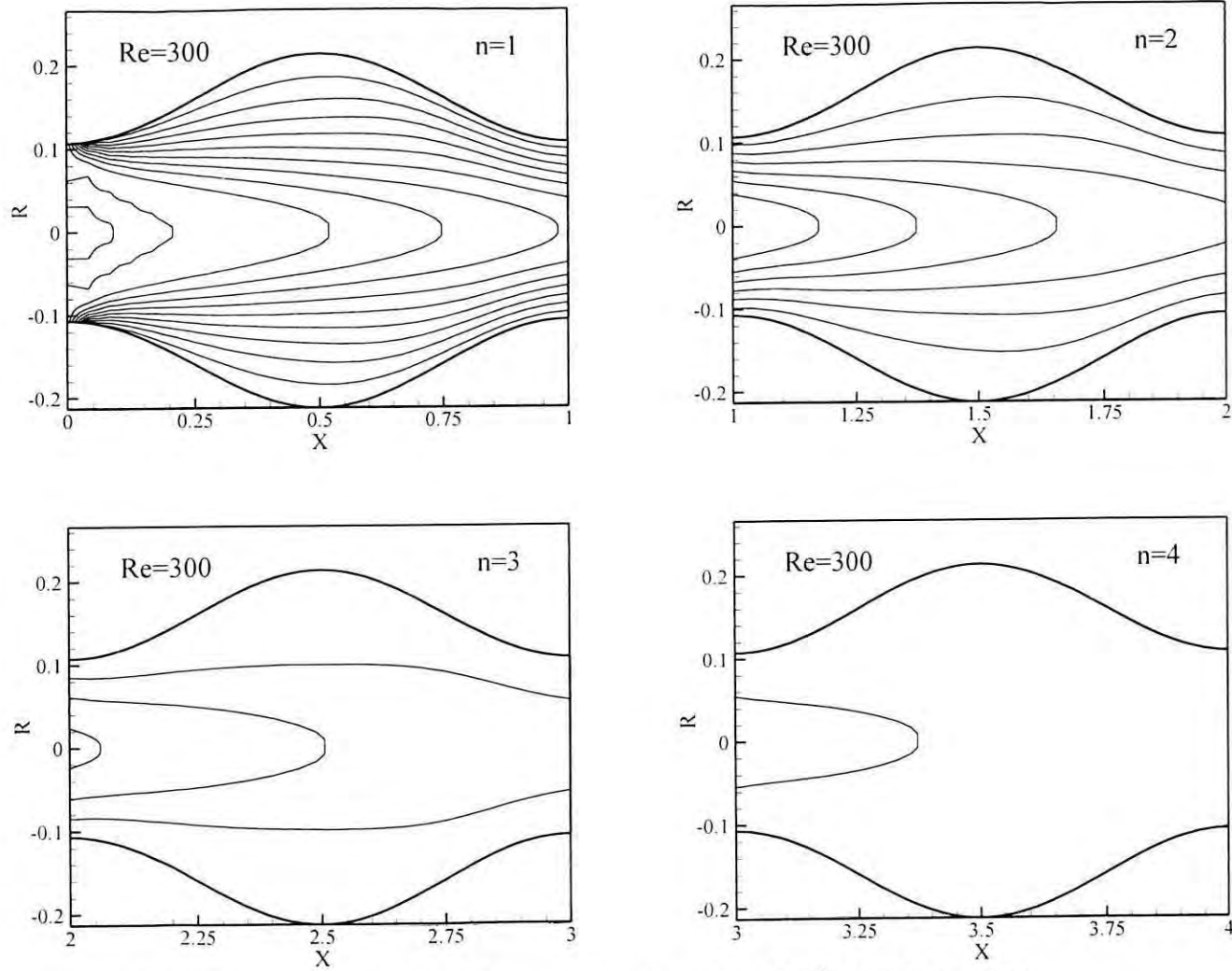


Fig. 4.51(e) Contours of normalized temperature for $n=1$ to 4, $L^*=19.0$ & $Re=300$

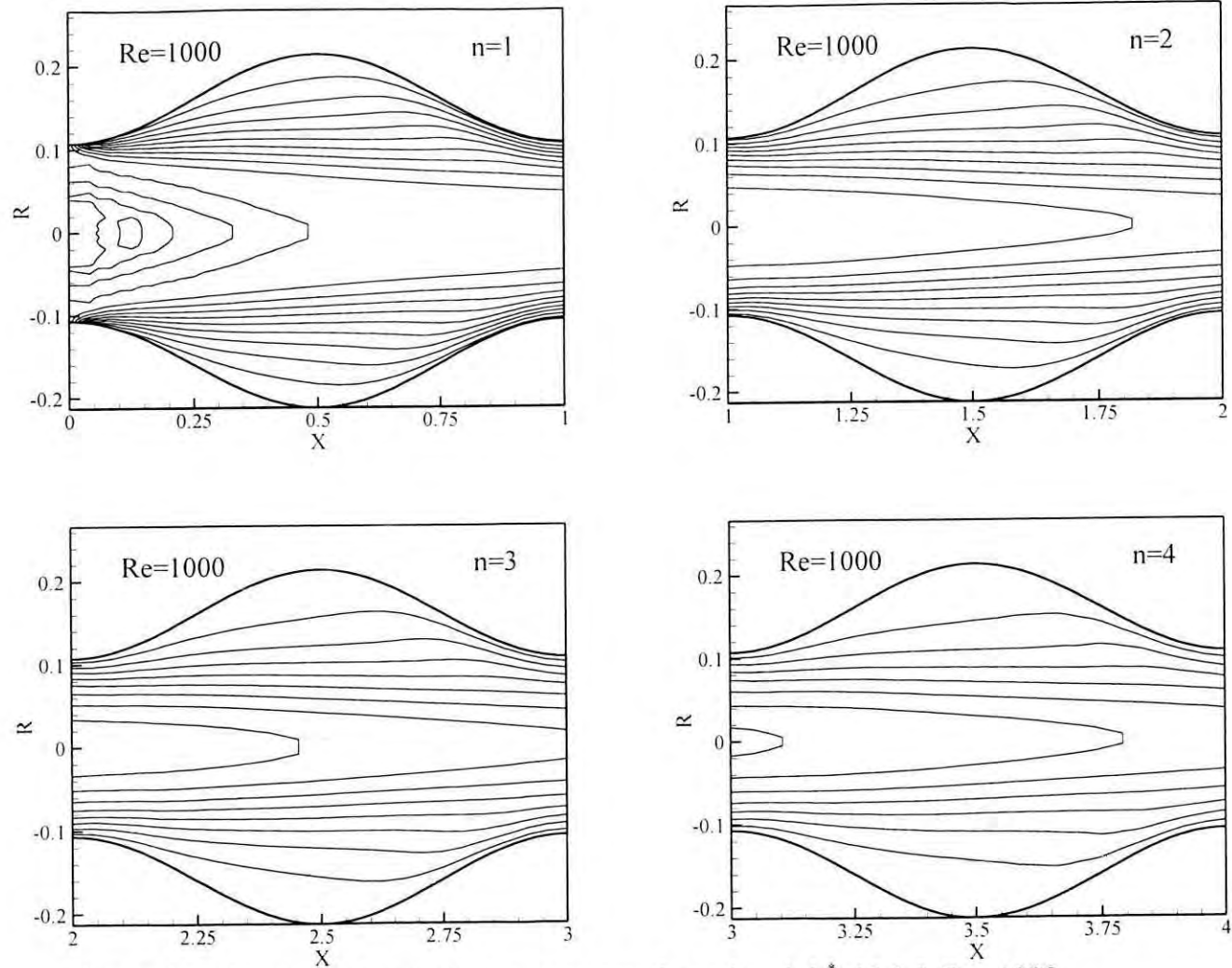


Fig. 4.51(f) Contours of normalized temperature for $n=1$ to 4, $L^*=19.0$ & $Re=1000$

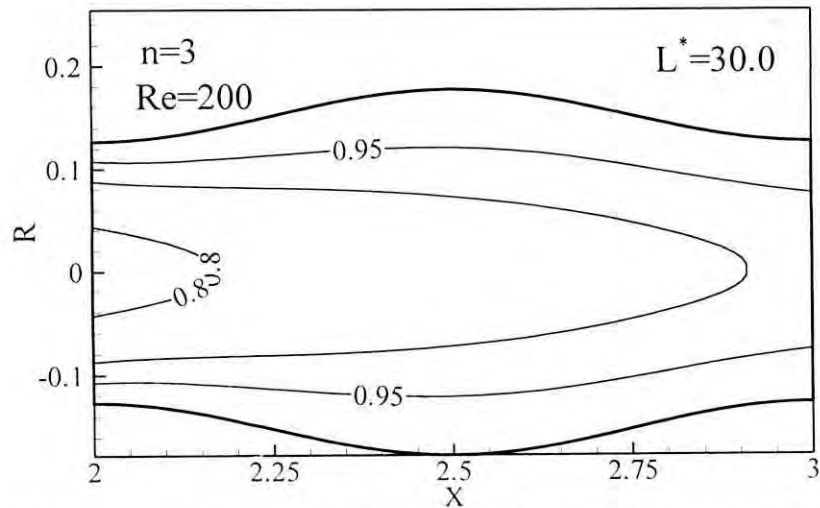
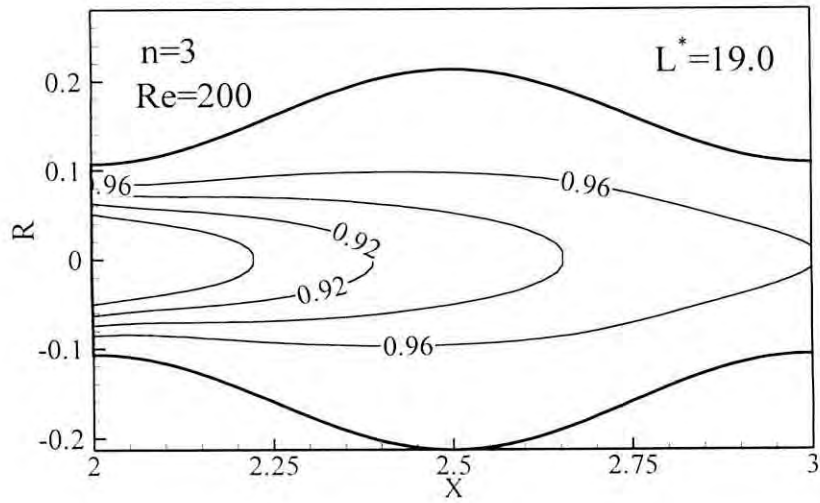
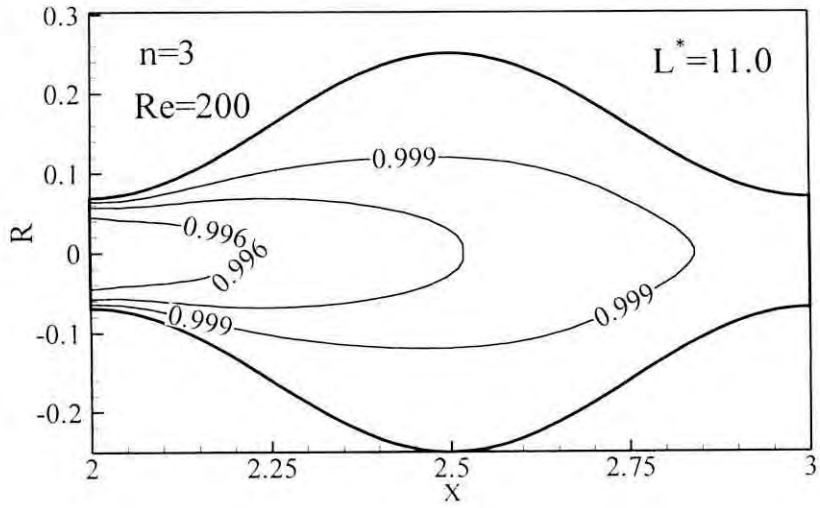


Fig.4.52 Contours of normalized temperature for third cycle & $Re=200$ for $L^*=11.0, 19.0, 30.0$

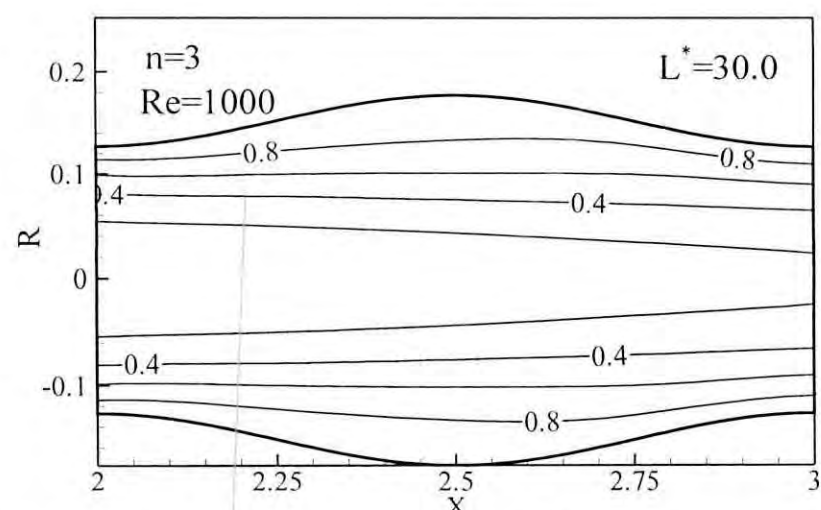
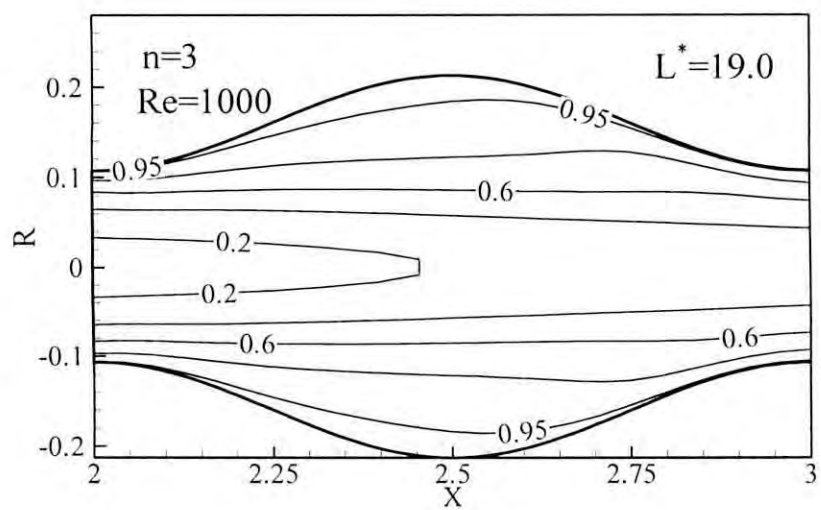
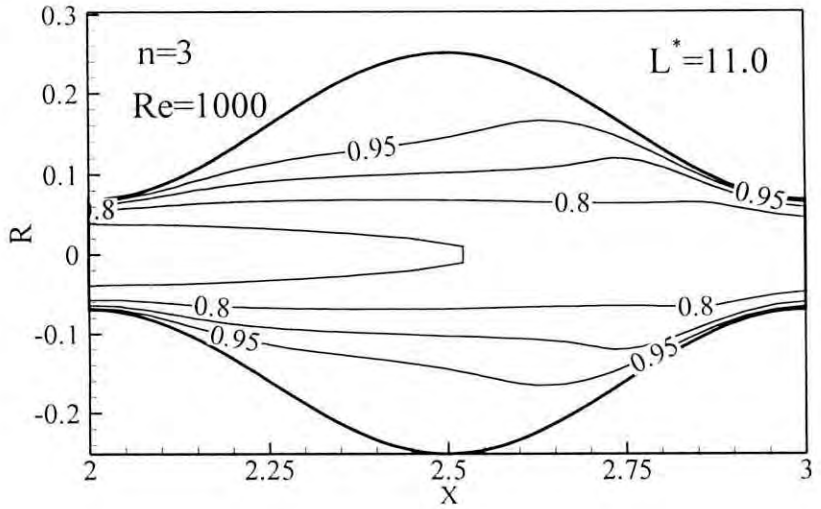


Fig.4.53 Contours of normalized temperature for third cycle & $Re=1000$ for $L^*=11.0, 19.0, 30.0$

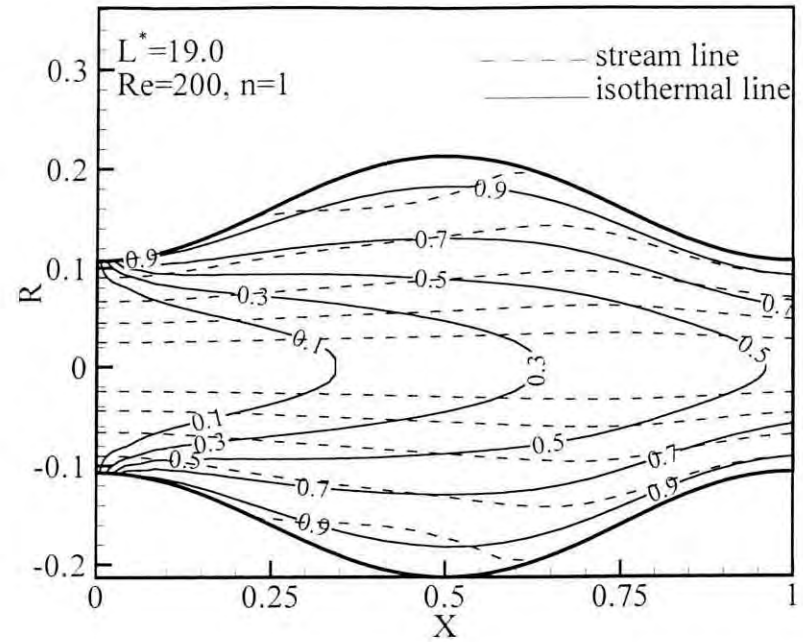
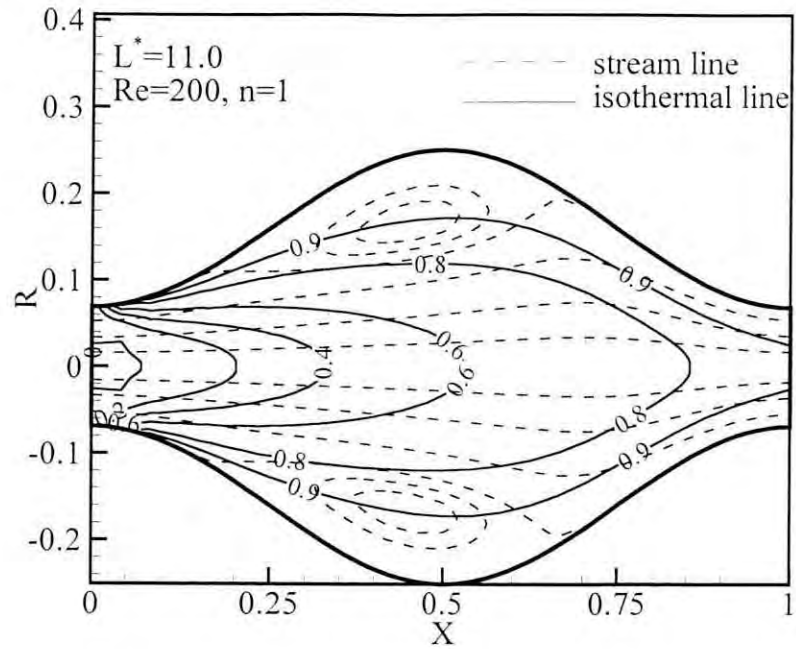


Fig. 4.54 Combination of streamlines and isothermal lines for first cycle at $Re=200$ & $L^*=11.0$ & 19.0 , ($\Delta\theta=0.2$, $\Delta\psi=0.2$)

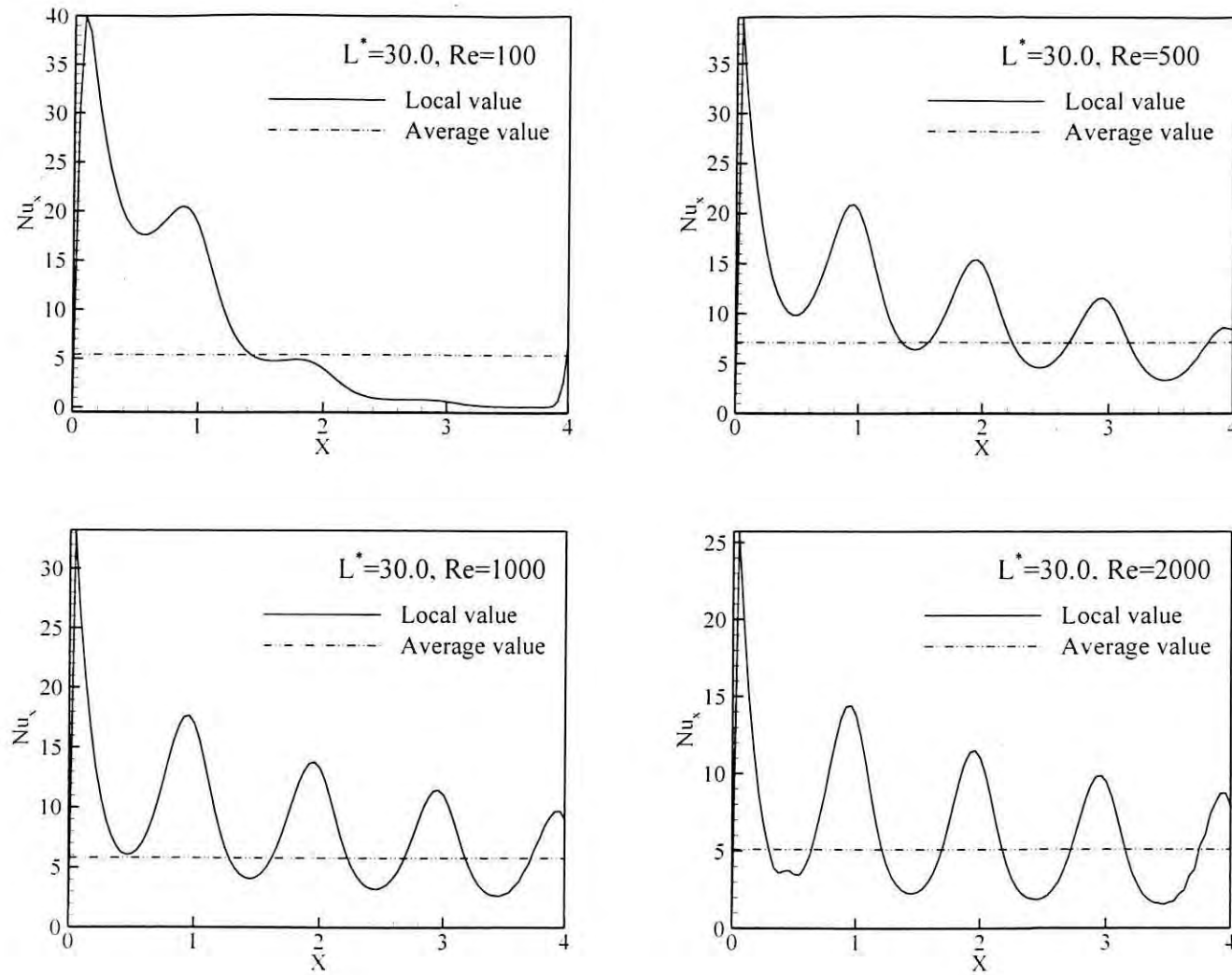


Fig. 4.55 Distribution of local Nusselt number as a function of channel length for $L^* = 30.0$

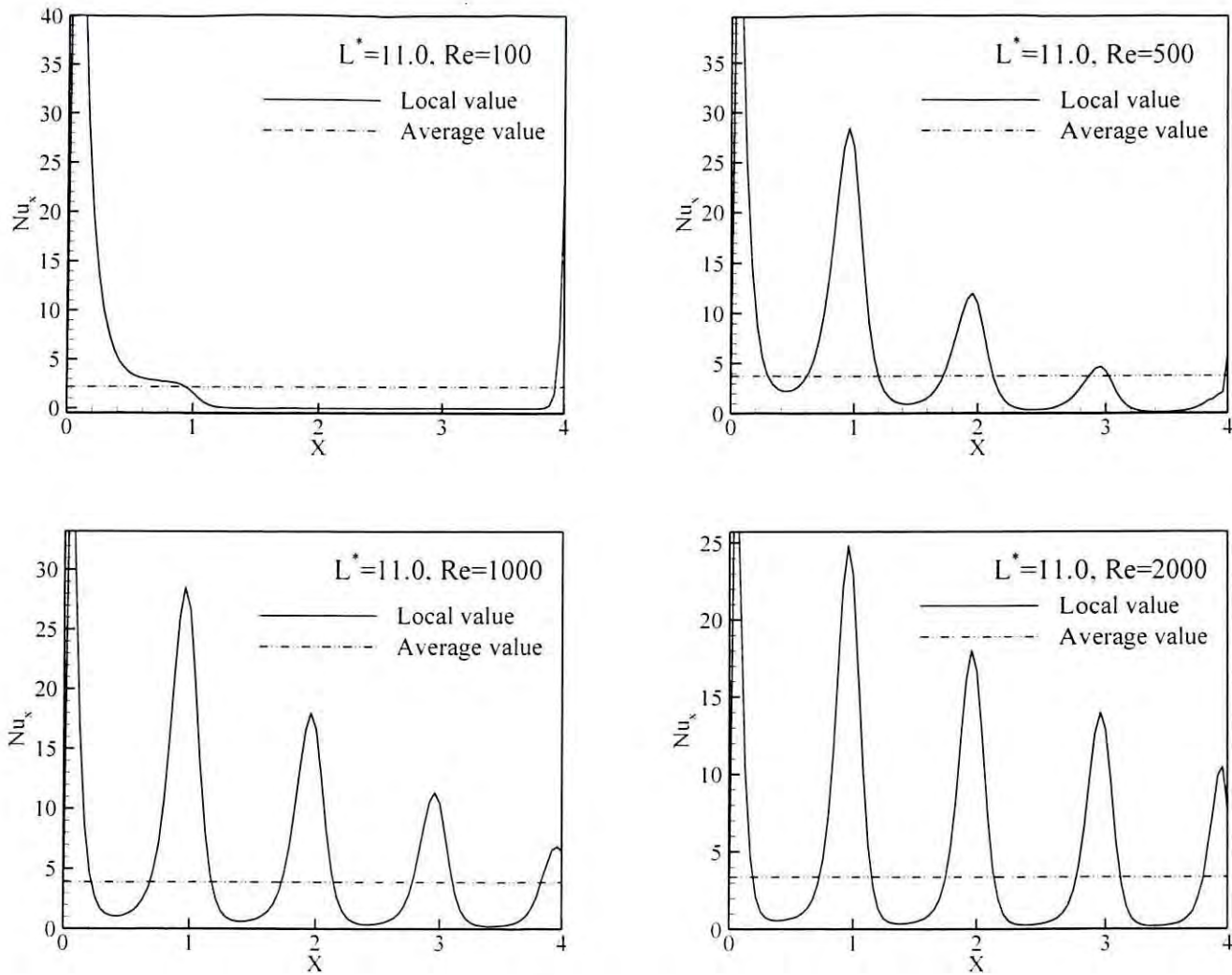


Fig. 4.56 Distribution of local Nusselt number as a function of channel length for $L^* = 11.0$

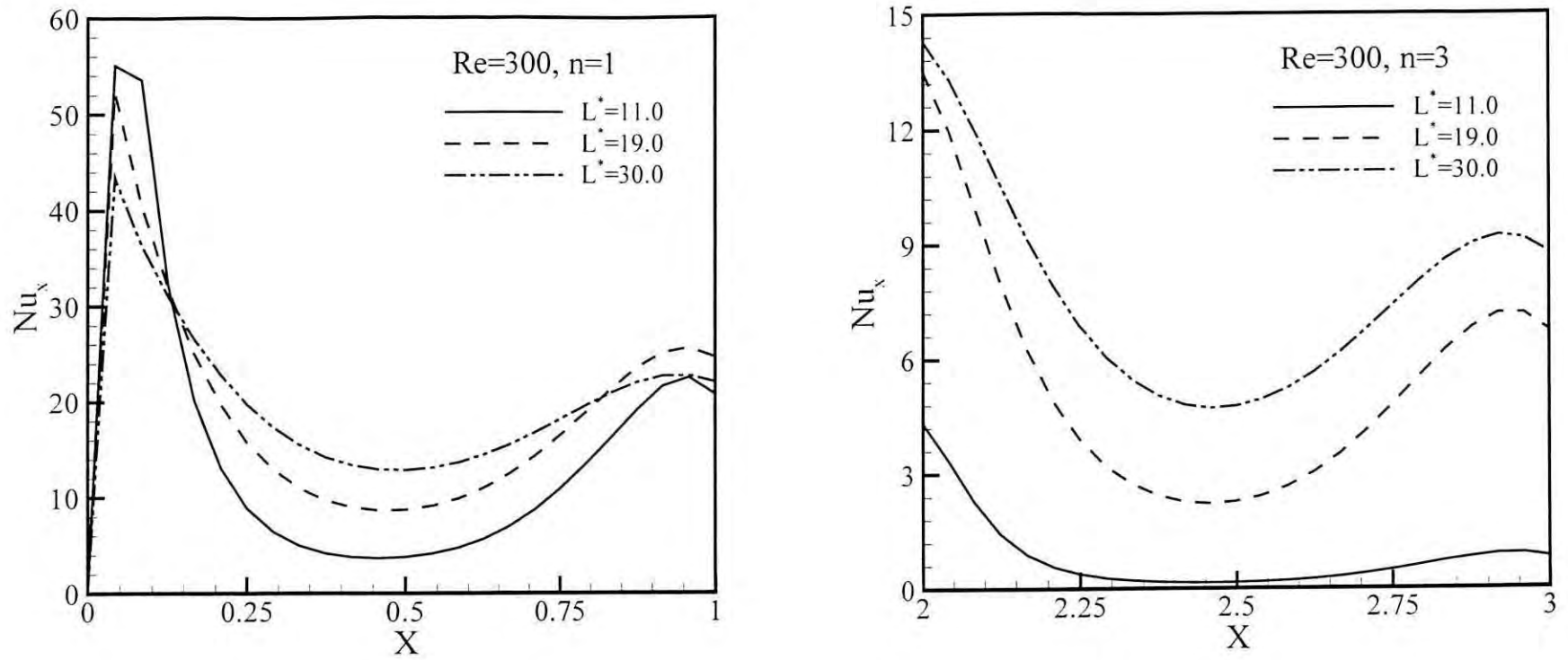


Fig. 4.57 Local Nusselt number distribution for first and third cycles, $Re=300$ & $L^* = 11.0, 19.0, 30.0$

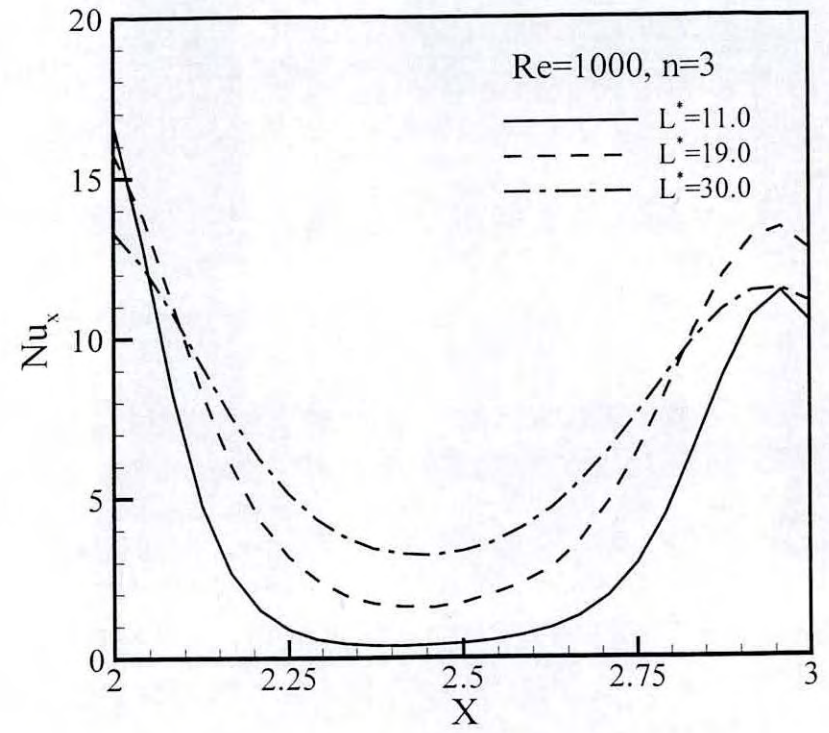
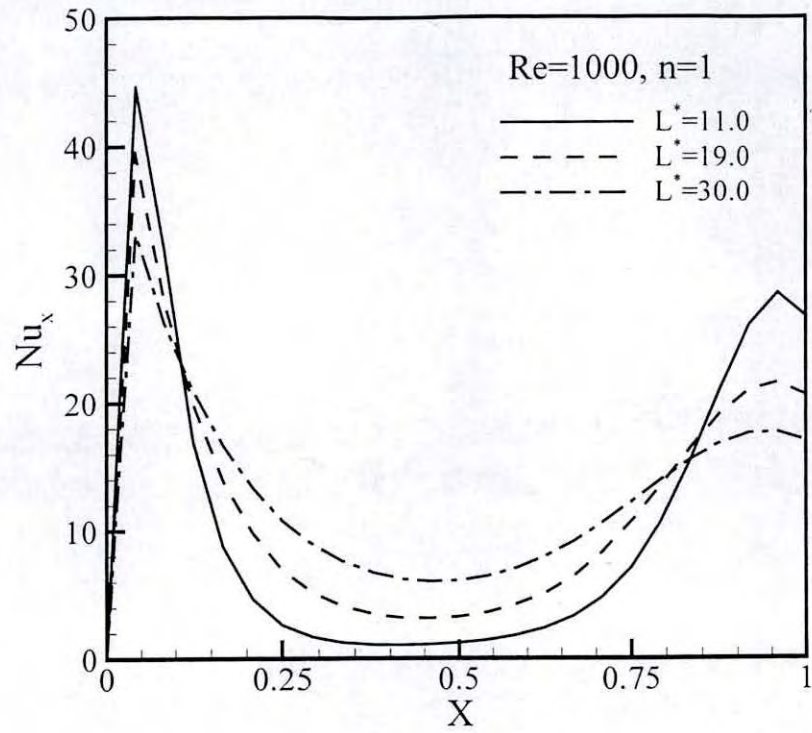
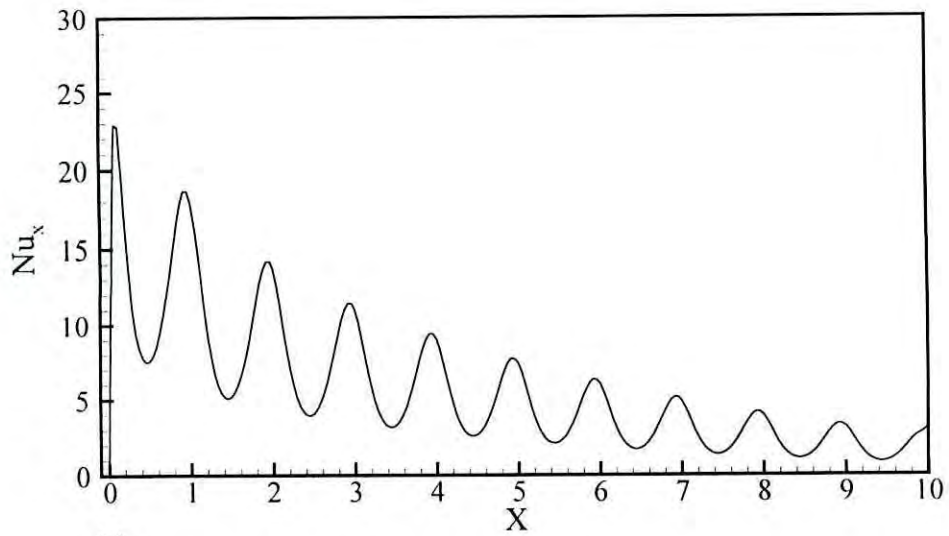
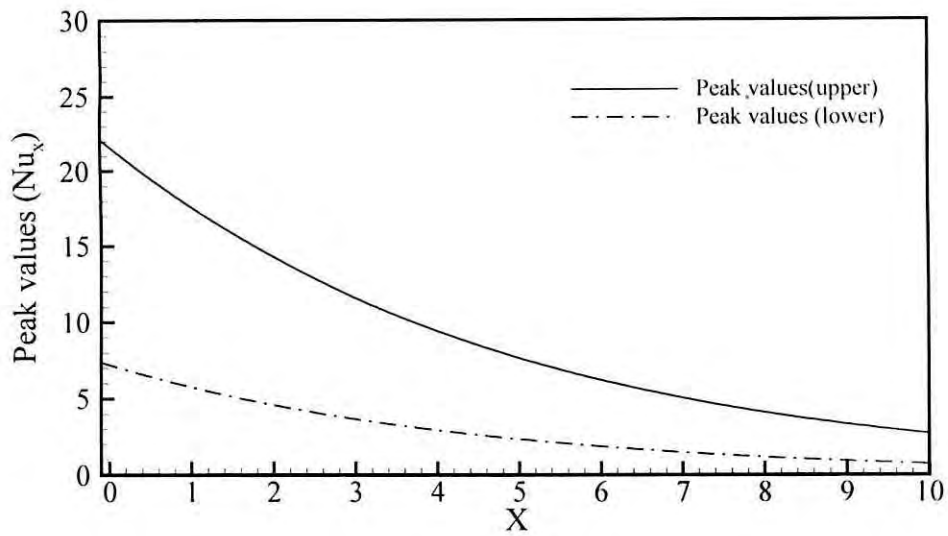


Fig. 4.58 Local Nusselt number distribution for first and third cycles, $Re=1000$ & $L^* = 11.0, 19.0, 30.0$



(a)



(b)

Fig. 4.59 (a) Local Nusselt number distribution for 10 wave for $L^*=19.0$, $Re=300$
 (b) Decay of upper & lower peak values of Nusselt number along the channel for each cycle for $L^*=19.0$, $Re=300$

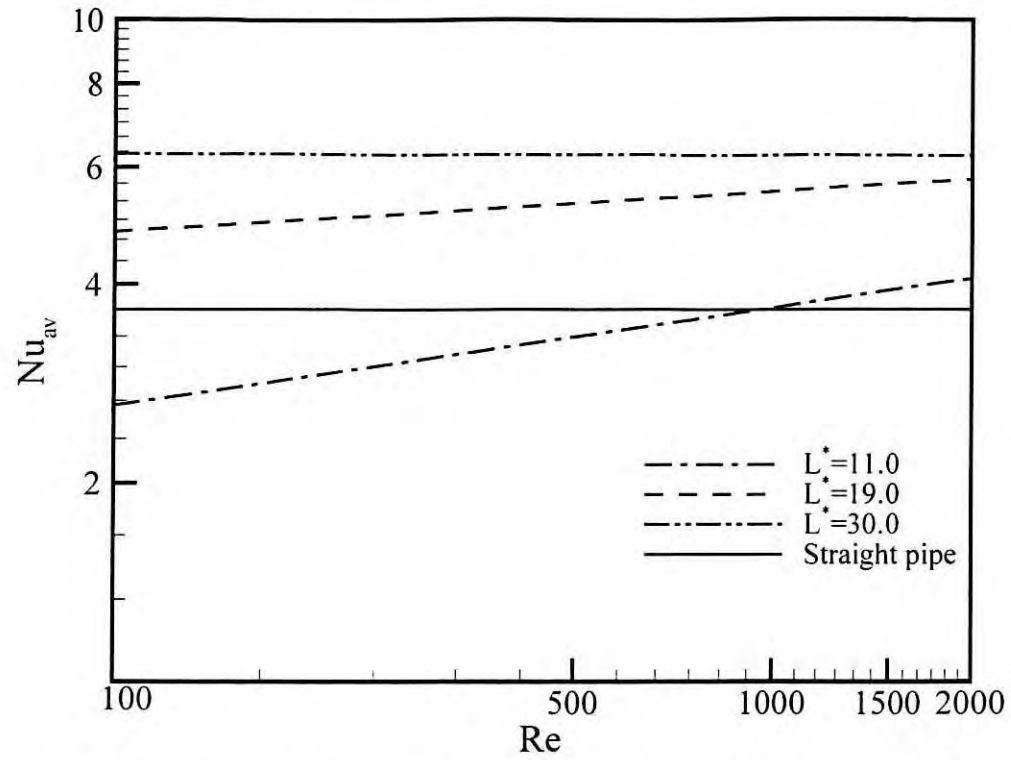


Fig. 4.60 Distribution of average values of Nusselt number per wavelength with Reynolds numbers at different geometric parameter L^*

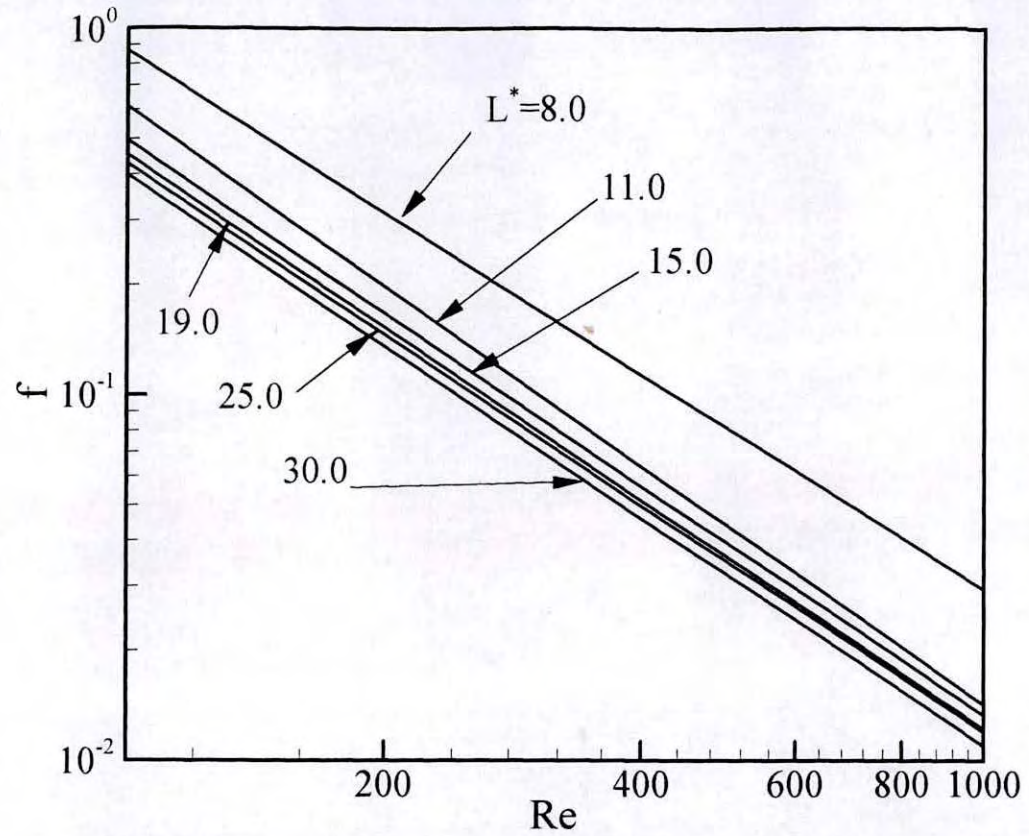


Fig.4.61 Mean friction coefficient per wave length as a function of Reynolds number for plane geometry at $L^* = 8.0, 11.0, 15.0, 19.0, 25.0, 30.0$

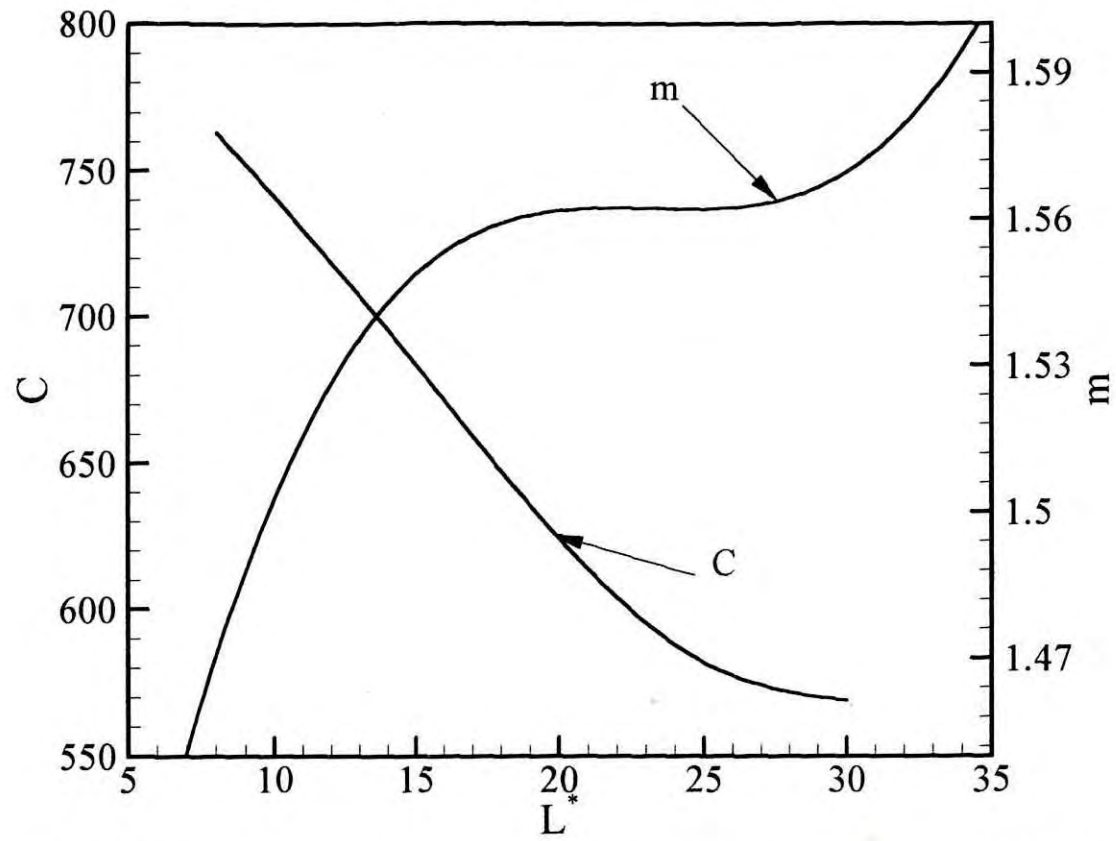


Fig.4.62 Variation of correlation constant (C) and correlation exponent m with L^*

